SOFTWARE-IN-THE-LOOP APPLICATIONS FOR IMPROVED PHYSICAL MODEL TESTS OF OCEAN RENEWABLE ENERGY DEVICES USING ARTIFICIAL INTELLIGENCE

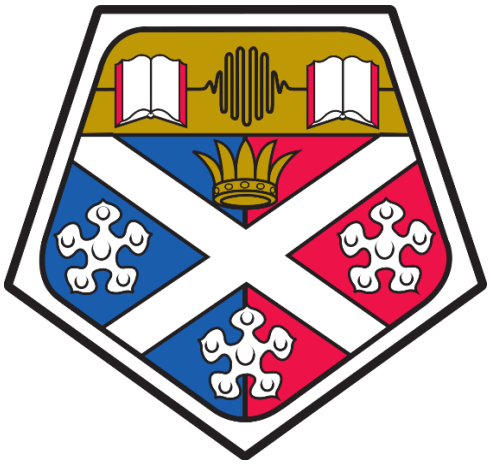

Xue Jiang

Department of Naval Architecture, Ocean and Marine Engineering

University of Strathclyde

This thesis is submitted for the degree of Doctor of Philosophy

July 2020

This page is left blank intentionally

To my mother, for her unconditional love;

My supervisor Longbin Tao, who teaches me;

Atilla Incecik, who advises me and supports me;

without them, none of this work would have been possible.

DECLARATION

This thesis is the result of my own original work and includes nothing, which is the outcome of work done in collaboration except where specifically indicated in the text. It has not been previously submitted, in part or whole, to any university or institution for any degree, diploma, or other qualification. The copyright thereof belongs to the author under the terms of United Kingdom Copyright Acts as clarified by Strathclyde University Regulation 3.50.

Signed: Xue Jiang

Date: 12.07.2020

Xue Jiang

Strathclyde

ABSTRACT

Experimental research in laboratory is a necessary and useful method to explore the full potential of a device. Because it does not only require much less money than the prototype at sea test, it also provides more reliable results compared to numerical simulations. Hence, it is significantly vital to make accurate model tests of the concerned ocean renewable energy (ORE) devices possible. For this reason, this study for a PhD degree has been finished and a thesis, therefore, is produced.

There is a need for a method to provide linear or nonlinear real-time power-take-off forces to the wave energy converting mechanism in the water during the experiment. More urgently, it is essential to overcome the discrepancy caused by following Froude-scaling law and Reynold-scaling law in the test of a model-scaled FOWT. Two applications for WECs and FOWTs are proposed separately, to meet the challenges.

Following the conceptual design of the software-in-the-loop (SIL) application for a WEC, an innovative generic platform, which can explicitly provide a real-time PTO damping force in terms of either linear or non-linear (at different scales) is developed and characterised by 1349 drop tests. Subsequent physical model tests of a OWSC WEC device are carried out. The power efficiency of the OWSC WEC device under different PTO strategies is then estimated based on the analysis of experimental results. The best linear damping in regular waves is driven by gaining 80 in the control function, while 160 for nonlinear PTO damping. Furthermore, it is revealed that nonlinear PTOs have no distinct advantage in the amount of electricity output, but can lead to better stability and broader damping range.

Following the conceptual design of an AI-based hybrid testing application for a FOWT system, a prediction module of the rotor thrust is needed to be estimated and optimised in the first place. For this reason, a considerable amount of simulations under various

conditions are carried out by fully-coupled computation software, and the results obtained are used to train an artificial intelligence structure. Then a prediction module which depends on five inputs, and gives one output rotor thrust, is estimated mathematically. The mathematical module is converted to the control function in the program in a controller to execute it in real-time tests. Therefore, the AI machine is sometimes referred to as the SIL application for FOWTs, which consists of a prediction module obtained by AI training, a controller, and the program in the controller. The AI machine is the key component to implement the AI-based real-time hybrid model (AIReaTHM) testing methodology.

As one of the highlights in the present study, the AIReaTHM testing rig is developed, and bench tests are carried out with a manoeuvrable motion simulator. The comprehensive testing results are analysed for three purposes: 1, validating the AIReaTHM testing methodology. 2, assessing the influences of wind speed, wind turbulence intensity, wave spectrum, input hydrodynamic motions on rotor thrust are reflected by the SIL application. 3, evaluating the systematic uncertainty in the testing rig, which is to be compensated by further improving the testing system. The effect of the surge frequency, wave spectrum and wind models have on the targeted thrust is discussed. The time delay in the testing system is identified as within 0.1s, and the overall uncertainty from the testing rig is 5-15KN (the minimum rotor thrust is 508KN, hence the uncertainty is 0.98%-2.95% in percentage) when compared to the AI prediction.

The testing rig developed is further applied to a 1:73 model of a Hywind floating wind turbine. 4 testing campaigns are carried out, and 303 independent tests are conducted. Testing results with the real-time rotor thrust provided by the AI-based software-in-the-loop application are compared with the other three comparative testing patterns. They are tests with a constant rotor thrust, without any rotor thrust, with AI predicted rotor thrust but without wave inputs, and in only wave conditions respectively. The performance of

the rotor thrust obtained by the AI prediction agrees well with the benchmark testing results. Then, the hydrodynamic responses of the model are compared among those four testing patterns, for both regular wave tests and irregular wave tests in terms of time histories, RAOs, statistical analysis, and spectral analysis. The RAOs of the model under three testing patterns are given for regular wave tests. The hydrodynamic response revealed that the AIReaTHM is better than applying a constant rotor thrust atop of the model, though further improvement is required to meet realistic response.

In the final chapter, conclusions are drawn and original contribution of this PhD study is outlined. Besides, a few points concerning future work are addressed.

ACKNOWLEDGEMENTS

Greatly appreciate to my supervisor Longbin Tao, who is not only a prestigious professor but also has shown people his decent characters. He has provided full support to my PhD work during the most challenging time. I thank the research director Mehmet Atlar and the Dean Atilla Incecik, because they are always looking forward to seeing my successful finish of my PhD. They have even appointed a new supervisor -Professor Longbin Tao for me. Without their help, this challenging research would not have born any fruits.

Special thanks to Professor Longbin Tao again for many things. He has been very understanding of my situation and my hardship; he has always been helping to his best. Throughout the polishing of this thesis, I have received a great deal of support and assistance. His expertise was invaluable in many aspects.

Completing this work would have been all the more difficult were it not for the support and friendship provided by the other PhD candidates at the department of naval architecture, ocean and marine engineering, University of Strathclyde.

Also, I would like to thank my parents and brother who experienced all of the ups and downs of my research. They are always there for me. Special thanks to Dr Xu Liang from whom I have learnt a lot.

Also I would like to thank admin staff in our department, for example Susan Pawson has been very helpful during the whole process of my PhD, Lynn Samson is very kind as well. Certainly there are many others who have been doing a good job, gratitude to them.

Importantly, there are my friends, Joanna McClure, Simon McClure, Li Dong, Sybil Wan and many many others, who are of great support in deliberating over my problems and difficulties. Beautiful friendship also provides a happy distraction to rest my mind outside of my research. Particular gratitude to my best friend, Joanna McClure, for her listening and helpful guide.

I also want to acknowledge the University of Strathclyde Research Studentship for their financially supporting my PhD research. The support from the hydrodynamic lab of the University of Strathclyde is also highly appreciated.

TABLE OF CONTENTS

List of Publications

Twelve Journal publications as well as one manuscript under review has been achieved during the PhD candidate period from 2016-2019. And four of them are mainly about the work described in the thesis, which are listed below:

1. **Development and validation of an AI-based hybrid testing approach for spar-type floating wind turbines** (Authors:Xue Jiang, Longbin Tao, Xu Liang; manuscript not yet published)[1]
2. **Analysis and real-time prediction of the full-scale thrust for floating wind turbine based on artificial intelligence** (Authors: Xue Jiang, Sandy Day, David Clelland, Xu Liang; publication date: Mar 1, 2019 in Ocean Engineering)[2]
3. **An innovative generic platform to simulate real-time PTO damping forces for ocean energy converters based on SIL method** (Authors: Xue Jiang, Sandy Day, David Clelland; publication date: Dec 15, 2018 in Ocean Engineering)[3]
4. **Hydrodynamic responses and power efficiency analyses of an oscillating wave surge converter under different simulated PTO strategies** (Authors: Xue Jiang, Sandy Day, David Clelland; publication date: Dec 15, 2018 in Ocean Engineering)[4]

List of Tables

List of Figures

1 Introduction

Ocean Renewable Energy (ORE) stands out from various sustainable energy sources, due to the merits of being clean, 24-hours available, and high energy intensity. However, the Levelised Cost of Energy (LCOE) of the technologies harnessing energy from the ocean and the wind above, are still relatively high, which shows the space to improve the ORE devices. Therefore, the wave energy converters (WECs) and floating wind turbines (FOWTs) are mainly considered in this thesis. As reported or reviewed in numerous literature both in history and from current world-leading research organisations, the energy contained in the ocean is extremely huge, no matter in the form of wave motions or the wind blowing.

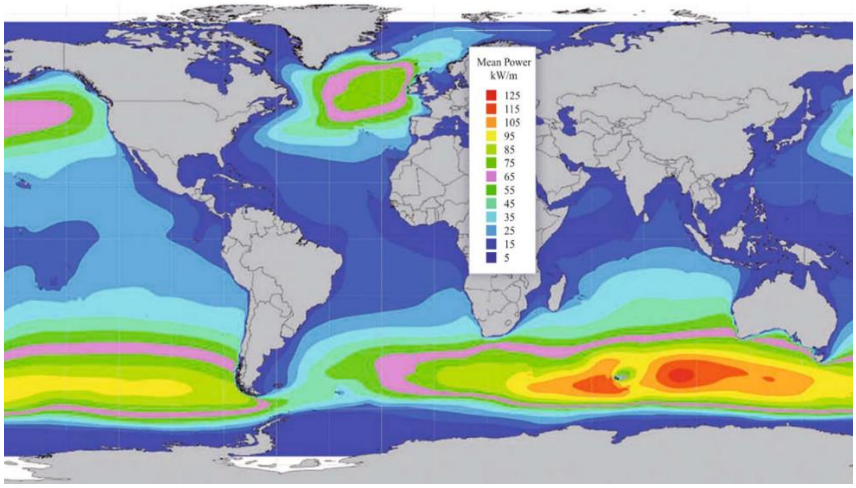

Figure 1.1 Global distribution of mean wave power density in kW/m[5]

Wave power density is demonstrated in Figure 1.1. If successfully exploited, wave energy will make a significant contribution to meeting global energy demands while reducing the negative impact on climate change and environmental pollution, by reducing the rate of consumption of fossil fuels. However, the development of exploiting wave energy is now facing new challenges. Although there are more than one thousand patents were registered between 1799 to 1990, the activity of converting wave energy remained mainly at the academic level[6]. From 1990 to 2011, prototype converters aiming at large-scale energy production were deployed worldwide with activities and interest on a steep upward trend[7]. However, from 2011 up to the present, the number of the prototype being deployed continues on a downward trend with fewer countries reporting developers who are actively advancing their technologies toward commercialisation or have achieved a significant amount of milestones along that path. In general, though people have already reached the goal of extracting electric energy from the motion of ocean waves, the electricity produced is still far from the purpose of commercialisation or popularisation. Indeed, there is a lot of academic and commercial research dedicated to developing the enormous potential electricity for human use. The Scottish Government has set ambitious targets for electricity generation from wave and tidal resources to contribute to its objective of securing 100% of Scotland's electricity requirements from renewable sources by 2020. Furthermore, the majority of money is budgeted on subsequent energy conversion technologies.

On the other hand, the wind has excellent potential as a clean and sustainable energy source, and it has been reported that 189 GW of wind electricity was delivered in Europe in 2018 [8]. This has led to wind energy becoming the second-largest form of power generation in 2019, set to exceed gas installations [9]. Currently, the development and utilisation of wind energy mainly rely on wind turbines, including onshore wind farms and offshore wind farms. The total installed capacity of global wind power reached

591GW in 2018. However, onshore wind power has a number of limitations compared to offshore wind power. For example, noise pollution and visual pollution of onshore wind energy are relatively large. It requires a large amount of land resources and will be restricted by different factors such as the local environment, tourism, air traffic management. At the same time, the energy density of onshore wind is much lower than offshore wind, since the wind energy is proportional to the cube of wind velocity, and the wind velocity offshore is higher than onshore. Besides, the offshore wind faces fewer obstacles and blows more longer continuously. As a result, wind energy installation has gradually moved from land to sea and even deep sea. The structure has also evolved from fixed to floating.

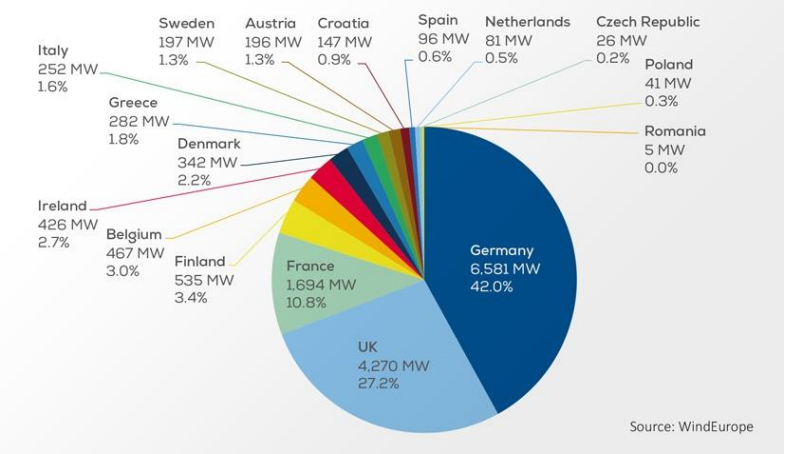

Figure 1.2 EU country shares of new wind energy installed in 2018 [8]

It is exciting to note that we have seen a few recent achievements, especially the deployment of the Hywind floating wind farm in Scotland in 2017[10], which is the first floating wind farm in the world operated by Equinor and Masdar. As recently reported in Norway, it has formed a market value of 117 billion, but still needs government subsidies, which gives the space to improve the power efficiency of Hywind by optimisation of its design.

The key challenges this thesis are dedicated to is to enable cost-effective accurate model tests of ocean renewable energy devices, thus to maximise the electricity output by Tank tests with different design solutions for WECs, FOWTs respectively.

1.1 Background

1.1.1 THE STATE-OF-THE-ART DEVELOPMENT OF WAVE ENERGY CONVERTERS

In the recent decade, a few comprehensive industrial concepts have been developed. Aquamarine Power installed Oyster at the EMEC in August 2009. On 20 November 2009, Oyster was officially launched and connected to the National Grid (UK). Besides, it kept connecting to a grid during the period of 2009-2015. In 2014, The Pelamis Wave Power Pelamis company launched the Pelamis project, which also successfully provided power to the national grid of Scotland. In the meantime, the Archimedes Waveswing proposed by AWS Ocean Energy Ltd was tested in Portugal. At the other end of the world, the United States proposed a Azura concept of a WEC to supply energy to the power grid in North America.

WEC is a device used to extract energy from the ocean waves. A typical WEC usually consists two main parts: the physical interface mechanism and the power take-off system. The physical interface is the mechanical structure of the WEC placed in the water. However, the key part is the PTO system, which converts the harvested wave energy into the electrical energy. No matter what is the energy conversion mechanism, the final output of a WEC is depended on the PTO.

Nowadays, numerical modelling results are still very often referenced as validation of new designs of single devices or arrays, due to the difficulties in modelling of a model-scaled PTO in the lab. Most recently, two additional modelling techniques have been developed, 1) spectral-domain modelling introduced by Folley and Whittaker[11]. 2)

model identification firstly implemented by Davidson et. Al. [12]. However, in numerical modelling, the PTO is usually oversimplified.

For example, Forehand et al.[13] proposed a fully coupled Wave-to-Wire Model of an array of wave energy converters, to explore the power conversion in Matlab, where a hydraulic PTO was simplified and modelled. However, numerical modelling and validation are not reliable enough, especially we have seen a lot underperforming prototype devices in the harsh ocean environment, which are validated by numerical modelling at the design stage. Furthermore, a growing number companies who initially had a considerable interest in wave energy utilisation are investing elsewhere or having growing financial difficulties due to a combination of high up-front development and capital costs, underperforming prototype devices together with underestimating the inherent technical challenges related to the harsh ocean environment. For example, in 2013, Voith Hydro decided to shut down WaveGen who developed the LIMPET power station. One year later, the Pelamis went burst. The Aquamarine Ltd, which developed the OWSC WEC Oyster 800 device, stopped their business in November 2015.

Though the waves carry enormous power potential in the open sea which is claimed to be comparable to the world's current power consumption [6, 14-17], only the reliable and cost-effective wave energy conversion technology will be possible to meet the daily use of electricity. It has been well noted that probably a certain control strategy can be used to control the PTO so as to maximise the output power. For example, Henriques et al.[18] developed a PTO control of an oscillating-water-column spar-buoy wave energy converter, where hardware-in-the-loop simulation is used in experiments to characterise the proposed control algorithms; JHals et al.[19] proposed a model-predictive controller to exploit the full absorption potential of wave-energy converters; Tom et al.[20] used the Pseudo-spectral control which allows optimising the controller design to achieve the optimisation of the output power of an oscillating surge WEC. Other exploration of

control strategy such as adaptive control [21], phase control [22] has achieved very limited success in improving the performance of the device, and further validation testing still requires the absence of a proper PTO simulation in the Lab. Though better control strategies have been explored for more than a decade, there has not yet one such development could be used to address the technology gap for the commercial use of wave energy.

Recently, Liliana et al. [23] reviewed the performance of various state-of-the-art wave energy converters and concluded the most existing WEC devices are still at the Research & Development (R&D) stage and highlighted that in the future, wave energy farms can play a very active role from the point of view of coastal protection. Besides, nowadays ocean energy developers are more aware of the need to increase device reliability and performance while reducing costs. Accurate testing of devices before deployment is even more crucial - an aspect which is the motivation for this study. To address the technology gap, the project is aimed at developing a generic PTO simulating Platform, which can be widely applied to provide a real-time PTO damping force at different scales to enable accurate model tests for the promising new WECs.

1.1.2 THE STATE-OF-THE-ART DEVELOPMENT OF FOWTS

After gained practical benefits from the widespread use of land-based wind turbines and offshore wind turbines, it is an inevitable trend to develop floating wind turbines, due to various advantages:1) Small increases in wind speed yield significant increases in energy production with faster and steadier wind in the deeper sea meaning that much more electricity could be produced. 2) Floating turbines address concerns of visual pollution or disruptive noise, by allowing wind farms to be pushed farther offshore and out of sight. 3)Population centres tend to cluster near the coastlines, where FOWTs can supply electricity without competing for valuable land 4) Floating wind farms have many of the

same advantages as land-based wind farms, such as clean energy, eco-frindly, sustainable. In the shallow water stage, offshore wind turbines with fixed foundations are very economical, but with the increase of water depth, the construction costs of fixed foundation wind turbines will rise sharply, increasing the construction and maintenance costs of the entire wind farm. When the water depth exceeds 60 meters, floating offshore wind turbines will be more economical than stationary ones.

Denmark establish the first modern wind turbine in 1978. Twelve years later, the first offshore wind farm was created in the same country, and in 2009, the first floating fan appeared in Norwegian waters with a capacity of 2.3MW [24]. For offshore wind power, since the depth of seawater ranges from a few meters to several kilometres, the type of infrastructure structure will change with the change of water depth, and offshore floating wind turbines are mainly used in deep water areas, with a water depth more than 50 meters. According to the forecast of the Global Wind Energy Council GWEC, the global average annual installed capacity of wind power will increase by 55GW by 2023. Wind power is growing rapidly worldwide. The top five countries of wind power installation in 2018 are listed in Table 1.1.

Table 1.1 The top five countries of both land and offshore wind installation in 2018

Inland wind	Capacity(MW)	Offshore wind	Capacity(MW)
China	21200	China	1800
US	7588	UK	1312
Germany	2402	Germany	969
India	2191	Belgium	309
Brazil	1939	Denmark	61

In 2017, the world's first commercial floating wind farm, Hywind,(as shown in Figure 1.3) went into production in Scotland with a scale of 30MW, with an average water depth of 320m [25]. It has been reported that since its installation, Hywind has achieved an average capacity factor of 65% [26, 27].

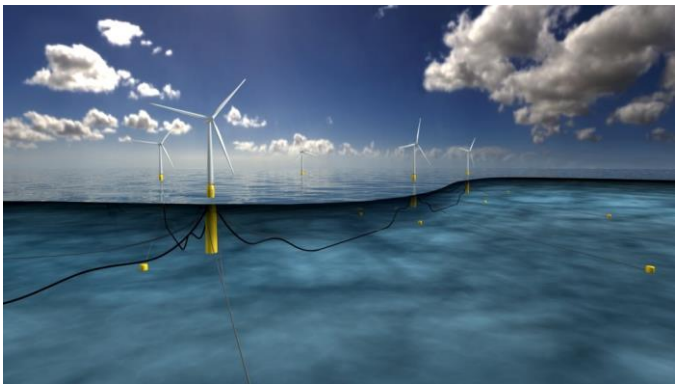

Figure 1.3 World's first floating wind farm(Scotland Hywind)

Before the Hywind pilot park is reported to deliver electricity to the grid [25], this spar-type floating wind turbine has experienced extensive modelling and testing analysis, as shown in Figure1.4. In 2017, the principal objectives of the 5*6MW pilot wind farm were to verify the new up-scaled design, the reliability and availability of multiple turbines, and to cultivate a supply chain, thereby demonstrating the viability of a future commercial-scale park. As reported, the new up-scaled design shows a 17% reduction in weight (1917t/MW versus 2304t/MW) and 25m draught reduction from 100m to 75m compensated for by an increased diameter of the spar. However, the new design also experienced a critical fabrication challenge. Indeed, Statoil and Masdar have the ambition to reduce the costs of energy from the Hywind floating wind farm to 35-52£/MWh by 2030. Because global demand for electricity is expected to climb by up to 25% by 2040 and the world is pursuing economic and sustainable energy sources to keep up with this considerable demand growth.

Figure1.4 Timeline of the development of the Hywind Project

Figure 1.5 Donghai bridge offshore wind farm

In China, the National Offshore Wind Power Demonstration Project established the 103MW wind farm near Shanghai Donghai Bridge in 2009; however, the average water depth is only 10 meters as shown in Figure 1.5. The wind farm consists 34 Sinovel's 3MW offshore wind turbines located 8-13 km from the coastline, with a total installed capacity of 103MW, which can be used by more than 200,000 households in Shanghai for one year.

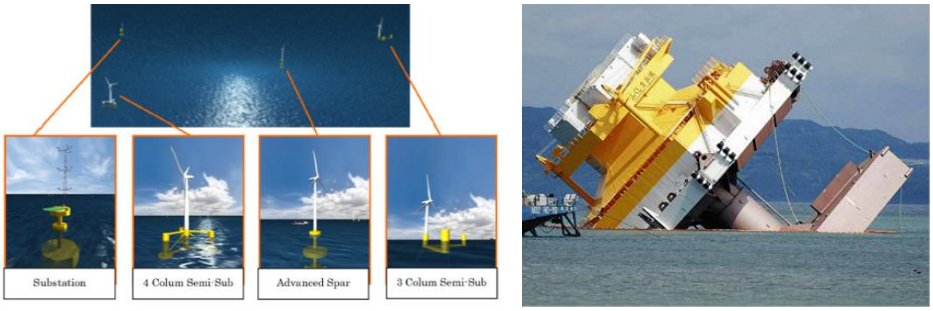

Figure 1.6 FORWARD project in Japan(picture is provided by Prof Tomoki Ikoma)

Besides, Japan developed a pilot offshore wind farm with three FOWT (2MW,7MW and 5MW) and a floating substation; the details are listed in Table 1.2. However, a topple-over accident is reported after harsh wind environments (information is provided by Prof Tomoki Ikoma). Similarly, though some achievements of Hywind project are of significance, new challenges of the operating on floating wind turbines are also of significant concerns when design new FOWTs, because it is tough to build robust and

secure wind farms in water deeper than 60 m. Moreover, wave action, and wind at faster speed, particularly during heavy storms or hurricanes, can damage wind turbines.

Table 1.2 Facility specifications of the FORWARD project

Facility Name	Scale	Wind Turbine Type	Floater Type	Installation Year
Floating Wind Turbine I	2MW	Downwind	Compact Semi-Sub	2015
Floating Wind Turbine II	7MW	Upwind	V-shape Semi-Sub	2016
Floating Wind Turbine III	5MW	Upwind	Advanced Spar	2017
Floating Substation	25MVA/66KV	Substation	Advanced Spar	2015

At present, although researchers in the field of floating turbines have proposed many numerical solution models to calculate the dynamic response of floating turbine systems under the combined action of a single or complex environmental loads, and the OC3 project has combined different numerical calculation methods with measured data verification and comparison. However, because the floating turbine is a complex coupled dynamics system, different degrees of assumptions and simplifications have been made in the development of the numerical solution tool, and the dynamics of the floating fan in a complex environment cannot be fully simulated. In addition, the results of the numerical calculation of the fan can only be used as a reference at the design stage. The validity and reliability of the calculation results are difficult to guarantee, cannot be applied directly to engineering as a reliable result. Therefore, model tests are essential in the design process and for validation purposes, and accurate model tests before investment in ORE devices, particularly for FOWTs, are vital and essential. However, the Froude-Reynold scaling conflict exists in current model tests of FOWTs, and it is the critical challenge in the model test of FOWTs, it is hoped that this thesis will go some way in meeting the challenge.

1.2 Research motivation and objectives of the thesis

Motivated by meeting the need of accurate model tests for ORE devices, one of the research objective is to develop a low-cost innovative PTO simulator which can be used to test wave converters' performance when a simulated linear or non-linear PTO damping is employed. Thus making it possible to reach an optimal design for different WEC/PTO combinations at the testing stage. Driven by the need to overcome the discrepancy in Froude-scaling law and Reynold-scaling law for FOWT model tests, another research objective for this thesis is to propose a new cost-effective testing approach aiming at resolving the discrepancy, as well as overcoming the limitations in hydrodynamic labs. Hence, the thesis will offer appropriate solutions to meet the critical challenges illustrated in the literature review, and software-in-the-loop (SIL) applications are designed and imported into hybrid testing as the strategy.

1.3 Aims of the thesis

Figure 1.7 Software-in-the-loop applications for the use of accurate model tests

After a thorough literature review on the model tests of WECs and FOWTs, the challenges are addressed. Hybrid tests are widely used to overcome the difficulties in model tests of FOWT. The main work should be exploration and evaluation of the ideas behind hybrid

testing, especially the use of SIL applications in hybrid tests. Therefore, two SIL applications for accurate model tests of WECs and FOWTs are to be proposed and validated respectively. Two testing platforms with two SIL applications will be developed and characterised as shown in Figure 1.7. Finally, the two physical hybrid testing approaches will be applied to model tests of two specific models, i.e., a OWSC WEC and a spar-type FOWT. To demonstrate the two research content in a coherent order, the following sub-objectives are set to achieve the overall aim and main objectives.

- Proposing two conceptual designs of the SIL applications imported in hybrid tests for WECs and FOWTS
- Construction of the generic testing platform with the SIL application for WECs to provide real-time power-take-off (PTO) forces (will be indicated as the PTO simulating platform hereafter.), and the characterising study of the PTO simulating platform based on numerous standard drop tests.
- Tank tests of a 1:128 OWSC WEC model under different PTO strategies simulated by the PTO simulating platform.
- Estimation of the predict module used in the AI-based SIL application for FOWTs, based on data pools obtained from numerical computations by FAST.
- Construction of the AI-based Real-time Hybrid Model (AIReaTHM) testing rig for FOWTs based on the AI machine formed by the prediction module and a real-time controller.
- Validation of the AIReaTHM testing methodology as well as the uncertainty study of the testing rig by bench tests.

- Tank tests with a 1:73 model of a spar-type FOWT under different rotor thrust conditions, which correspond to different wind environments, by the AIReaTHM testing rig.

1.4 The scope and outline

The content of the thesis consists of eight chapters, and a core description of each chapter is supplied below.

Chapter 1: Introduction

This chapter includes introduction, background, motivation, aim and scope, the outline of the thesis.

Chapter 2: A review - challenges for accurate model tests of ORE devices

A review of the challenges for accurate model tests of WECs and FOWTs, hybrid tests, application of SIL method are given respectively.

Chapter 3: Development and characterisation of the PTO simulating platform

This chapter addresses the construction of the PTO simulating platform, as well as the detailed characterising process by 1349 standard drop tests. The results are used to validate the PTO simulating methodology as well as demonstrate the behaviour of the physical PTO simulating platform. Besides, the relationship curves between damping torque and the trigger velocity, as well as the relationship equations, are concluded. The uncertainty exists in the methodology, testing results, and components are also discussed.

Chapter 4: Model tests of a OWSC WEC device with the PTO simulating platform

This chapter presents the experimental investigation on the power performance of a OWSC WEC with different power take-off (PTO) damping strategies (provided by the PTO simulating platform) in both regular and irregular waves. The hydrodynamic performance of the OWSC WEC under different damping modes, in regular waves and

irregular waves, is observed. Additionally, the best gain (gain is a parameter in the control function in the SIL application) corresponding to the best PTO strategy is obtained. Also, it is released that the phase difference between the buoy velocity and wave elevation of the model in irregular waves has the same trend as that in regular waves. Moreover, nonlinear PTO strategies have no distinct advantage in the amount of electricity output but have better stability and broader damping range.

Chapter 5: Establish of the prediction module for real-time rotor thrust

In this chapter, numerous aero-hydro-servo-elastic coupled simulations are carried out in time-domain to observe the performance of the real-time thrust acting on the rotor of the OC3-Hywind offshore floating wind turbine. The study focuses on investigating the correlation between inputs (surge motion, pitch motion, wind conditions, etc.) and the targeted output (rotor thrust) in the time domain. Besides, artificial intelligence (AI) techniques are used to estimate a prediction model of real-time thrust based on the data pool formed from FAST simulations. Additionally, the impact of the pitch and surge RAOs of the floating foundation and the wind velocity are quantitatively studied. It reveals that the high-frequency response of thrust is dominated by wave change, whereas the low-frequency response is dominated by wind change. Therefore, it is indicated to use the mean score and oscillating component of the rotor thrust separately to account for the dominating influence regarding high-frequency and low-frequency response, respectively.

Chapter 6: Development and validation of the AIReaTHM testing rig

This chapter presents an AI machine/SIL application consisting of a prediction module and a real-time executive controller, which can be used in the tank to allow real-time hybrid model tests of a spar-type floating wind turbine. In the beginning, the substructures, components, and operating principals of the application are introduced,

then a bench testing platform is developed to study the characteristics of AI-based Hybrid Testing Methodology. Next, the results of qualification tests utilising a manoeuvrable motion simulator are illustrated. The measurement shows good agreement with the prediction values of the rotor thrust in the experimental loop, in terms of the mean score and oscillating amplitude of the real-time rotor thrust. Moreover, by analysing the residues of the measurement and the prediction values of the rotor thrust, both the time delay and systematic uncertainty (which are to be compensated by improving the instruments in the testing rig) are identified.

Chapter 7: Model tests of a spar-type FOWT with the AIReaTHM testing rig

This chapter demonstrates the model tests of a spar-type FOWT. After introducing the 1/73 model and necessary preparations prior to the model tests, 303 tests are carried out. Free decay tests, regular wave tests, and irregular wave tests are discussed independently to serve different discussing purposes. The analysis of regular wave tests and irregular wave tests follows a similar manner; 1) the performance of the rotor thrust under different conditions is given at first. Thus some insight into the worth of the SIL application of the FOWT is obtained; 2) the corresponding hydrodynamic response under different conditions by AIReaTHM tests is also provided and discussed; 3) analysis with comparative cases, hence to make both the hydrodynamic and aerodynamic performance of the AIReaTHM testing rig to be estimated. Three comparative testing patterns are used during the model tests.

Chapter 8: Conclusions

Conclusions, original contributions, and future work suggestions are provided in this chapter.

2 Literature review - challenges for accurate model tests of ORE devices

In this chapter, the challenges of accurate model tests of both WEC devices and FOWTs are demonstrated by substantial literature review on the state-of-the-art testing research of both, respectively. The problem can be solved by hybrid testing. Hence, a substantial review on hybrid tests is also given subsequently. Finally, a short introduction of Software-in-the-loop(SIL), which is the solution used in a hybrid test to overcome the problems for accurate model tests of ORE devices, is included.

2.1 WEC testing and challenges

Initially, some researchers performed experiments with an orifice plate representing the PTO in CFD simulation or without considering the damping effect induced by the PTO system. For instance, Sykes et al.[28] investigated the hydrodynamic performance of a Fixed type axis Symmetry Cylindrical Oscillating water column device using a boundary element model WAMIT without considering the damping effect induced by the PTO system. Current testing concerning a PTO system for WECs only involves in minimal linear PTO damping force, which is usually provided by very simple damping actuators. Richard et al.[29] reviewed how a linear generator can be used as a power take-off unit to apply a damping force. Most recently, for testing concerning the PTO, people tend to simulate quite limited linear damping using air or other dampers. For example, Zhipeng et al.[30] conducted a series of model tests for a heaving-buoy wave energy converter using various air dampers to simulate the PTO damping. However, those methods only can represent some linear generators, and in many cases, the PTO system produces

nonlinear damping forces. The non-linear PTO currently is only considered studies based on numerical modelling. Besides, there was no literature reporting about the tank tests with the consideration of a nonlinear PTO damping strategy. Therefore the challenge of accurate model tests of WEC devices is the PTO modelling at lab-scale.

Of course, some researchers also recommend to build model-scale hydraulics or the electro-mechanical PTO systems. There exists a few well known PTO solutions employing hydraulic systems, turbines, and linear generators, as shown in Figure2.1[31]. However, it is expensive and even impossible to miniaturise systems such as hydraulics for tank-scale test, because the frictional loads don not scale which will result in the wrong response. Furthermore, small scale mechanical or pneumatic systems generally do not work very well. Thus it is impossible to compare the efficiency of different PTO systems considering the vast difference existing among PTO mechanisms.

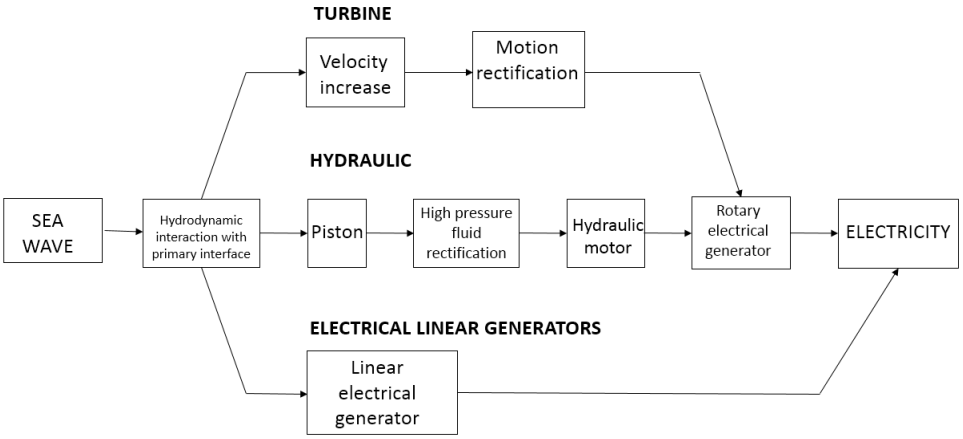

Figure2.1 Alternative PTO mechanisms

Moreover, there is a lack of benchmark testing in published studies due to the absence of a generic PTO simulating platform. Therefore, in this thesis, one of the main tasks is to propose a generic way of providing real-time PTO forces at different scales to enable accurate model tests of WECs. Furthermore, a simplified, scaled Oyster 800[27] model is adopted in this study. Oyster 800 is an oscillating wave surge converter (also referred as OWSC WEC in this thesis), which makes use of the enhanced horizontal fluid particle

movement of the waves in coastal areas, with a water depth of 10-20 meters. It mainly oscillates horizontally in the swell, and are usually deployed in the deeper water.) there are a few literatres discussing the deployment, characteristics and hydrodynamic performance of the Oyster model [31-34]. But the published experimental studies of the Pyster device are rare. Furthermore, the power performance of it under different PTO strategies are of significant interests to know. The hydrodynamic performance of it with different PTOs have not yet been investigated before.

2.2 FOWT testing and challenges

In 2006, the Marintek Marine Technology Laboratory in Norway conducted a model test on a 1/47 scaled model of a 5MW Hywind FOWT, to study the dynamic response of the fan under the combined action of wind and waves[35]. Principle Power also conducted a model test for the WindFloat semi-submersible floating fan, and the scale ratio is1:67[36]. From 2007 to 2009, Ishihara et al.[37] conducted a model test of a semi-submersible floating fan with a sloshing plate. They mainly studies the dynamic response of the floating fan under wave load, which simplifies the wind turbine and mooring system. Sethuraman et al.[38] performed a model test on a designed stepped spar floating fan with a reduction ratio of 1: 100. Olinger et al.[39] conducted a comparative test of TLP and Spar type FOWTs in a marine engineering pool with a scale ratio of 1: 100. Guanche and Wehmeyer et al.[40] conducted a model test with a simplified wind turbine model. Froude scaling law is typically used in traditional tank tests. However, using Froude scaling for the wind turbine rotor as well will lead to incorrect aerodynamic loads for the full-scale turbine because the turbine forces react to aerodynamic loads that are Reynolds-scaled. Traditionally, modelling a floating wind turbine in the laboratory environment involves testing a working rotor in a simulated wind field generated by a series of fans.

Experimental studies with a wind field generated by a series of fans in a tank are usually used to examine aerodynamic performance of a floating wind model. Some people tend to improve the devices to produce better simulated wind field. For example, Martin et al. tried to account for Reynolds effects by appropriate distortion of the rotor geometry[41], however, it is incredibly challenging to construct and operate a working scale rotor due to the large size, not to mention the very lightweight, and sophisticated control requirements, see references [42-45]. Moreover, examples are given by Chujo et al. [46] for a spar offshore FWT, Muller et al. [47] for a semi-submersible FWT and Goupee et al. [48] for the spar, semi-submersible and TLP. Recently, Dagher et al. [49] performed basin model tests on three 1/50 scale floating wind turbines (TLP. Hywind, submersible) to investigate the physical data of the rigid body motions, accelerations and loads for different floating wind turbine platform technologies. For those experiments, high-quality wind environments were created in an offshore basin via a new wind machine that exhibits negligible swirl and low turbulence intensity in the flow field. However, there turned out to be an apparent discrepancy between the data obtained and the FAST predictions, which might be due to the unsuccessful scaling effect of aerodynamic forces. Ahn and H. Shin et al. [50], carried out tank test on a 1/128 model scaled spar-type floating wind turbine, concluding that the thrust force induced in model tests are much smaller due to the low Reynolds number. Shin et al. [51] carried out model tests on the OC3-Hywind floating offshore (FOWT) wind turbine with the rotating rotor effect caused by wind in a wide tank, and it was found that the motions of the FOWT differed from the FAST computations, and it is difficult to tell which one is correct. Thus, it is believed, both the Froude and Reynolds similitudes cannot be satisfied simultaneously at any rate.

Researchers also have turned to non-geometric blades or new solutions to overcome the impossible, correct scaling of the aerodynamic response on a FOWT system. For example, a model test on a Tri Floater 5MW wind turbine with a scale reduction ratio of 1:50. This

test designed the blades of the wind turbine to meet the similar thrust of the wind turbine at a low Reynolds number while actively controlling the speed of the wind wheel, measuring the torque produced. Boulluec et al.[24] Performed a model test on their proposed floating fan. The rotor blades can produce torque and thrust similar to real-scale fans at different Reynolds numbers. Azcona et al. [52] tried to replace the wind turbine rotor with a ducted fan, which gives the correct mean thrust and provides some aerodynamic damping. Lucas I. Lago et al. [53] tried to modify the wind turbine's airfoil shape and chord length in order to obtain improved performance at low Reynolds numbers. A key challenge in today's wind basins is accurate wind generation, as structural obstacles may influence the flow.

2.3 Hybrid testing

The simulation of wind loading for tank testing of FOWTs still presents a variety of severe challenges. Therefore, hybrid approaches stand out, because it allows exploring the effects of different wind environments, rotor configurations and control strategies, without complex rotor models and without generating wind on the fuel tank.

In Europe, the project of INNWEIND.EU has carried out a series of pool model tests for FOWTs, providing experimental data support for DeepCwind OC4 semi-submersible floating wind turbine. In this test, wireless measurement and sensing technology were used to reduce the influence of the wiring harness placed on the model, and the mass of the platform and the overweight part of the cabin were pre-corrected. In the first phase of the test, a controllable speed-adjusting fan is installed at the position of the nacelle, to simulate the force of the fan blades on the tower. As shown in Figure 2.2, the structure of the fan nacelle is simplified. In the second phase of the model test, a model of a 10 MW TLP floating wind turbine is used, and different wave directions, combined conditions of wind and waves, are adopted.

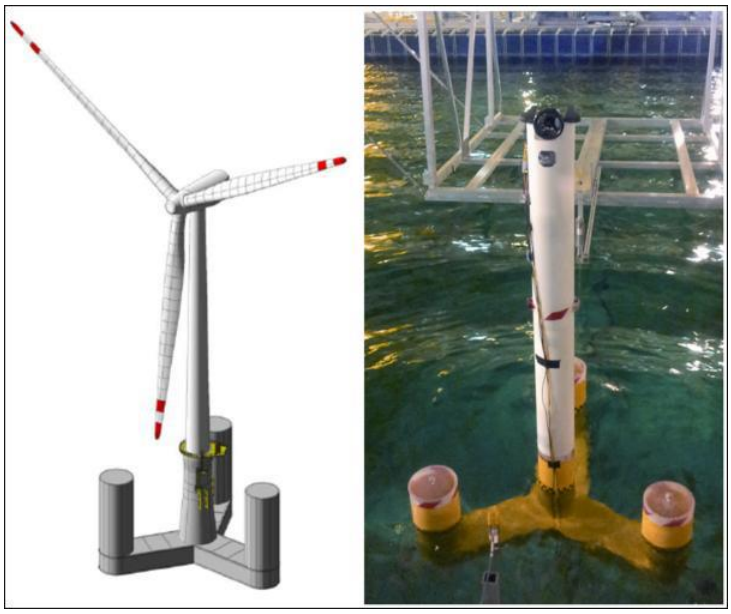

Figure 2.2 The model test of DeepCwind OC4[52]

In US, Christian et al[54]. conducted a model test of a semi-submersible floating turbine-WindFloat- at UC Berkeley. As shown in Figure 2.3, the model scale ratio is 1: 105. The wind turbine is replaced by a rotating disk. The rotation of the disk with the same thrust coefficient simulates the gyro effect. This test mainly studies the dynamic response of the floating body under the action of wind.

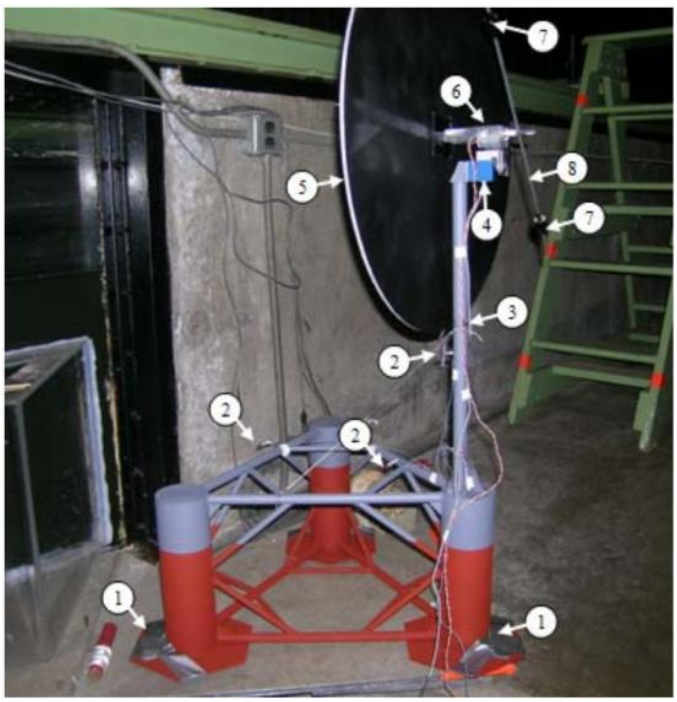

Figure 2.3 Model test of WindFloat[54]

Bachynski and Sauder et al[55-57] performed a real-time hybrid simulation test on a semi-submersible floating fan in a MARINTEK pool. The aerodynamic simulation was calculated in real-time by a numerical calculation tool and then applied by a cable connected to the top of the tower. In the case of aerodynamic forces that meet a similar Reynolds number, the gyro effect cannot be simulated, as shown in Figure 2.4.

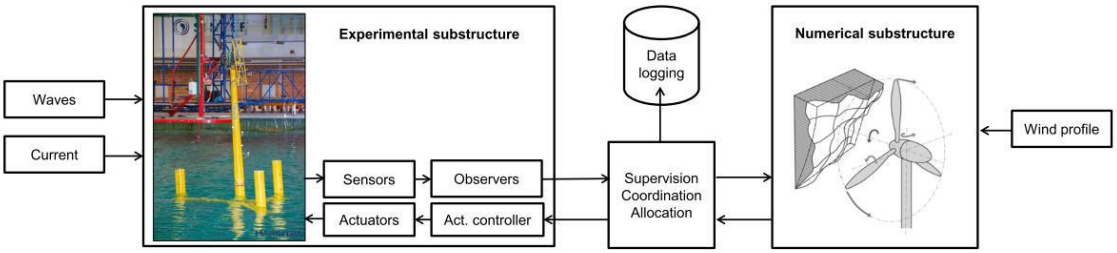

Figure 2.4 The hybrid testing method for a FOWT in MARINTEK[55]

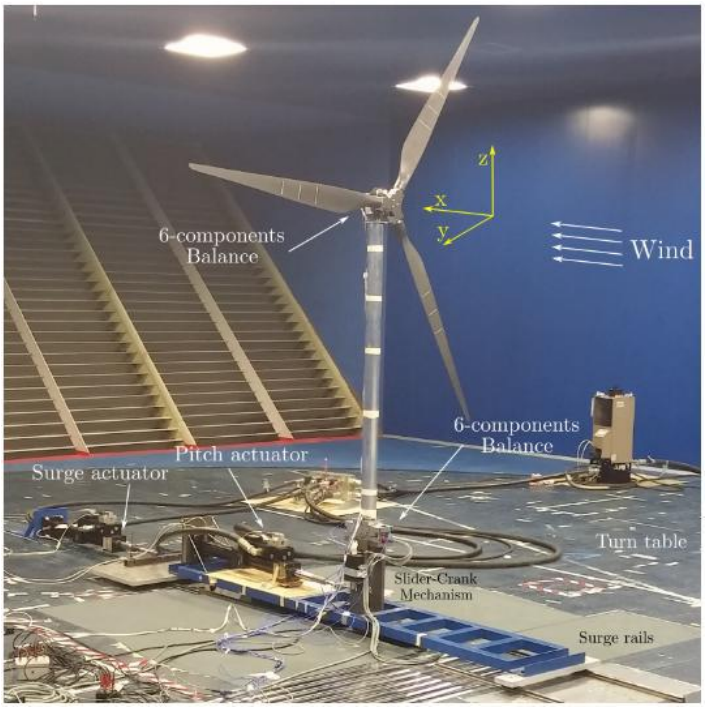

Figure 2.5 Model test with a 2-dof model testing system[58]

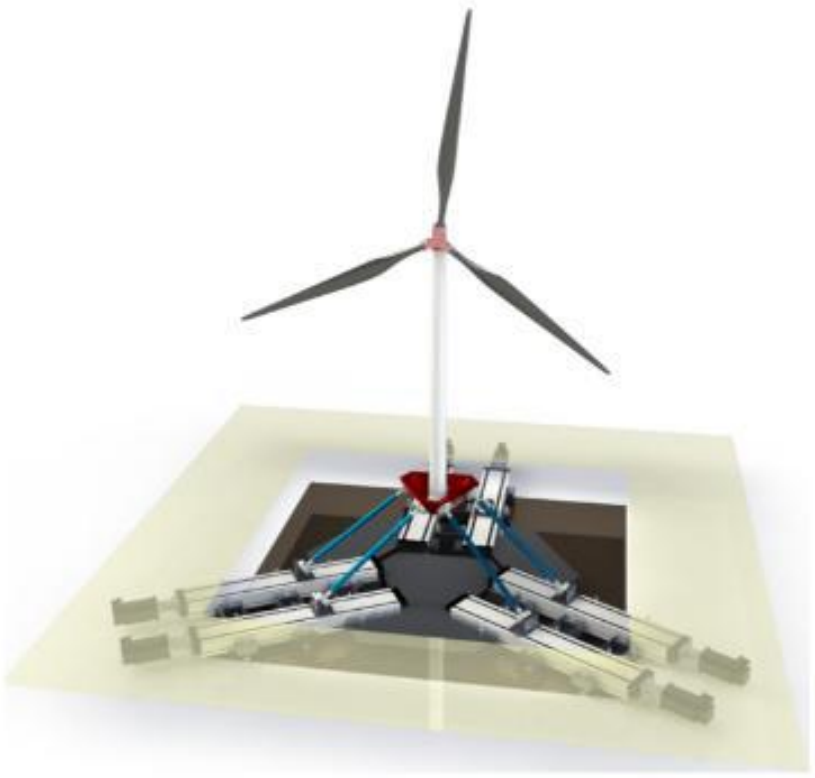

Figure 2.6 Model test with a 6-dof model testing system[59]

Bayati et al[58, 59] adopted an innovative FOWT testing method by modifying the scaling relationship of the fan, and the test of the floating fan was carried out in a wind tunnel. The movement of the floating body was simulated using a two-degree-of-freedom and six-degree-of-freedom mechanical structure. This test focuses on the study of the aerodynamic part of the fan. The fan model is more precise and the measurement acquisition system is more complete. At present, the construction of the two-degree-of-freedom test verification has been completed and the six-degree-of-freedom joint test is still being further optimized as shown in Figure 2.5 and Figure 2.6 respectively.

In summary, a few recent articles review the approaches of simulating wind loading on floating wind turbines in wave tanks and initially describes the deployment of a “software in the loop” (SIL) approach. For example, Sauder [56] proposed a real-time hybrid model testing of a braceless semi-submersible wind turbine. Fowler et al [57] use a high-speed fan located on the model in line with the rotor drivetrain to generate the thrust component

of the wind load. Bayati et al [58] proposed a six-degree-of-freedom platform to simulate the motions of the platform of the floating wind turbine. Moreover, the velocity of the platform is calibrated in real-time using a modified version of the FAST aero-hydro-servo-elastic simulation code, which proves it possible to use the thrust calculated from FAST to generate the equivalent thrust in the model test. Chujo et al [59] attach a lightweight line at the rotor hub and tension. Kraskowski et al.[60] use a fan rotating at a constant speed in stationary air generating a predefined thrust to represent the mean rotor thrust. This allows for easy adjustment of the mean wind load and simulation of mean mooring offsets. In 2016, SINTEF Ocean and the Norwegian University of Science and Technology developed a fully dynamic hybrid testing technique for the model testing of offshore structures, including wind turbines, which they named ReaTHM® testing [60]. This is an extension of traditional hydrodynamic model-scale testing, in which the system under study is dismantled into physical and numerical parts. In a numerical partition, the wind field is simulated by Turbsim [61], and the aerodynamic load calculations are carried out in full-scale using the open-source code AeroDyn [62]. Subsequently, in [56] Sauder et al studied a braceless semi-submersible wind turbine, revealing unstructured uncertainties in the ReaTHM testing method, induced by hardware/software issues or network overload, or varying actuator performance due to temperature. Other case studies using the ReaTHM method have also been carried out [57, 63, 64]. In the ReaTHM® testing procedure, the aerodynamic response obtained from NREL programs (including Turbsim and AeroDyn) is related to the physical model in real-time by using Froude-scaling law. Day et al. [65] also tried to run a revised version of FAST code as the numerical partition of a hybrid testing approach similar to ReaTHM. Indeed, the Aerodyn is used to output a real-time thrust in a wind field simulated by Turbsim. As well, the real-time thrust is expected to be used as the command to drive a fan in a basin after applying Froude-scaling law. It is important to mention that the rotor thrust that comes from

AeroDyn computation is usually at full-scale, and the fan in the water basin is at model-scale. However, the most striking result of those trails is that the fan did not rotate at all, which might be a result of the complexity of the data of aerodynamic forces from AeroDyn.

Therefore, motivated by the problems and research potentials mentioned above, a new hybrid approach to utilise the idea of "software-in-the-loop" in which an active control system drives an actuator in real-time to provide a real-time rotor thrust for accurate model tests of FOWTs is proposed.

2.4 Application of SIL in hybrid testing

Conducting scale-down model tests is considered to be the most economical and reliable research method for ORE devices. However, during model testing, the law of scales imposes strict requirements on model weight and size. Requirements limit the deployment of condition monitoring systems; it is challenging to achieve wind. Lack of accurate simulation of loads, including wave and wind loads, defects the accuracy and reliability of model tests. For example, when down-scaling the PTOs of WECs, it is not possible to miniaturise systems such as hydraulics for a tank-scale test – and even if you could, the frictional loads do not scale, so predictions are wrong. Similarly, impossible it is to miniaturise a wind turbine pitch control rotor and to scale aerodynamic forces when wave loads are Froude scaled. Still, it does not work for friction in a PTO or for aero forces on a rotor. Difficulties also occur in the modelling of advanced control systems – e.g. reactive control for PTO and pitch control for FOWT. However, it can be included in hybrid tests by using SIL method.

In the meantime, SIL/hardware-in-the-loop(HIL) testing techniques have been developed and used in various fields. In the SIL application, code/program is compiled and used to recreate a particular behaviour by running the real-time controller connected the

simulation software. SIL is powerful and could be a possible way to offer brand new approaches to the experiments on ocean renewable energy devices. SIL experiments with concurrent simulations to study the structural behaviour of large scale buildings was proposed in the 1970s in Japan[66]. The idea developed and became a standard tool for studying damage-reducing components for buildings or bridges. In the field of automotive engineering, similar ideas have been applied to test the noise propagation among individual parts, such as gearboxes noise[67-69]. The United States [70]and Europe [71]also have active communities focusing on the development and use of SIL testing method. The development of SIL required an unprecedented interaction between the various disciplines of numerical and experimental methods, signal processing and control engineering. Each discipline was also individually challenged by some new requirements, which led to exciting developments: new classes of numerical methods were, for instance, developed that proved superior to classical (e.g. Runge-Kutta) methods in terms of stability and efficiency for stiff problems[72]. Novel finite element formulations for slender structures were developed, with a special treatment of axial properties that allowed real-time dynamic simulations of cables [73]. New error quantification criteria of a SIL test were developed in [74].In addition to those examples of fundamental developments, advanced methods, such as stability analyses based on Delayed Differential Equations[75] were applied to new types of problems. ReaTHM testing has been identified as a promising technology, however, in the field of marine technology, few hybrid tests for WECs have been reported; see [76, 77] and references therein. Therefore, SIL is considered to be the solution, and appropriate SIL applications for both are proposed separately in this section.

In summary, the challenge of accurate model test for WECs is the lack of a generic PTO simulation method at lab-scale. Similarly, the challenge of accurate model test for FOWTs is the lack of an executive method in the lab to overcome the scaling conflict

between Froude-scaling law and Reynolds-scaling law. Then, hybrid testing approach insert with SIL applications are expected to solve the problems.

3 Development and characterisation of the PTO simulating platform

This chapter describes the development of a generic power-take-off (PTO) simulating platform which consists a Software written in Labview, and necessary electrical components to implement the software-in-the-loop (SIL) conception. It can be used to provide a simulated real-time linear or non-linear PTO damping forces for the accurate model tests of WECs. Furthermore, it will enable investigation of the maximum power output of WECs, thus making it efficient and inexpensive to explore different PTO solutions. The PTO simulator is supposed to behave suitably according to typical damping models employed in tests. Hence 1349 calibrating tests are carried out to demonstrate the behaviour of the PTO simulator. A series of relationship curves of the trigger velocity and the produced damping torques are obtained. Also, the corresponding equations for each curve are drawn by fitting the experimental data, for both the linear and non-linear PTO damping modes (n=1, n=2) of the software. Moreover, correlation curves for input gains and the produced damping force coefficients (which are the coefficients from the fitted equations) are provided. The correlation indicates the PTO simulation platform's capacity of simulating linear PTO can reach the damping force coefficient range of 40-220 and can reach 10-70 for quadratic damping.

3.1 The SIL application of providing real-time PTO damping forces for WECs

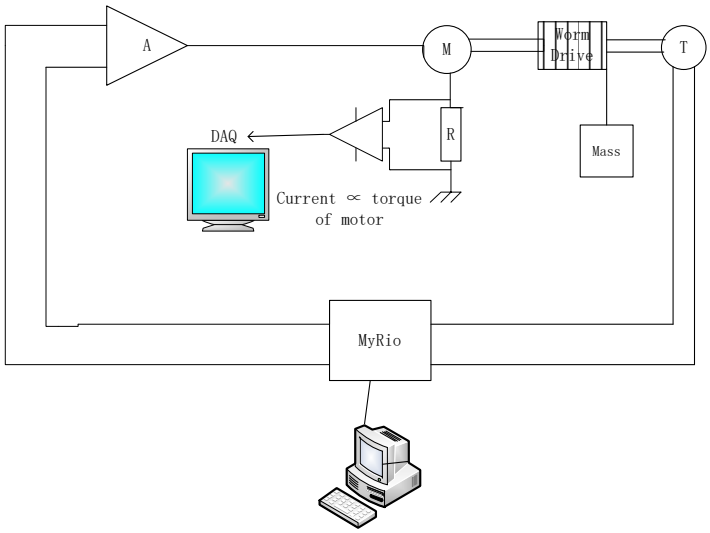

Figure 3.1 The conceptual design of a SIL application providing real-time damping forces

When a PTO system draws electricity from a WEC mechanism in the water, a damping torque/force is generated. Thus, in this thesis, the linear or nonlinear PTO systems are simplified into linear or nonlinear damping force functions and can recreate a model-scaled real-time damping force in laboratories by actively control a motor to generate a force following the corresponding linear or nonlinear functions after applying Froude scaling law. For this purpose, the SIL simulating method is adopted which uses an innovative control loop running on an inexpensive real-time controller coupled to a DC motor which generates the PTO damping torque, as shown Figure 3.1. In current research, a MyRio controller is adapted to execute the program written in 'Labview' (a programming software on the computer), a DC motor 'M' is adopted to deliver the PTO damping force, and the program in controller (where control function is the reflect of the aimed damping function) controls the motor to provide a linear or quadratic damping force. However, in the real executive process, a power amplifier (A), a tachometer(T) and a trigger force are also needed. In the calibrating process, a falling mass is used to trigger the rotation of the motor. A resistive current sensor(R)is used as an external measurement

of the damping torque generated on the motor shaft. A separate Data Acquisition System (DAQ) is used to record time histories of the current signal from the resistive current sensor(R), and velocity signal from the tachometer(T), and they are all analogue.

Some simple mathematic is used to convert the physical quantities to the damping torque or force of interests, according to Newton's second law and third law.

$$F_{damping} = weight = m \times g \tag{3.1}$$

$$T_{dampingS} = F_{damping} \times d / 2 \tag{3.2}$$

where $F_{damping}$ stands for the damping force, $T_{dampingS}$ stands for the damping torque produced by the motor, d is the diameter of the worm drive connected to the output shaft of the DC motor.

A current sensor is designed in the loop to measure the current of the DC motor to give a prediction on the dynamic damping torque ($T_{dampingD}$). According to the proportional relationship between the current and torque for a DC motor.

$$T = k_T \times I \tag{3.3}$$

However the proportional relationship will be slightly affected by the properties of the motor itself and environmental factors, e.g. motor temperature, so calculation of $T_{dampingD}$ based on dropping masses are used to characterise $T_{dampingS}$, because, in fact, the trigger force of the SIL application will be provided by moving WEC mechanism in the water, instead of any falling masses, which reaches a static balance stage for measuring in drop tests. And the comparisons between the two damping torques ($T_{dampingS}$ & $T_{dampingD}$) will be discussed as the main source of the uncertainty of PTO simulating platform in Page 47. Because during tank tests, the reading of the current sensor is directly used as the reading of the damping torque.

The damping function in the program is described as

$$F(t) = \frac{gain}{100}\dot{y}(t)^n \tag{3.4}$$

where the *gain/100* is a user-supplied scaling factor due to the use of an amplifier in the SIL application, $F(t)$ is the damping force, and $\dot{y}(t)$ is the velocity, which is the derivative of the displacement $y(t)$ concerning time t. When "n=1", the platform will simulate a real-time linear PTO damping force, similarly when "n=2", the platform will simulate a real-time quadratic damping force. In this thesis, damping forces are presented in the form of damping torques in experiments, therefore, damping force equals damping torque hereafter.

The targeted damping equation is described as

$$F(t) = \varsigma_P \times \dot{y}(t)^n \tag{3.5}$$

where ς_P represents the coefficient of the real-time PTO damping force.

3.2 Development of the PTO simulating platform

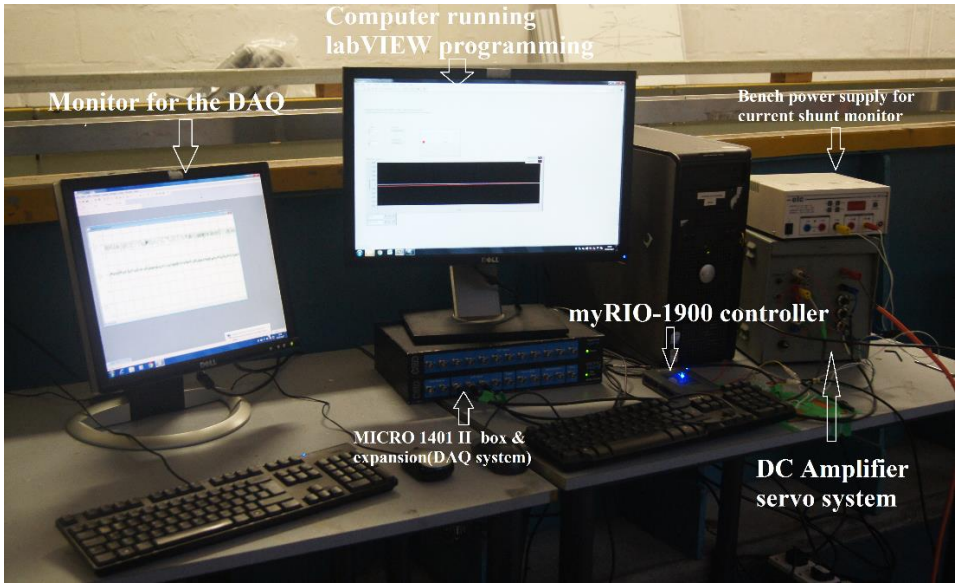

Figure 3.2 Components of the PTO damping simulation platform

The electrical part of the PTO testing platform is designed to implement the SIL application, so as to produce a target damping torque and simultaneously enable one to monitor and record the data including torque, position and velocity signals. Therefore, some electrical equipment is used as shown in Figure 3.2. The LabVIEW program in the controller is shown in Figure 3.3 and Figure 3.4. The DC motor is a GR12CH printed armature motor fitted with a tachometer and a position encoder. A DC amplifier servo system is therefore used to control the motor to rotate, and a National Instruments MyRIO-1900 controller executes the LabVIEW program. Furthermore, a high-accuracy current sensor equipped with a current shunt monitor is used to measure the torque generated by the motor. MICRO 1401 II and Spike is used as the data acquisition system (DAQ).

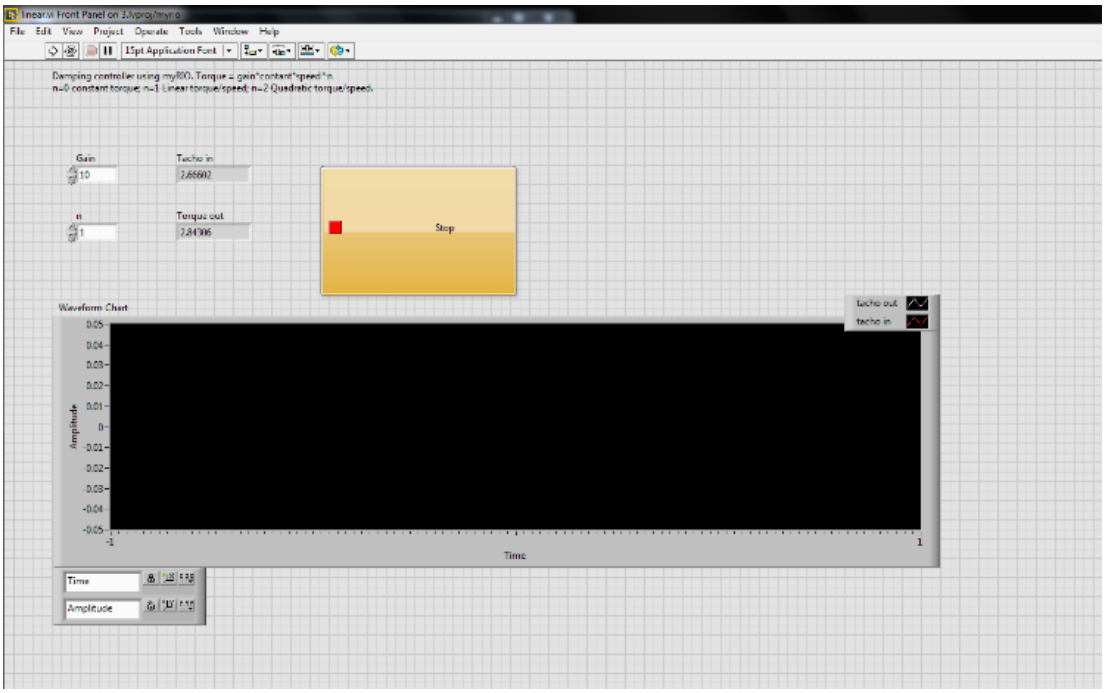

Figure 3.3 Front panel of the LabVIEW program

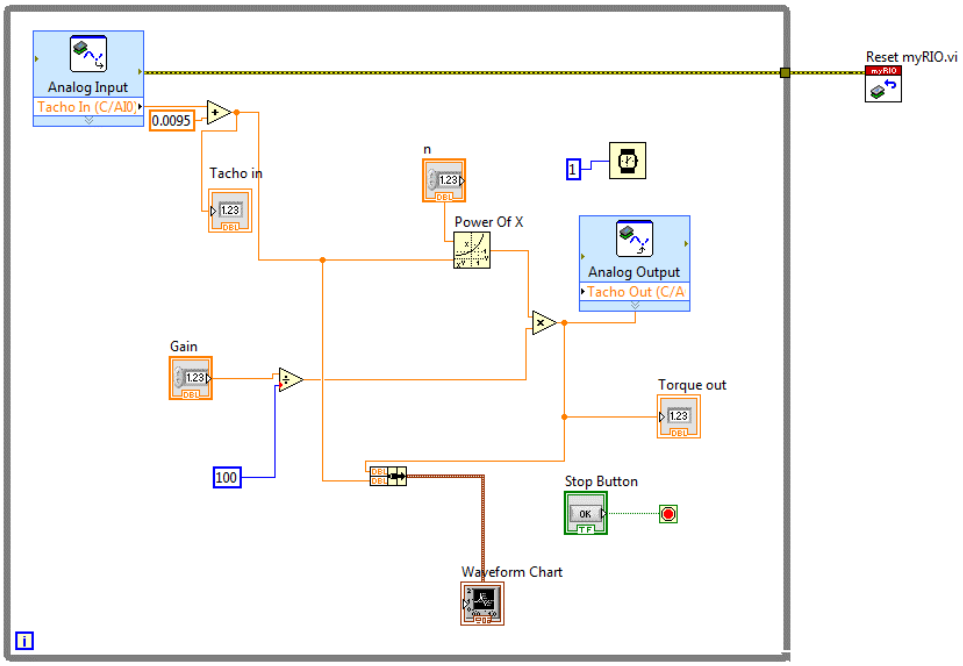

Figure 3.4 Block diagram underneath the front panel

3.3 Characterising Tests

To demonstrate the behaviour of the physical PTO simulating platform, 1349 drop tests are carried out. The idea of using drop tests to calibrate the system is for three purposes.

(1) for one standard drop test, a mass is used to trigger the actuating motor to produce a corresponding damping-torque ($T_{dampingD}$), which is measured by a self-made torque sensor (the key circuit is the current shunt). Besides, a referred damping-torque ($T_{dampingS}$) is also obtained by the calculation based on the drop mass. Therefore, it is aimed to make it possible to evaluate the uncertainty in using the reading of the self-made torque sensor as the true value of the produced damping torque, by comparing the referred damping-torque with the measurement by a current-shunt torque sensor. Because when the PTO simulating platform is used in a tank test, the test is a dynamic process, and the trigger will be dynamic velocity instead of a velocity caused by a dropping mass which reach at an equilibrium state soon.

(2) as the trigger velocity in a dropping test reach at an equilibrium state soon, it enables data collection, including the reading of the torque sensor, the value of the trigger velocity.

(3) it is enabled to demonstrate the behaviour of the PTO simulating platform by increasing the weight of the dropping mass. For example, for one specific control function of the software (gain=80, n=1), which represents one specific PTO damping, a serious of weights are selected to produce different trigger velocities as shown in Table 3.2. In the meantime, corresponding damping-torques produced in the drop tests are also marked by the reading of the torque sensor($T_{dampingD}$)as well as the calculation of the referred damping-torque($T_{dampingS}$) then the relationship curves between the velocity and $T_{dampingS}$ or $T_{dampingD}$ are obtained. Furthermore, the fitted equations for each curve can be obtained. Then it can be observed if a linear relationship between the damping torque and the velocity could be achieved by the SIL application. Likewise, a group of linear PTO damping forces at different scales can be achieved by changing the gains in the control function in the SIL application. Similarly, quadratic PTO damping can be simulated when the index n set to be 2. The gains used for characterising process for both n=1, and n=2 are listed in Table 3.3.

3.3.1 EXPERIMENTAL SET-UP

Table 3.1 Details of the mechanical set-up

Component	Parameters	Dimension
Frame Stand	Total height	2.1m
	Total width	1.6m
Transmission wire	Total length	1.8m
	Drop distance	1.3m
	Diameter	3mm
Hook	Weight	0.1kg
Worm drive	Diameter	70mm

Table 3.2 Selected weights (kg) used in the drop tests

	M1	M2	M3	M4	M5	M6	M7
n=1	—	0.4	0.5	0.6	0.7	0.8	0.9
n=2	0.3	0.4	0.5	0.6	0.7	0.8	0.9
	M8	M9	M10	M11	M12	M13	M14
n=1	1	1.1	1.2	1.3	1.4	1.5	1.6
n=2	1	1.1	1.2	1.3	1.4	1.5	1

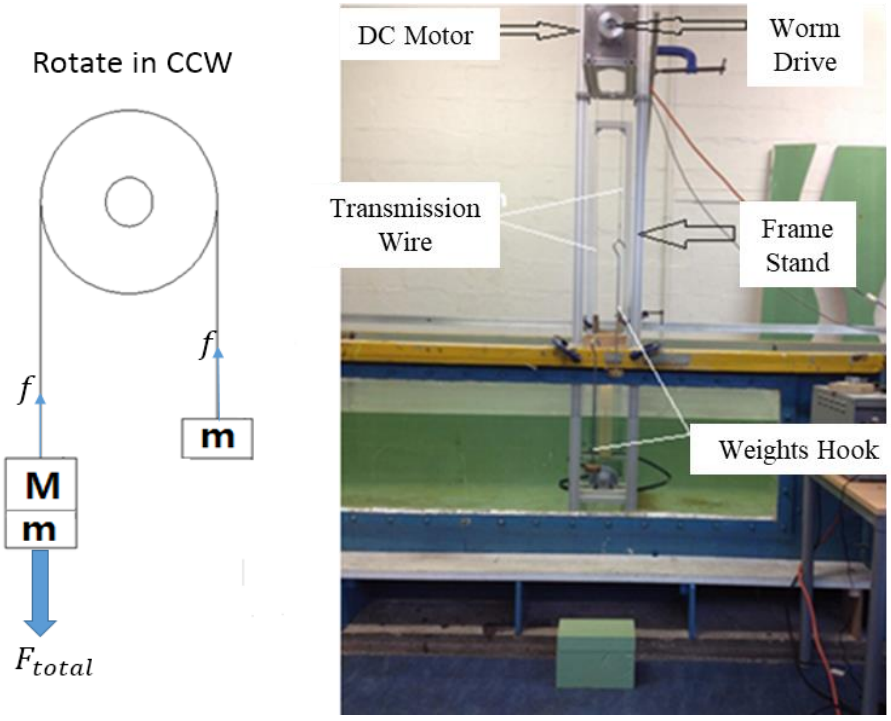

Figure 3.5 a) Pretension in drop tests, f is the pre-tension caused by "m", and F_{total} is the driving force caused by "M"; b) Experimental setup for dropping tests

For all of the drop tests, wire pretension is applied using two 0.1 kg masses-"m", as shown in Figure 3.5 (a). The pretension is necessary in order to hold the wire on the worm and also to ensure a minimum tension in the multi-strand wire to minimise the initial wire 'stretch'. The mass M is used to drive the wire to produce an input speed. The experimental set-up of the PTO Testing Platform used for the drop tests comprises an

aluminium mounting frame, the DC motor, a worm drive, multi-stranded steel transmission wires and two weight-hooks, as shown in Figure 3.5 (b).

Table 3.3 Selected gains for drop tests

	Available Gain range	Gain1	Gain2	Gain3	Gain4	Gain5	Gain6
n=1	20-120	20	40	60	80	100	120
n=2	40-200	40	80	120	160	200	—

3.3.2 RESULTS DISCUSSION

In this section, it is investigated how the damping torque behaves when different weights are used to drive the PTO simulation platform under different input gains of the linear or quadratic control function.

3.3.2.1 DATA PROCESSING

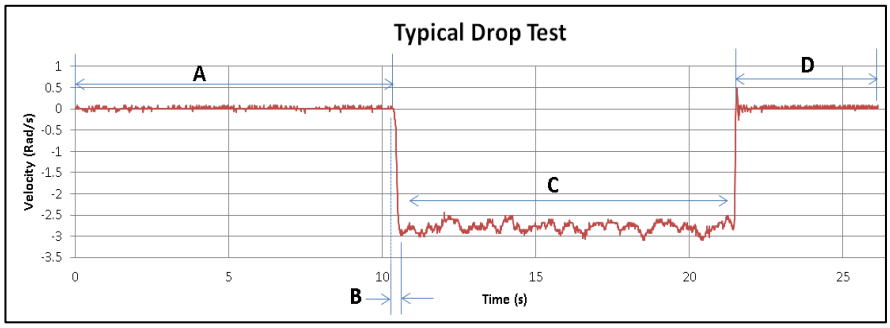

Figure 3.6 Time history of the velocity from one typical drop test monitored by DAQ

At first, the time history of the velocity from one typical drop test is used to demonstrate the data selection and processing. As shown in Figure 3.6, the drop test can be classified into four distinct periods. During period A, the mass is at rest, 1.5m above the final point. Period B is the acceleration period of the mass after release and period C is the equilibrium state. In period D, the mass has travelled 1.3m and reaches its final point. The velocity for state C is selected as the trigger velocity (V), the velocity(V) and corresponding damping torque($T_{dampingS}$) (which is obtained by calculation using Equation 3.1 &3.2) can decide a point representing ine drop test in the characterising plotting. Actually, to be cautious with experimental research, each typical drop test has been carried out a few

repeated times amd the mean values of the V and $T_{dampingS}$ are shown in Figure 3.7 &Figure 3.10. The value for $T_{dampingD}$ is obtained in the same manner. and the average value is used as the value of velocity obtained from one test.

3.3.2.2 Linear PTO control functions (n=1)

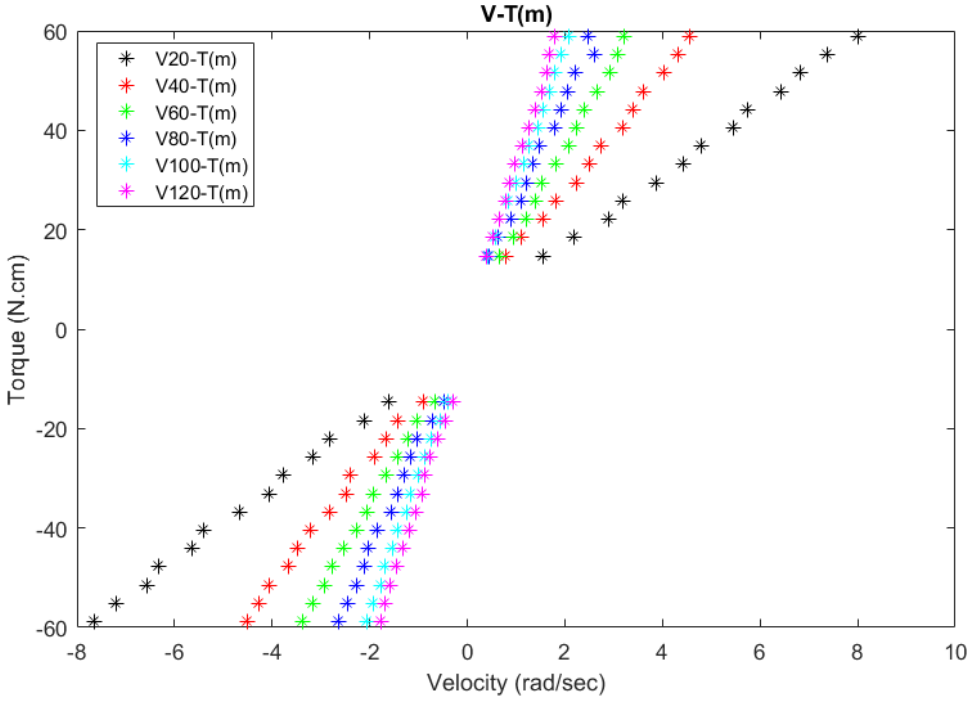

Figure 3.7 Relationship of velocity and damping torque($T_{dampingS}$)

Under the linear control function in the software in the loop, the relationship between velocity (V) and the damping torque $T_{dampingS}$ (the definition of $T_{dampingS}$ seeing section 2.4.1) are shown in Figure 3.7, in which each point comes from the average values of the three repeated drop tests. Data points located in the positive torque region represent the drop tests in a counter-clockwise (CCW) direction, which means for those drop tests, each time a specific weight is applied on the worm to drive the motor to rotate in the CCW direction. Similarly, the points located in the negative torque region are the results of drop tests in a clockwise direction. Different gain values are indicated by the colour of the star

points, black representing the lowest gain value and pink representing the highest gain value (see Figure 3.8&Figure 3.11).

As shown in Figure 3.7, a linear relationship between torque and velocity for each of the different gain value is achieved, and as we increase the input gains for the PTO simulation platform, the slopes of the linear damping increase as well. As the gain increases, the slope of the lines increases, ς_P value increase too. That represents an increasing damping coefficient. Then each equation is drawn from each group of linear data. Moreover, the damping coefficient can be derived from the fitted equation in Table 3.4. The fitted equations are in the form of $F(t) = \varsigma_P \times \dot{y}(t) + u$, in which u is the uncertainty of the linear PTO simulation discussed in Section 2.3. In this study, six different gain values for linear damping cases were examined and the damping coefficients were measured at *gain* = 20, 40, 60, 80,100,120 respectively, with the corresponding damping ratios=44.22, 73.66, 107.9, 129.5, 167.2, 194.6 in counterclockwise direction and ς_P = 46.12, 77.57, 105.6, 133.4, 169.9, 191.2, respectively as shown in Table 3.4.

Table 3.4 Table of fitted functions based on $T_{dampingS}$ for linear PTO

Gain	Fitted damping equation	
	CCW	CW
20	$F(\mathrm{t}) = 44.22\dot{y}(t) + 2.834$	$F(t) = 46.12\dot{y}(t) - 2.425$
40	$F(t) = 73.66\dot{y}(t) + 4.585$	$F(t) = 77.57\dot{y}(t) - 1.933$
60	$F(t) = 107.9\dot{y}(t) + 2.277$	$F(t) = 105.6\dot{y}(t) - 1.909$
80	$F(t) = 129.5\dot{y}(t) + 4.934$	$F\left(t\right) = 133.4\dot{y}(t) - 2.571$
100	$F(t) = 167.2\dot{y}(t) + 3.445$	$F(t) = 169.9\dot{y}(t) - 2.925$
120	$F(t) = 194.6\dot{y}(t) + 2.003$	$F(t) = 191.2\dot{y}(t) - 4.143$

In dynamic model testing, the $T_{dampingD}$ is directly monitored and used to give a prediction of PTO damping instead of $T_{dampingS}$. Therefore relationship curves between $T_{dampingD}$ and

real-time instantaneous velocities are obtained as well. It is seen in Figure 3.8, the linear damping is assured though it may result in absolute uncertainty. Therefore, the fitted equations for the six groups of ballpoints in Figure 3.8 are also obtained. The corresponding damping ratios are ς_P =45.24, 76.4, 112.7, 139, 176.9, 206.5, in the counterclockwise direction and ς_P = 47.57, 80.25, 111.9, 141.7, 179.7, 203.1, respectively as shown in Table 3.5 and the uncertainty in methodology is reflected in the difference of ς_P, which is discussed in section 3.3.3.

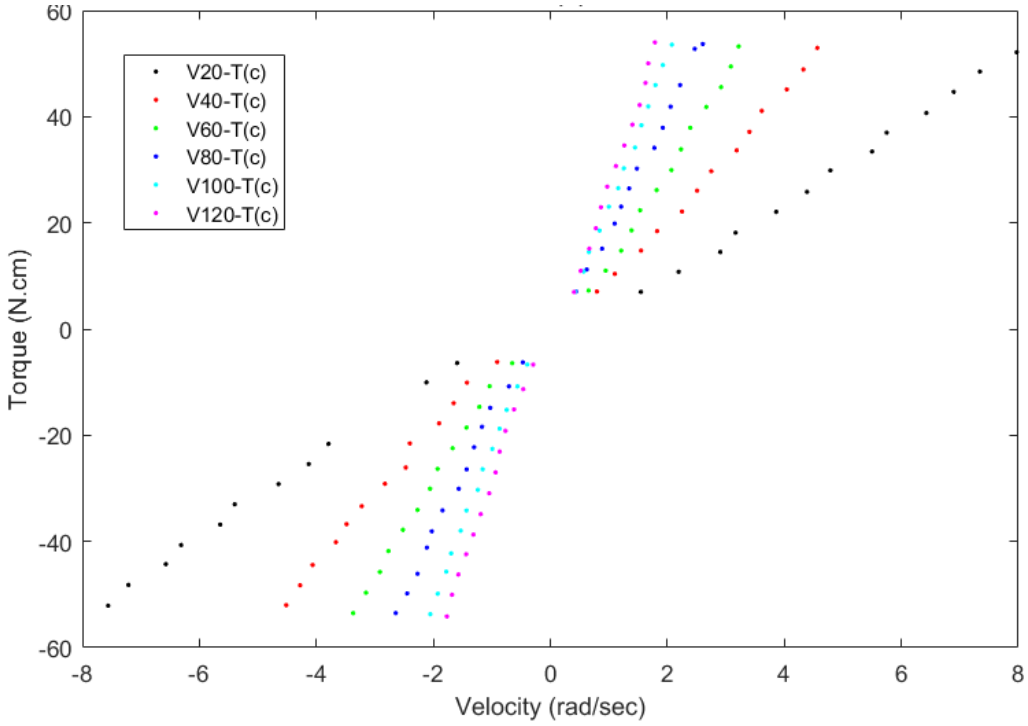

Figure 3.8 Relationship of velocity and damping torque ($T_{dampingD}$)

As this PTO simulation platform is designed to work in real-time in labs, therefore, gain-coefficient relationship curves are also drawn for generic use, in which the ς_P value in each fitted equations is used as the linear damping coefficient. As shown in Figure 3.9, easy to use Gain-Damping coefficient curves are obtained, and the blue lines stand for the Dc and Gain relationship in a counterclockwise, and red lines in clockwise. Solid lines denote $T_{dampingS}$ as the damping torque, while lines with dot symbols representing $T_{dampingD}$.

Table 3.5 Table of fitted functions based on $T_{dampingD}$ for linear PTO

Gain	Fitted damping equation	
	CCW	CW
20	$F(t)=45.24\dot{y}(t)-5.154$	$F(t)=47.57\dot{y}(t)+6.228$
40	$F(t)=76.4\dot{y}(t)-3.622$	$F(t)=77.57\dot{y}(t)-1.933$
60	$F(t)=112.7\dot{y}(t)-5.911$	$F(t)=105.6\dot{y}(t)-1.909$
80	$F(t)=139\dot{y}(t)-3.407$	$F(t)=133.4\dot{y}(t)-2.571$
100	$F(t)=176.9\dot{y}(t)-4.949$	$F(t)=169.9\dot{y}(t)-2.925$
120	$F(t)=206.5\dot{y}(t)-6.294$	$F(t)=191.2\dot{y}(t)-4.143$

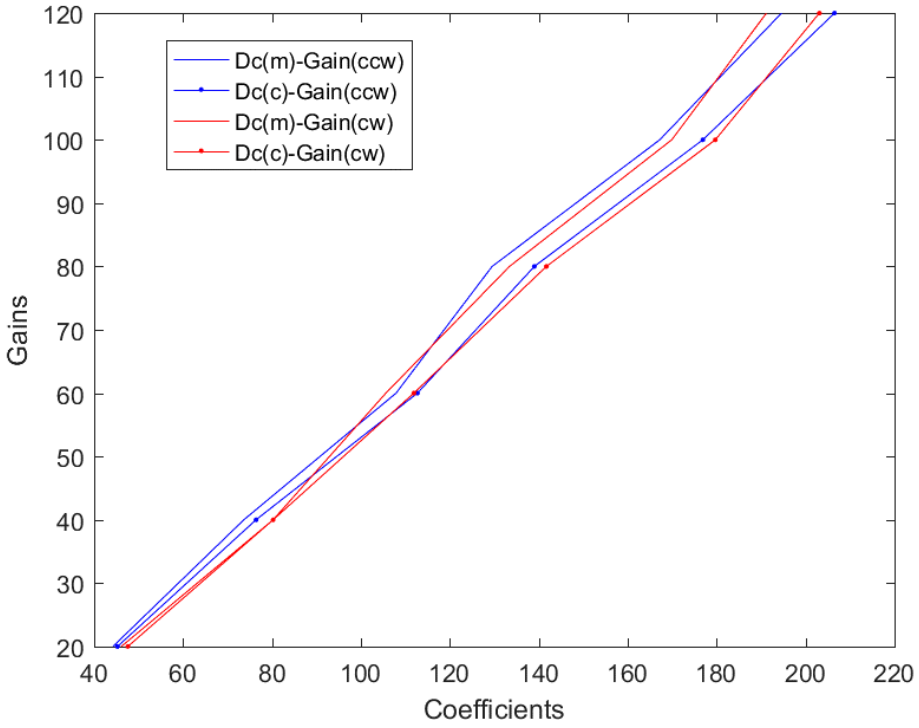

Figure 3.9 Relationship of input gains and linear damping force coefficients

3.3.2.3 QUADRATIC PTO CONTROL FUNCTIONS(N=2)

With the quadratic control function in the software in the loop, the relationship between velocity (V) and the damping torque $T_{dampingS}$ could be drawn as shown in Figure 3.10. It is learned from Figure 3.10, that the quadratic relationship of the produced damping and the trigger velocity is achieved, where the trigger velocity should be motion velocity of

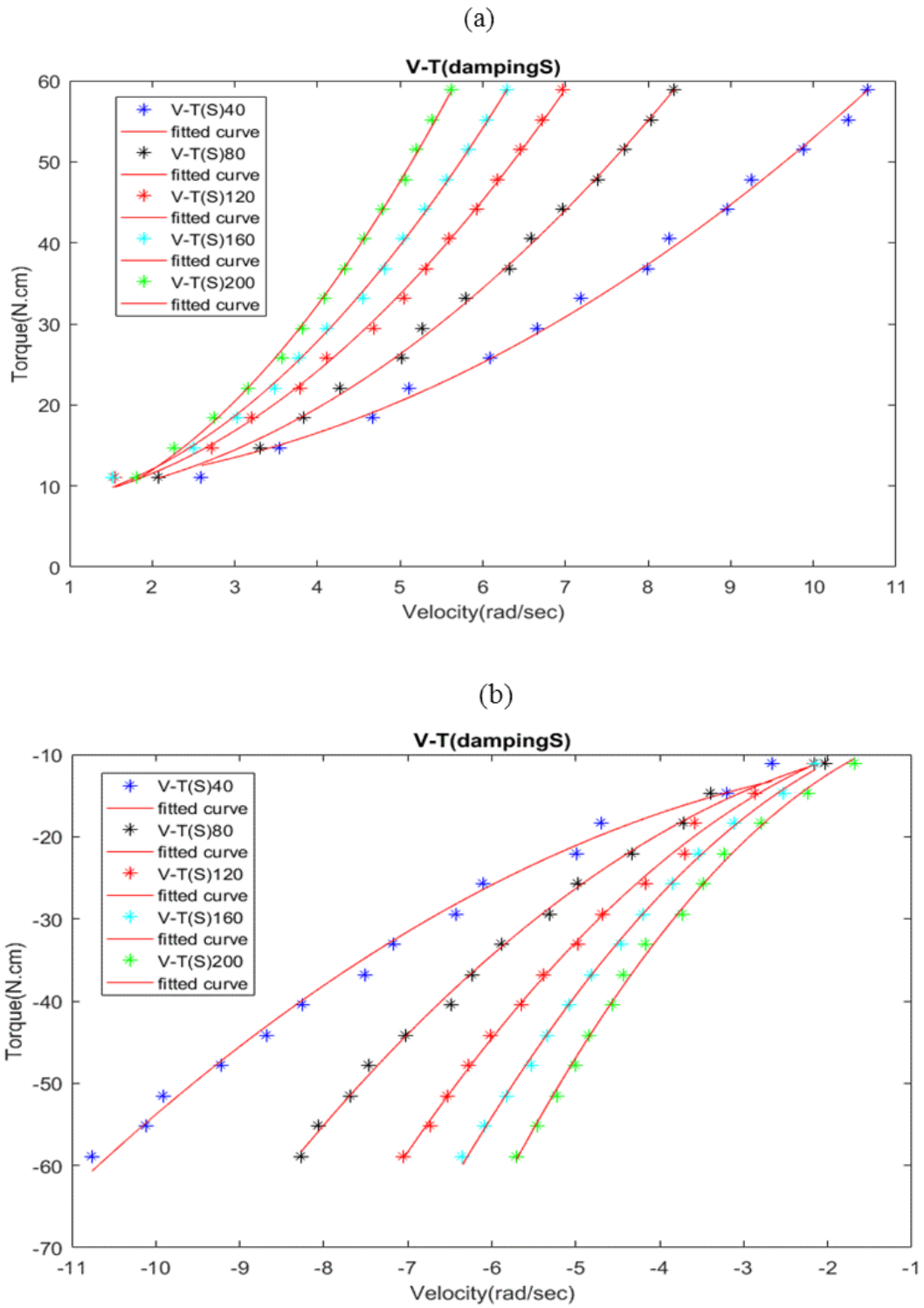

Figure 3.10 Relationship of velocity and damping torque($T_{dampingS}$): a) is the curves for tests drop in CCW direction; b) is the curves for tests fall in CW direction

the wave energy converter devices when using the platform in tank testing. For different five gains, the PTO simulation platform is shown to be able to produce different quadratic PTO damping. Similarly, the essential fitting tool is also used to draw the quadratic

equations, as listed in Table 3.6.As gain increases, the parabolic radian of the fitted curves in crease in the meantime. It means an increasing quadratic damping coefficient. The damping coefficient ς_P can be derived from the fitted equation in Table 3.6. The fit equations are in the form of $F(t)=\varsigma_P \times \dot{y}(t)^2 + u$, likewise, the u is also the uncertainty for quadratic PTO simulation discussed below in section 3.2.3. In this study, five different gain values for nonlinear damping cases were examined, and the damping coefficients were measured at *gain* = 40, 80, 120, 160, 200, with the corresponding damping ratios ς_P =17.11, 29.18,41.6, 51.93, 66.98, in counter-clockwise direction and ς_P = -17.24, -29.15, -42, -53.21, -64.81, respectively as shown in Table 3.6.

Table 3.6 Table of drawn functions based on $T_{dampingS}$ for nonlinear PTO

Gain	Fitted damping equation	
	CCW	CW
40	$F(t)=17.11\dot{y}(t)^2+9.619$	$F(t)=-17.24\dot{y}(t)^2-10.16$
80	$F(t)=29.18\dot{y}(t)^2+7.799$	$F(t)=-29.15\dot{y}(t)^2-7.843$
120	$F(t)=41.6\dot{y}(t)^2+7.334$	$F(t)=-42\dot{y}(t)^2-6.254$
160	$F(t)=51.93\dot{y}(t)^2+6.809$	$F(t)=-53.21\dot{y}(t)^2-5.602$
200	$F(t)=66.98\dot{y}(t)^2+5.182$	$F(t)=-64.81\dot{y}(t)^2-5.851$

Similarly, for quadratic PTO damping, when the $T_{dampingD}$ is directly used to give a prediction of PTO damping in real-time testing, uncertainty is also introduced. Learnt from the relationship curves between $T_{dampingD}$ and real-time velocities in Figure 3.11, the quadratic relationships are reduplicated, and the uncertainty could also be reflected in the ς_P in the fitted equations. The fitted equations are listed in Table 3.7 as well as the corresponding damping ratios ς_P =17.59, 30.48, 43.22, 52.42, 66.99 in counterclockwise direction and ς_P = -17.66, -30.54, -43.78, -55.19, -67.87, respectively. And the quadratic

coefficients are used as the non-linear damping coefficients to acquire the Dc-Gain curves, as shown in Figure 3.12, in which, the two solid lines are based on $T_{dampingS}$, and the other two dotted lines are related to $T_{dampingD}$. The blue ones are in CCW direction and red lines in CW direction.

Table 3.7 Table of drawn functions based on $T_{dampingD}$ for nonlinear PTO

Gain	Fitted equation	
	CCW	CW
40	$F(t)=17.59\dot{y}(t)^2+1.323$	$F(t)=-17.68\dot{y}(t)^2-1.539$
80	$.F(t)=30.48\dot{y}(t)^2-0.3805.$	$F(t)=-30.54\dot{y}(t)^2+0.6612$
120	$F(t)=43.22\dot{y}(t)^2-0.583$	$F(t)=-43.78\dot{y}(t)^2+1.913$
160	$F(t)=52.42\dot{y}(t)^2-0.8192$	$F(t)=-55.19\dot{y}(t)^2+2.362$
200	$F(t)=66.99\dot{y}(t)^2-2.54$	$F(t)=-67.87\dot{y}(t)^2+2.511$

(a)

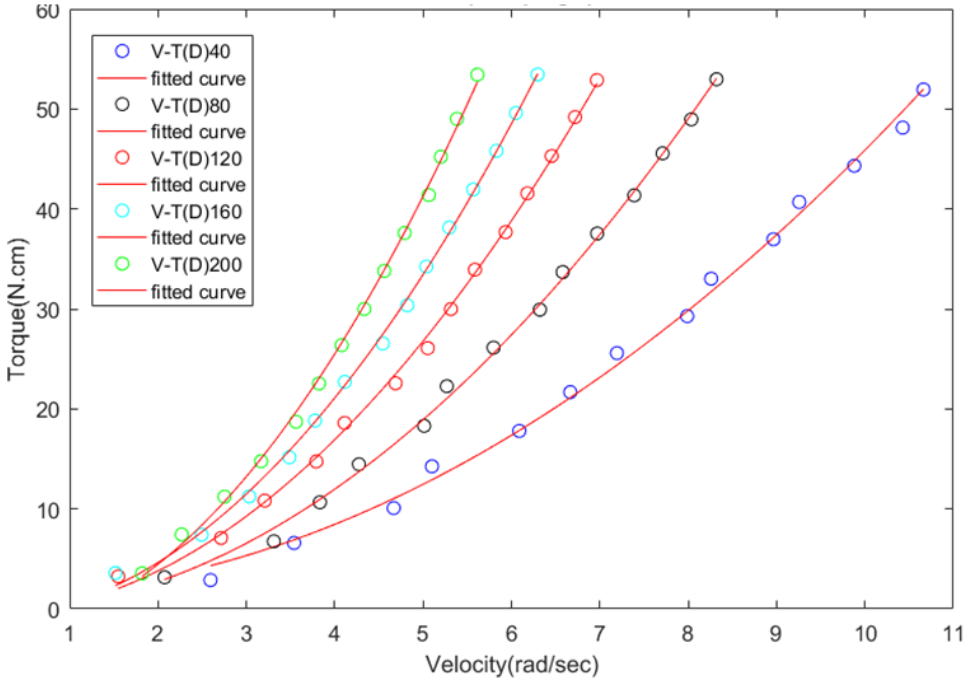

(b)

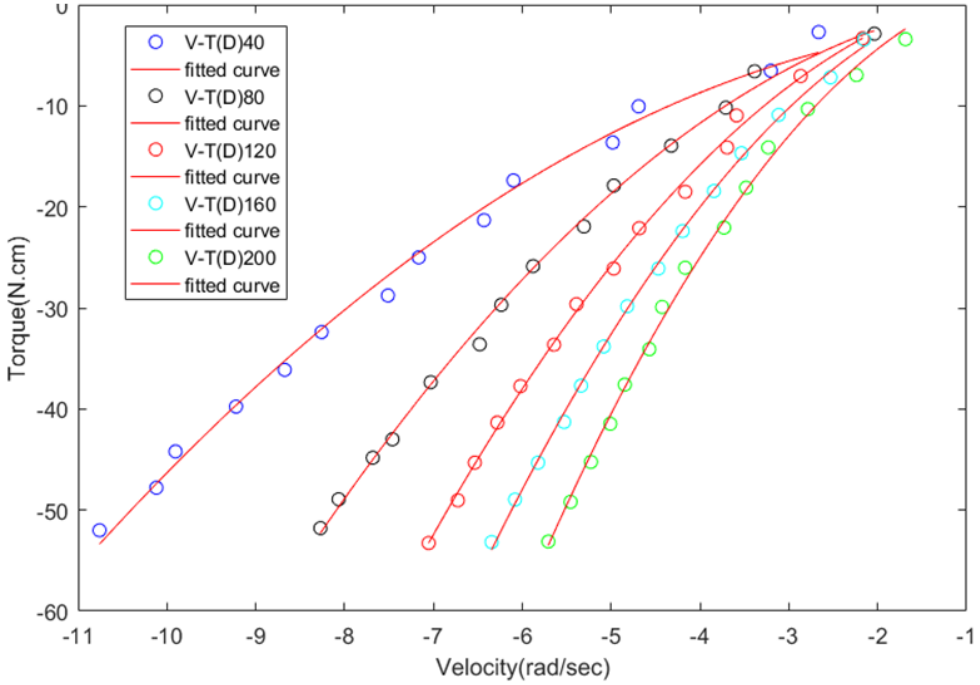

Figure 3.11 Relationship of velocity and damping torque($T_{dampingD}$) ; a).is the curves for tests drop in CCW direction;b).is the curves for tests drop in CW direction)

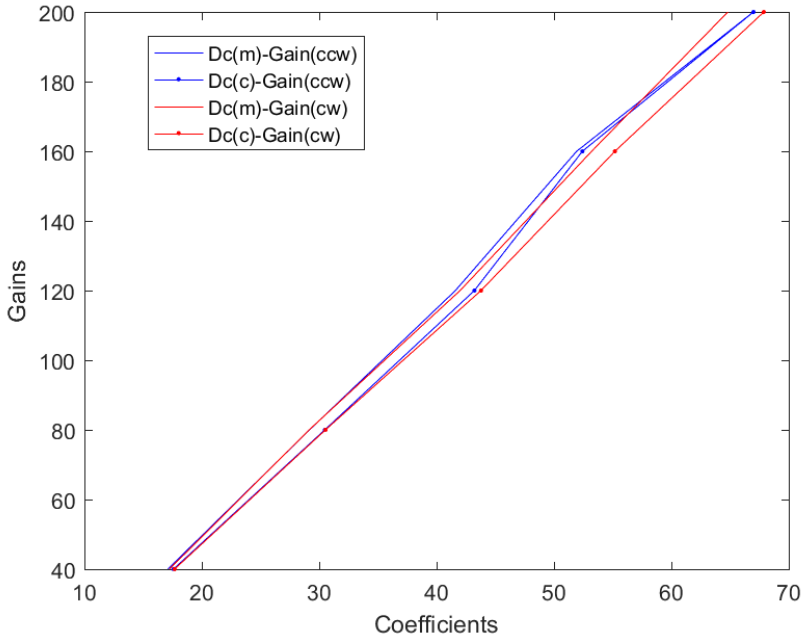

Figure 3.12 Correlation between input gains and coefficients of quadratic damping force

It is noted that a large proportion of research about wave energy devices did not include an uncertainty analysis of their experiments. As pointed out by Lamont-Kane et al. [78],

physical tests suffer from errors compared to the actual value of the quantity of interest because physical tests and measurements may not be wholly repeatable and reproducible. Without considering the uncertainties, one may get different results from each testing even with the same facilities and model. Therefore, it is more meaningful to give a range that contains the measured result and

$$Y = y \pm U \tag{3.6}$$

where the Y is the measurand, that is the value of the particular quantity to be measured. y is the estimated value of the measurand, and the U is the expanded uncertainty defined as

$$U = k \times u_c(y) \tag{3.7}$$

where the k is the coverage factor decided by the level of confidence needed. The $u_c(y)$ is the combined standard uncertainty which is calculated based on standard uncertainty. Judging by the two components in Equation (3.7), the expanded uncertainty can be interpreted as a combined standard uncertainty with a level of confidence. Hence, the k can be explained as (assuming the level of confidence is 95% here) there is 95% chance that the simulated PTO damping Y is

$$y - U \le Y \le y + U \tag{3.8}$$

where the expanded uncertainty is within $\pm u$ for simulated PTO and independent on time as shown in Table 3.8.

Table 3.8 Comparison of difference between the targeted and fitted equations

	Control function	**Fitted equation(y)**		U
n=1	$F(t) = \varsigma_P \times \dot{y}(t)$	$F(t) = \varsigma_P \times \dot{y}(t) + u$	$F(t) = \varsigma_P \times \dot{y}(t) + u$	$\pm u$
		$F(\mathrm{t}) = 44.22\dot{y}(t) + 2.834$	$F(t) = 46.12\dot{y}(t) - 2.425$	± 2.834
		$F(t) = 73.66\dot{y}(t) + 4.585$	$F(t) = 77.57\dot{y}(t) - 1.933$	± 4.585

		$F(t)=107.9\dot{y}(t)+2.277$	$F(t)=105.6\dot{y}(t)-1.909$	± 2.277
		$F(t)=129.5\dot{y}(t)+4.934$	$F\left(t\right)=133.4\dot{y}(t)-2.571$	± 4.934
		$F(t)=167.2\dot{y}(t)+3.445$	$F(t)=169.9\dot{y}(t)-2.925$	± 3.445
		$F(t)=194.6\dot{y}(t)+2.003$	$F(t)=191.2\dot{y}(t)-4.143$	± 4.143
n=2	$F(t)=\varsigma_P\times\dot{y}(t)^2$	$F(t)=\varsigma_P\times\dot{y}(t)^2+u$	$F(t)=\varsigma_P\times\dot{y}(t)^2-u$	$\pm u$
		$F(t)=17.11\dot{y}(t)^2+9.619$	$F(t)=-17.24\dot{y}(t)^2-10.16$	± 10.16
		$F(t)=29.18\dot{y}(t)^2+7.799$	$F(t)=-29.15\dot{y}(t)^2-7.843$	± 7.843
		$F(t)=41.6\dot{y}(t)^2+7.334$	$F(t)=-42\dot{y}(t)^2-6.254$	± 7.334
		$F(t)=51.93\dot{y}(t)^2+6.809$	$F(t)=-53.21\dot{y}(t)^2-5.602$	± 6.809
		$F(t)=66.98\dot{y}(t)^2+5.182$	$F(t)=-64.81\dot{y}(t)^2-5.851$	± 5.851
	U_{max}	$+9.619$	-10.16	

It is found that the uncertainty in the measurement, components, and methodology leads to an uncertainty of the PTO simulation, and it can be observed by the bias in Table 3.8. However, based on the experimental data, the F(t) is a torque with a value between 0 and 60 N*cm. When decbribing the maximum bias as a percentage of the maximum F(t), the uncertainmy is approximately 15% for CCW, and 17% for CW. This might be not good enough, thus uncertainty from three aspects is subsequently investigated. The uncertainty of the PTO simulation platform in this section includes three main parts, 1) the change in the measurement is calculated based on data of repeated drop tests; 2) the uncertainty from components consisting the physical SIL testing platform and 3) the uncertainty of the methodology of using current measurement($T_{dampingD}$) to give prediction on the physical damping torque ($T_{dampingS}$).

3.3.3 UNCERTAINTY OBSERVED IN TESTING RESULTS

Evaluation of a component of standard uncertainty is a method for the assessment of uncertainty by the statistical analysis of series repeated observations. For a measurand Y that is measured by N independent repeated observations y_k, the best-estimated value is the arithmetic mean of the N observations:

$$\bar{y} = \frac{1}{N}\sum_{k=1}^{N} y_k \tag{3.9}$$

The variance of the comments is given by

$$s^2(y) = \frac{1}{N}\sum_{j=1}^{N}(y_j - \bar{y})^2 \tag{3.10}$$

The deviation of the mean is granted by

$$s(y) = \sqrt{s^2(y)} = \sqrt{\frac{1}{N}\sum_{j=1}^{N}(y_j - \bar{y})^2} \tag{3.11}$$

Assume standard uncertainty merely is the positive square root of the difference of the mean and is expressed as

$$u(y) = s(y) \tag{3.12}$$

Then the change in measurement can be described as the observation/calculation of the standard deviation of the measures, as shown in Figure 3.13 and Figure 3.14.

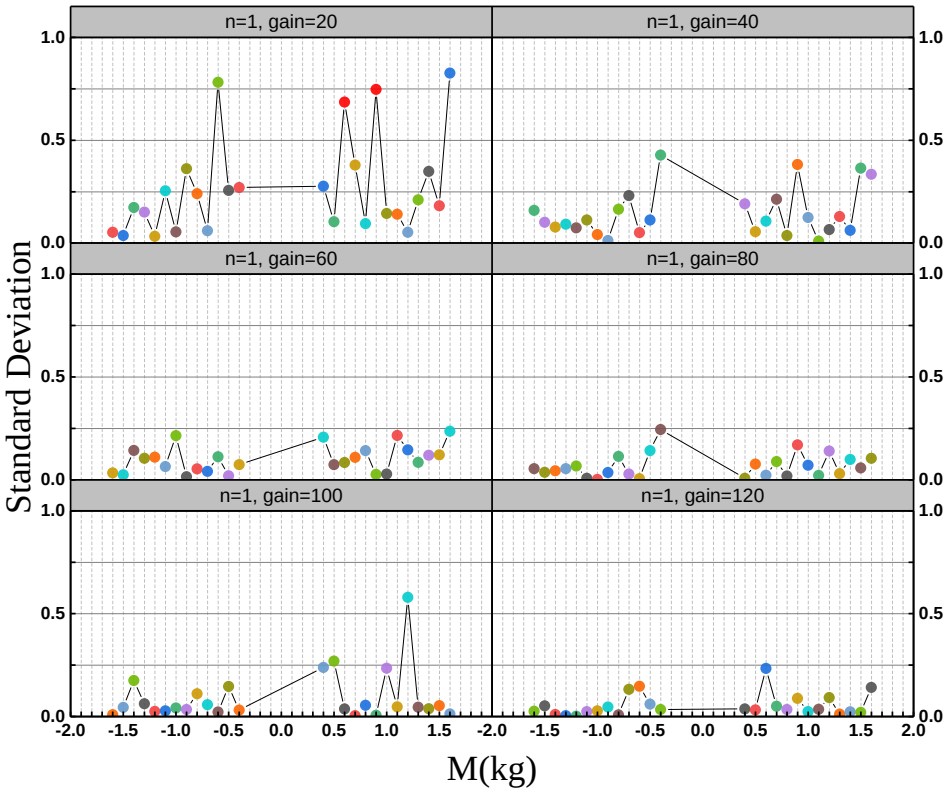

Figure 3.13 Trellis plot of the standard deviation of velocity measurements in linear cases

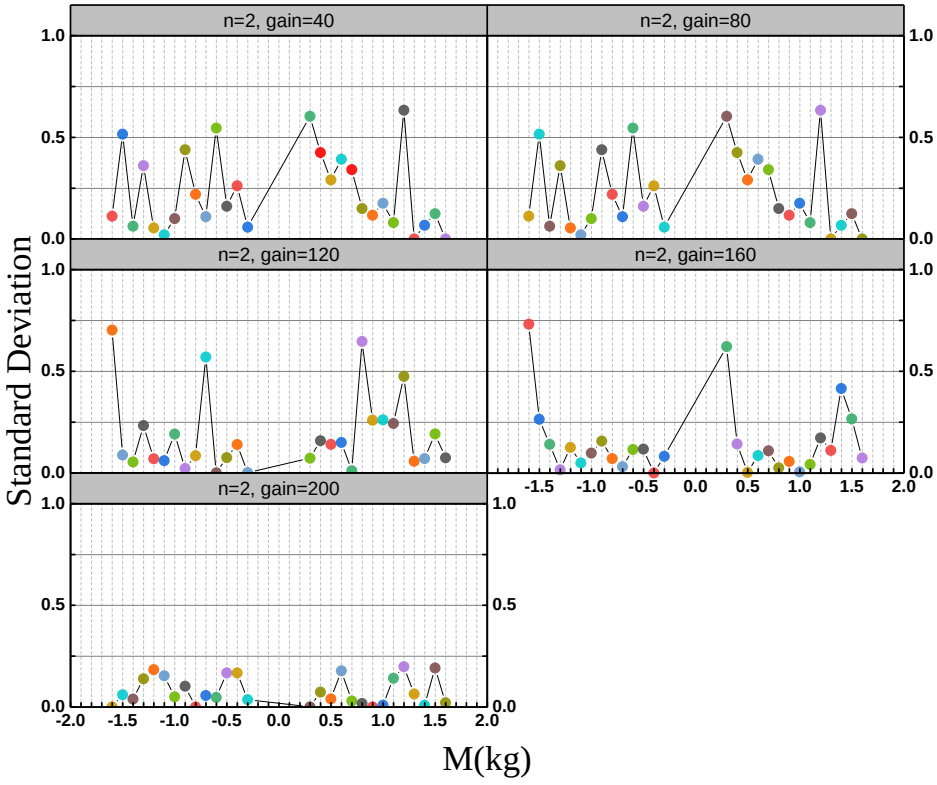

Figure 3.14 Trellis plot of the standard deviation of velocity measurements in nonlinear cases

3.3.4 UNCERTAINTY IN COMPONENTS

Uncertainty in components is also the main source of uncertainties for the innovative PTO simulation platform. This uncertainty is usually obtained by a) experience with or general knowledge of the behaviour and properties of relevant materials and instruments; b) manufacturer's specifications; c) data provided in calibration and other certificates; d) uncertainty assigned to reference data taken from handbooks. An uncertainty in components adopted in our experiments is given in Table 3.9.

The raw data obtained from the data acquisition system for one standardized drop test is shown above. The data we collected from the current sensor and tachometer are voltages, so it is needed to make a unit conversion before output, as the resolution of the current sensor is 10A/75mV, we use a unit conversion coefficient 333.33 added to the voltage, in order to output the signals from current sensor in Amp, making it 133.33A/volt. The resolution of the tachometer is 333.333 rpm/volt. Thus, calculations show that unit for current signals output in Spike (which is the software interface with the DAQ) is Amp, and for tachometer signals is rpm. Then the data in the unit of rpm and amp is sampled into excel, then input into MATLAB for plotting.

Table 3.9 Properties of critical components

Meaningful parameters	Component	Data from sheet	Uncertainty source	Uncertainty
Damping constant	Motor	17 N cm/A	Nominal value from the manufacturer (temperature dependent)	+/-0.1Ncm/A
Velocity measurements	Tachometer	3V/1000rpm	Typical analogue tacho linearity.	+/- 1%
Current measurements	Current shunt	±1.4% Gain Error, 0.3 μV/°C Offset Drift 0.005%/°C Gain Drift (Max) linearity	From manufacturers' Datasheet	+/- 1.4%
Current measurements	Current shunt monitor		From manufacturers datasheet	+/- 0.1%
Offset	Amplifier	Manually adjusted to zero to within +/- 0.01 volt.	Unbalance in zero calibration	Result in the unbalance between simulated PTOs in CCW and CW directions

Linearity	Amplifier	+/-0.25%		
Current rating	Amplifier	2A continuous/ 10A peak (for 1 second)	When the current exceeds, rated current amplifier output current is reduced.	Limit drop weights so that amplifier operates within current rating.
Power rating	Amplifier	48W continuous/240 W peak(for 1 second)	When power exceeds, rated amplifier output power is reduced.	Limit drop weights so that amplifier operates within power rating.
Raw data	Data acquisition system (MICRO 1401 II)	16 bit +- 10V	Resolution +/- 0.003 V	Ignored
	MyRio Controller	12 bit 0-5V	Resolution +- 0.001V	Ignored
Measurement of "d"	Worm drive diameter	Based on the average for multiple measurements	the "d" used for calculation of $T_{dampingS}$	+/- 0.1mm
Test weights	Mass	M1 class weigths	From manufaccturers data sheet	+/- 0.001 kg

3.3.5 UNCERTAINTY IN METHODOLOGY

As demonstrated in results discussion, measurement of the current sensor is adopted to predict the dynamic damping torque ($T_{dampingD}$) in dynamic tank testing which causes a tiny uncertainty in methodology. The uncertainty caused by using the current measurement as the torque measurement is quantitatively analysed in this section.

Because for DC motors and generators, it is concluded that the torque produced by motor proportion to the current flows through the motor, which is described as

$$T = k_T \times I \tag{3.13}$$

where k_T is the constant coefficient of motors, therefore it is designed to measure the dynamic damping torque by measuring the current of the motor. However, there is an absolute uncertainty of using current measurement to predict the physical damping torque. Therefore, comparisons between two damping torques for both linear PTO and nonlinear PTO is presented in Figure 3.15, where black data represents the data for counterclockwise and red for clockwise. We can draw a rough inference that $T_{dampingD}$ is

precisely proportional to $T_{dampingS}$, and the proportion coefficient is reasonably close to 1, so $T_{dampingD}$ can be a prediction of $T_{dampingS}$ when simulating a dynamic PTO.

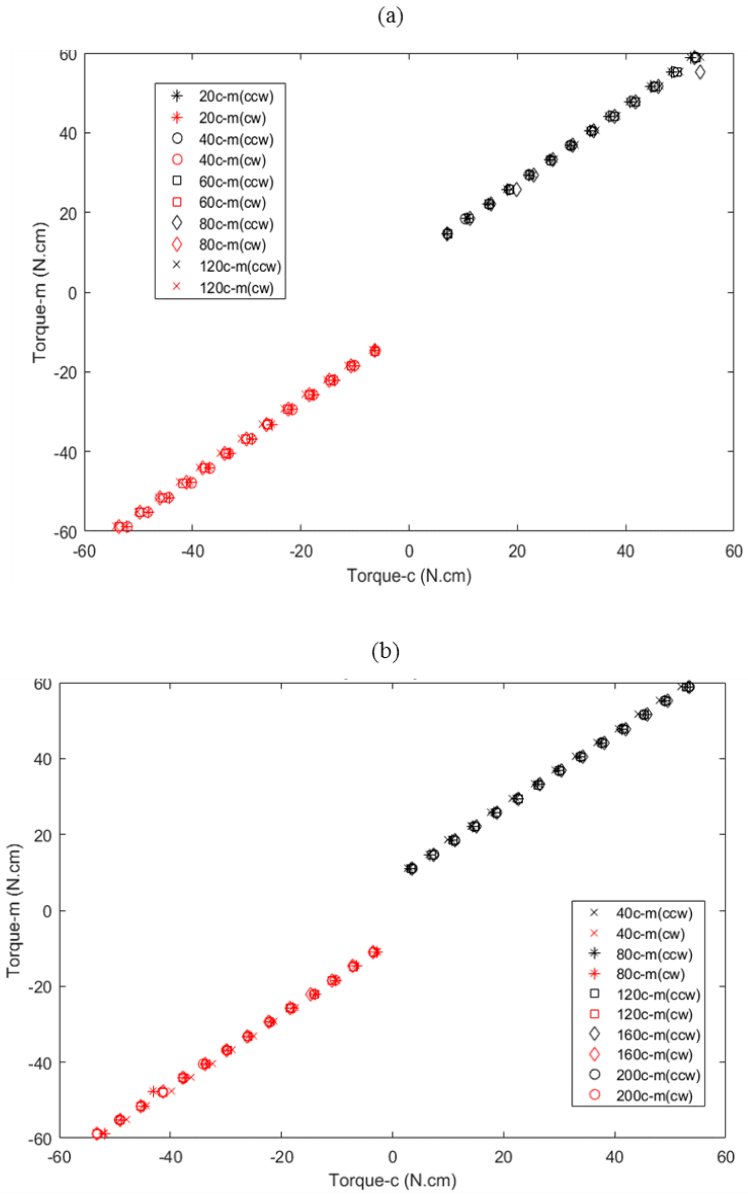

Figure 3.15.a) for linear cases and b) for nonlinear cases

3.4 Summary

A novel experimental PTO simulation platform is constructed based on the SIL simulating methodology. A large number of drop tests are performed to calibrate the PTO simulating platform, as well as to demonstrate the idea of proposing a generic PTO simulator, and the following conclusions are drawn:

- This PTO simulation platform can produce linear PTO damping and nonlinear damping in a wide range (quadratic damping is taken as a simple nonlinear example);
- Reasonable correlation curves between the input gains of the PTO simulation platform and the coefficients of simulated PTO damping forces are achieved for both linear and quadratic cases.
- The correlation indicates the PTO simulation platform's capacity of simulating linear PTO can reach 40-220 and can reach 10-70 for quadratic damping regarding damping force coefficient.
- Dynamic torque measurement is adopted to predict the dynamic damping torque in dynamic tank testing which causes a tiny uncertainty in methodology, and the possibility is quantitatively analysed;
- Gain-Damping coefficient curves are drawn and able to be used as a reference to simulate customer-suited PTO damping

After demonstrating the idea of proposing a generic PTO simulator of WECs in a lab, as well as proving the feasibility of the physical PTO simulating platform, this PTO simulating platform will be deployed in the tank tests with a 1:40 scaled model of a OWSC WEC in next chapter.

4 Model test of a OWSC WEC device with the PTO simulating platform

Wave tank tests in this chapter are conducted with three significant purposes; 1) to further demonstrate the use of the innovative simulation platform in tank tests, by applying an OWSC WEC device to the platform, 2) with the simulated real-time damping force (linear or nonlinear, various scaled) to study the output power efficiency and hydrodynamic response of the OWSC WEC in regular waves or irregular waves, 3) to find the reliable coefficient of PTO damping under different wave conditions, and indicate the potential use of the platform in PTO optimisation. Taking a OWSC WEC in this thesis as an example, best PTO damping coefficients are drawn for both linear and nonlinear damping modes, then the best PTO load could be used to design a physical PTO system or to estimate the potential to optimise an existing PTO system in the corresponding wave conditions.

4.1 Introduction

With the PTO simulating platform, it becomes possible to reach an optimal design for different PTO combinations at the design or testing stage. Moreover, by changing the input gains of the PTO simulating platform, PTO damping forces at different sizes could be simulated. Therefore, a 40th scaled OWSC WEC device is applied on this platform, and numerous tank tests in both regular and irregular waves with linear or nonlinear PTO damping strategies are carried out in[4]. Also as demonstrated in [78], investigation of the uncertainties existed in physical testing are necessary, so another purpose of the modeld tests carried out in this section is to have some insights into the uncertainties clarified in chapter 3.

A series of model tests are conducted in a wave tank to investigate the power performance of a OWSC WEC in regular and irregular waves under various simulated PTO damping forces, with the idea to locate the best design strategy of the PTO damping load in mind. The effects of the incident wave amplitude, frequency and PTO damping on the dynamic response and power capture efficiency of the WEC are studied. The output power efficiency in irregular waves is also determined and compared with that in regular waves.

4.2 Experimental methodology

In developing a WEC, the critical issues are the assessment of the hydrodynamics. The responses of OWSC WEC involve complex interactions between waves and the structure with damping[79]. It is noted that only the surge motion of the floater is considered in this study, based on the operation principle of the Oyster 800[34, 80, 81]. The governing equation of the flap motion in surge can be expressed as below:

$$m\ddot{x}(t) + c\dot{x}(t) + kx(t) = F_0 \sin \omega t \tag{4.1}$$

in which $x(t)$ is the instantaneous surge position of the flap, $\ddot{x}(t)$ and $\dot{x}(t)$ are the acceleration and velocity of the flap, respectively. m is the total mass of the system, which includes the net mass of the flap m and the added mass due to the fluid. c is the damping coefficient of the system, which includes the structural damping coefficient due to the mechanical friction c_0 and the external damping coefficient from the PTO c_p. k is the hydrostatic restoring force coefficient. ω is the angular frequency of the incident waves, $\omega = 2\pi/T$, where T is the wave period. F_0 is the peak value of the wave excitation force. For the complete response to a system driven by $F_0 \sin \omega t$, refer to[82-84].

The steady-state solution for Equation (4.1) can be expressed as:

$$x(t) = \frac{X}{2} \sin(\omega t - \frac{\pi}{2} + \beta) \tag{4.2}$$

where X is the maximum surge displacement of the flap, initially, β should be the phase difference between the surge velocity and wave excitation forces, as the resonance is usually indicated by a zero value of β. For the present cases, the wavelengths are relatively more substantial than the geometry size of the paddle (L/D>3.0, L being the wavelength and D being the geometry size of flap, i.e., the width of flap), which means the wave periods are sufficiently long in this study. It can be assumed that the wave excitation force is in phase with the wave elevation, as is asymptotically true for longwave periods[85]. Thus, in the following discussions, β is approximated by the phase difference between the flap velocity and the wave elevation.

The absorbed power in this chapter is defined as follows:

$$P = F_{damping} \times v_{WEC} \tag{4.3}$$

where $F_{damping}$ is the damping torque applied on the wave converter, while v_{WEC} is the surging velocity of the converter. The root-mean-squared power values are used to plot the power curves.

4.3 Model Testing

During Tank Testing, both regular wave tests and irregular wave tests are carried out. The tank tests of a OWSC WEC with the PTO simulating platform are carried out at the smaller hydrodynamic lab in Henry Dyer Building of University of Strathclyde, which is 21.6m long, 1.6 wide and 0.45m deep.

4.3.1 Facilities and preparation for model tests

Tank facilities: the experiment was carried out at the smaller Hydrodynamics Tank (Figure 4.1) of the University of Strathclyde. The tank is equipped with a highly repeatable four-flap type absorbing wave maker which consumes the reflected, radiated wave from the device and makes sure the generated wave is consistent during a single

test. A high-quality variable slope beach is installed at the end of the tank to eliminate wave reflection and equipped with a wall-mounted heater to minimise the temperature variation. Data acquisition is achieved by the PC based modular data acquisition system.

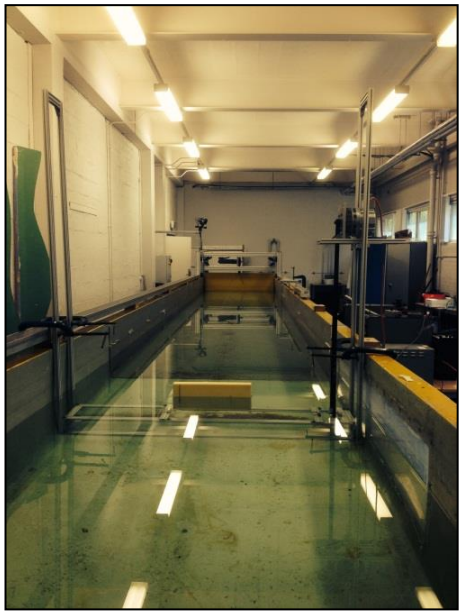

Figure 4.1 the Hydrodynamic lab in Henry Dyer Building

International Towing Tank Conference (ITTC)[86] recommended that the ratio of the breadth of the device to the width of the tank should not exceed 0.25, to reduce the blockage effect caused by waves radiating off the tank walls. A scale of 40 is therefore used to size the paddle to as dictated by the breadth of the tank where the tests are conducted. The aspect ratio is kept similar to the OWSC WEC Oyster 800. Therefore, the geometric model scale ratio is $\lambda = 1{:}40$ and the scaling factors were determined according to Froude's law of similarity as shown in Table 4.1, the model is installed on an experimental frame as the paddle shown in Figure 4.2. To make the manufacturing of the model easier, some details of the real device of Oyster 800 are not represented on the model, hence it is a notional or simplified model.

Table 4.1 General properties about the model

Full-scale parameters		Model parameters	
Paddle height	12.2m	Paddle height	305mm
Distance to seabed	16m	Distance to bottom of the tank	400mm

a b

Figure 4.2 Experimental setup

Experimental setup: as shown in Figure 4.2, on the frame stand which is consists of aluminium alloy profiles, one DC motor, two gears (one small, one big), two bearings, a rotary axel and a 1/40 scaled model paddle are installed on it. The paddle is the pitching flap that has a large surface area and is easily excited by waves. The paddle is attached to a rigid aluminium alloy plate, which in turn connects to a stainless steel axel. The paddle, plate and axle act as a rigid body. The stainless steel axle runs through two bearings. This allows the paddle to pitch smoothly, and the simulated PTO damping to be applied to it. The bearings are attached to a stationary rigid aluminium alloy frame, and the rotation of axel caused by the pitching paddle is transferred to the other shaft of a gear–belt-gear system, enable the motor to stay out of the water, at the top of the frame. Thus the wave force can be transferred to the output shaft of the motor, where a damping torque

following the programming in myRio controller is produced while electricity is drawn from wave motions.

Transfer mechanism: to successfully transfer the motion of paddle to the output shaft of the motor, a pre-tension is applied on the belt, and the belt tension mainly depends on the height of the stand, as shown in Figure 4.2. For designing the frame stand, we take both the wave heights of dominating wave energy and the nearest standard timing belt into consideration, aiming at identifying a height which is higher than the highest wave and slightly higher than a specified standard timing belt. Besides, the belt is made from neoprene, which is a corrosion-resistant material and slightly extends under fatigue since it is critical to guarantee the excellent quality transmission of the motion of the paddle. The transfer ratio produced by the timing belt is 9.6.

Calibration of wave probes: the water surface profile was measured via two-wire resistance type wave probes. The model was set at 9m downstream of the wave generator, and two wave probes are placed to measure the wave elevation as shown in Figure 4.3. Before installation, the probes are calibrated by moving up and down on a calibration frame with holes precisely machined at 5mm intervals. The wave probes were calculated over a range of +/-40mm, with the main focus on waves of +/-20mm. A calibration curve is given in Figure 4.4. As the typical linear fitting curve and the fitted conversion equation show, the coefficient used to convert from voltage of the probe to the wave height (mm) for is 92 mm/V with a bias as 0.24mm, for positive wave elevation. Similarly, it is obtained the conversion coefficient 94mm/V for inlet wave probe for negative wave elevation with a bias as 0.39mm. For the fixed wave probe, it is 97mm/V with a bias 0.26mm for positive wave elevation and 96 mm/V with a bias as 0.8mm for negative wave elevation.

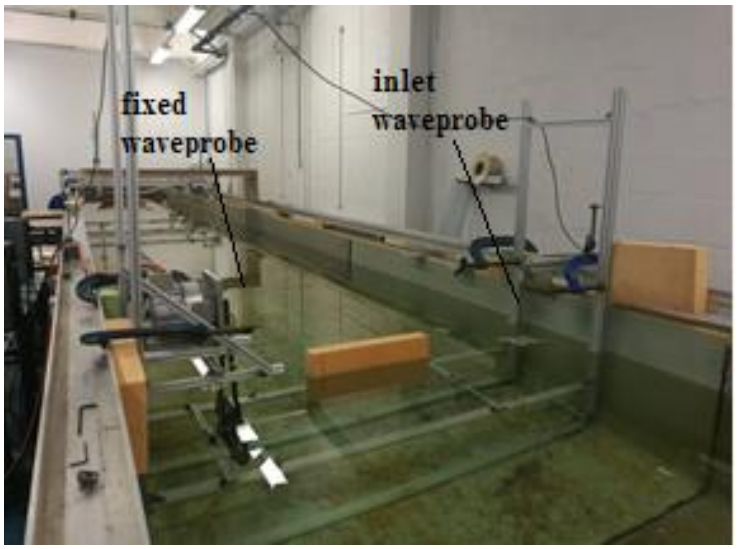

Figure 4.3 Location of wave probes

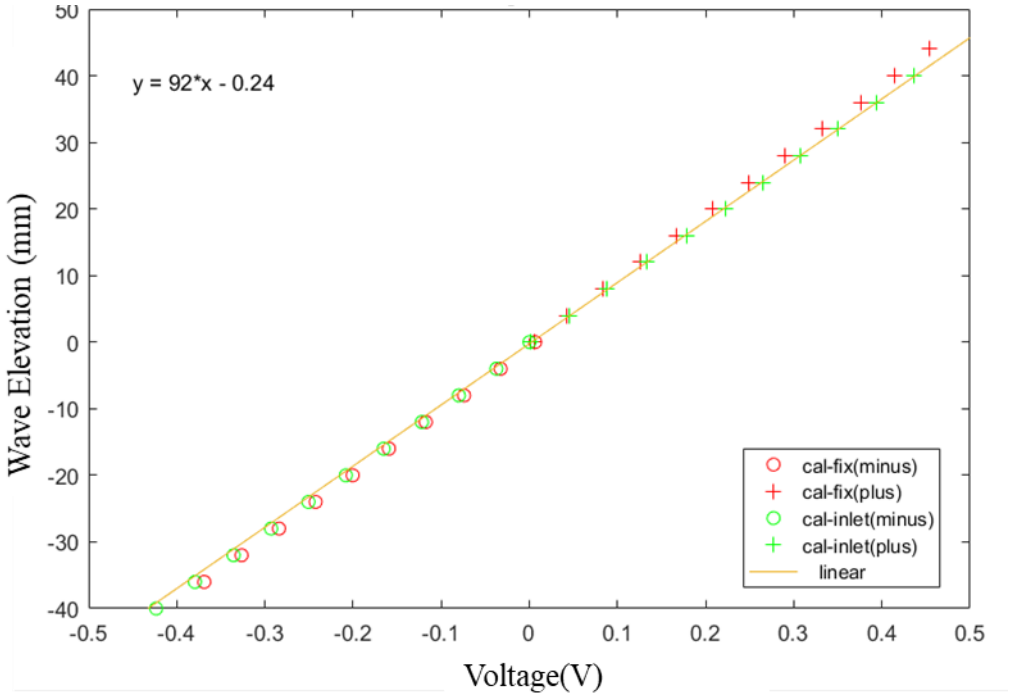

Figure 4.4 Calibration of wave probes

Data monitor: monitor torque, position and velocity are measured voltage from the tachometer, current from the current sensor, which is time-continuously monitored by a DAQ system, to give a prediction of the rotating speed, damping torque and the paddle position.

4.3.2 EXPERIMENT PROCEDURE

There are 188 tests carried out in total, and the process of some tests are stoped for various reasons, hence they are not considered in this section, and the tests used for analysis are given in the Appendix 2. The experiment is carried out in the same procedure as shown in the attached quick time movie file in Appendix 5. Furthermore, the procedure can be described as 4 steps on condition that all the electrical components are powered on.

Step 1: start the data monitoring of the DAQ system by the spike (which is the packaged software of the DAQ device we used), and it can be noticed that the time history is started. The signals of one test are shown in Figure 4.5.

Step 2: start the SIL application in LabVIEW.

Step 3: start the wave makers, but it takes a few seconds for the waves to pass to the wave probe, and another few seconds to pass to the flap.

Step 4: the data is monitored by the DAQ system, when the waves finished, the monitoring can be stopped, and the whole time histories of one test are obtained.

4.3.3 DATA PROCESSING

Take the test under linear damping of gain 80 and frequency 0.8Hz as an example. Data are firstly monitored at a sampling 100Hz, as shown in Figure 4.5 (a)(b). Figure 4.5(a) presents the time history of input velocity and output velocity, wave elevation measured from wave-probe. It is obvious that the output velocity is smaller in amplitude than the input velocity of the paddle due to the existence of the simulated PTO damping the real-time. Besides, the wave elevation measured by the inlet wave probe and the fixed wave probe are given as well. Moreover, the PTO damping force is measured as well which is shown in Figure 4.5(b). Then the output power is obtained by Equation(4.3), as shown in

Figure 4.6(b). Moreover, a few of the cycles of the signal are selected for the root-mean-squared (RMS) calculation of the power as shown in Figure 4.6(a)

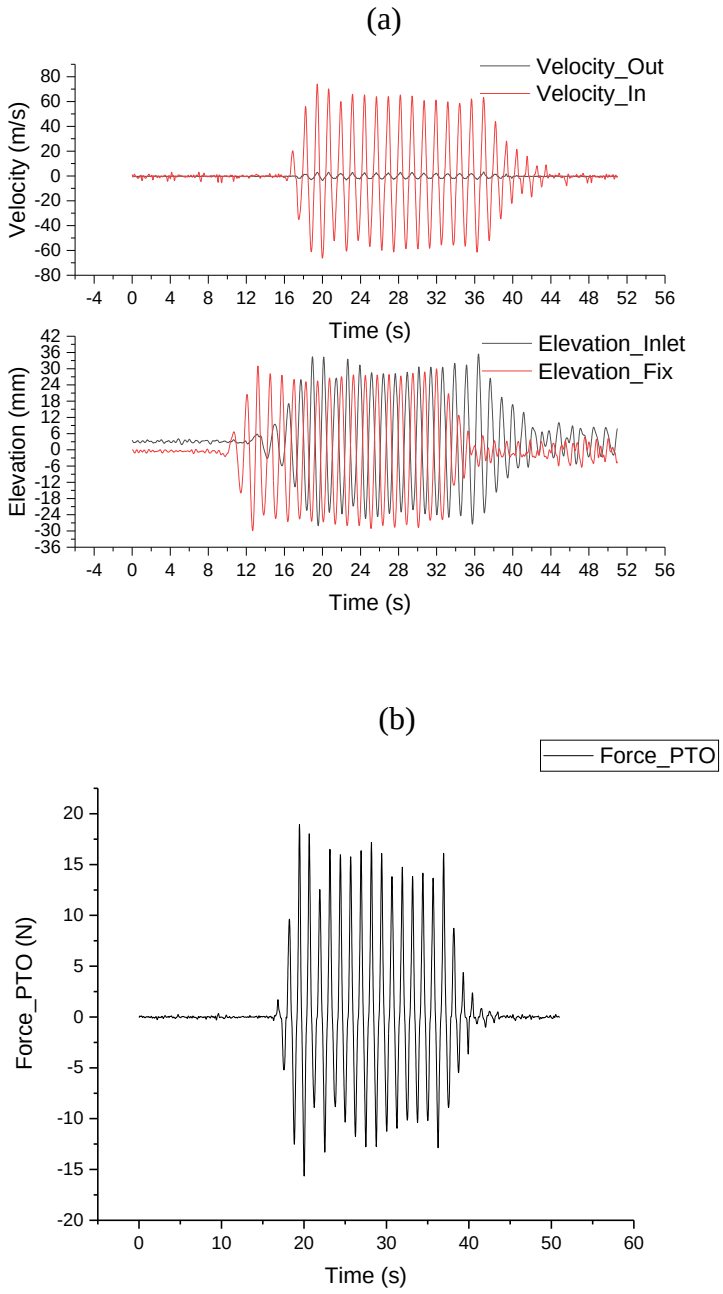

Figure 4.5 Time history of the significant data monitored from one typical test

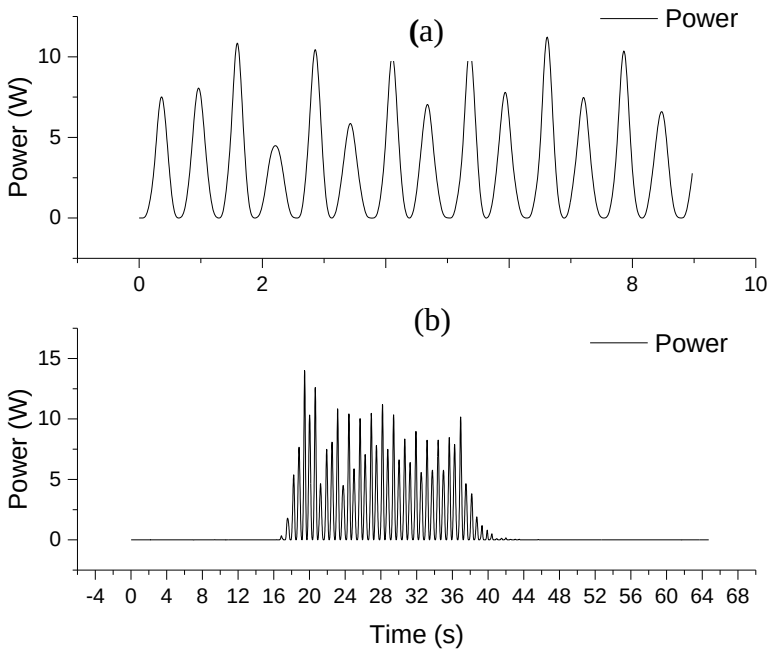

Figure 4.6 Time history of output power: a) the selected data from (b) used for statistical analysis; b) the output power for one typical test

The root-mean-square power values are used to plot the coherence between the absorbed energy and the wave frequency, and the RMS value is used as a predicted power. The output power of the WEC model is given in in

Figure 4.6 (a), when the PTO strategy is linear damping under gain80, and when the wave height is 4m, the wave frequency is 0.8HZ.

4.3.4 REGULAR WAVE TESTS

For regular waves, the effects of the main influential parameters (including the incident wave height, wave frequency, phase difference between the flap velocity and wave elevation) on the output power were quantitatively studied. Six damping coefficients(the damping coefficients are the first degree coefficients in the linear equations obtained by dropping tests in the above chapter for linear damping; the second-degree coefficients in the fitted nonlinear equations for quadratic damping) of the linear PTO damping is examined under constant incident wave height and increasing wave frequencies. A power

curve of electricity output along with wave frequency for each PTO strategy simulated by the PTO simulating platform is given, under both linear damping mode and nonlinear damping mode.

4.3.4.1 TEST MATRIX

A 1/40 scaled model of OWSC WEC is adopted in tank tests. The scaled water parameters are obtained according to Froude's law of similarity, and they are listed in Table 4.2. The PTO simulating platform is used to providing PTO damping at various scales to the WEC during tank tests. For one PTO damping, 12 wave frequencies were used for 12 experiments in the regular wave experiment. 7 linear damping and 7 nonlinear damping which stands for 14 PTO strategies are used to collect data for further analyses on the behaviour of output power. The gains are input control parameters used in the control function for producing PTO damping. As pointed out in above, each gain can be regarded as a damping coefficient either in a linear case or nonlinear case. The gains selected for use are listed in Table 4.3.

Table 4.2 parameters used in regular wave tests

Full scale		**Tank scale**	
Wave height	2m	Wave height	50mm
Water depth	25.2m	Water depth	630mm
Wave frequency	0.06-0.2372Hz	Wave frequency	0.4-1.5Hz

Table 4.3 Parameters used for different PTO strategies

f (Hz)	**0.4**	**0.5**	**0.6**	**0.7**	**0.8**	**0.9**	**1.0**	**1.1**	**1.2**	**1.3**	**1.4**	**1.5**
Gains for linear damping	20	40	70	80	90	100	120					
Gains for nonlinear damping	20	40		80			120	160	180	200		

As shown in Table 4.3, according to simple mathematics equation

$$N_f \times N_g = N_t \tag{4.4}$$

in which N_f is the number of frequencies (12), N_g is the number of gains (7*2), N_t is the number of tests, therefore during regular wave testing, 168 individual tests are carried out. For each test, the same monitor and processing method is used and demonstrated below.

4.3.4.2 THE BEHAVIOUR OF OUTPUT POWER

In this section, the experimental measurements are analysed to provide insights into the impacts the linear PTO damping or nonlinear damping has on the output power. Figure 4.7 clearly shows that the linear damping with gain 80 is the best linear PTO damping coefficient, with which the OWSC WEC absorbs the maximum power from the wave movement.

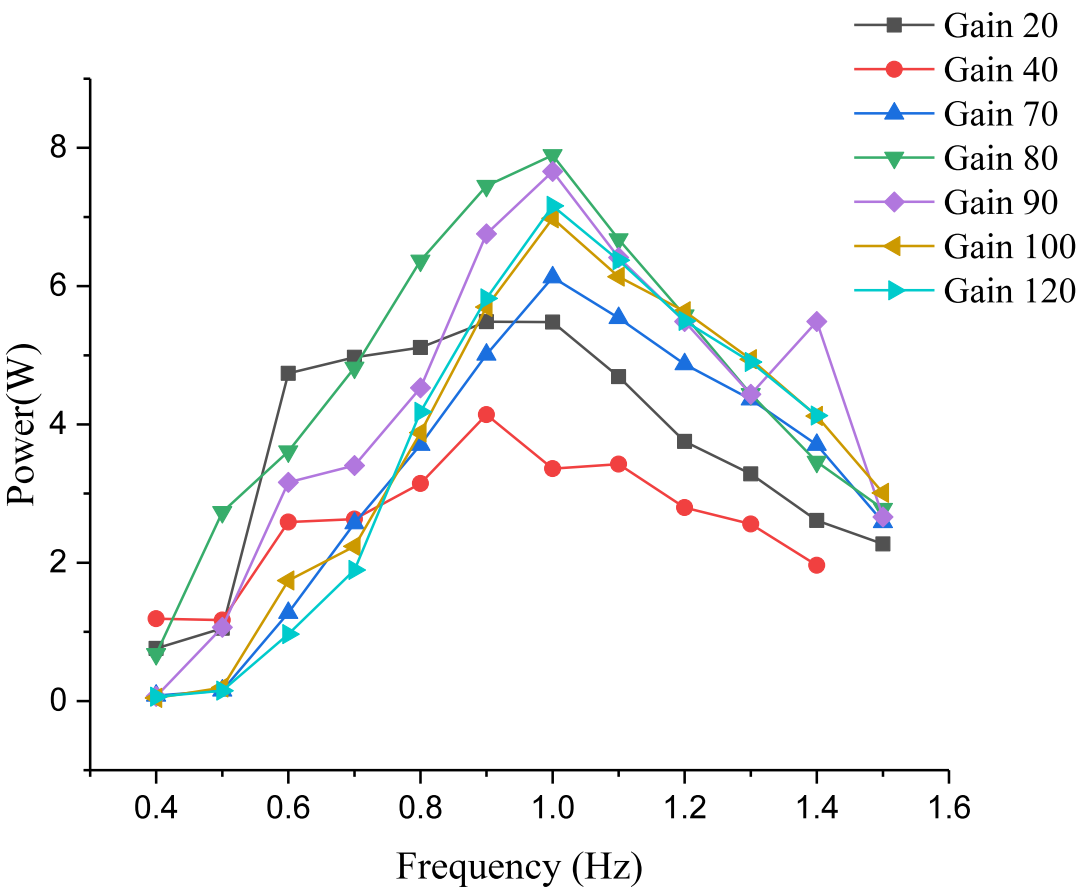

Figure 4.7 Power output curves for linear damping

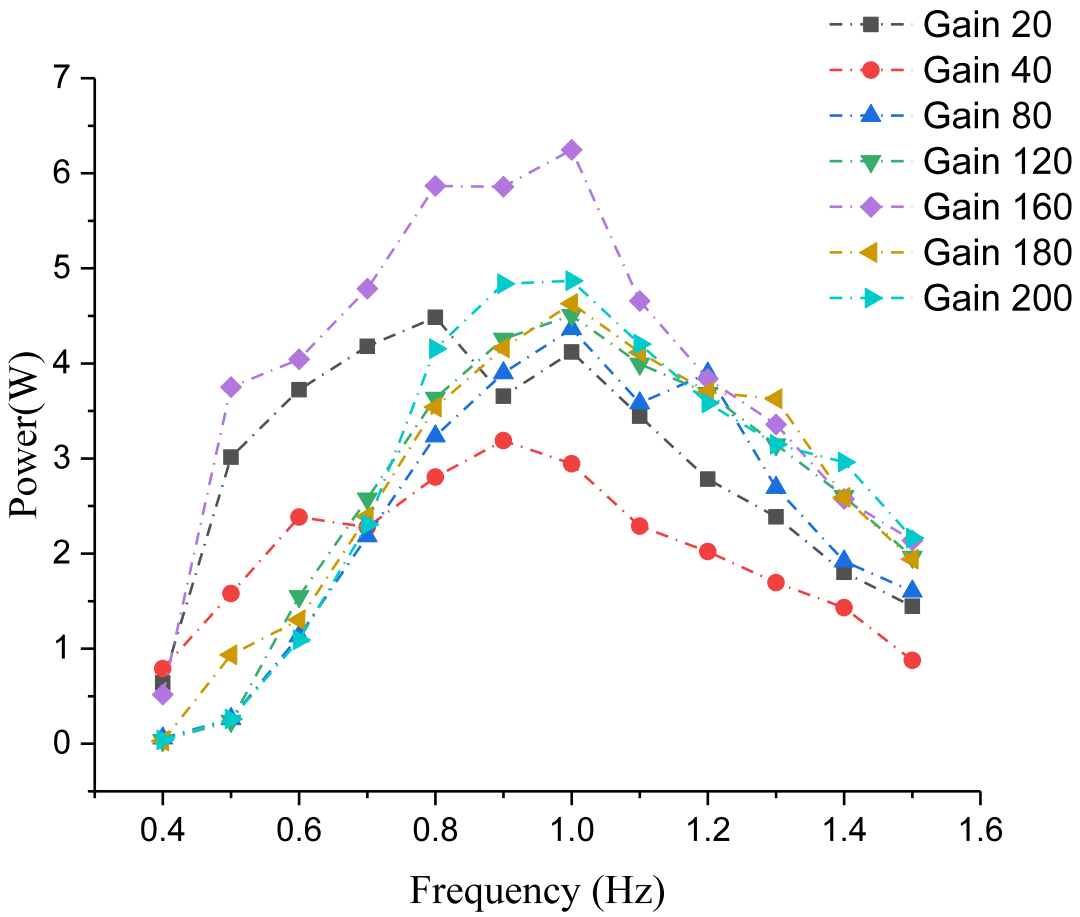

Figure 4.8 Power output curves for nonlinear damping

Similarly, as shown in Figure 4.8, the quadratic PTO damping works best with the input gain of 160 (the corresponding damping coefficient is 51.93 in CCW rotation and 53.21 in CW rotation, see Chapter 2). For nonlinear damping, it is noted that the lowest damping coefficient (gain20) works more effective with the ocean waves in low frequency range. For higher frequencies (above 0.9Hz) the output power generally increases while the damping coefficient increases in between gain 40 and gain 160, it reaches the maximum at gain160 and starts decreasing while the coefficient increases. For the linear damping, the lowest damping coefficient also (gain20) copes better than gain40 and gain70, shows its advantage in low-frequency waves. The output of electricity is shown to increase as the linear damping coefficient increases and reach a maximum at gain80, then starts to decrease as the gain increases. It is noticeable that the curves are not as smooth as

expected, and it is attributed to a number of reasons which may potentially cause the fluctuation of the curves:

1) The insufficient sensitivity of the wave probes, because the wave height measured by the wave probe is changing as the wave frequency varies, and the changing in the measured wave height is ignored during data process and plotting.
2) As discussed in Chapter 2, there is a certain amount of uncertainty existing in the PTO simulator.
3) The scaled OWSC WEC device model is limited to represent the real mass and real conditions of an actual OWSC WEC device.

4.3.4.3 HYDRODYNAMIC PERFORMANCE OF THE MODEL

The dynamic response may have a significant effect on the power performance of ocean wave energy converting devices. RAOs are traditionally used to observe the hydrodynamic responses of a ship. However, for WEC, the phase difference between wave elevation and paddle pitching can give significant instructions on the active control design of a WEC. The maximum power is assumed by different researchers to be observed at a resonance. The resonance is usually indicated by a zero phase difference between the paddle velocity and wave excitation force. For the present study, this corresponds to a zero phase difference between the buoy velocity and wave elevation. Figure 4.9 shows the time histories of the wave elevation ratio $R(t)$ and buoy motion in pitch $x(t)$ for different damping coefficients under the wave frequency of 0.8Hz. It can be seen that there is no apparent difference observed for different damping coefficients, which means this phase difference is not PTO dependent in the case of a scaled OWSC WEC model. Therefore, experiments based on the PTO strategy of linear_gain80 and nonlinear_gain160 are taken for examples to further study the behaviour of the phase difference. The damping torque is observed in the phase of the rotating velocity of the

paddle when wave frequency is above 1.0Hz as shown in Figure 4.10 and Figure 4.11. Furthermore, the introduced ratio $R(t)$ is defined by as below for the analyses of hydrodynamic performance in the following.

$$R_a(t) = \frac{a(t)}{\max[a(t)]} \tag{4.5}$$

$$R_v(t) = \frac{V(t)}{\max[V(t)]} \tag{4.6}$$

in which $R_a(t)$ is the wave elevation ration $a(t)$ is the wave elevation, $\max[a(t)]$ is the maximum value of the wave elevation, $R_v(t)$ is the pitching velocity Ratio, $V(t)$ is the pitching velocity, $\max[V(t)]$ is the maximum of pitching velocity. Hence the $R_a(t)$ and $R_v(t)$ are presented in Figure 4.9-Figure 4.11.

（a）

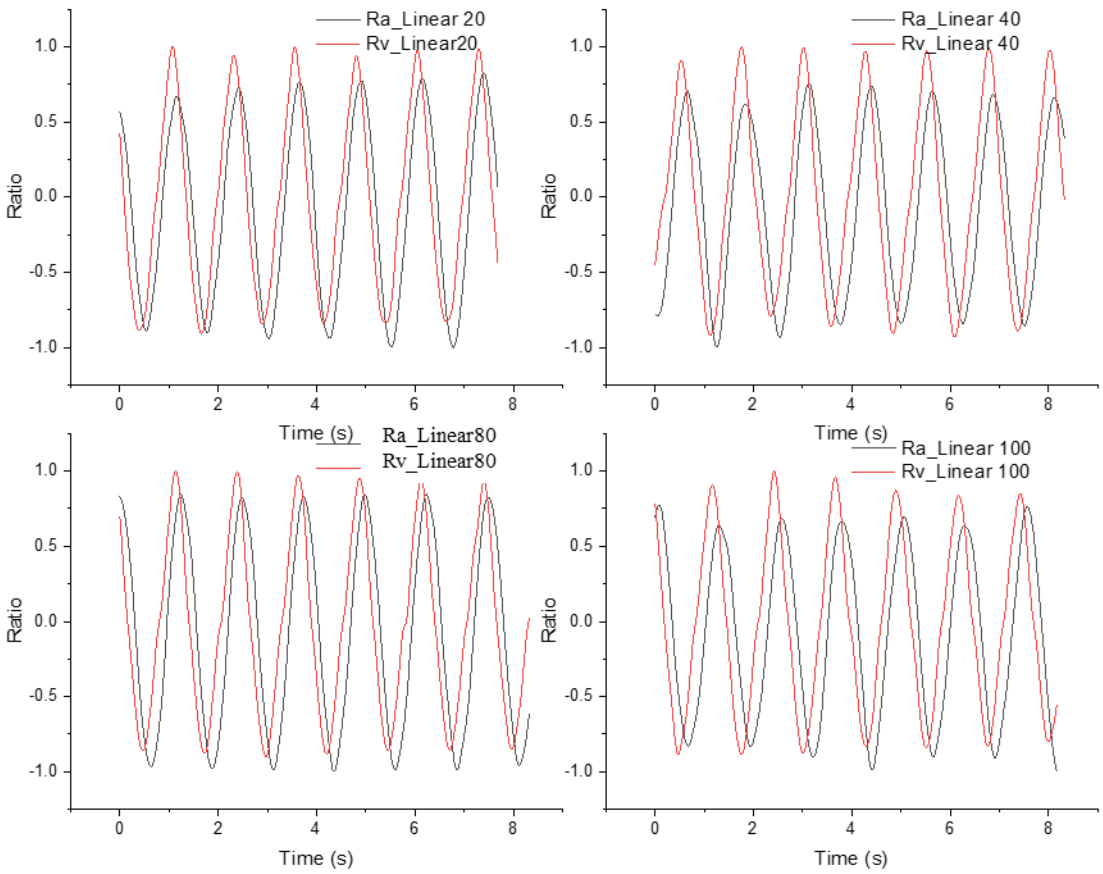

(b)

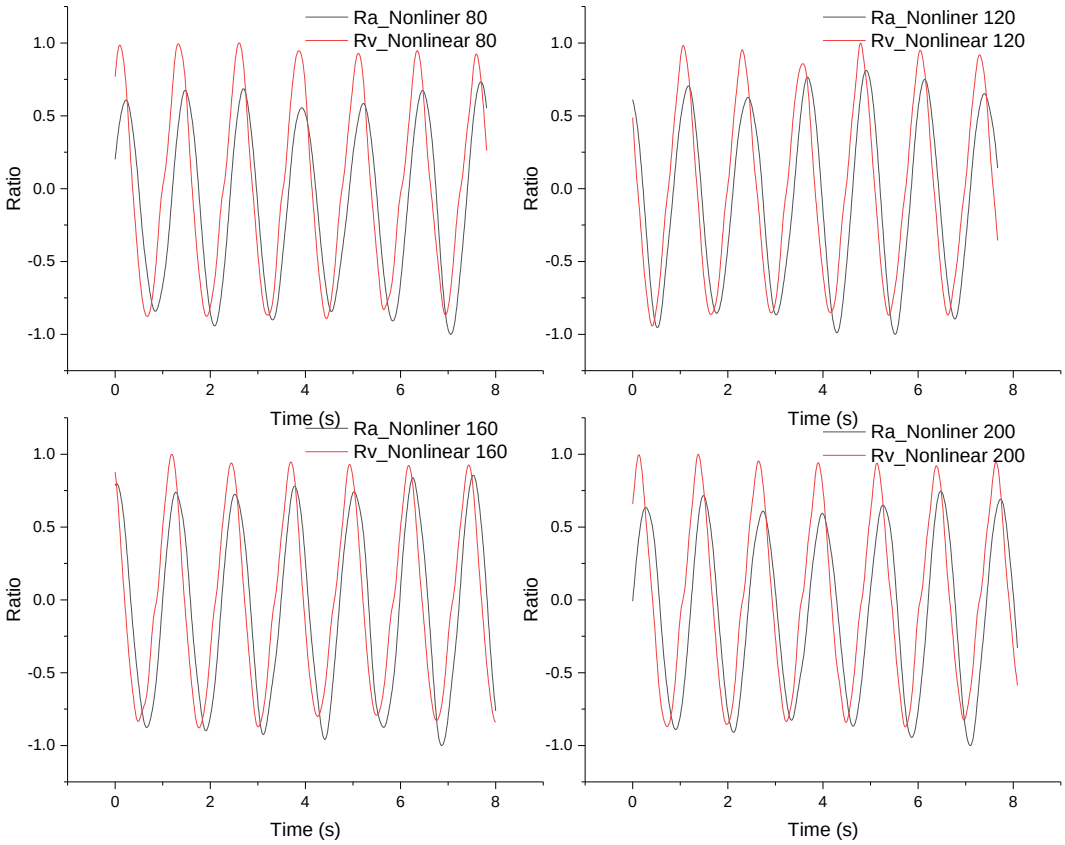

Figure 4.9 Time history of the ratio of wave elevation and buoy velocity for different input gains in regular wave tests under 0.8Hz; a) is for under linear damping, b) is for under nonlinear damping

Figure 4.10 shows the time histories of the wave elevation ration $R(t)$ and buoy motion in pitch $x(t)$ for one standardized damping coefficient under different wave frequencies between 0.4Hz-1.5Hz. The instantaneous buoy velocity $\dot{x}(t)$, which is monitored by a tachometer concerning time t regarding the paddle velocity during the experiments, is also shown in Figures. The time difference between the buoy velocity $\dot{x}(t)$ and wave elevation $a(t)$ is denoted as Δt. Thus, the phase difference can be obtained by the relationship:

$$\frac{\beta}{2t} = \frac{\Delta t}{T} \tag{4.7}$$

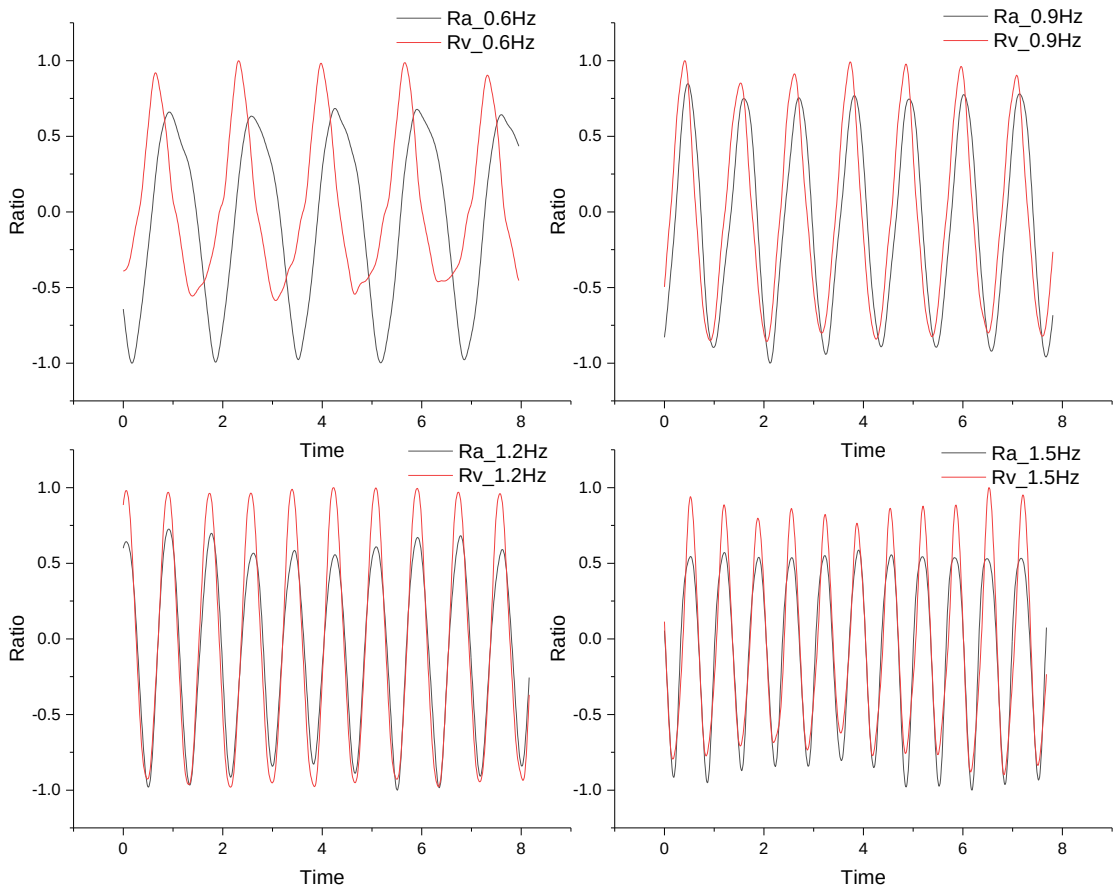

Figure 4.10 Time history of the wave elevation and buoy velocity in regular wave tests under linear damping of gain80

Figure 4.11 shows Time history of the wave elevation and buoy velocity in regular wave tests under nonlinear damping of gain160. And it is also observed that the buoy moves with the same period as the incident waves, but the phase difference between the buoy velocity and wave elevation decreases with an increase in wave frequency, and resonance is indicated usually happen when the wave frequency is above 1.0Hz.

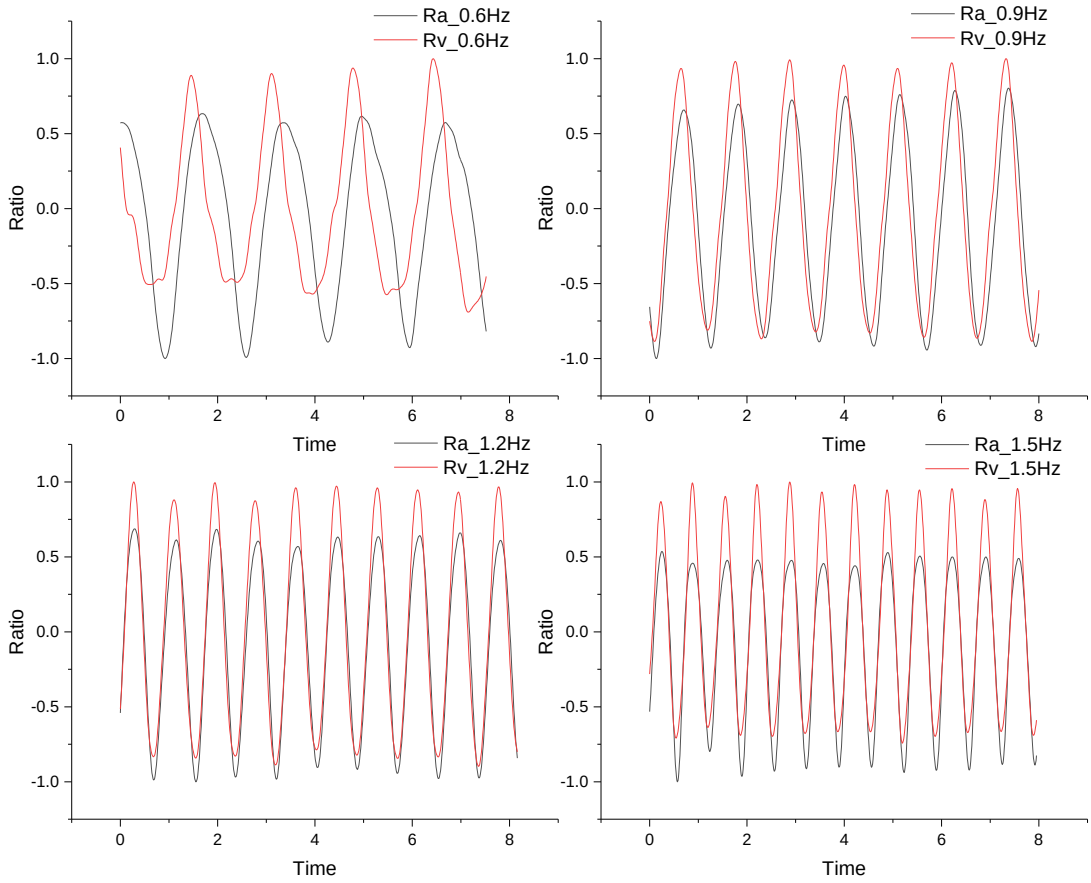

Figure 4.11 Time history of the wave elevation and buoy velocity in regular wave tests under nonlinear damping of gain160

4.3.5 IRREGULAR WAVE TESTS

4.3.5.1 TESTING MATRIX

Irregular sea states indicate wave conditions and energy distribution within the expected frequency range for given wind speed in the ocean or at a specific location in the sea. Some well-recognised spectra corresponding to particular areas can be applied to models in tank testing equipment. For traditional irregular wave tests the the well-estimated JONSWAP spectrum is used. Therefore, during the irregular wave tests, both a user-defined wave spectrum and a generic JONSWAP spectrum are adopted The spectra are applied by computer software in the testing facility which directs the wave maker to produce the desired wave conditions. Data measuring of each tank test runs for 450s to

reduce the transient response caused by the start and stop of the facility in the tank. However, it is believed the testing results based on JONSWAP spectrum might have more academic meaning to publish, this section is mainly focused on the tests based on JONSWAP spectrum as shown in Figure 4.12, and the result of from tank tests under user-defined spectra are reviewed as a comparison in the following section.

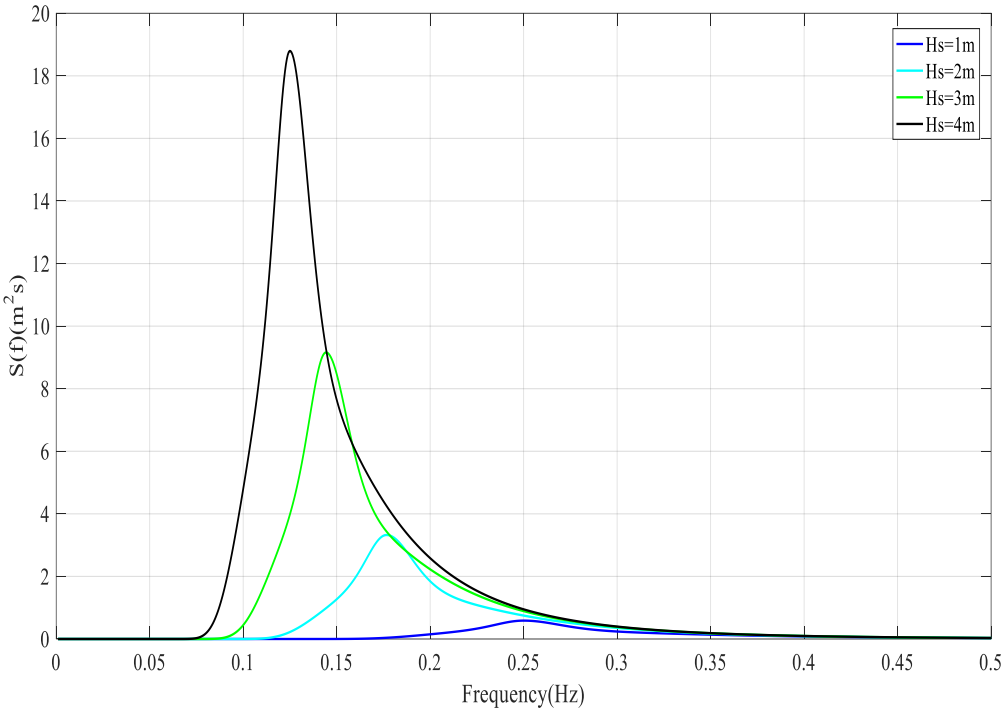

Figure 4.12 JONSWAP spectrum used in the irregular tank tests

There are two main parameters determine the shape of the JONSWAP spectrum and the specific sea conditions generated. They are mean wave period T_m and the significant wave height H_s. T_m and H_s are related by the following equation;

$$T_m = 4 \times \sqrt{H_s} \tag{4.8}$$

The model is a 40th of the existing device of the 'OWSC WEC'. The duration of the test for the irregular spectrum is calculated according to the Froude's law of similarity,

$$T_{test} = \frac{T_{full}}{\sqrt{R}} = \frac{T_{full}}{\sqrt{40}} \tag{4.9}$$

where T_{full} is usually 30 minutes.

The parameters used for the JONSWAP spectrum and tank tests are listed in Table 4.4.

Table 4.4 Spectrum parameters

Spectrum Parameters	Test parameter	
Wave height(H_s)	T_p	T_{test}
1m	4s	285s
2m	5.66s	285s
3m	6.93s	285s
4m	8s	285s

4.3.5.2 THE BEHAVIOUR OF OUTPUT POWER

Table 4.5 Test files based on JONSWAP spectrum

Linear damping							
H_s =1m	gain80	gain120					
File name	h1l8r	h1l12r					
H_s =2m	gain80	gain90	gain120	gain400	gain800	gain0	gain-80
File name	h2l8r	h2l9r	h2l12r	h2l41r	h2l83r	h2l0r	h2ln8r
H_s =3m	gain80	gain90	gain120	gain400	gain800	gain0	gain-80
File name	h3l8r	h3l9r	h3l12r	h3l41r	h3l83r	h3l0r	h3ln8r
Nonlinear damping							
H_s =1m	gain160						
File name	h1n16r						
H_s =2m	gain80	gain160	gain200	gain400	gain1200	gain2000	gain-160
File name	h2n8r	h2n16r	h2n20r	h2n41r	h2n125r	h2n0r	h2nn16r
H_s =3m	gain80	gain160	gain200	gain1200	gain0		
File name	h3n8r	h3n16r	h3n20r	h3n125r	h3n0r		

Due to the limitation of the time of using the hydrodynamic tank, a limited number of irregular wave tests based on the JONSWAP spectrum as mentioned above are carried out, unlike in regular wave tests, 12 trials for each gain are carried out. Moreover, Table 4.5 lists all the file names of irregular wave tests based on the JONSWAP spectrum used for data analysis.

A MATLAB programme is developed to analyse the data in each test file, and a few statistic values for relevant parameters are obtained, for instance, the standard deviation of wave height, the RMS of damping torque, the RMS of output power from the paddle calculated from Equation (4.3). The RMS power values for each test files are used to draw the power curves against wave heights and PTO damping as shown in Figure 4.13. It can be seen that the output power of the OWSC WEC model(paddle) increase linearly as the wave heights increase, and the linear curve for bigger damping coefficient tends to have a bigger slope, though the power reaches the maximum at linear damping gain80 and nonlinear damping160 in regular wave tests. It is seen from Figure 4.14, for the same significant wave height, the output power for linear damping is slightly higher than the nonlinear damping, though it may result in less stability in the corresponding PTO system.

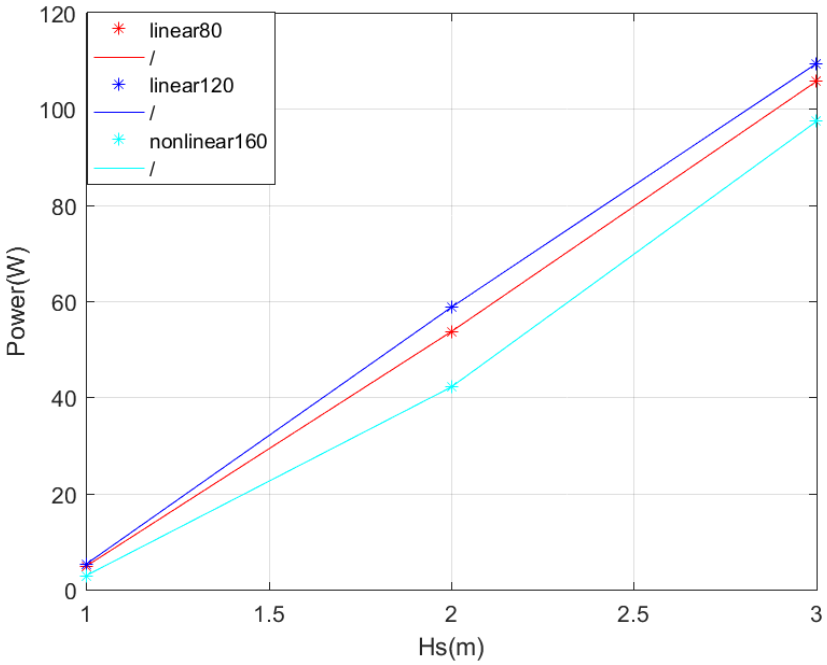

Figure 4.13 Power changes along wave heights

Figure 4.14 presents the changing of output power along with the changing of damping gains for two different significant wave heights, namely when Hs=2m and Hs=3m. The red one is for 3m, and the black one is for 2m. Each star point located on the line is an RMS value of the output power from each test file. As shown by the two lines, it is concluded the output power increase hugely as the PTO damping increase before it reached gain100, and it keeps almost stable in between gain100 and gain500, then reduce slightly when its further increase.

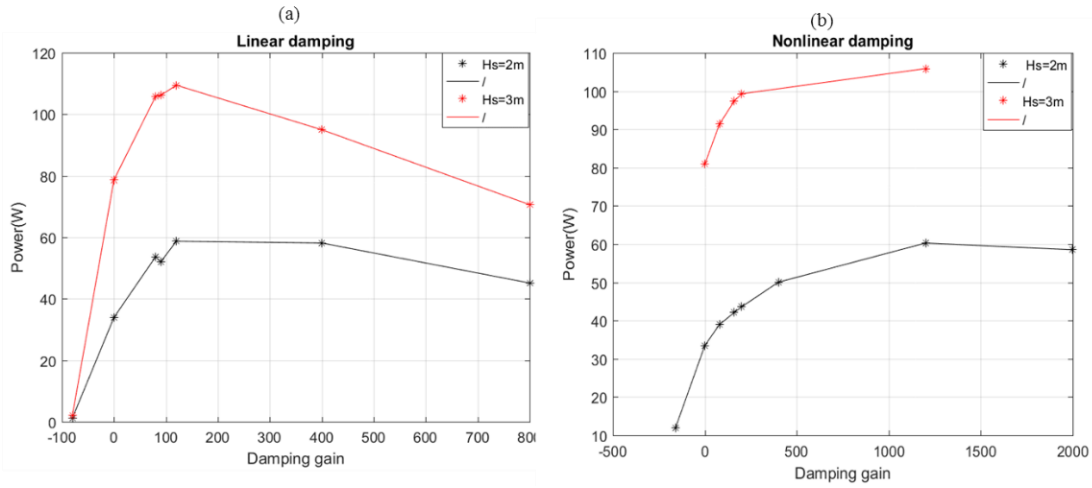

Figure 4.14 Power changes along with input gains for linear PTO or non-linear PTO: a) is for linear PTO; b) is for nonlinear PTO

Similarly, the power increase much less than for linear damping cases, and tends to be stable when it reaches gain500, and it keeps almost stable even when the damping gain increase to 2000. Therefore, it is believed by the author that the nonlinear damping has a wider gain range and have better gain applicability though it does not show many advantages on the increase of power amount. Moreover, it is also proved for both linear damping and nonlinear damping cases, that higher significant waves produce more electricity if without considering the stability and the robustness of the real PTO system.

4.3.5.3 HYDRODYNAMIC PERFORMANCE OF THE MODEL

During the irregular wave tests, a few overtopping events were observed as shown in Figure 4.15. Overtopping is believed can significantly reduce the power output, when the wave passes over the top of the paddle. However, the output power curves indicate that it may not have a significant influence.

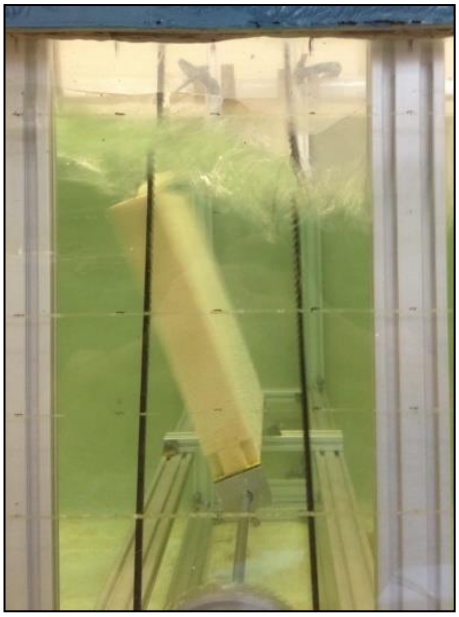

Figure 4.15 Side view of the effects of overtopping

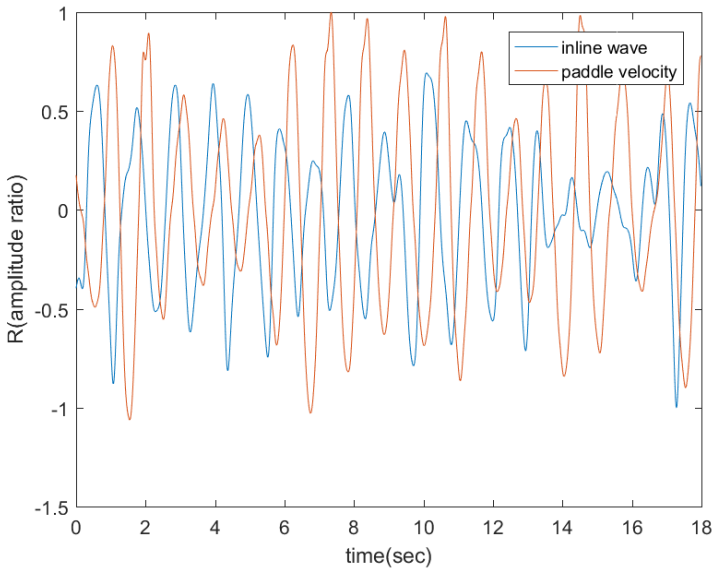

Figure 4.16 Time history of the wave elevation and buoy velocity in irregular wave tests under linear damping of gain80

As demonstrated in Equation (4.5) and (4.6), an amplitude ratio is defined during the observation of the hydrodynamic performance of the model in tank testing. Figure 4.16 shows the time histories of the wave elevation ratio $R(t)$ and buoy motion in pitch $x(t)$ for the linear damping gain80 in irregular wave testing under the JONSWAP spectrum when Hs=3m. Figure 4.17 presents the time histories of the wave elevation ratio $R(t)$ and buoy motion in pitch $x(t)$ for the nonlinear damping gain160 during the same seconds and under the same wave spectrum. It can be seen from the pictures that there is no big difference in the phase whether adopting the linear PTO or nonlinear PTO strategy. The paddle velocity is slightly behind but following the inline wave movement.

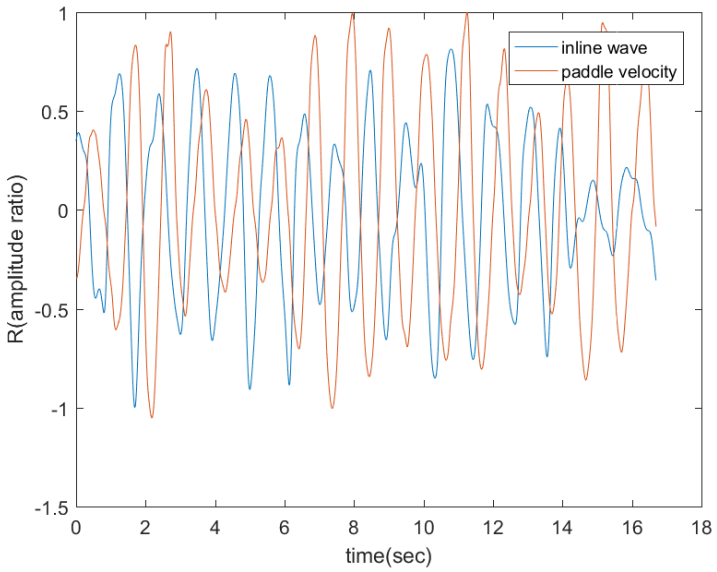

Figure 4.17 Time history of the wave elevation and buoy velocity in irregular wave tests under nonlinear damping of gain160

The final response is not pure sinusoidal so that it can be written as:

$$x(t) = \frac{X}{2}\sin(\omega t - \frac{\pi}{2} + \beta) + epsilon(t) \qquad (4.10)$$

where $epsilon(t)$ is a non-sinusoidal component, whose wave energy is small, and the sinusoidal response is the principal component of the response.

The JONSWAP and the user-defined spectrum used in experiments are both unimodal, and the main energy is determined by the frequency at that peak. The response energy of other frequencies is small. Therefore, the sinusoidal response is roughly presented.

4.4 Comparison of the output power in regular wave and irregular wave

4.4.1 Comparison between linear and nonlinear damping in regular wave tests

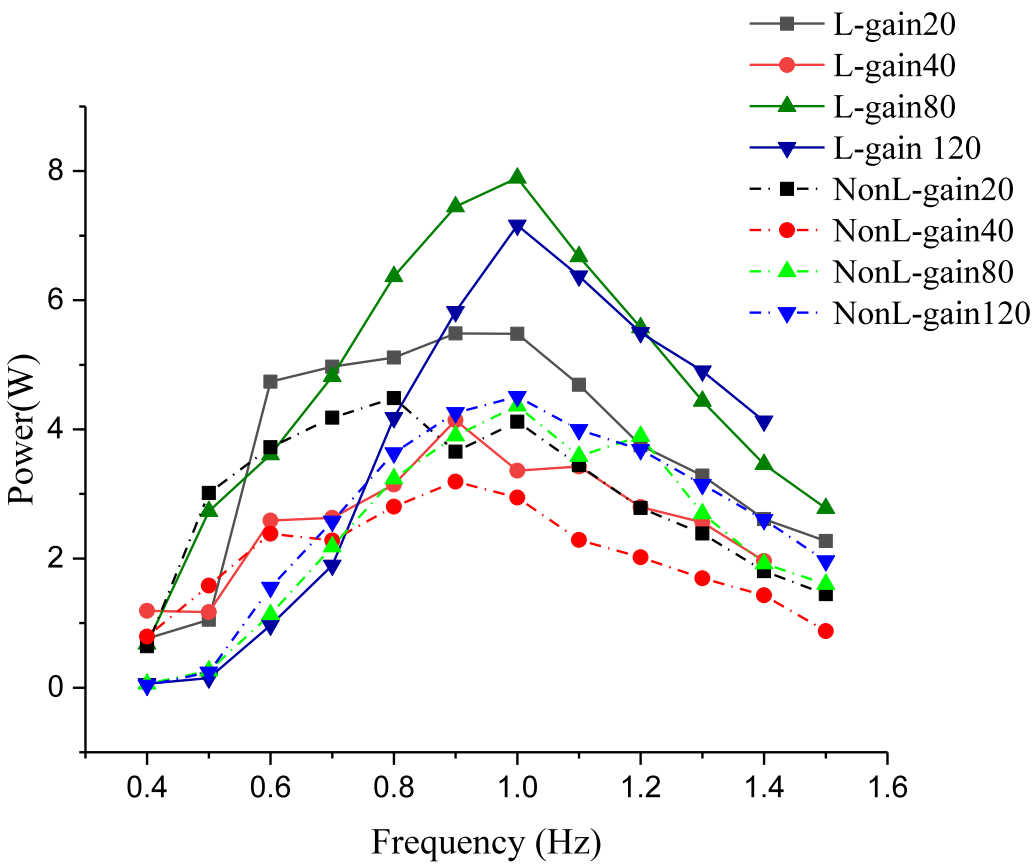

Figure 4.18 Power comparison of the same gains for linear damping and nonlinear damping

Though the linear damping and nonlinear damping have best electricity output power at different gains, and the nonlinear damping has much wider gain range, it is critical to learning the different output behaviour at the same gains for linear PTO damping and nonlinear PTO damping. Therefore, Figure 4.18 shows the power comparison of the same gains for both linear damping and nonlinear damping. It is seen that, for the same gain, the linear PTO produce more electricity. Figure 4.19 shows the power curves of the best three gains for both linear PTO damping and nonlinear PTO damping. It can be concluded that the nonlinear damping has better PTO stability, better gain applicability though it does not show many advantages on the increase of power amount.

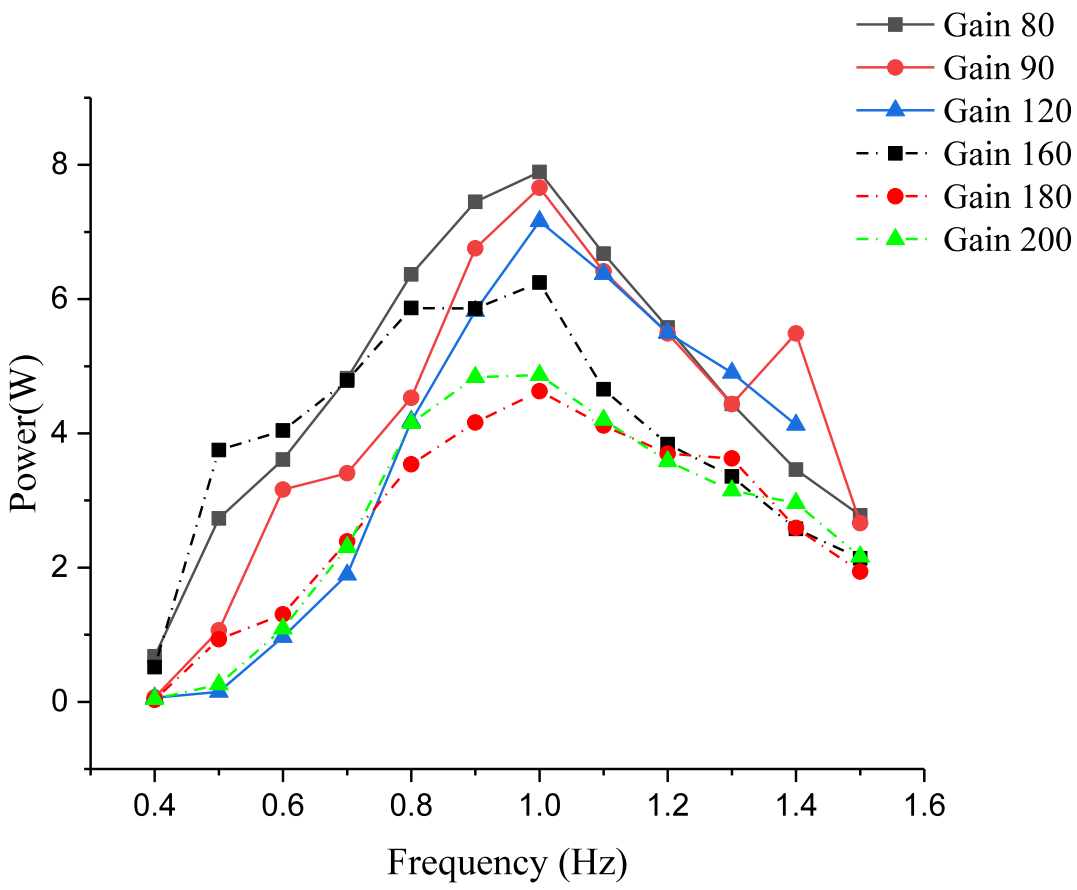

Figure 4.19 Power comparison of the best three curves for linear damping and nonlinear damping

4.4.2 JONSWAP SPECTRUM AND USER-DEFINED SPECTRUM

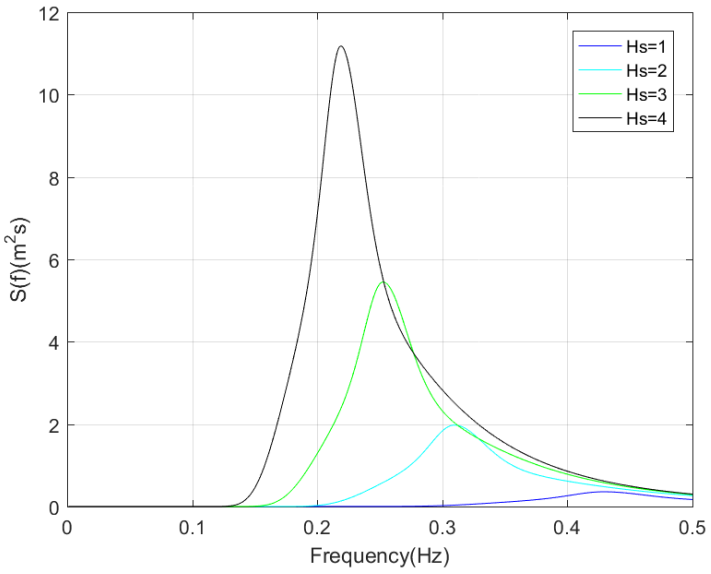

Figure 4.20 User-defined spectrum

In order to have further insight into the behaviour of the output electricity and explore more possibility in the ocean, apart from the classic JONSWAP spectrum, a series of user-defined spectrum as shown in Figure 4.20, are used to describe a possible energy spectrum of in the real ocean, proving the feasibility of the PTO simulator. The power curves are also obtained by the same methods, which are shown in Figure 4.21. It is obvious that this spectrum produces much less electricity than the JONSWAP spectrum. The conclusions drawn from above are further validated, that the nonlinear damping has no obvious advantage in the term of the output electricity power but have better gain applicability and system stability.

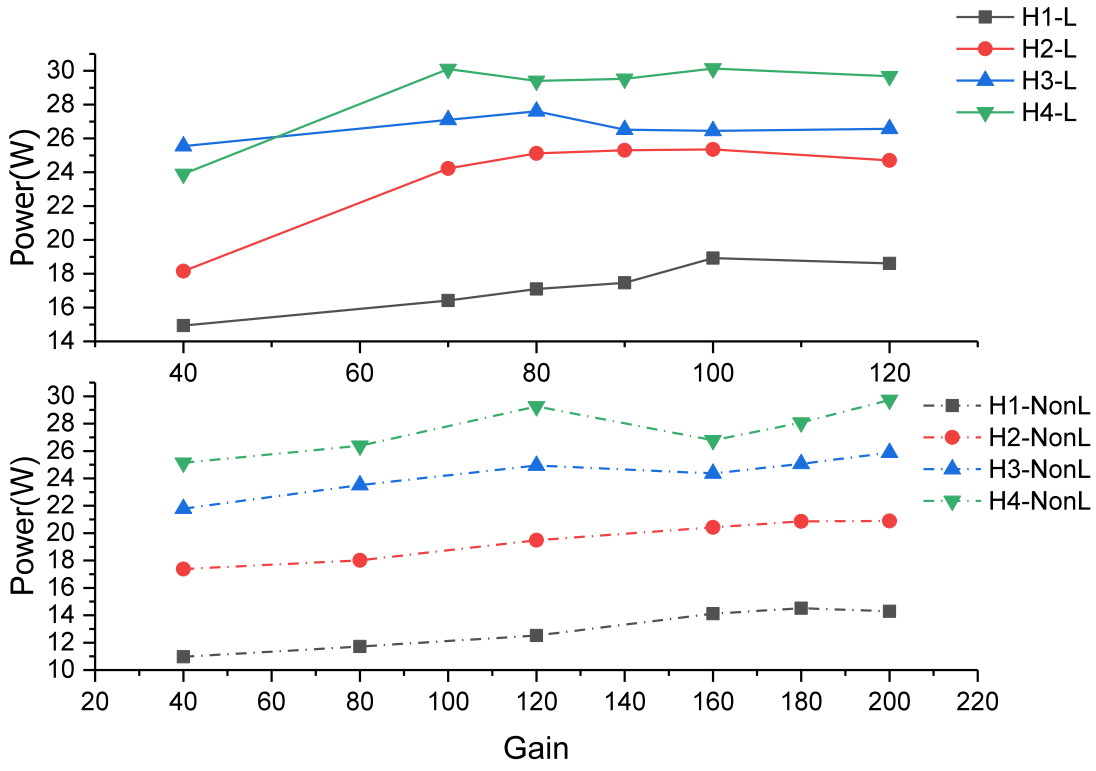

Figure 4.21 Power curves for different wave heights, linear damping, non-linear damping in JONSWAP spectrum (H1=1m, H2=2m,H3=3m,H4=4m)

Compared to Figure 4.14, Figure 4.21 shows a narrower gain range no matter in linear damping cases or nonlinear damping cases so that it can be seen as a zoom-in plotting. For linear damping when the significant wave heights are 1m and 2m, the electricity

production increases smoothly as the gain increases and reaches at a maximum when the gain is 100, then keeps stable. However, when the significant wave heights are 3m and 4m, the output electricity fluctuates to the maximum where the gain is also 100. The distance between different power curves is small and unequal. For nonlinear damping, the 1m power curve and 2m power curve seem to increase more smoothly than linear damping and reach the maximum at gain180. However, the 3m power curve and 4m power curve reach at the maximum at gain200 or later, the distance between different power curves are more obvious and tend to be equal.

4.5 Summary

Based on the different damping modes available in the experimental PTO simulation platform, numerous varying PTO strategies are simplified as the PTO damping, and they are simulated to be applied to a OWSC WEC model device. A number of corresponding tank tests are carried out, and a series of output electricity power curves are obtained. Hence, the PTO simulating platform works well even with the uncertainty clarified in the above chapter. This allows the best gain values for each control function for both linear and non-linear PTOs to be identified. Some conclusions are drawn:

- The best output damping coefficient for linear damping in regular waves is gain 80.
- The best output damping coefficient for nonlinear damping in regular waves is gain 160.
- The comparison of power efficiency under nonlinear PTO damping and linear damping shows that nonlinear PTOs have no distinct advantage in the amount of electricity output, but have better stability and broader damping range.

- Hydrodynamic performance analyses in term of the phase difference are presented, which indicates the OWSC WEC is entirely submissive to waves and the phase control may be that effective as others.
- The power efficiency in the JONSWAP spectrum under different water parameters is drawn.
- Comparison of the output power in different wave spectrum has been carried out, indicating the approach to a full range of ocean possibility. And the electricity output power in JONSWAP spectrum is found to be (approximately 300%) higher than in user-defined frequency for the same wave parameters.

5 Development of the prediction module for real-time rotor thrust

Real-time hybrid testing is the most feasible method to overcome the Froude-Reynolds scaling conflict for testing floating wind turbines, although it simultaneously introduces interface mishaps between the physical and numerical partitions such as system instability caused by time delays, fidelity loss, poor disturbance rejection. In order to address these issues, this thesis presents an artificial intelligence (AI) approach by developing a prediction module and a real-time executive controller, which can be used in the physical tank to allow real-time hybrid model tests of a spar-type floating wind turbine. First of all, a prediction algorithm is needed to be established to support the AI application. Therefore, this chapter focuses on proposing a useful rotor thrust prediction model of a 'Hywind' FOWT for the use of simulating a rotor's behaviour in fully coupled experiments. Numerous aero-hydro-servo-elastic coupled simulations are carried out in time-domain to observe how the OC3-Hywind offshore floating wind turbine behaves under those different conditions. For the environmental conditions, four types of different combined wind and wave conditions are generated to observe how the rotor thrust varies under different conditions with the aim to simulate and predict it in real-time. Moreover, the effect of the pitch and surge motions of the floating foundation on the real-time thrust of the wind turbine is quantitatively examined, and one simulation model of the thrust acting on the rotor is established by system identification techniques regarding high frequency and low-frequency response separately to account the dominating influence. The prediction model is obtained by artificial neural network method to train a black box

by the data from a simulation of LC 1-LC 6 (which are general sea states from Northern Sea). Additionally, the effect of turbulence on the thrust force is investigated.

5.1 The SIL application for providing the real-time rotor thrust for FOWTs

Artificial intelligence, represented by the artificial neural network, has achieved unprecedented development in the last decade. AI technology has been successfully applied in many fields, such as Tesla's self-driving technology, Apple's Siri, Google's Allo, and many other applications [87]. Early in 1936, the mathematical model of the Turing machine was first proposed by Alan Turing [88], who believed such a general-purpose machine could solve problems like humans. To fulfil the general-purpose machine, four elements are needed: 1. input; 2. intermediate state; 3. rule table; 4. output. Particularly, Elements 2 and 3 are necessary to our modern understanding of AI algorithm. We can regard the AI algorithm as the generative algorithm that lets a computer write an algorithm itself by machine learning or deep machine learning. The fundamental architecture of the AI algorithm is the artificial neural network, which is inspired by the biological neural network in humans. With the development of convolutional neural networks, AI algorithm has come to consist of more and more layers, and deep machine learning is usually used to train such a multi-layered AI algorithm. The algorithm is hierarchical, with the uppermost layer consisting of the algorithm of the symbolic world as a mathematical system, and the bottom layer being part of the physical world. The levels that exist in the middle are for the programmer's code or the microcontroller [89].

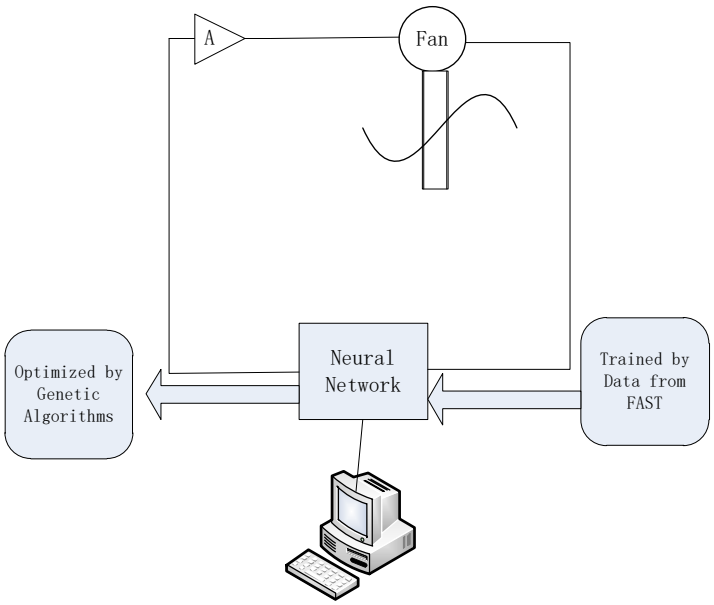

Figure 5.1 The conceptual design of a SIL application providing real-time rotor thrusts

Nowadays, artificial intelligence or the artificial neural network has been applied in prediction in many fields, such as forecasting the stock market index [90], predicting the dynamic viscosity of the aqueous nanofluid of TiO2 [91], and many other cases. In the present study, an AI-based SIL application is used to control a fan atop of a spar model to simulate the aerodynamic thrust load on a spar-type FOWT, as shown in Figure 5.1.To reproduce aerodynamic rotor thrust correctly acting on the physical spar model. Thus, a prediction module can predict the rotor thrust in real-time with an acceptable degree of accuracy are required. For this purpose, the fully-coupled calculation code of floating wind turbines -FAST is used to run simulations under different environments, and time histories of the quantities of interests are used for analysis to obtain a reasonable frame structure of the prediction module. Then derived frame structure consists of five inputs and one output, will be trained by artificial techniques based on the neural network architecture to achieve the applicable prediction module, details can be found in the publication[2].

5.2 Model description of the full-scale FOWT

To predict the sophisticated dynamics of the spar-type floating wind turbine, a coupled aero-servo-hydro-elastic model which integrates wind-inflow, the turbine control system (servo), hydrodynamic and structural-dynamic (elastic) models is adapted to run the simulations.

The spar-buoy concept -"Hywind" floating wind turbine is initially developed by Statoil of Norway. Then by NREL, aspects of the original data are adjusted slightly to make the platform appropriate for supporting the NREL 5-MW baseline turbine. To differ from Statoil's original Hywind concept, it is referred to as "OC3-Hywind". The OC3-Hywind floating wind turbine concept is adopted as the model in this study. We use the turbine specifications of the National Renewable Energy Laboratory (NREL) offshore 5-MW baseline wind turbine, as given in Ref[92, 93]. Moreover,Figure 5.2 presents a model built from the data reflecting the floating system properties documented in[93]. As can be seen in Figure 5.2, a spar type platform is used to support the wind turbine. Table 5.1 lists the specification details of the model

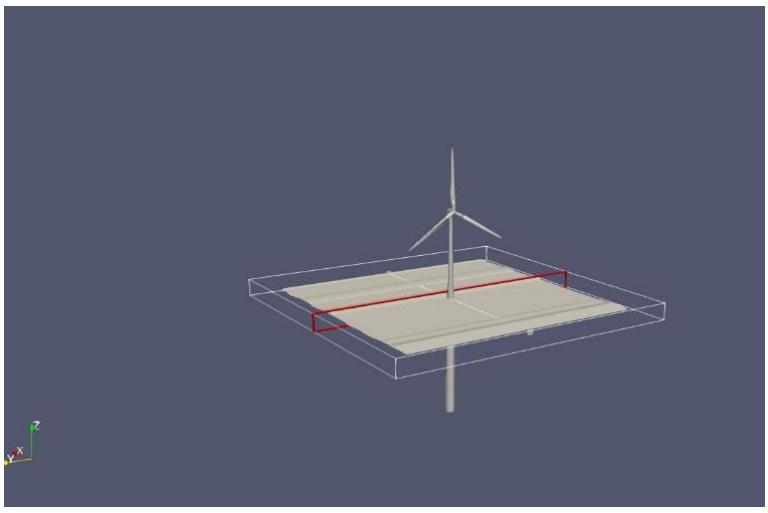

Figure 5.2 Building up the model for simulation

Table 5.1 General properties of the model

Item	Value
Rating	5 MW
Rotor configuration	Upwind, three blades
Cut-in, rated,cut-out wind speed	3m/s,11.4m/s, 25m/s
Total draft below sea water level(SWL)	120m
Height to the base above SWL (top of platform)	10m
Height to Tower Top (Yaw Bearing) Above SWL	87.6m
The position of tower CM above SWL Along Tower centerline	43.4m
Tower Structural-Damping Ratio (All Modes)	1%
Nacelle dimension(length,width, height)	14.2m, 2.3m, 3.5m
Platform diameter above the taper	6.5m
Platform diameter below the taper	9.4m
Rotor nacelle assembly(RNA)mass	350000kg
Tower mass	249718kg
Platform mass, Including ballast	7466000kg
CM Location Below SWL Along Platform Centerline	89.9155 m
Platform Roll Inertia about CM	4,229,230,000 kg•m2
Platform Pitch Inertia about CM	4,229,230,000 kg•m2
Platform Yaw Inertia about Platform Centerline	164,230,000 kg•m2
Number of mooring lines	3
Angle Between Adjacent Lines	120º
Depth to fairleads below SWL	70m
Depth to Anchors Below SWL	320m
Radius to Anchors from Platform Centerline	853.87m
Radius to Fairleads from Platform Centerline	5.2m
Unstretched Mooring Line Length	902.2m
Mooring Line Diameter	0.09 m
Equivalent Mooring Line Mass Density	77.7066 kg/m
Equivalent Mooring Line Weight in Water	698.094 N/m
Equivalent Mooring Line Extensional Stiffness	384,243,000 N
Additional Yaw Spring Stiffness	98,340,000 Nm/rad
Baseline control in Region 3	GSPI and constant torque

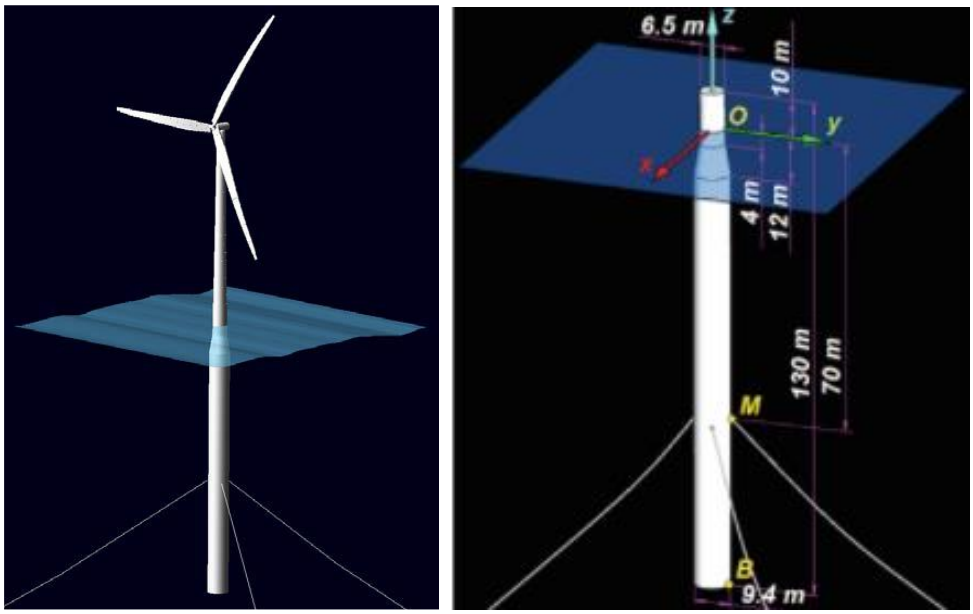

Figure 5.3 Properties of the floating system

As shown in Figure 5.3, the tower base overlaps with the top of the platform and is located 10 m above the still water level (SWL). Although the top of the tower protrudes with the yaw bearing, it is situated at 87.6m above SWL. The distribution characteristics of the tower are based on the base diameter of 6.5m, which is matched with the top width of the platform. Moreover, the base thickness of the tower is 0.027m, top diameter 3.87m, thickness 0.019m. The tower is 10 meters above the SWL and cantilever to the top of the floating platform, which is considered rigid. The model is moored by a mooring system which is spread with a delta connection. However, in the calculation, the delta connection is eliminated, and the mooring system is modified with a yaw spring to meet the proper general yaw stiffness.

5.3 Load cases adopted for simulation

Concerning collecting data to train the model, four types of different coupled wind and wave conditions are generated to the classic model “OC3_Hywind”. Namely, frequency-changing regular wave vs steady wind, regular wave(at constant frequency) vs speed-varying steady wind, irregular wave and turbulent wind, and irregular wave and corresponding steady wind. Aero-hydro-servo-elastic coupled simulations of the floating

wind turbine under those different environmental conditions are performed in time-domain to estimate how the OC3-Hywind offshore floating wind turbine behaves under those conditions of various types.

In order to investigate the behaviour of the FOWT during its entire deployment period, the sea states selected are based on the analysis of the proposed deployment site in the sea. Besides, the wave conditions are characterised by a JONSWAP spectrum. Hence, Table 5.2 lists all the load cases used in simulation. For each simulation, it runs 600s to get an observation of the steady effect. However, only the data in between 300s-500s(because as shown in Figure 5.11, the signal showns stable properties in between 300s-500s) is selected for statistic calculation and analyses, in order to get rid of the transient effect arising in the initial simulation stage.

Table 5.2 List of all the load cases used in the simulation

Load Case	Enabled DOFs	Wave Conditions	Wind Conditions
LC1	Platform(floater), tower, drivetrain, blades	Regular airy: H=2m, ω =0.1, 0.2, …, 3.5 rad/s	Steady, no shear u =8 m/s
LC2	Platform, tower, drivetrain, blades	Regular airy: H=2m ω =0.5 rad/s	Steady, no shear u =2, 4, …,18 m/s
LC3	Platform, tower, drivetrain, blades	JONSWAP spectrum H_s =4.55 m, T_p =9.00s, γ =2.45	IECKAI model $\bar{u}$ =11.40 , TI=20.45
LC4	Platform, tower, drivetrain, blades	JONSWAP spectrum H_s =1.5 m, T_p =6.61s, γ =1.00	IECKAI model $\bar{u}$ =11.40 , TI=20.45
LC5	Platform, tower, drivetrain, blades	JONSWAP spectrum H_s =4.55 m, T_p =9.00s, γ =2.45	Steady, no shear u =11.40 m/s
LC6	Platform, tower, drivetrain, blades	JONSWAP spectrum H_s =1.5 m, T_p =6.61s, γ =1.00	Steady, no shear u =11.40 m/s

To simulate the natural environment, the sea states at the proposed site is characterised by the JONSWAP spectrum, which is described as follow in a lecture of MIT OpenCoursWare[94]:

$$S(\omega)=\frac{\alpha g^2}{\omega^5}\exp\{-1.25\left(\frac{\omega_p}{\omega}\right)^4\}\gamma^{\exp(-0.5(\frac{\omega-\omega_p}{\sigma\omega_p})^2)} \tag{5.1}$$

where, $\alpha=5.061\left(\frac{\omega_p}{2\pi}\right)^4 H_s^2[1-0.287\log\gamma]$; $\sigma=0.07$ for $\omega<\omega_p$, and $\sigma=0.09$ for $\omega\geq\omega_p$; $\omega_p=2\pi/T_p$. H_s is the significant wave frequency, ω_p is the peak frequency, γ is the peak enhance coefficient.

Moreover, for the wind field with a turbulent inflow, the IEC Kaimal spectral turbulent model is used to characterise the wind conditions. When the atmospheric stability is zero, the spectra for the three wind components, $K=u,v,w$ (u is horizontal wind speed) are as follow:

$$S(f)=\frac{4\sigma_K^2 L_K/\bar{u}_{hub}}{\left(1+6fL_K/\bar{u}_{hub}\right)^{5/3}} \tag{5.2}$$

where f is the cyclic frequency and L_K is an integral scale parameter, which is defined as:

$$L_K=\begin{cases}8.10\Lambda_U, K=u\\ 2.70\Lambda_U, K=v\\ 0.66\Lambda_U, K=w\end{cases} \tag{5.3}$$

According to IEC 61400-3 standard, the turbulence scale parameter $\Lambda_U=0.7\cdot\min(60m,H_{hub})$. However, because $H_{hub}=90m$, then $\Lambda_U=42$. The relationships between the standard deviations are defined to be: $\sigma_v=0.8\sigma_u$, $\sigma_w=0.5\sigma_u$,

$\sigma_u = \frac{TI}{100}\bar{u}_{hub}$, TI is the turbulence intensity, $\bar{u}_{hub}$ is the mean (total) wind speed at the reference height. Then the wind spectrum of LC 3 and LC 4 is as shown in Figure 5.4.

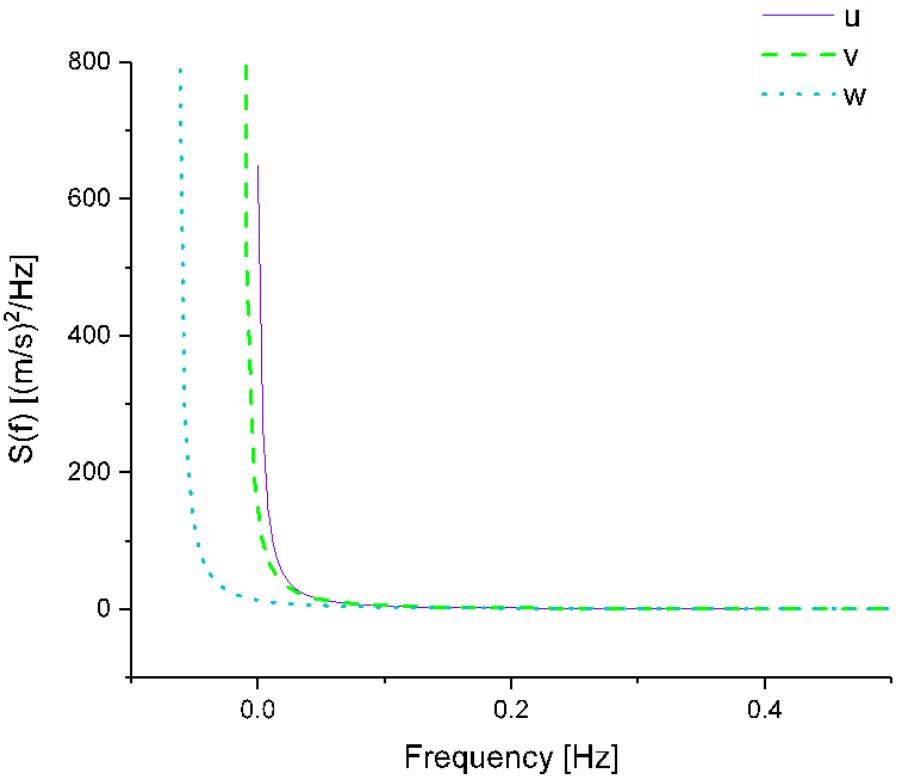

Figure 5.4 Spectrum of the wind adopted in LC 3&4

5.4 Methodology used to obtain data for model training

The aero-hydro-servo coupled simulation code FAST [25] developed by the National Renewable Energy Laboratory (NREL) is used to simulate the dynamic performance of the OC3-spar floating wind turbine in various wind fields.

5.4.1 Fully coupled motions

When the fully dynamic coupling between the floating foundation and the wind turbine is taken into consideration, the coupled motions of the floating foundation in time domain is expressed as follow[95]:

$$M_{ij}(q,u,t)\ddot{q}_j = F_i(q,\dot{q},u,t) \tag{5.4}$$

q : the input of the six DOFs (heave, sway, surge, roll, pitch and yaw);

u : control inputs;

M_{ij} : the (i, j) component of the inertia mass matrix;

$\ddot{q}_j$: the acceleration of DOF j;

$\dot{q}$: velocity input of the DOFs;

F_i : force applied on DOF i .

Because of the balance of forces for the system, the total force applied to the system should be as follow:

$$*F_i + F_i = 0 \tag{5.5}$$

where $*F_i = *F_i^{Hub} + *F_i^{Nacelle} + *F_i^{Tower} + *F_i^{Floater} + *F_i^{Blades}$;

$F_i = F_i^{Aero} + F_i^{Hydro} + F_i^{Gravity} + F_i^{Elastic} + F_i^{Drivet} + F_i^{Mooring}$.

5.4.2 HYDRODYNAMIC MODELLING

In this study, both regular waves, and irregular (JONSWAP spectrum) waves are generated to form the coupled load conditions. Airy wave theory is adapted to model the wave kinematics, including both regular and irregular waves. For regular waves, the wave elevation (ζ) is represented as a sinusoid with a single amplitude (wave height) and frequency. Irregular waves are expressed as a summation or superposition of multiple wave components, as described by an appropriate wave spectrum[96]:

$$\zeta(t) = \frac{1}{2\pi}\int_{-\infty}^{\infty} W(\omega)\sqrt{2\pi S_{\zeta}^{2-sided}(\omega)}e^{j\omega t}d_{\omega} \tag{5.6}$$

where, $W(\omega)$ is the Fourier transform of a realisation of a white Gaussian noise time-series process with zero mean and unit variance. Equation (5.6) represents the wave

elevation as an inverse Fourier transform of the desired two-sided power spectral density, $S_{\zeta}^{2-sided}$ where *j* is an imaginary number and ω is an individual wave frequency.

Potential-flow theory and strip theory (via Morison's equation) are used to model the hydrodynamic loads. The forces acting on the floater (floating foundation) consist of diffraction, radiation and hydrostatic forces as well as the restoring forces from the mooring lines and the added inertia of the fully coupled turbine. Therefore, the total external load acting on the floating foundation $F_i^{Floator}$ is described as follow:

$$F_i^{Floator} = -A_{ij}\ddot{q}_j + F_i^{Hydro} + F_i^{Mooring} \tag{5.7}$$

where, A_{ij} is the (*i*, *j*) component of the added mass matrix, F_i^{Hydro} is the i th component of the applied hydrodynamic load on the floating foundation, $F_i^{Mooring}$ is the i th component of the load on the floating foundation from the mooring lines.

However, F_i^{Hydro} consists of three parts: radiation, diffraction and hydrostatic, hence:

$$F_i^{Hydro} = F_i^{Excitation} + F_i^{Hydrostatic} - F_i^{Radiation} \tag{5.8}$$

where, $F_i^{Excitation}$ is the total excitation load from incident waves, which is the result of the undisturbed pressure field (Froude-Krylov) and wave scattering (diffraction loads), $F_i^{Hydrostatic}$ is the restoring forces of a freely moving body. $F_i^{Radiation}$ is steady-state hydrodynamic forces and moments. Thus we get

$$F_i^{Hydrostatic} = \rho g V \delta_{i3} - C_{ij}^{Hydrostatic} q \tag{5.9}$$

$$F_i^{Radiation} = \int_0^t K_{ij}(t-\tau)\dot{q}_j(\tau)d_\tau \tag{5.10}$$

$$F_i^{Hydro} = F_i^{Excitation} + \rho g V \delta_{i3} - C_{ij}^{Hydrostatic} q_j - \int_0^t K_{ij}(t-\tau)\dot{q}_j(\tau)d_\tau \tag{5.11}$$

$\rho g V \delta_{i3}$: the buoyancy force from Archimedes' principle; thereof, δ_{i3} is the (i,3) component of the Kronecker-Delta function;

$-C_{ij}^{Hydrostatic} q_j$: Hydrostatic and torque variations resulting from the effects of the water-plane area and the center of buoyancy (COB); thereof, $C_{ij}^{Hydrostatic}$ is the (*i,*) component of the linear hydrostatic restoring matrix;

K_{ij} : the wave radiation retardation kernel - the impulse-response function of the radiation problem;

t : simulation time;

τ : user variable time.

5.4.3 AERODYNAMIC MODELLING

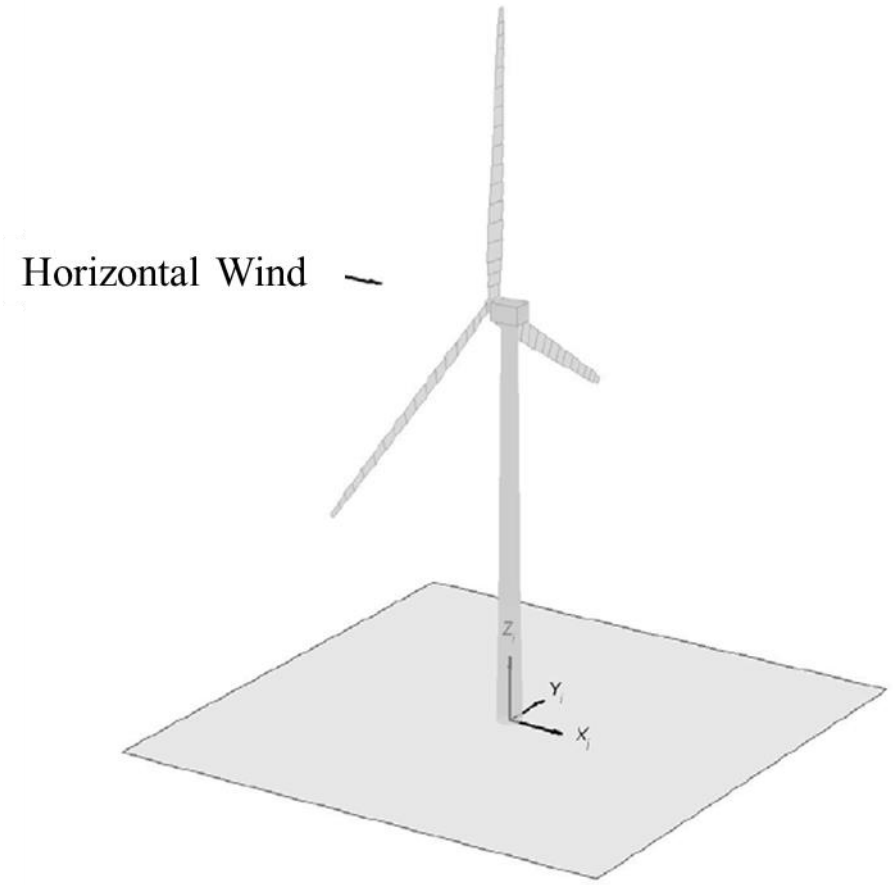

Figure 5.5 The global coordinate system concerning the wind field[97]

In this study, both steady wind fields and turbulent wind fields are generated to couple with different wave conditions. For the convenience of describing the wind field, it is assumed that the inflow wind direction is horizontal as shown in Figure 5.5.

Power-Law wind profile is used to determine the mean *u*-component velocity at each height in the wind filed, the equation is:

$$u(z) = \bar{u}_{hub}\left(\frac{z}{H_{hub}}\right)^{P} \tag{5.12}$$

in which, $\bar{u}_{hub}$ is the horizontal wind speed at reference height; H_{hub}: the reference height for the wind file, P is the power-law exponent for the wind shear profile.

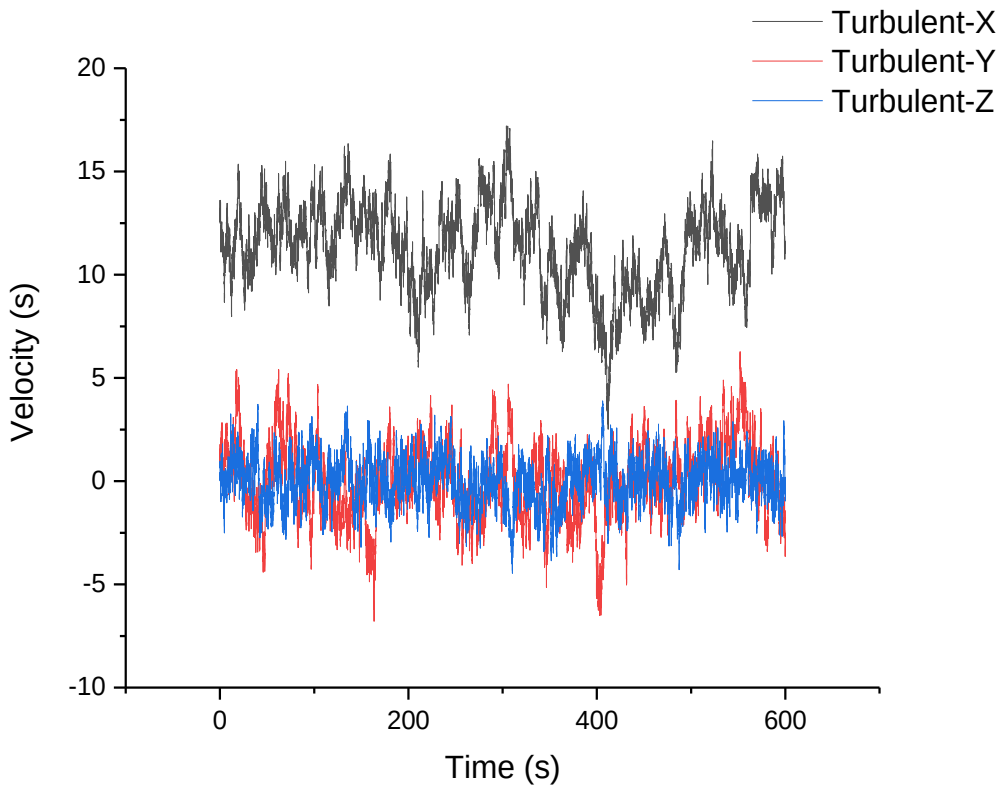

Figure 5.6 History of wind speed in the turbulent wind field

As discussed in section 5.3, Figure 5.4 displays the spectrum of turbulent wind. Moreover, Figure 5.6 plots the history of wind speed. As shown in Figure 5.6, the slow slow-varying component forms the turbulence. However, in the natural world, not only the amplitude of the wind speed varies, but also the speed direction is time-dependent. Therefore, a

spatial coherence model is introduced to represent the phase difference of wind velocity at different spatial points. The correlation between the same wind components at two spatially separated points (e.g., *ui-uj* correlation) is described as follow:

$$Coh_{i,j} = \exp\left(-a\sqrt{\left(\frac{fr}{\bar{u}_{hub}}\right)^2 + \left(0.12\frac{r}{L_c}\right)^2} \right) \tag{5.13}$$

where, the coherence decrement $a = 0.88$, the coherence scale parameter $L_c = 73.5m$ (IEC 61400-1 2nd ed.). f is the cyclic frequency, r is the distance between points i and j on the grid. The Taylor's frozen turbulence hypothesis is adapted to translate wind defined in two-dimensional planes into three spatial dimensions, using the mean wind speed as the advection speed. Therefore, it generates a time series containing the three wind speed vectors at each point in the grid accordingly.

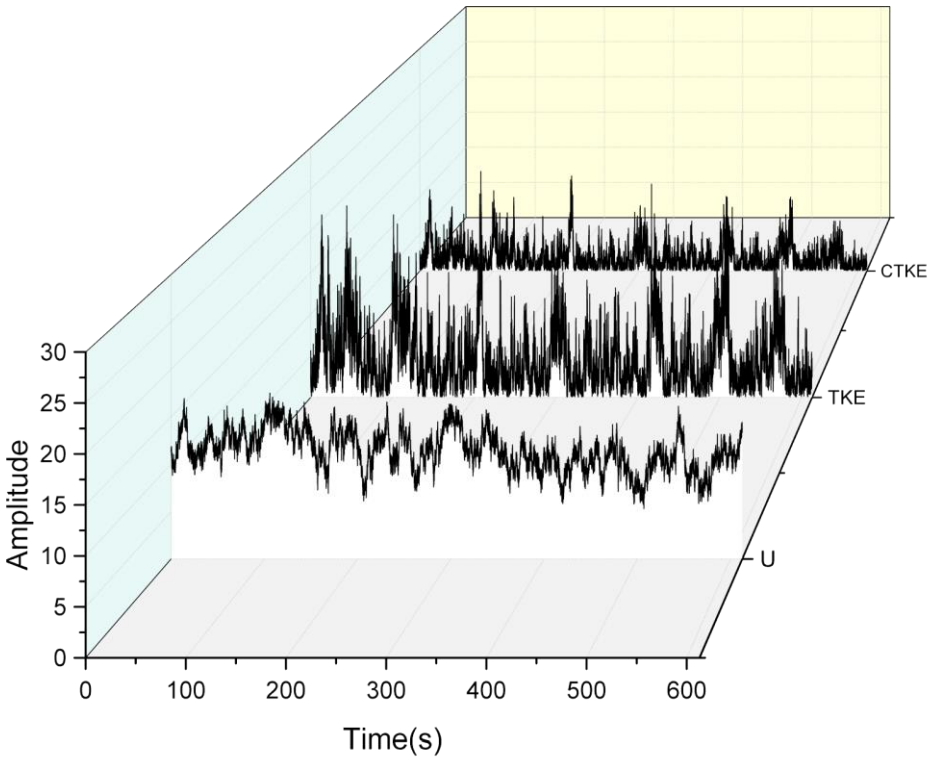

Figure 5.7 Energy distribution along the turbulent velocity

The blade element momentum (BEM) solution including the Pitt/Peters correction model is used to calculate the aerodynamics of horizontal axis wind turbines. For analysis purposes, coherent structures have been defined regarding coherent turbulent kinetic energy (CTKE), and the turbulent kinetic energy (TKE) is used to model the power spectrum as shown in Figure 5.7.

5.4.4 MOORING SYSTEM MODELLING

For mooring modelling, the closed–form solution[98] of the classic single line is reformulated into a piecewise, multi-segmented system as shown in Figure 5.8 (where r_i is the node position vector, $x_i z_i$ is a local frame, XYZ is the global coordinate system). This piecewise system is composed of a collection of nodes and elements. The mean forces in the mooring system, including elasticity, weight (in fluid), and geometric nonlinearities, are accounted.

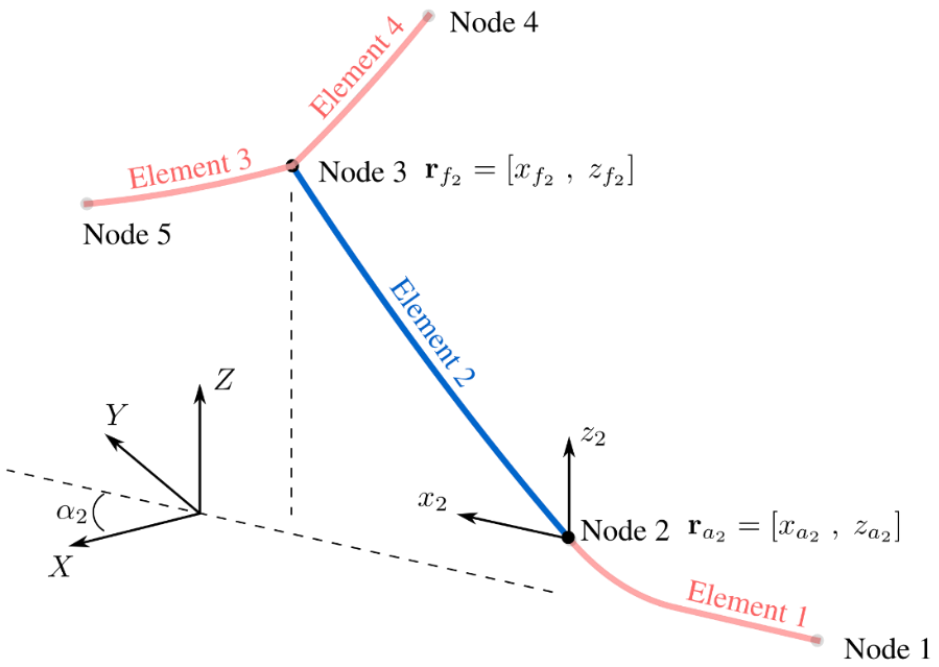

Figure 5.8 the piece-wise, multi-segmented system of a classic mooring line[99]

Their contribution at each element's anchor and fairlead are added to the corresponding node it attaches to. h_i and l_i are the relative height and length between $Element_{(i)}$ and $Element_{(i+1)}$,the solution process can be demonstrated by the flowchat given in Figure 5.9. H_i and V_i are the total force at $Element_{(i)}$ in horizontal direction andd vertical direction.

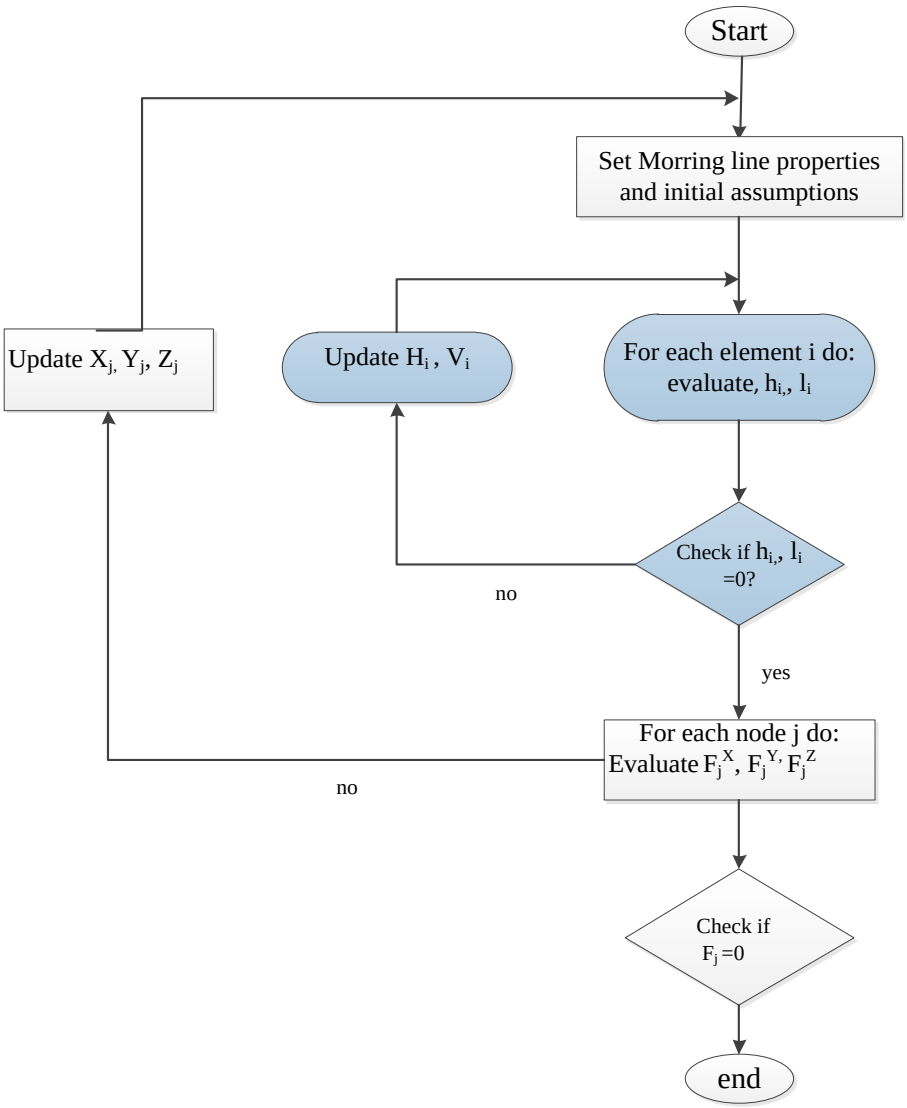

Figure 5.9 Flowchart of the mooring solver procedure

The evaluation of the two continuous analysis catenary equations of each element based on the horizontal and vertical offsets obtained through the nodal displacement relationship. The element is defined as a component that connects two adjacent nodes. Evaluating the force balance equation for each node as follow:

$$\{F\}_X^j = \sum_{i=1}^{n}[H_i \cos(\alpha_i) - F_{X_j}^{ext}] = 0$$
$$\{F\}_Y^j = \sum_{i=1}^{n}[H_i \sin(\alpha_i) - F_{Y_j}^{ext}] = 0 \quad (5.14)$$
$$\{F\}_Z^j = \sum_{i=1}^{n}[V_i] - F_{Z_j}^{ext} + M_j g - \rho g B_j = 0$$

where, H is the horizontal fairlead force, V is the vertical fairlead force, $n = 1, 2, ...$ is the elements at the node j, F^{ext} is the external force in the global coordinate system. Once the element fairlead (H, V) and anchor (H_a, V_a) values are known at the element level, the forces are transformed from the local $x_i z_i$ frame into the global XYZ coordinate system.

5.4.5 CONTROL AND ELECTRICAL-DRIVE MODELLING

A conventional variable-speed, variable blade-pitch-to-feather control modelling strategy is usually used for onshore NREL 5-MW turbines, However, the conventional pitch-to-feather control usually results in a reduction of the steady-state rotor thrust when increase wind speed above rated. Therefore, in this research, two modifications are adapted as listed in Table 5.3, and a time step is added for the Bladed-style DLL controllers, which is independent of the ServoDyn time step. Moreover, a linear ramp and first-order low-pass filter are applied to the blade-pitch command from the Bladed-style DLL.

Table 5.3 Control System Property Modifications[100]

Proportional Gain at Minimum Blade-Pitch Setting	0.0062 s
Integral Gain at Minimum Blade-Pitch Setting	0.0009
Constant (Rated) Generator Torque in Region 3	43,090 N*m

5.5 Establishing the prediction model

This section provides the analyses of data from simulations and proposes two models. The frame structure of the prediction model of the thrust acting on the rotor is obtained by the data from LC1 and LC2; the simulation model is estimated by system identification

techniques regarding high frequency and low-frequency response separately to account the dominating influence. The prediction model is then trained by the data from simulations of LC3-LC6.

5.5.1 ROTOR THRUST PREDICTION UNDER LC 1

In this section, a series of simulations of frequency-increasing regular wave conditions and speed-increasing wind conditions are carried out to observe their effect on the real-time rotor thrust. The wind speed of uniform wind field is 8m/s, and 35 frequencies of 0.1 -3.5 rad/s of regular waves with a constant wave height of 2m, are used to run the simulations. The outputs of one standard simulation are shown in Figure 5.10. As pointed out in [101, 102], the same phenomenon is observed from the series simulation, that for numerous environmental conditions, the significant responses are the surge and pitch motions. Moreover, thrust is fundamentally due to the relative wind speed experienced by the turbine blades. For example, if the platform is fixed, then the relative wind speed experienced by the edges will be the same as the true wind speed.

However, for a floating wind turbine, the platform is moving back and forward relative to the wind, and in this case, the turbine blades experience the relative wind speed. Since we are only looking at wind and wave direction in the x-axis, then the platform motions are predominately pitched and surge i.e. roll, yaw, sway is practically zero as shown in Figure 5.10. When the platform pitches or surges, this adds a component to the relative wind speed. Hence when predicting the thrust for a floating wind turbine, only surge, pitch (which provide the corresponding component of wind) and the actual wind speed are accounted for. Therefore, the surge and pitch motions of the platform are extracted from the outputs to observe their correlation with the aerodynamic thrust in this section.

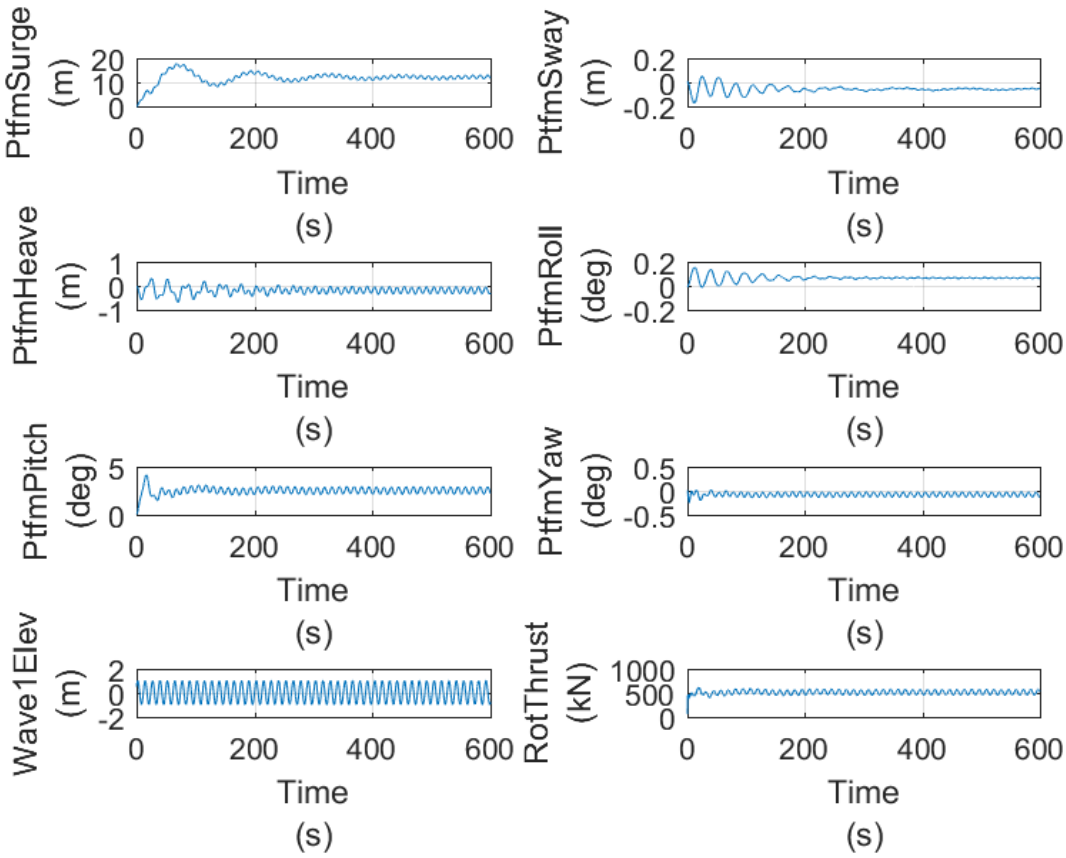

Figure 5.10 Some outputs from one standard simulation under ω=0.5 rad/s, u =8 m/s

To observe the correlation between surge, pitch, and thrust, two 4th order Buttherworth filters are designed to separate the thrust, surge, and pitch signals into two independent components (high-frequency component and low-frequency component), respectively. The cut-off frequency for both high pass filter and low pass filter is 0.01 Hz, to include all the data of the three signals (surge, pitch, and thrust). Also, the transfer function is expressed regarding b and a [103]as:

$$H(z)=\frac{B(z)}{A(z)}=\frac{b(1)+b(2)z^{-1}+b(3)z^{-2}+b(4)z^{-3}+b(5)z^{-4}}{a(1)+a(2)z^{-1}+a(3)z^{-2}+a(4)z^{-3}+a(5)z^{-4}} \quad (5.15)$$

where, b and a are the transfer function coefficients of the 4th-order filters.

For the high pass filter:

$b=[0.9990,-3.9959,5.9938,-3.9959,0.9990]$

$a=[1.0000,-3.9979,5.9938,-3.9938.0.9979]$

for the low pass filter:

$$b = [2.3759, 9.5035, 14.2550, 9.5035, 2.3759] \times 10^{-14}$$

$$a = [1.0000, -3.9979, 5.9938, -3.9938, 0.9979]$$

Once the filters are designed, the three signals can be separated. One example when ω =1.9 rad/s, u =8 m/s is given in Figure 5.11 (see separation analyses for other cases in Appendix 6). Figure 5.11 illustrates that the filters are efficient to separate the properties of the original signal into two independent parts.

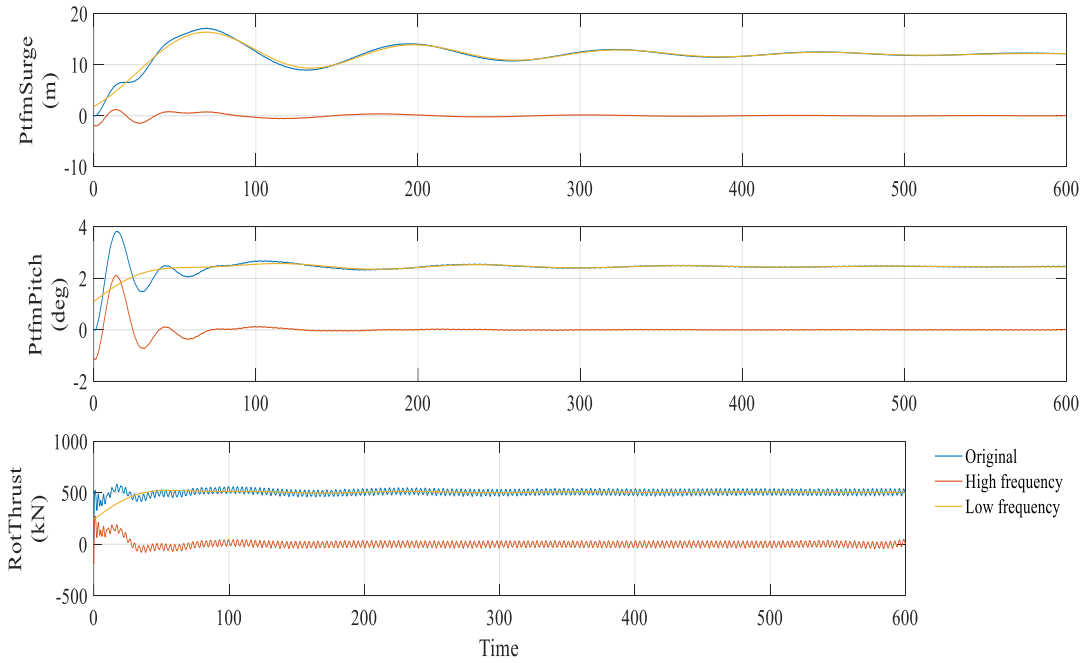

Figure 5.11 Separation of the three signals at ω =1.9 rad/s, u =8 m/s

Table 5.4 Separated components of the signals for a range of ω at the wind speed of 8m/s

wind	wave			surge_high		pitch_high		thrust_high		surge_lo	pitch_low	thrust_low
wind(m/s)	w(rad/s)	f(Hz)	Hs(m)	H(m)	f(Hz)	A(deg)	f(hz)	T(KN)	f(hz)	H(m)	A(deg)	T(KN)
8	0.2	0.032	2	1.49	0.033	0.133	0.031	11.969	0.033	11.817	2.422	504.803
8	0.5	0.08	2	1.504	0.080	0.760	0.080	116.955	0.086	11.963	2.455	506.259
8	0.7	0.111	2	0.859	0.111	0.098	0.111	37.112	0.112	11.951	2.449	505.373
8	0.9	0.143	2	0.509	0.142	0.076	0.142	42.554	0.143	11.983	2.449	505.133
8	1.2	0.191	2	0.249	0.188	0.049	0.188	49.369	0.195	11.936	2.445	504.777
8	1.5	0.239	2	0.119	0.236	0.029	0.235	51.131	0.243	11.962	2.446	504.705
8	1.6	0.255	2	0.090	0.254	0.024	0.250	50.143	0.263	11.957	2.446	504.722
8	1.9	0.302	2	0.040	0.298	0.012	0.295	46.066	0.302	11.958	2.446	504.711
8	2.2	0.35	2	0.018	0.334	0.006	0.342	43.475	0.350	11.966	2.447	504.744
8	2.5	0.398	2	0.012	0.556	0.005	0.386	44.313	0.397	11.950	2.445	504.512
8	2.9	0.462	2	0.020	0.455	0.011	0.453	63.071	0.461	11.958	2.446	504.636
8	3.5	0.557	2	0.014	0.548	0.009	0.547	24.485	0.558	11.961	2.446	504.691

The static calculation results of the separated components for all simulations included in load cases 1 are shown Table 5.4. As seen in the figure, it is noticed that low-frequency components of the three signals (surge_low, pitch_low, thrust _low) tend to be independent on wave frequency. However, the high-frequency components (surge_high, pitch_high, thrust _high) tend to be dependent on the wave frequency. Therefore, a response amplitude operator (RAO) for the three signals(surge_RAO, pitch_RAO and thrust_RAO)are defined as follow :

$$surge\_RAO = \frac{surge}{H} \tag{5.16}$$

$$pitch\_RAO = \frac{pitch}{H} \tag{5.17}$$

$$thrust\_RAO = \frac{thrust}{120} \tag{5.18}$$

where, H is the wave height/amplitude of the regular waves in these equations, surge and pitch are the amplitudes obtained and listed in Table 5.4. in order to present thrust properties in a close scale as RAOs, a scaling coefficient 120 is introduced. Thus, the RAOs are presented in Figure 5.12. It is noticed in Figure 5.12, there might be a linear correlation between thrust _high, surge_high and pitch_high when the wave frequency increases. Then the structure of the mathematical model to predict the high-frequency component of the aerodynamic thrust is assumed to be as:

$$RAO\_thrust\_high = k_1 \times RAO\_pitch\_high + k_2 \times RAO\_surge\_high + c(\omega) \tag{5.19}$$

where k_1, k_2 are model parameters, and $c(\omega)$ is a constant modification relative to wind speed, which could be identified by using the data of inputs(RAO_surge_high , RAO_thrust_high) and outputs($thrust\_RAO\_high$).

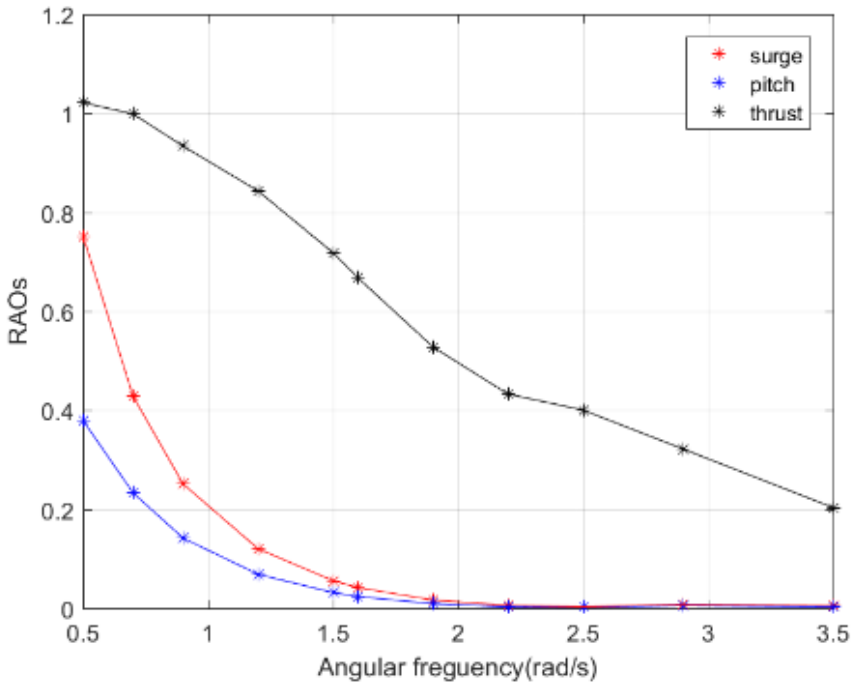

Figure 5.12 the RAOs of the surge, pitch, and thrust at a range of ω at the wind speed of 8m/s

5.5.2 ROTOR THRUST UNDER LC 2

Table 5.5 separated components of the surge, pitch, and thrust for a range of u at the ω=0.5 rad/s

wind	wave			surge_high		pitch_high		thrust_high		surge_low	pitch_low	thrust_lov
wind(m/s)	w(rad/s)	f(Hz)	H (m)	H(m)	f(Hz)	A(deg)	f(hz)	T(KN)	f(hz)	H(m)	A(deg)	T(KN)
2	0.5	0.08	2	1.474	0.080	0.732	0.080	97.768	0.080	1.102	0.196	134.074
4	0.5	0.08	2	1.477	0.080	0.736	0.080	103.036	0.080	3.763	0.761	225.799
6	0.5	0.08	2	1.487	0.080	0.746	0.080	113.295	0.080	7.355	1.508	347.780
8	0.5	0.08	2	1.504	0.080	0.760	0.080	116.955	0.086	11.973	2.456	506.397
10	0.5	0.08	2	1.497	0.081	0.775	0.079	133.277	0.087	18.030	3.707	724.560
12	0.5	0.08	2	1.352	0.081	0.672	0.079	184.146	0.083	20.070	4.121	792.488
14	0.5	0.08	2	1.356	0.081	0.673	0.079	167.927	0.083	16.023	3.286	634.720
16	0.5	0.08	2	1.368	0.079	0.672	0.078	161.980	0.087	13.850	2.840	556.172
18	0.5	0.08	2	1.362	0.079	0.670	0.078	162.021	0.087	12.524	2.563	507.111

Since the low-frequency component of the three observed signals are independent on wave frequencies, in this section, the frequency of regular waves (Airy) is 0.5 rad/s, and velocities of u =2, 4, …,18 m/s of steady wind, are used to run the simulations, for observing the effect of wind speed on aerodynamic thrust. Similarly, the static calculation of the separated components for all simulations included in load cases 2 is carried out, and the results are listed in Table 5.5. Different from being independent of wave frequencies, the low-frequency components of the three signals vary dramatically as the

wind speed changes. As the RAOs of the three signals are defined above, the analyses carried out all based on RAOs in this section, as shown in Figure 5.13. As can be seen in Figure 5.13(a), the high-frequency components of surge and pitch tend to be steady when the wind speed increase, while the high-frequency thrust component increases slightly, which is primarily described by the $c(u)$ in the structure of the mathematical model. So when Equation(5.19) modified with an offset, the structure is able to predict the high-frequency component when wind speed changes. Therefore, the fabric used to predict the thrust-high is modified as:

$$RAO\_thrust\_high = k_1 \times RAO\_pitch\_high + k_2 \times RAO\_surge\_high + c(\omega) + c_1 \quad (5.20)$$

where, c_1 is a constant offset related to wind speed.

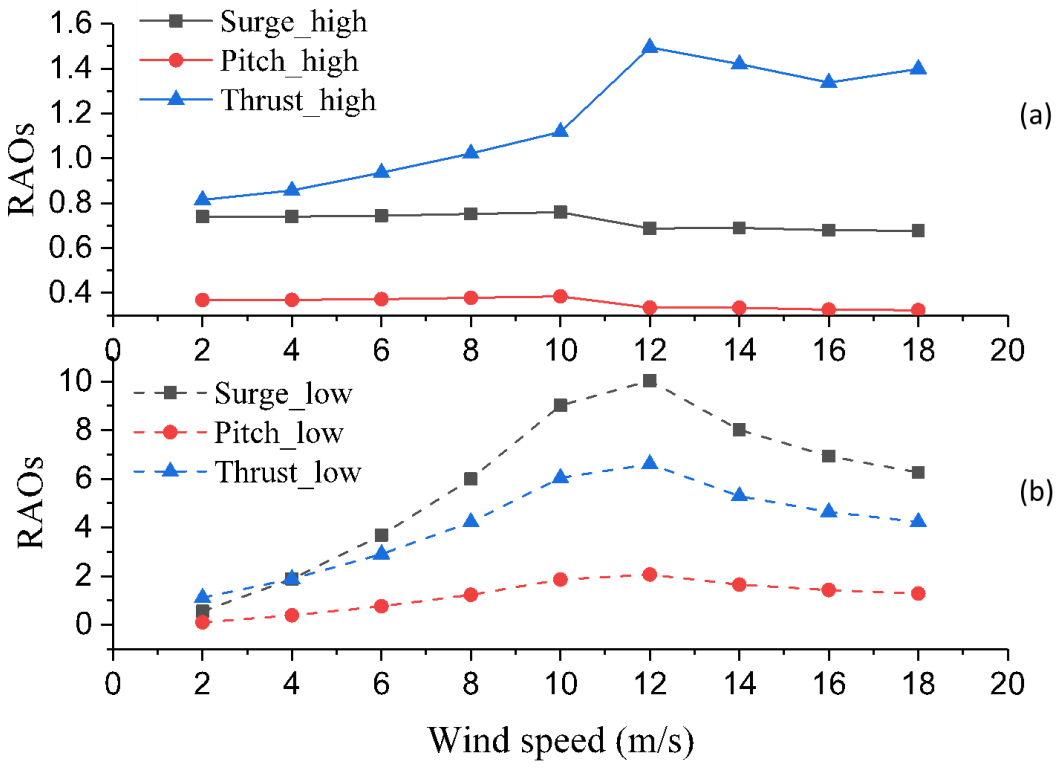

Figure 5.13 Behaviours of the high or low components of the surge, pitch, and thrust at a range of wind speed at ω=0.5 rad/s

Additionally, it is observed in Figure 5.13(b), that there is an apparent linear correlation among surge_low, pitch_low, thrust _low when the wind speed increase from 2m/s to 8m/s, and they all reach the maximum when the wind speed is 12m/s. Therefore the structure of the mathematical model to predict the low-frequency component of aerodynamic thrust is assumed to be as:

$$RAO\_thrust\_low = k_3 \times RAO\_pitch\_low + k_4 \times RAO\_surge\_low + k_5 \times wind\_speed + c_2 \tag{5.21}$$

where k_3 , k_4 , k_5 are also model parameters, but different from k_1 , k_2 , and c_2 is an allowable constant offset to make up the uncertainty might result from the linear structure. It will be identified by using the data of inputs RAO_surge_high , RAO_thrust_high) and outputs($thrust\_RAO\_high$) as discussed below.

5.5.3 Analysis of rotor thrust

As discussed above, two structures are obtained to predict the aerodynamic thrust, the structures(Equation 5.20 & 5.21) are as follow:

$$RAO\_thrust\_high = k_1 \times RAO\_pitch\_high + k_2 \times RAO\_surge\_high + c(\omega) + c_1$$

$$RAO\_thrust\_low = k_3 \times RAO\_pitch\_low + k_4 \times RAO\_surge\_low + k_5 \times wind\_speed + c_2$$

For the simplicity of scientific discussion, RAO_pitch_high , RAO_surge_high are represented as inputs u_1, u_2 , and RAO_pitch_low , RAO_surge_low as inputs $*u_1, *u_2$ to differ from, $RAO\_pitch\_high\ RAO\_surge\_high$. Similarly, the output $thrust\_RAO\_high$ will be discussed as Y_{low} , and Y_{high} . As the model structures and some input and output signals are obtained, the values of adjustable parameters in the given model structure could be estimated by minimising the error between the model output and the measured response. The output y_{model} of the linear model is provided by:

$y_{model}(t) = Gu(t)$ where G is the transfer function, $y_{model}(t)$ is the simulated response of the model for a given input $u(t)$ (such as $u_1, u_2, *u_1, *u_2$). The principal of determining G is minimizing the difference between the model output $y_{model}(t)$ and the measured output $y_{meas}(t)$ (such as Y_{low}, Y_{high}). The minimisation criterion is a weighted norm of the error, $v(t)$, where: $v(t) = y_{meas}(t) - y_{model}(t)$.

Therefore for Equation (5.20), the output $y_{model}(t)$ is related to four inputs in total, which are $RAO\_pitch\_high, RAO\_surge\_high, \omega, Y_{high}$ (discussed as $u_1, u_2\ u_3, u_4$). Then the transfer functions are obtained as follow:

From u_1 to y_{model}: $$G_1(s) = \frac{864.9s - 107.4}{s^2 + 1.853s + 2.271} \quad (5.22)$$

From u_2 to y_{model}: $$G_2(s) = \frac{-266.6s + 90.01}{s^2 + 2.105s + 1.861} \quad (5.23)$$

From u_3 to y_{model}: $$G_3(s) = \frac{52.48s - 9.524}{s^2 + 5.725e^{-10}s + 1.374} \quad (5.24)$$

From u_4 to y_{model}: $$G_4(s) = \frac{-0.2402s + 1.105}{s^2 + 1.379s + 1.317} \quad (5.25)$$

Fit to estimation data reaches 99.12%, the mean square error is 0.0206 when compared to the original signal.

For Equation (5.21) the output $y_{model}(t)$ is related to four inputs in total, which are $RAO\_pitch\_low, RAO\_surge\_low, wind\_speed, Y_{low}$ (discussed as $*u_1, *u_2\ *u_3, *u_4$). Then the transfer functions are obtained as follow:

From $*u_1$ to y_{model}: $$G_1(s) = \frac{-19.72s + 2.124}{s^2 + 3.86s + 0.1255} \quad (5.26)$$

From $*u_2$ to y_{model}: $$G_2(s) = \frac{-4.211s + 2.433}{s^2 + 4.208s + 1.718} \quad (5.27)$$

From $*u_3$ to y_{model}: $$G_3(s) = \frac{3.712s - 0.2842}{s^2 + 1.407s + 1.009} \quad (5.28)$$

From $*u_4$ to y_{model}: $$G_4(s) = \frac{0.1383s - 0.1432}{s^2 + 0.04644s + 0.6857} \quad (5.29)$$

5.5.4 ESTABLISING THE PREDICTION MODULE BASED ON LC3-LC6

Real sea states are more complex than regular-wave and steady-wind conditions. To predict the thrust, data for four comparative coupled environmental conditions (LC3-LC6) are considered, by which the effects of turbulence and wave spectrum on the thrust force are also investigated. For LC3-LC4, JONSWAP spectrum and IECKAI turbulent model are adopted to characterise the environmental conditions, and corresponding simulations are undertaken. To observe the effect of turbulence inflow on the aerodynamic thrust, the identical steady wind cases are simulated as well. The output of some significant response of LC3 are shown in Figure 5.14.

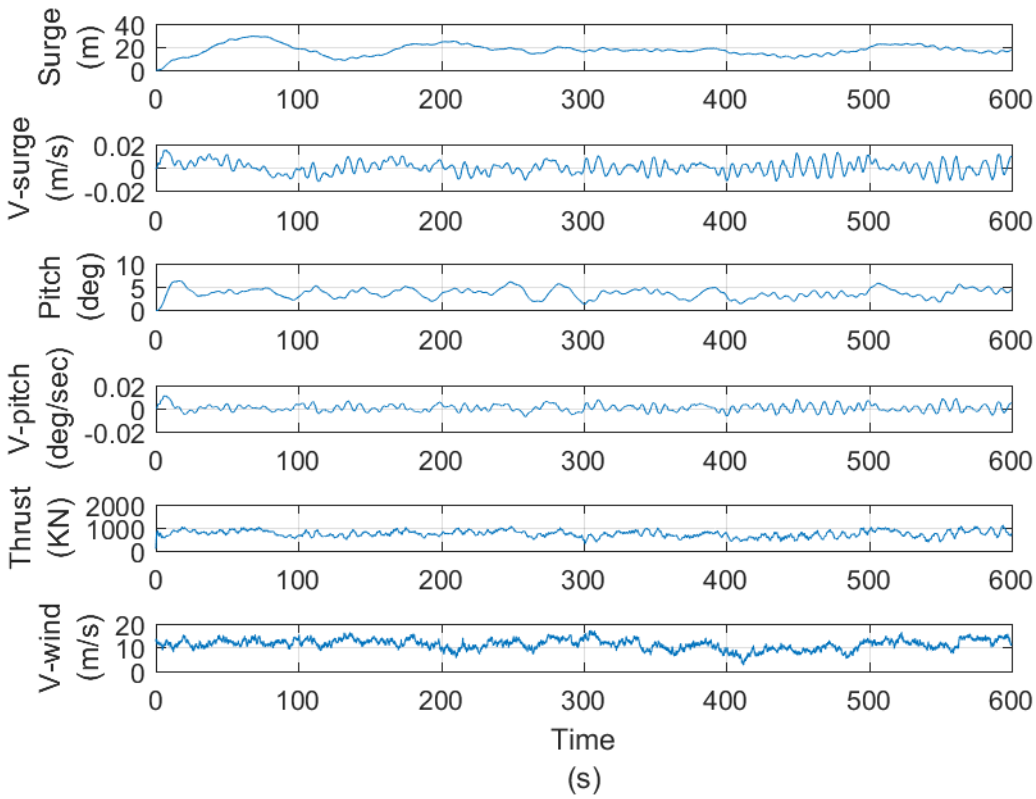

Figure 5.14 Significant outputs from a simulation of LC 3

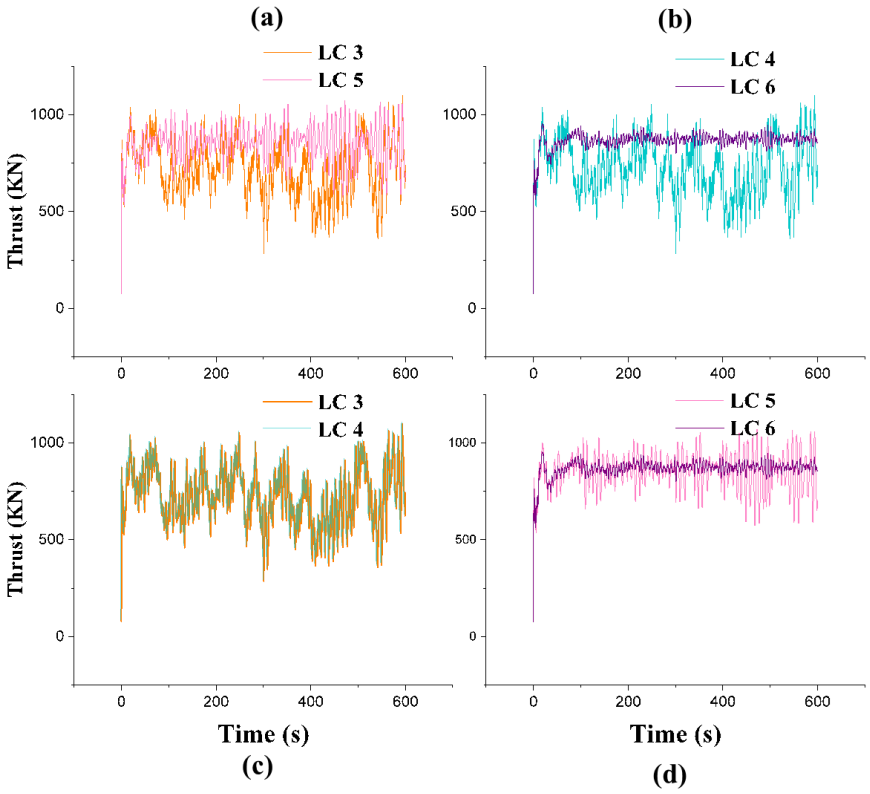

Figure 5.15 Thrust comparison of LC 3 -LC 6

It is seen in Figure 5.15 (a)&(b) that the average thrust force is just slightly varied by the turbulence. Although the inflow is turbulent, the mean wind speed of LC3, LC4 is identical to that of the uniform wind field LC5, LC6. Therefore, the mean thrust force acting on the rotor is nearly the same. Nevertheless, the thrust force becomes very unstable in the presence of turbulence. Figure 5.15 (c) compares the thrust forces of identical turbulent inflows but different wave spectrum parameters, and it is learned that in the presence of turbulence the influence of wave changes on aerodynamic thrust are ignorable. However, as shown in Figure 5.15 (d), which compares the thrust forces of identical steady wind inflow but different wave conditions, the changes in parameters of wave spectrum have impacts on the behaviour of the thrust, though the mean thrust force is almost the same. Therefore, data of five inputs are included in training a model to predict the thrust force acting on the rotor for comprehensive environmental conditions like LC3-LC6. If the model is written in the term of $A(z)y_{model}(t) = B(z)u(t) + e(t)$, the

inputs $u(t)$ includes the pitch($u_1(t)$), the velocity of pitch ($u_2(t)$), the surge($u_3(t)$), the velocity of surge, and the velocity of wind($u_5(t)$). Of course, $y_{model}(t)$ is the real-time thrust, $A(z)$ and $B(z)$ are the estimable parameters of the model. Thus one thrust force prediction model is obtained, *e(t)*is the noise source. The estimable parameters are as follows:

$$A(z) = 1 - 2.191z^{-1} + 1.884z^{-2} - 1.069z^{-3} + 0.5424z^{-4} - 0.3577z^{-5} + 0.2575z^{-6} - 0.08479z^{-7} - 0.001325z^{-8} + 0.04657z^{-9} - 0.02854z^{-10}$$

$$B_1(z) = 59.61z^{-1} - 330.3z^{-5} + 634.7z^{-6} - 364z^{-10}$$

$$B_2(z) = 99.66z^{-1} - 158.8z^{-3} - 119.6z^{-4} - 275.7z^{-5} - 584.1z^{-7} - 351.5z^{-8} - 29.44z^{-9}$$

$$B_3(z) = -51.46z^{-1} + 31.95z^{-4} + 30.17z^{-5} - 10.65z^{-10}$$

$$B_4(z) = -43.35z^{-1} + 24.39z^{-2} + 27.39z^{-3} - 4.442z^{-7} + 19.42z^{-8} + 50.99z^{-9} + 51.06z^{-10}$$

$$B_5(z) = -0.1884z^{-1} + 0.3314z^{-2} - 0.214z^{-3} + 0.3012z^{-4} - 0.4324z^{-5} + 0.4156z^{-6} - 0.2558z^{-7} + 0.115z^{-8} - 0.2601z^{-9} + 0.2063z^{-10}$$

Generally, the bigger the dataset is, the more accurate model will be obtained, and the model will slightly increase when the database reaches a certain level. For the model proposed in this chapter, the size of the dataset is 192000, and the accuracy of fitting to estimate data is [98.88 98.73 99.84 99.69] % .The mean square error is [2.396 2.336 0.02436 0.01664] respectively for LC3-LC6. The final prediction error for the above model is 1.194.

5.5.5 AI- PREDICTION TOOL BASED ON THE ESITIMATED MODULE

The main idea of using machine learning to obtain the prediction algorithm is to recognise the underlying relationships between the inputs and output of interests through sufficient training data pool. Figure 5.16 illustrates the structure of an artificial neural network,

which is composed of the input layer, the hidden layers, and the output layer. In this study, the inputs are surge position, surge velocity, pitch position, pitch velocity, wind velocity. In each hidden layer, four neurons are used to process the input signals. As more data are used to train the structure, a set of weights are obtained for the input defined.

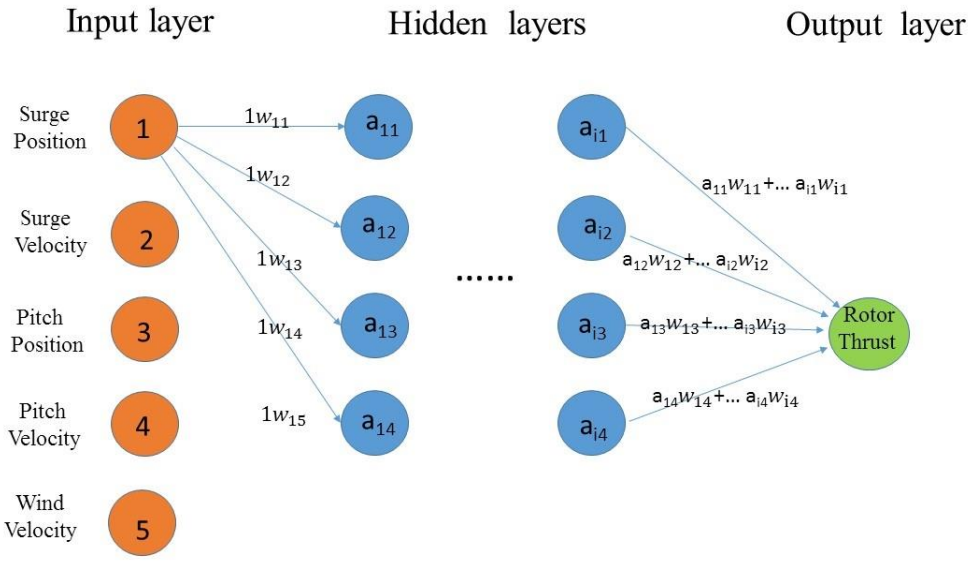

Figure 5.16 The NNT structure used for the prediction module

The five inputs have the same importance, and each input neuron is given weight at each synapse. Similarly, for each neurone in the next layer, outputs of all synapses coming to that neuron are added to the weighted sum, by applying an activation function (commonly a sigmoid function) and a bias. The output of that function will be used as the input for the next synapse layer. Correspond to the mathematical model discussed in[2], which is based on a ten-layers' construction, and if we assume it is a four-layers' prediction algorithm to be used in the AIReaTHM testing rig, then the mathematical model is obtained as follow:

$$Rotorthrust(z) = 1 - 2.138z^{-1} + 1.704z^{-2} - 0.8157z^{-3} + 0.2501z^{-4}$$

$$Surge(z) = -8.164z^{-1} + 0.49z^{-2} + 34.74z^{-3} - 26.58z^{-4}$$

$$V_{surge}(z) = -69.88z^{-1} + 0z^{-2} + 65.43z^{-3} - 16.58z^{-4}$$

$$Pitch(z) = -156.2z^{-1} + 0.62z^{-2} + 0.90z^{-3} + 156.2z^{-4}$$

$$V_{pitch}(z) = -374.6z^{-1} + 0z^{-2} + 291.9z^{-3} + 552.2z^{-4}$$

$$V_{wind}(z) = -43.22z^{-1} + 0.5691z^{-2} + 15.04z^{-3} + 11.21z^{-4}$$

then the control equation of the real-time thrust can be described as:

$$\begin{aligned} \text{Rotorthrust} = & -t_1 \times \text{thrust1} - t_2 \times \text{thrust2} - t_3 \times \text{thrust3} - t_4 \times \text{thrust4} \\ & + s_1 \times \text{surge1} + s_2 \times \text{surge2} + s_3 \times \text{surge3} + s_4 \times \text{surge4} \\ & + sv_1 \times \text{surge\_vel1} + sv_2 \times \text{surge\_vel2} + sv_3 \times \text{surge\_vel3} + sv_4 \times \text{surge\_vel4} \\ & + p_1 \times \text{pitch1} + p_2 \times \text{pitch2} + p_3 \times \text{pitch3} + p_4 \times \text{pitch4} \\ & + pv_1 \times \text{pitch\_vel1} + pv_2 \times \text{pitch\_vel2} + pv_3 \times \text{pitch\_vel3} + pv_4 \times \text{pitch\_vel4} \\ & + w_1 \times \text{wind\_vel1} + w_2 \times \text{wind\_vel2} + w_3 \times \text{wind\_vel3} + w_4 \times \text{wind\_vel4} \end{aligned}$$

In which, coefficients ($t_1, t_2, t_3, t_4, s_1, s_2, s_3, s_4, sv_1, sv_2, sv_3, sv_4, p_1, p_2, p_3, p_4, pv_1, pv_2, pv_3, pv_4, w_1, w_2, w_3, w_4$) are the weighted sum shown as the polynomialcoefficients in each component of the mathematical model. As for the thrust components, an estimated thrust and a total weight coefficient is used as an intermediate output for each layer, and they are reduced from the rotor thrust in the control equation of the program in Labview.

5.6 Summary

In this chapter, comprehensive simulations based on the classic model of 'OC3-hywind'floating wind turbine have been carried out, and the data from simulations has been analysed in great details to obtain the structure of the thrust force prediction model. Moreover, artificial neural network techniques are used to train the primarily obtained structure to gain well established mathematical models which can be used as control functions in the experiments to provide real-time thrust varying with the input signals including surge, surge velocity, pitch, pitch_velocity, wind speed and wave conditions. After gaining the prediction module, in the following chapters, a real-time controller is used to execute the prediction algorithm in the model tests. Therefore, the AI machine

discussed in this thesis incorporates five inputs, a predictive algorithm/module (the predictive module is obtained through AI training, and executed by program in controller), and one output. The five inputs are the instantaneous surge displacement, velocity, pitch displacement, velocity, and wind velocity. The output is the rotor thrust.

Also, based on the AI machine, an experimental rig which enables the real-time model testing of a spar-type floating wind turbine is developed. Moreover, a bench testing platform is developed to characterise the AI-based Real-Time Hybrid Model (AIReaTHM) testing rig. Results from the bench tests utilising a manoeuvrable motion simulator are used to justify its feasibility. Finally, tank tests of a 1:73 model of spar-type FOWT are carried out as an example utilising the AIReaTHM testing methodology.

6 Development and validation of the AIReaTHM testing rig

Based on the AI machine, a new testing rig which enables the real-time model testing of a spar-type floating wind turbine is developed. Hereafter, the acronym AIReaTHM testing (AI-based Real-Time Hybrid Model testing) is used to indicate the real-time hybrid testing approach with the AI application. Moreover, a bench testing platform is further developed to study the characteristics of the AIReaTHM testing rig. Results from the bench tests utilising a manoeuvrable motion simulator are used to demonstrate its feasibility.

6.1 Introduction

In order to have a thorough analysis of the real-time rotor thrust, and different data pools are used to train a prediction module to have the ability to predict the real-time rotor thrust of a floating wind turbine in a hybrid testing system, the mathematical module is going to be established in this chapter. Therefore, the AI machine to be proposed incorporates five inputs, a prediction algorithm/module (the prediction module is obtained through AI training, and executed by a program in the controller), and one output. The five inputs are the instantaneous surge displacement, velocity, pitch displacement, velocity, and wind velocity. The output includes aerodynamic forces, but this PhD research takes only the rotor thrust as the output, hence the coupling effects concerning other aerodynamic forces are not yet considered in this research. Based on the AI machine, a new experimental rig which enables the real-time model testing of a spar-type floating wind turbine is developed. Hereafter, the denomination AIReaTHM testing is used to indicate the real-time hybrid testing approach with the AI application. Moreover, a bench testing platform

is developed to study the characteristics of the AIReaTHM testing rig in Chapter 5. Results from the bench tests utilising a manoeuvrable motion simulator are used to justify its feasibility. It is worth noting that a OC3-Hywind FOWT is selected to demonstrate the new testing approach in Chapter 4, 5 and 6 and it is the FOWT used for the first commercial floating wind farm in the world. In this chapter, simulations are mainly done for an OC3-Hywind to form the data pools.

As the first attempt of artificial intelligence techniques being applied in the hybrid testing method for FWTs, the originality lies in the following factors: 1. the AIReaTHM testing method does not rely on any third-party codes, such as AeroDyn or Turbsim, compared to ReaTHM testing[57], because the underlying predicting algorithm between selected inputs and outputs has been pre-obtained by AI technology; 2. the time delay and overall uncertainty of the AIReaTHM testing rig is quantitatively identified by bench tests; 3. once the experimental rig is built, no more code-code interface is needed; 4. the new hybrid testing system is able to overcome the inherent Froude-Reynolds scaling conflict in laboratories. However, it has also some shortcomings; for example, the uncertainty inherent to the component used in the experimental rig can directly result in uncertainty in the AIReaTHM testing system. In addition, the AI machine is dependent on the big data cloud, which is used to train the prediction algorithm, but only data from FAST computing has been available up to now. To make the AIReaTHM testing system more realistic, better components to build the testing rig and more realistic data from pilot floating wind farms will be needed.

6.2 Development of the hybrid test approach for FOWTs based on SIL method

Making use of the available components in the Kelvingrove hydrodynamic lab of Strathclyde University, an AIReaTHM testing rig is built up as shown in Figure 6.1. Four inputs of the AI machine -instantaneous surge displacement, velocity, pitch displacement,

velocity - are provided by the physical model in the basin. These four parameters are initially model-scale and simultaneously converted to full-scale by the Froude Scaling Law in the controller. The time history of the wind velocity is pre-stored in the controller as the fifth input of the prediction module.

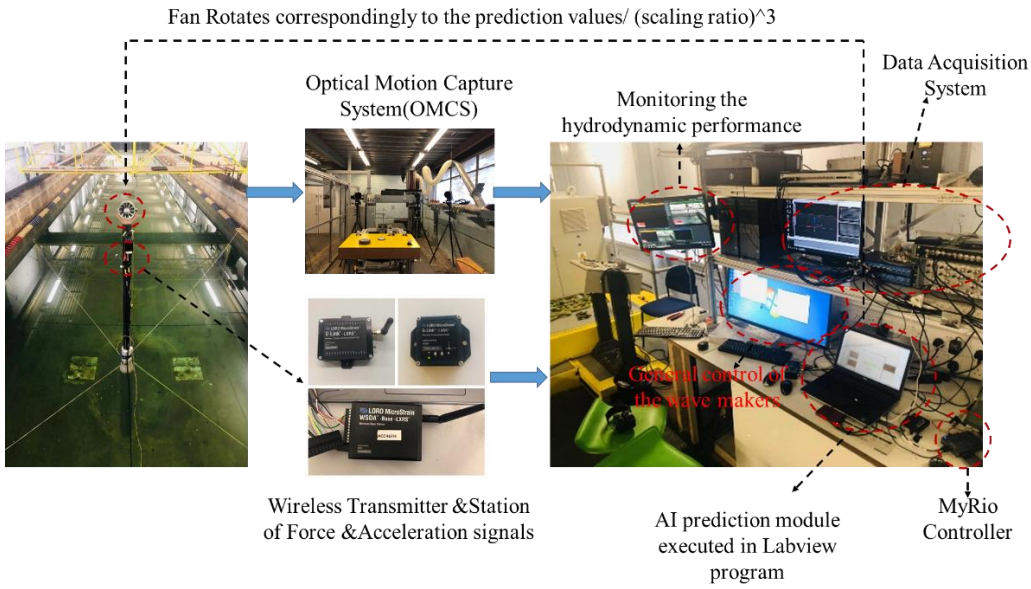

Figure 6.1 Experimental rig of the AIReaTHM testing approach

To summarize the procedure in the experimental loop, a load cell is used to measure the rotor thrust, and the signal of the load cell is transferred to the data acquisition (DAQ) system through a wireless transmitter and base station. The optical motion capture system is used to acquire the displacement in surge and pitch of the model in the basin. All the inputs are then transferred to the prediction module by the DAQ system. The prediction module outputs the rotor thrust as the command to drive the fan to rotate. The output (the rotor thrust) of the prediction module, however, is in full-scale and is divided by the cube of the scaling ratio before used to drive the fan to rotate. The wave makers are controlled by an independent computer. The real-time performance monitoring of each test is switched on. Moreover, the specifications of the instruments are listed in Table 6.1.

Table 6.1 Specifications of the instruments

Instrumentation	Type	Function	Range	Resolution /Accuracy
Controller	MyRio-1900	Receive inputs, execute the prediction module, generate output thrust command	IO: -10V-9.995V AO: -8g-7.996g	12 bits
Fan	S/N: LooA21592	Generate the thrust	0-20N	—
Thrust load cell	S/N:62260995	Measure the thrust	0-5V	0.00000001V
Calibrating weight	OIML M1	Calibration of load cells	100g-5000g	50 mg/kg
DAQ system	CED Spike	Monitoring	0-15V	16 bits
Motion simulator	Scotch Yoke	Generate the motion	1-120mm	unstable
Qualysis	Integerated Optical Motion Capture System	Motion capture	Dependent on the Arrangement of Cameras	0.00001mm

IO is for analog input and output channels; AO is for accelerometer

6.2.1 SELECTION OF THE OPERATING FREQUENCY

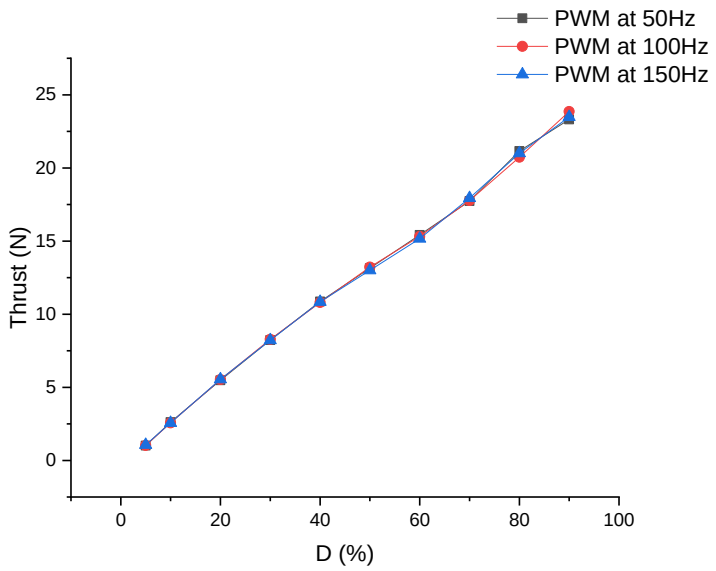

Figure 6.2 Thrust observation under PWM control at different frequencies

The operating frequency does not have an obvious effect on the targeted rotor thrust, as shown in Figure 6.2. So the three frequencies listed all work okay on control the thrust generation by a fan, but to be consistent with the operating frequency of the program used in the NI controller, the instruments used in the AIReaTHM testing approach are operated at a frequency of 100Hz; the rotor thrust is generated by Pulse Width Modulation (PWM). The operating frequency does not have an obvious effect on the targeted rotor thrust, as

shown in Figure 6.2. However, the prediction module tends to be affected by the frequency of the relevant training examples used to train it. Therefore, the frequency of the wind data(f1), the frequency of FAST calculation(f2), and the subsampling frequency of the data from the FAST calculation(f3), the frequency of training the prediction module(f4) are explored by using different databases to train the prediction algorithm. The second column of Table 6.2 lists the databases named by the four frequencies used in obtaining the prediction module, in the order as they are mentioned above, like 'f1_f2_f3_f4'. At the same time, the data components regarding pitch, pitch velocity, surge, surge velocity, and wind velocity form the database consisted of 5 vectors. For case 1, the database '20Hz_80Hz_20Hz_20Hz' is used to train the prediction algorithm, and prediction model A is obtained. The last three columns list the accuracy (compared to the estimation data), the final prediction error (FPE), and mean-square error (MSE), respectively.

Table 6.2 Details for software optimization

Case No.	Database Name	Database Size	Prediction module	Accuracy	FPE	MSE
1	20Hz_80Hz_20Hz_20Hz	72000×5	A	94.29%	65.38	65.32
2	80Hz_80Hz_80Hz_20Hz	48000×5	B	98.88%	2.395	2.392
3	20Hz_80Hz_20Hz_80Hz	36000×5	C	94.4%	66.78	66.68
4	20Hz_80Hz_20Hz_20Hz	36000×5	D	94.4%	66.78	66.68
5	80Hz_80Hz_80Hz_80Hz	144000×5	E	96.41%	26.94	26.93
6	80Hz_80Hz_80Hz_20Hz	144000×5	F	96.41%	26.94	26.93
7	80Hz_80Hz_20Hz_80Hz	36000×5	G	92.04%	132.6	132.6
8	80Hz_80Hz_20Hz_20Hz	36000×5	H	92.04%	132.6	132.6

As shown in Table 6.2, the change in the subsample frequency of the FAST computations does affect the size of the database (f_3). The more data are used to train the module to find the underlying relationship between the inputs and output, the final prediction errors tend to be more as well.. This can be observed by comparing model A with model C (or D, G, H). However, though model E &F are trained by a bigger database than model A (or C, D, G, H), they show better prediction performance. Comparing case 3&4 with case 7&8,

it is apparent that the inconsistency in f_1 and f_2 results in huge prediction errors. As a contrast of case 3, the database used in case 1 is doubling. However, the accuracy stays almost the same and prediction error varies a tiny amount. Model C, D, E, and F shows better stable prediction performance. Moreover, as learned from case 3&4 or 5&6 or 7&8, the f_4 of databases does not affect the accuracy or prediction errors. When the five simulated inputs are given to model D and Model E, the predicted thrusts are obtained and used to compare with the rotor thrust from FAST computation. The time histories of the model D's and Model E's output are shown in Figure 6.3. As can be seen in the figure, the time history from Model E's prediction is more covered by the measured data showing better agreement, which proves that Model E gives a better prediction of the rotor thrust, thus it is used in the AIReaTHM testing rig.

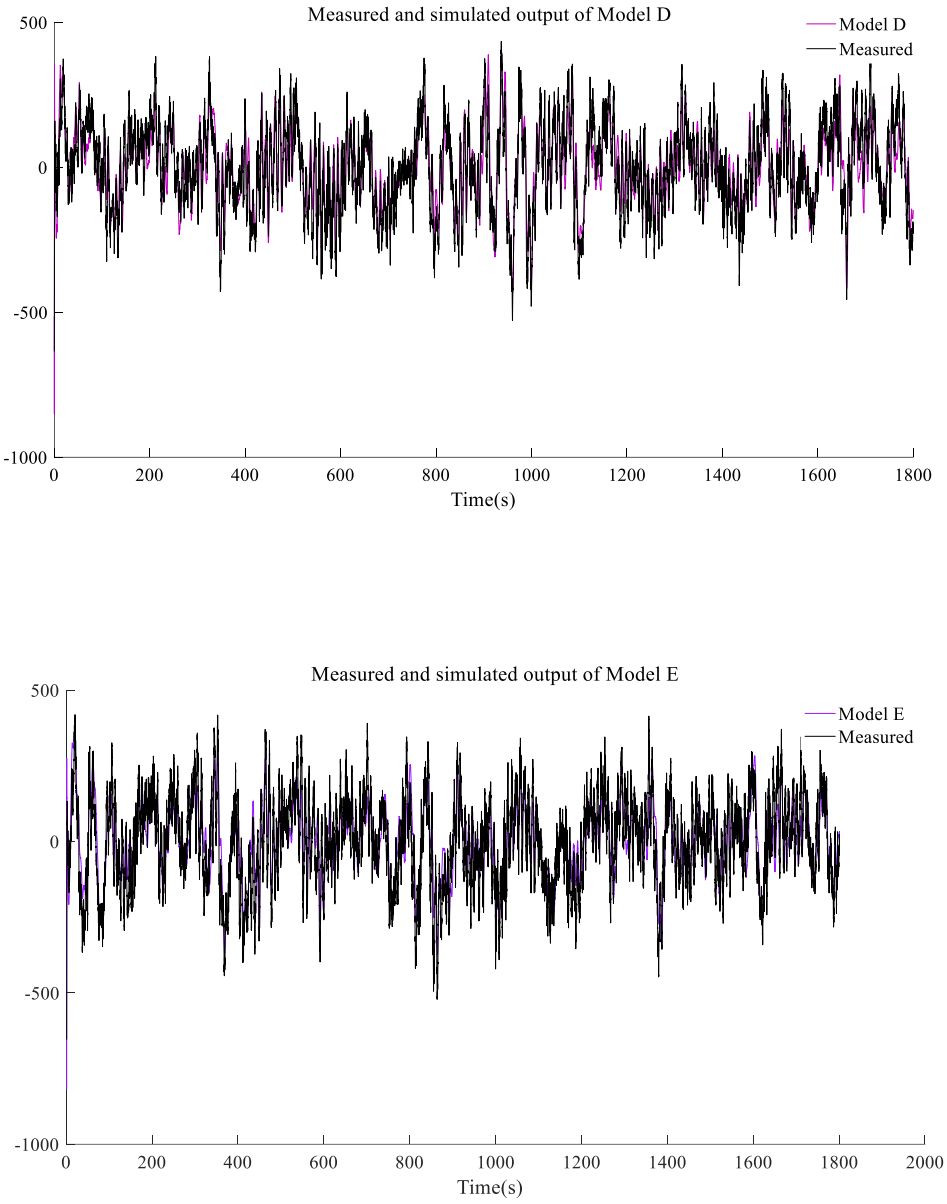

Figure 6.3 The output of the prediction modules compared with the measured

6.3 Characteristics of the hybrid testing approach based on bench tests

6.3.1 EXPERIMENTAL SET-UP

To validate the proposed AIReaTHM testing rig, a bench testing platform is developed to investigate how well the targeted real-time rotor thrust is predicted and implemented in the experimental loop. The diagram of the bench testing procedure is given in Figure 6.4.

A motion simulator based on the Scotch Yoke mechanism is developed, which provides the simulated surge motion in the bench testing procedure. As shown in Figure 6.4, while the surface waves were modelled physically in the tank by wave makers, the turbulent wind is numerically generated and pre-stored in the controller, as oncoming wind input for the prediction module. Additionally, the thrust calculation was carried out in full-scale in the prediction module. The red lines in Figure 6.4 represent numerical and software parts of the hybrid testing approach, while the blue lines are for the physical substructures. The hardware used to execute the thrust command is illustrated by grey cubes and circles. A controller is adopted to read in the motion and velocity profiles of the motion simulator, and they are scaled up using Froude scaling law to full scale before being entered to the prediction module in the controller, together with the full-scale wind field data produced by numerical simulation. Then a corresponding thrust is obtained by the software in controller. Similarly, to cope with model scale experiments, the profile of the real-time thrust command is scaled down to model scale to drive the fan to rotate, thus to generate a fan thrust. In this way, a series of bench tests are carried out.

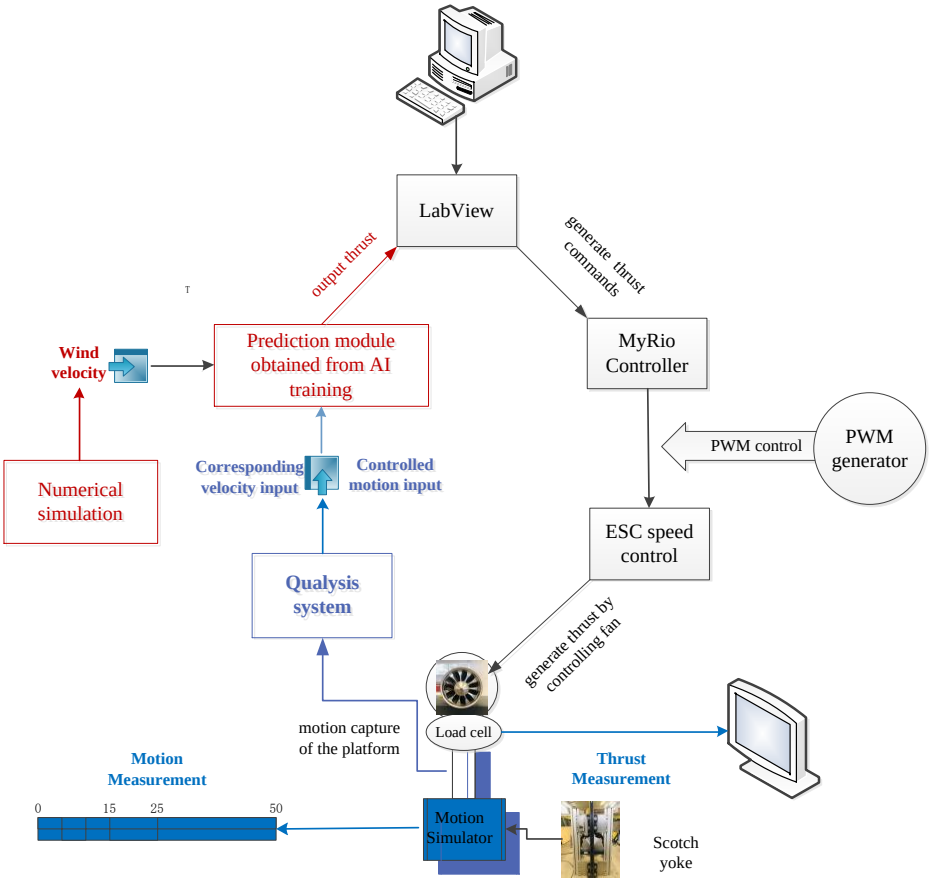

Figure 6.4 Diagram of the bench testing procedure

6.3.2 CALIBRATION OF THE INSTRUMENTS

The rotor thrust is measured by a load cell, and the presence of the inertial force caused by the acceleration of the motion simulator in bench tests is to be discussed and identified. This allows the inertial force to be removed from the reading of the load cell in each test. After removing the inertial force from the reading of the load cell, the rest of the reading is used as the measured value of the rotor thrust.

If uncertainty in the i th measured value of the final experimental result-thrust is described as following [104]:

$$\delta_i = \beta + \varepsilon_i \tag{6.1}$$

where δ_i is the difference between the measured value and the true value; β is the systematic error, which is usually a fixed component of the total error, and is sometimes referred as bias in experiments. β often result from the uncertainty in instruments used in

the experimental rig, ε_i is the random error of the i th measurement, and is referred to as repeatability error in experiments. Calibration is a practical method used to eliminate bias and system errors[105]. In fact, systematic errors are often summarily dismissed in books and articles on uncertainty analysis by a simple assumption that all bias errors have been eliminated by calibration. Uncertainty analysis of the AIReaTHM testing system, excluding the systematic uncertainty, is provided in section 6.4. Therefore, calibration tests of the main components are used as the main means to identify systematic uncertainty.

A fan is employed to generate the rotor thrust atop of a physical model. The compound is displayed in Figure 6.5 (a), the fan sits in a wooden holder upon the load cell. Data are measured by the load cell and collected by one high spectral resolution data acquisition system. The samples of the calibration tests are provided in Figure 6.5 (b), it can be seen that the thrust command(T_{target}) is proportional to thrust measurement($T_{measured}$) with a regression confidence of 99.99% (when regression confidence R2 is 100%, all the sample perfectly points fall on the regression line and follow the regression equation), Then it is proven that the stationary thrust measurement follows the thrust command quite well. However, when the fan rotates continuously, peak to peak noise among the blades is not ignorable. Thus necessary adjustment needs to be done to minimize the peak to peak noise of the 12-blade fan. Blades' gravity centers are adjusted to opposite each other, then produce a resultant aero centrifugal forces when it rotates. After the adjustment, the peak to peak noise caused by each blade is analyzed as shown in Figure 6.6

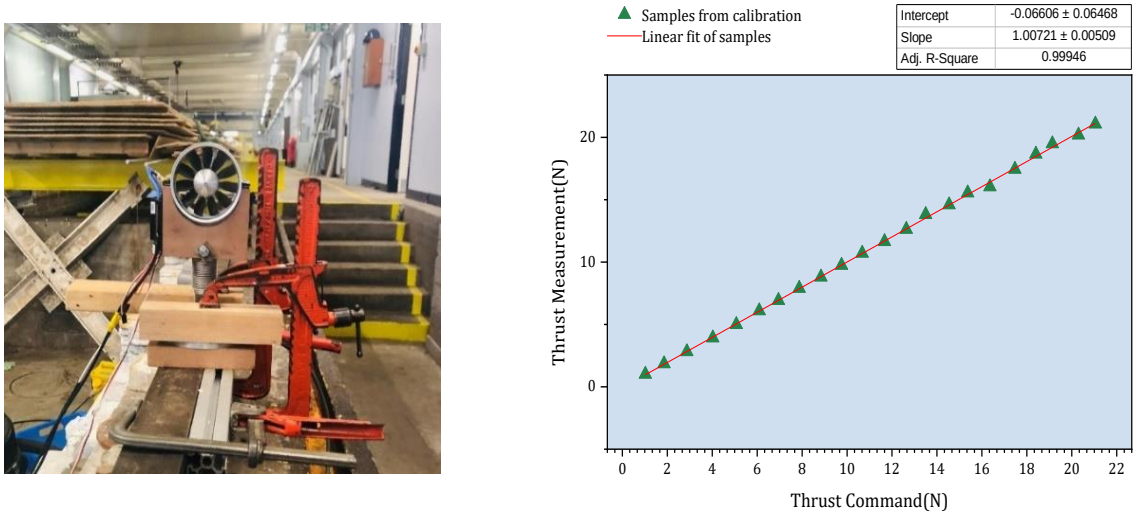

Figure 6.5 The set-up (a) and results (b) of the fan Calibration

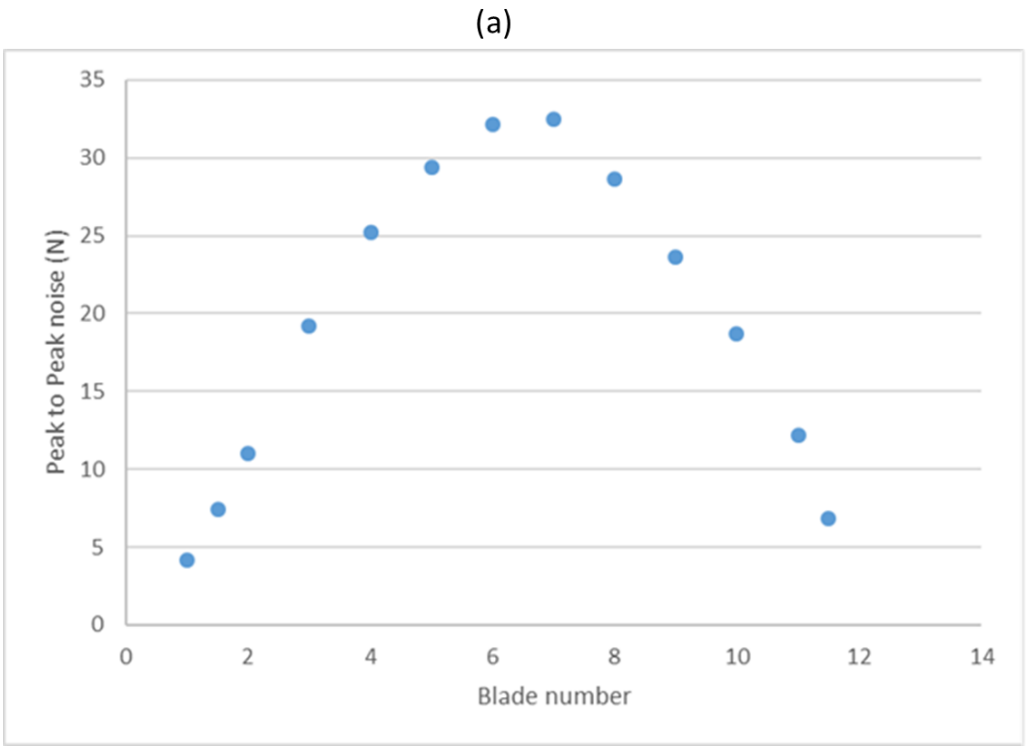

(b)

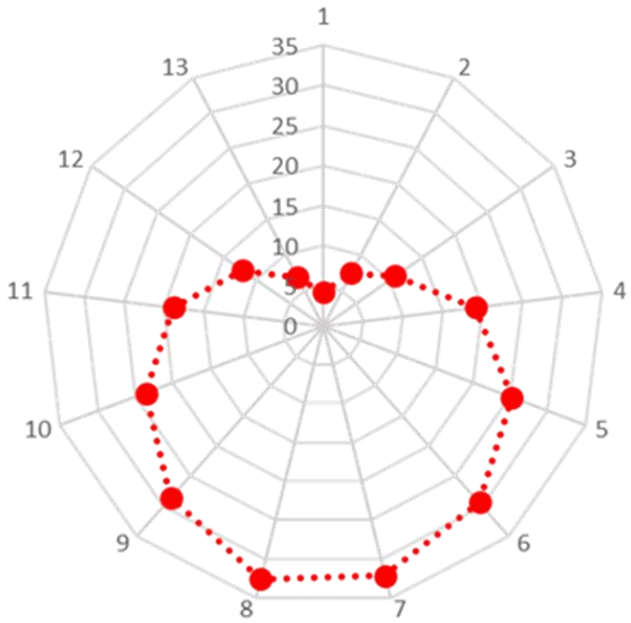

Figure 6.6 Blade balance after adjustment

Likewise, the load cell is calibrated by hanging increasing masses onto it, one drop test with the same mass are repeated three times to obtain one point shown in Figure 6.7, and 42 dropping tests are carried out in total. As a result, 14 points obtained from mass-dropping tests reveal a clear relationship between the thrust reading and voltage change of the load cell. Thus following the linear relationship obtained in Figure 6.7, a conversion Equation (6.2) used to secure the thrust reading.

$$T_{reading} = V \times 40.26499 \tag{6.2}$$

It is obvious that the uncertainty in the converting process is ± 0.18778 N, as concluded from the calibration tests. This uncertainty is passed to the final bias of each bench test.

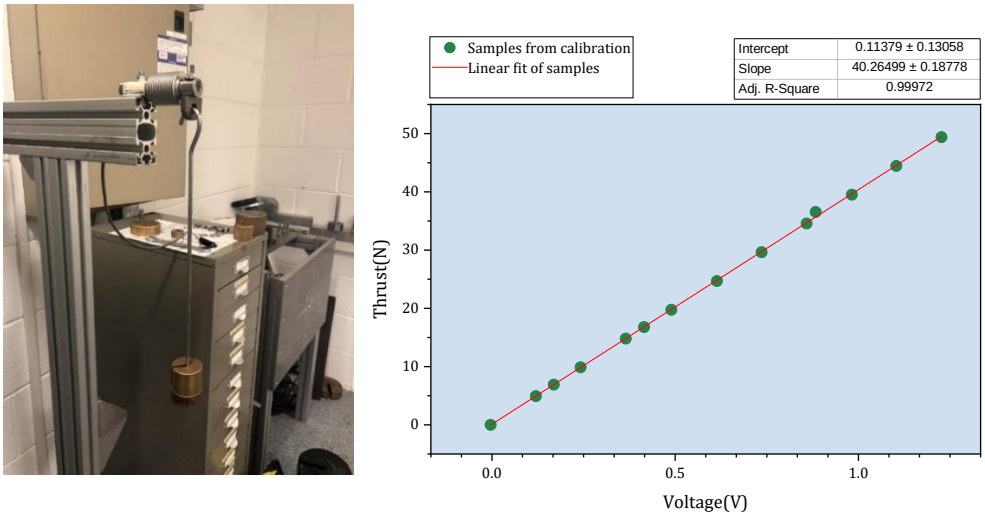

Figure 6.7 Calibration set-up and results of the load cell

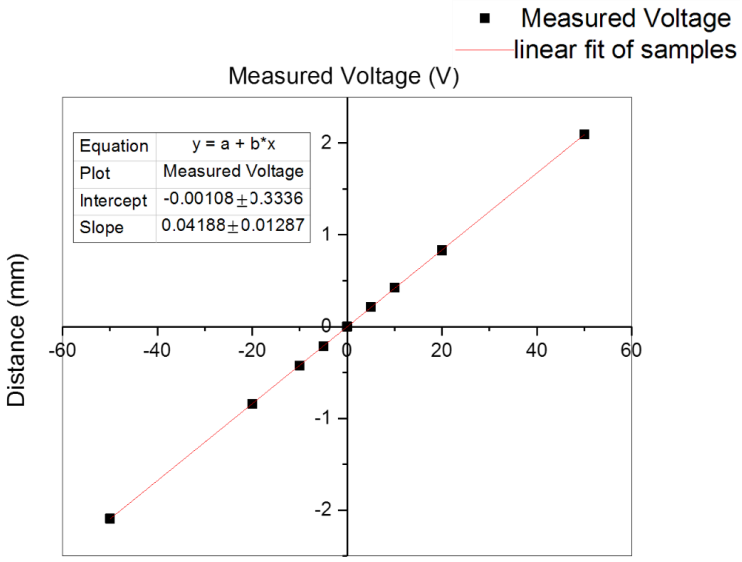

Figure 6.8 Calibration results of the LVDT measuring method

Calibration for the optical motion capture system (Qualysis[106]) is prepared by following instructions from the manufacturer. However, it is difficult to prove how well the motions are seized without any comparison; hence, a Linear Variable Differential Transducer (LVDT) is used as a comparative motion measurement at the bench testing stage. Therefore, the LVDT need to be evaluated, and the result is analyzed in Figure 6.8.Then LVDT's reading is monitored and used as the comparison to study the quality of Qualysis' motion capture for each bench test. More information on the uncertainty

caused by using the optical motion capture system is demonstrated in Section 6.5 of uncertainty discussion.

Indeed, there are other forms of systematic errors caused by issues such as transducer installation effects and environmental effects (such as temperature, humiliation, the water evaporation), which are not able to be quantitatively considered in this thesis. Therefore, the systematic uncertainty identified from bench tests will not consider those effects. Mean scores of repeated tests are used to minimise the influence of random uncertainty.

6.3.3 TESTING MATRIX

There are two modes designed for AI predicting the real-time rotor thrust: mode A and mode B. The prediction algorithm for mode A is trained by the data pool formed by FAST simulations under the conditions of regular waves (f= 0.1rad/s, 0.2 rad/s, …3.0rad/s) and steady winds (wind speed= 6m/s. 8m/s, …18m/s). Likewise, the prediction algorithm for mode B is also trained by data from FAST computations, but, under the conditions of five possible sea states described by wave spectrum and IECKAI turbulent wind model. To validate the two modes, a series of bench tests are designed and listed in Table 6.3, where v1…v5 is used to present the five surge frequencies to differ from f1…f4 in other chapters.

Table 6.3 Testing arrangement

Mode	Quantity of tests	Wind	Wave condition	surge
A	5	8m/s	Regular wave(f= 0.1rad/s, 0.2 rad/s, …3.0rad/s)	Surge at five frequency(v1,v2,v3,v4,v5)
A	5	10m/s		
A	5	12m/s		
A	5	14m/s		
A	5	16m/s		
Mode	Quantity of tests	Sea State		surge
B	5	SS1	SS1+	Surge at five frequency(v1,v2,v3)
B	5	SS2	SS2+	
B	5	SS3	SS3+	
B	5	SS4	SS4+	
B	5	SS5	SS5+	

6.4 Results

Prior to observing quantitative results of the bench tests, the presence of the initial force is discussed at first. To remove the initial force from the preliminary readings from bench tests, the initial mass is calculated and statistically analysed, and confirmed by the mass of the physical fan and its holder. After the initial force are removed from the experimental reading of the load cell, the measurement of the fan thrust is obtained and used for three main purposes: 1, to validate the feasibility of the AIReaTHM testing methodology; 2, to observe the effect surging motion has on the predicted rotor thrust; 3, to investigate the impact of a turbulence and wave spectrum has on the rotor thrust; 4, to identify the systematic uncertainty of the temporary testing rig used to validate the testing methodology, for further improvement.

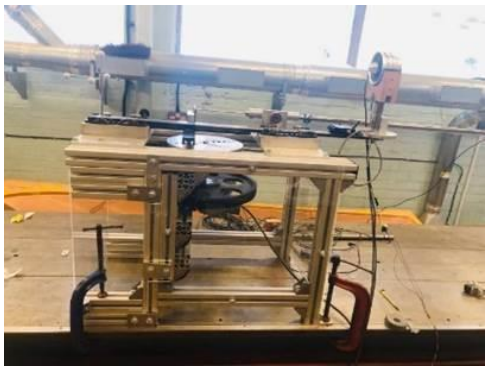

Figure 6.9 The fan located on the piston of the Scotch Yoke mechanism

The load cell's set-up is shown in Figure 6.9, the reading of the load-cell actually is dominated by the movement of the Scotch Yoke, rather than the change in the rotation of the fan. Therefore, the interpretation of the load cell consists of two parts; one is the inertial force (acceleration force) caused by the motion generated by the Scotch Yoke, the other part is the thrust generated by the fan. In order to remove the initial force from the experimental measurement, a few experiments only allowed the surge while switch off the fan rotation is carried out. In that case, the load cell’s reading should only be the inertial force, the readings from a typical experiment are shown in Figure 6.10, where the

velocity is the differentiate of the reading of LVDT, while acceleration of surging (a) is obtained by differentiating the velocity too.

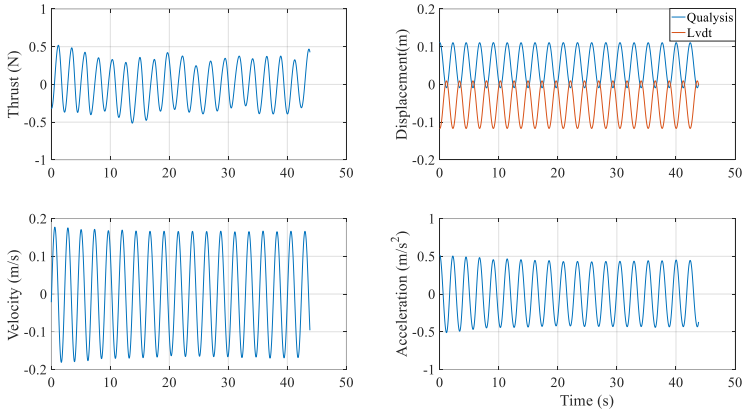

Figure 6.10 A typical experiment without fan rotating

The inertial force can be described as Equation (6.3) by Newton's Second Law

$$F_{inertial} = M_{inertial} \times a \tag{6.3}$$

Actually, the inertial force $F_{inertial}$ and acceleration a are as following

$$F_{inertial} = |F_{\max}| \sin(wt + \varphi_1) \tag{6.4}$$

$$a = |a_{\max}| \sin(wt + \varphi_2) \tag{6.5}$$

where, w is the angular frequency of the motion simulator (Scotch Yoke). If we ignore the phase difference, the mass causes the inertial force can be described as,

$$M_{inertial} = \frac{|F_{\max}|}{|a_{\max}|} \tag{6.6}$$

then the distribution of the inertial mass obtained by the above experiment varies as $|F_{\max}|$ and $|a_{\max}|$ vary per cycle, which is demonstrated in Figure 6.11(a).

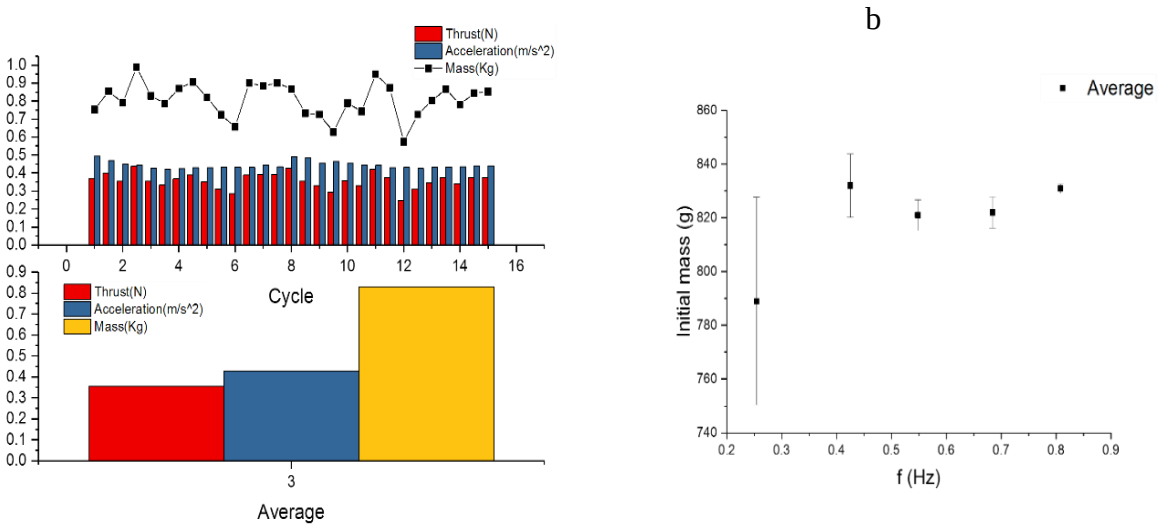

Figure 6.11 Distribution of the initial mass in a typical experiment

The inertial mass should be a constant value and can be obtained from the physical measurement. Then the inertial mass for a various individual experiment is measured and the reading is presented in Figure 6.12.

Figure 6.12 Weight of the mass of the physical fan and load cell

The weight of the load cell should be partly included in the referred mass, because the strain gage is located at the middle of the screw bar. Hence, from one-fourth to one-third of the load cell's weight could be considered. Then the referred mass is 820-853 grams, which agrees with the inertial mass from analysis of bench tests without fan rotating. In this way, the inertial mass is assumed to be 836 grams, then a corresponding inertial force

can be obtained based on basic calculation of the inertial mass and acceleration. Thus the reading of the load cell minus Therefore, the measurement discussed hereafter indicates the load cell's reading after removing the inertial force.

6.4.1 VALIDATION OF THE AIREATHM TESTING METHODOLOGY

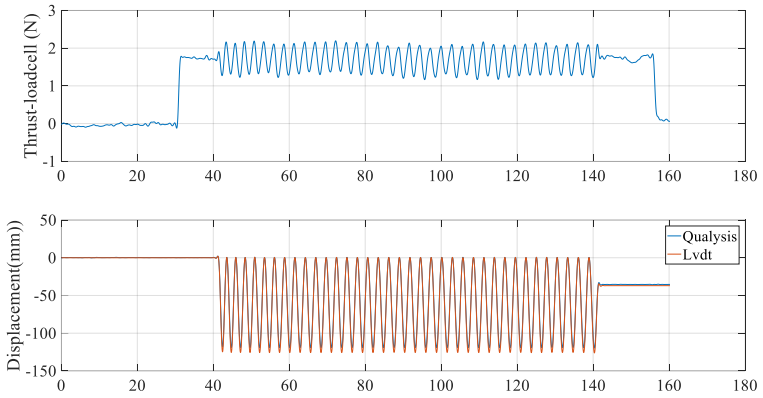

Figure 6.13 Measurement from one typical bench test

Figure 6.13 shows the data from one typical experiment when wind speed is 12mps, and the motion simulator surge at v2, however, only the data between 60s and 130s are selected for further analysis to avoid the transient reaction. At the chosen data from experiment's measurement is used to compare with the output rotor thrust command generated by the prediction module during the testing. Certainly the measurement is scaled up by Froude scaling law. Figure 6.14 presents the comparisons of AI prediction and measurement of the real-time rotor thrust under the wind speeds of 8m/s, 10m/s, 12m/s, 14m/s, 16m/s respectively when motion simulator surge at v1. It is evident that the measurement agrees well with the AI prediction output. However, the motion simulator is very unstable and has a terrible speed controller. For example, when the motion simulator is set to oscillate at v1, the period of each cycle of the motion is different, the gearwheels even got stuck a few times during the testing campaign. Secondly, though each time the control button is set to be the same speed(v1), the resulted mean frequency is however very different. For example, the five experiments shown in Figure 6.14, are

all supposed to be carried out under the same surge speed of v1; however, the measured mean frequencies of the surge inputs for five cases are 0.246, 0.260, 0.260, 0.239, 0.254 Hz respectively. Therefore the frequency of the oscillating/high-frequency component of the rotor thrust is unstable too. If possible it is wished a reliable speed control box can be used to replace the extremely old one,which even did not work initially.

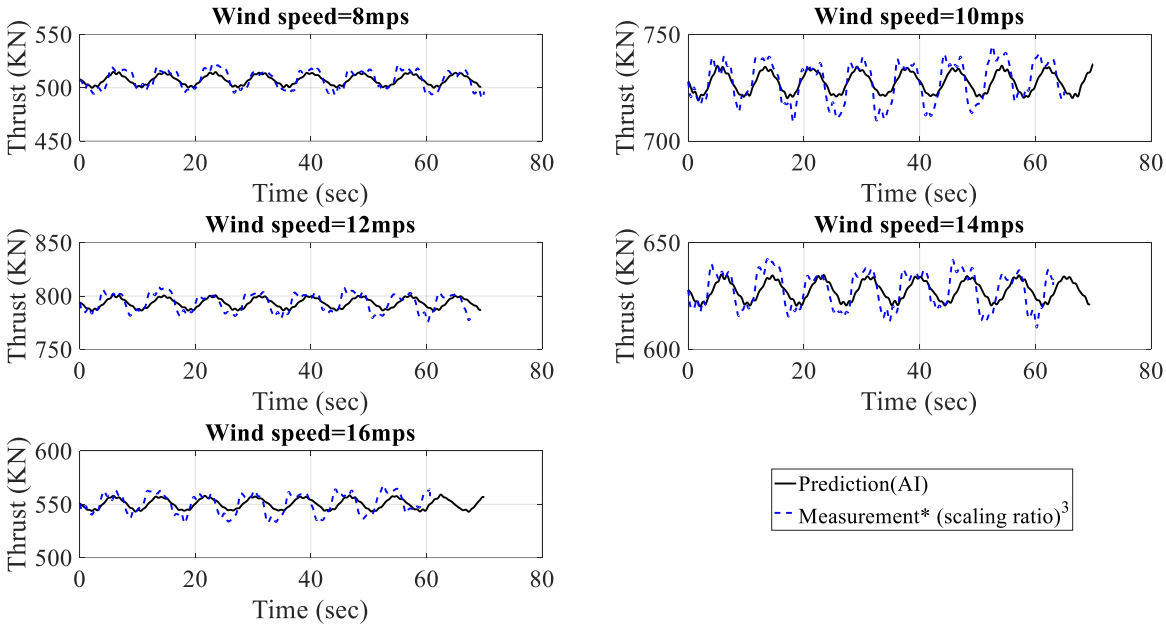

Figure 6.14 Experimental measurement compared with AI prediction

As concluded in[2], the average thrust corresponds to the low-frequency component of the rotor thrust, and it is dominated by the wind speed. The oscillating component of the thrust corresponds to its high-frequency component, and it is dominated by wave conditions. For the prediction (AI) which is the rotor thrust predicted by the AI prediction module applied on the hybrid testing rig only, it is apparent that the mean value of both AI prediction and FAST simulation is almost the same. The surge dominated component is fully predicted and well captured, though some disparity in the vibration frequency of the surge dominated component is noticed. In fact, the frequency disparity is reasonable because the surge motion in the bench tests is simulated by a Scotch Yoke mechanism, and the motion is unstable.

6.4.2 THE EFFECT OF SURGE FREQUENCY AND WIND SPEED ON THE ROTOR THRUST

A case-study of surging at v2 was chosen to obtain further in-depth information on the performance of the prediction module. Figure 6.15(a) compares the thrusts obtained under different wind speeds, and it reveals the difference in the average value of thrusts; however, the oscillating component of the thrusts shows generally same responses, because the surge inputs are set to be the same, even though the instability caused by motion simulator. Besides, the surge input of the bench tests seems to have no impact on the average value of thrusts.

It is also noticed that there is a tiny frequency difference between the AI prediction (solid lines in Figure 6.14, Figure 6.15, Figure 6.16) command of the rotor thrust (which is used to drive a fan to produce a simulated rotor thrust in the real-time test) and measurement of the rotor thrust (dash linesin Figure 6.14, Figure 6.15, Figure 6.16), which in fact are the reading of the load cell after removing the inertial force by an assumption that the inertial mass is 836 g. Details in concluding the inertial mass to be 836g are provided in section 6.3.1. As revealed in Figure 6.15 (b), the frequency difference only occurs when the motion simulator surges too fast. For the tests for the wind speed of 12m/s, some tests for surging frequency of 0.257 Hz and 0.367Hz, are not used for further analysis because the motion simulator could not wrok for a enough long period. However, when the surge frequency increase to 0.557Hz, the frequency difference between AI prediction and measurement becomes not ignorable. This also can be observed in Figure 6.15(a). Figure 6.15(b) shows the thrusts under the same wind speed, but the motion simulator surges at various frequencies. It is revealed that as the frequency of the surge input increases, the frequency of the oscillating component of the thrust also increases. In addition, the amplitude of the oscillating component rises slightly as the frequency increases. This is believed to be caused by the assumption used in abstracting the measurement of rotor thrust from the reading of the load cell, because the calculation of inertial force is

acceleration sensitive, and the acceleration comes from the derivation of surge motion. A further demonstration of the defects caused by using the fractional reading of the load cell as the measurement of the rotor thrust is given in Figure 6.16 where the same data used in Figure 6.15(b) are plotted separately for AI-prediction and measurement. Compared to the output from AI prediction, which is actually produced as the rotor thrust, the fractional reading of the load cell itself introduce certain mount of instability in both oscillating amplitude and frequency. Therefore, the method using a load cell to measuring the rotor thrust produced by the fan will be replaced in further reseaches.

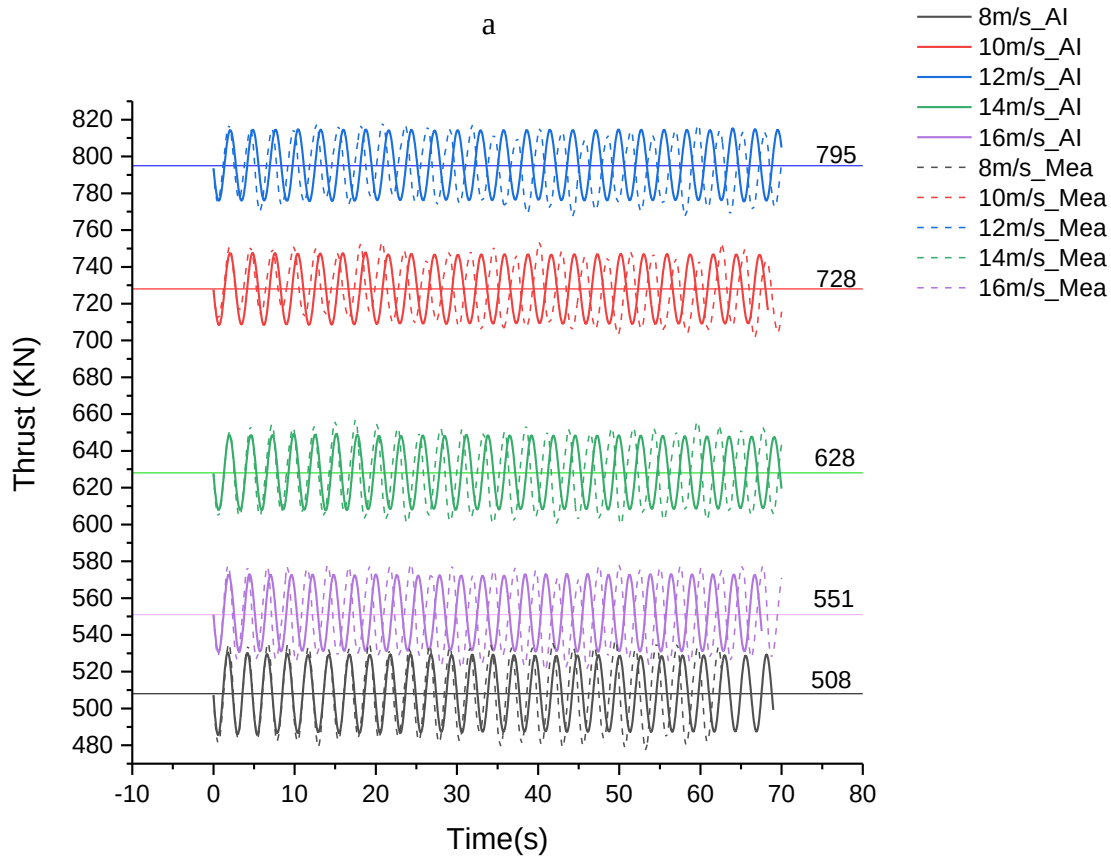

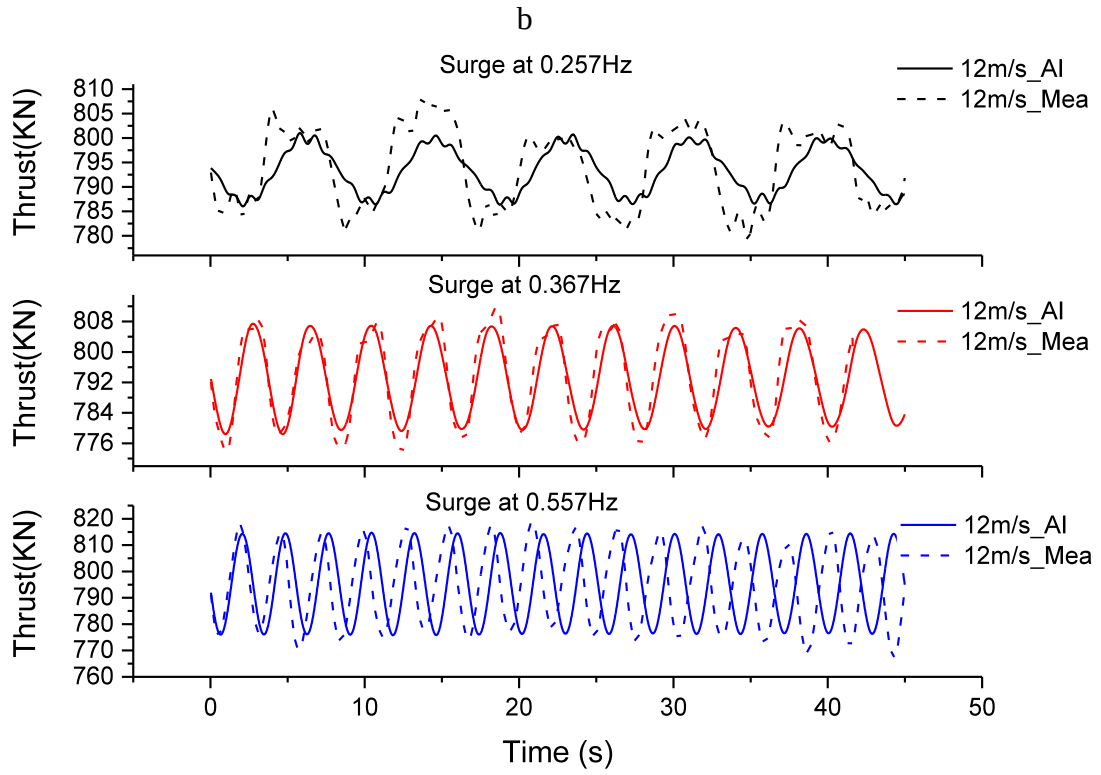

Figure 6.15 (a)Same surge frequency(0.557Hz) under different wind speeds;(b) Same wind speed(12m/s) under different surge frequencies

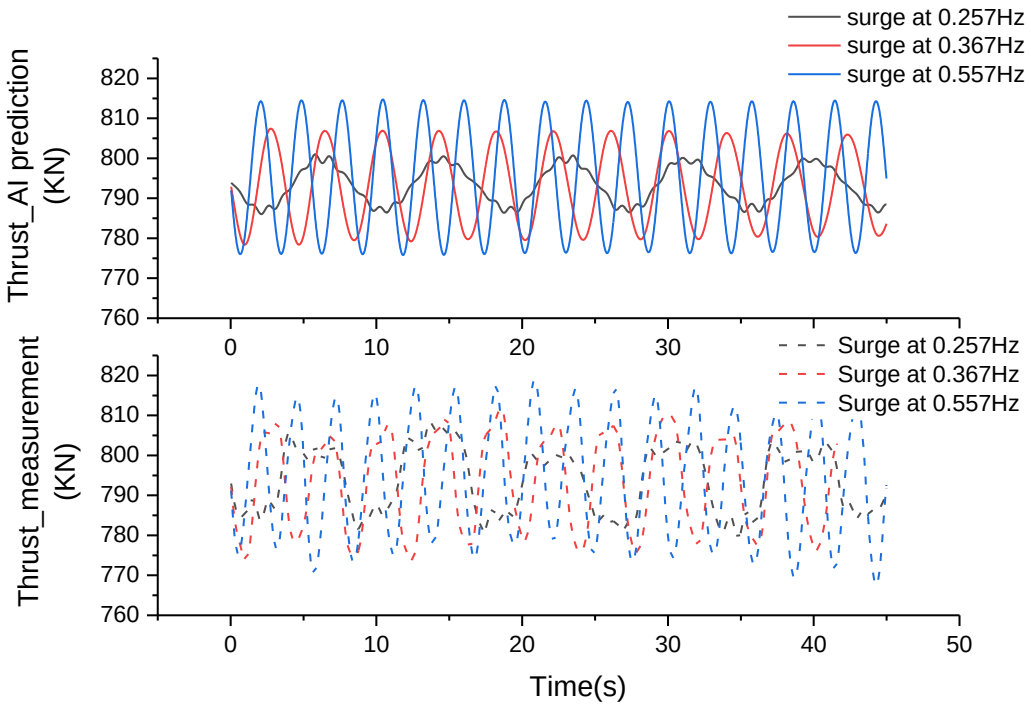

Figure 6.16 Data of AI_predicion or loadcell's reading independently

6.4.3 THE EFFECT OF TURBULENCE AND WAVE SPECTRUM ON THE ROTOR THRUST

Table 6.4 Environmental conditions of sea states

Sea State	Wave Conditions(JONSWAP spectrum)	Wind Conditions(IECKAI model)
SS1	H_s =4.55 m, T_p =9.00s, γ =2.45	$\bar{u}$ =11.40 m/s , TI=20.45
SS2	H_s =1.5 m, T_p =6.61s, γ =1	$\bar{u}$ =11.40 m/s, TI=20.45
SS3	H_s =1.25 m, T_p =6.36s, γ =1	$\bar{u}$ =9.18 m/s, TI=22.98
SS4	H_s =1.75 m, T_p =6.86s, γ =1	$\bar{u}$ =12.8 m/s, TI=19.31
SS5	H_s =2.75 m, T_p =7.8s, γ =1.41	$\bar{u}$ =16.8 m/s, TI=17.09
SS1+	H_s =4.55 m, T_p =9.00s, γ =2.45	$\bar{u}$ =11.40 m/s, TI=0
SS2+	H_s =1.5 m, T_p =6.61s, γ =1	$\bar{u}$ =11.40 m/s, TI=0
SS3+	H_s =1.25 m, T_p =6.36s, γ =1	$\bar{u}$ =9.18 m/s, TI=0
SS4+	H_s =1.75 m, T_p =6.86s, γ =1	$\bar{u}$ =12.8 m/s, TI=0
SS5+	H_s =2.75 m, T_p =7.8s, γ =1.41	$\bar{u}$ =16.8 m/s, TI=0

Table 6.4 illustrates the details of the wave condition and wind condition for each sea state. For wave conditions, the JONSWAP spectrum with different parameters is used. Concerning wind conditions, five IECKAI models with turbulence are used for SS1-SS2 (will together be indicated as ‘SSi’’as one icon if necessary hereafter), and SS1+to SS5+(will together be indicated as ‘SSi+’as one icon if necessary hereafter), are the five comparative sea states under the corresponding steady wind of each ‘SSi’.

Once bench tests for the sea states listed in Table 6.4 are carried out, the thrust samples when the motion simulator surges at v2 for the ten different sea states are presented in Figure 6.17. This figure is revealing in several ways. First, unlike in the other sea states with steady wind conditions SSi+, the thrust obtained for sea states with turbulent wind tend to be irregular and random, which proves the effect the turbulence has on the rotor thrust. However, the mean thrust of SS1 seems to decrease a little, compared with that of SS1+, similar drops are also noticed in SS2 to SS5. Hence, it is apparent that the existence of turbulence impacts both the instantaneous thrust and the mean thrust.

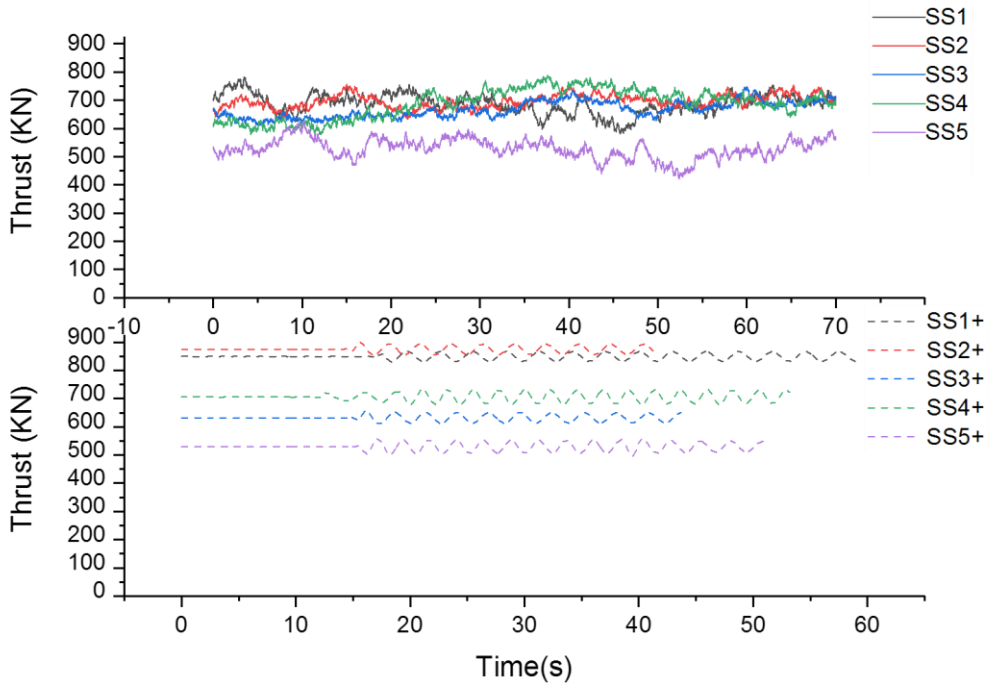

Figure 6.17 Time histories of rotor thrusts under different sea states

Moreover, for SS1 and SS2, the wind conditions are the same, but the different wave parameters are used for generating waves in the basin. As a result, the split-second thrust of SS1 and SS2 give different tracks, but the mean thrust stays almost the same. The difference is insignificant, which might indicate the slight influence the wave conditions have on the rotor thrust. It stands out that the mean thrust increases as the wind speed increases at first, but when it reaches the peak at 12m/s, it starts falling slowly, which tells the wind speed still plays the most significant role in affecting the rotor thrust, though the turbulence has an effect as well. The impact of the wave spectrum on the rotor thrust is reflected, however, it is minimal compared to the effect of wind conditions.

To summarise the results discussion, the testing rig imported a prediction module, which is obtained by deep machine learning and system identification, can predict the rotor thrust depend on the hydrodynamic input. In this validating tests, surge is used to simulate the pitch of the FWOT platform as a real-time input to the AIReaTHM testing rig. The results are given in terms of the AI prediction (which is the output from the AI prediction

module used to drive the fan), and measurement (which is the reading of the load cell after removing the inertial force). The results prove that the innovative AIReaTHM testing rig is capable to be used to provide a reasonably accurate rotor thrust in real-time model test of a FOWT.

6.5 Uncertainty discussion

The factors might cause uncertainty in future industry application (Hywind pilot park):

1) In order to select the most suitable instrumentation system for this experimental study, data input range and accuracy are considered as well as the physical size and weight of the sensors.
2) All components chosen for this study were compact, lightweight and provided high resolution and high data rates. In order to reduce the effect of coupling between the model and the land tri – axial accelerations at the nacelle and the model of center of gravity (CoG) and the fan thrust where transmitted using a high bandwidth wireless telemetry system.
3) failure in accurately predicting the platform behaviour by numerical tools are not avoided for this version of SIL application.

6.5.1 The time difference and the overall uncertainty

The optical measurement system provided the position and attitude of the FOWT at a frequency of 100Hz. The corresponding acquisition system is however running asynchronously, which involves some computational time, so measurements were received with a delay as shown in Figure 6.18. A tiny time delay in a per cycle is observed by comparing the time histories of the thrust measurement and AI prediction. Besides, 800KN residues are noticed now and the residue in Figure 6.18 is obtained by using thrust measurement minus AI prediction thrust.

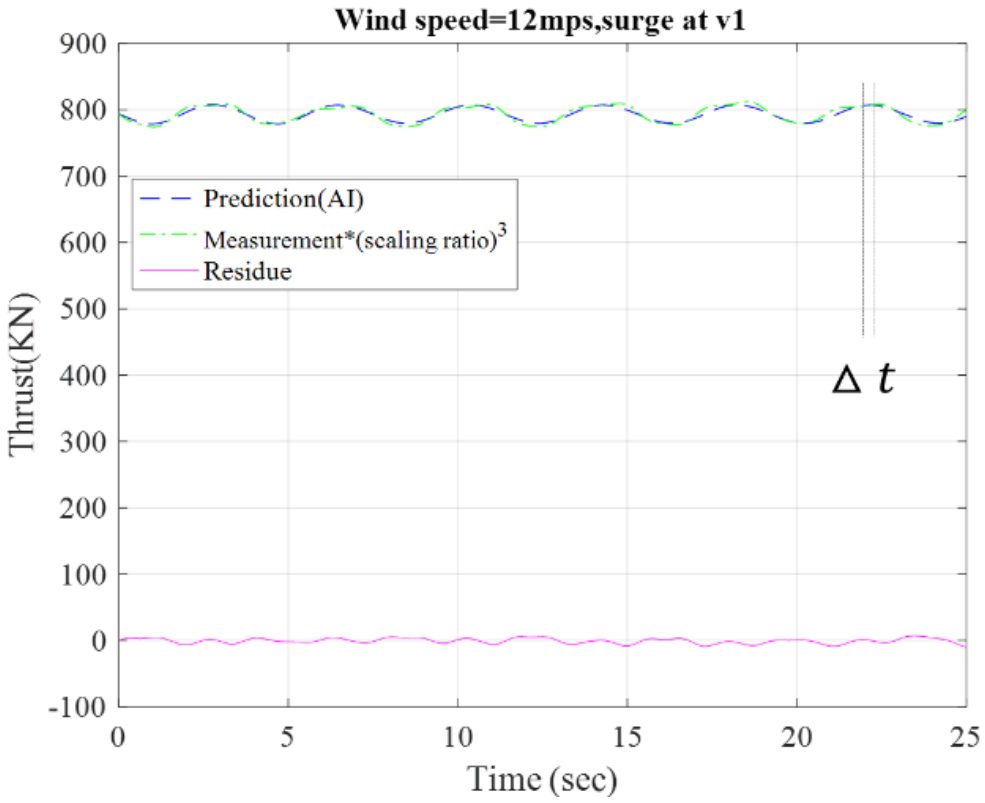

Figure 6.18 Time delay observed per cycle in time histories of the thrust

Figure 6.19 (a) presents the time delays observed in per cycle of one experimental recording (wind speed=8m/s, surge at v2). At the bottom of Figure 6.19 (a), each cycle period from AI prediction is listed. The red boxes stand for time delays between the AI prediction and measurement of rotor thrust. While the blank boxes represent time advances. The time delays are randomly located. For example, for cycle 1, the cycle period from AI prediction is 2.4073ms, however, the period of the first cycle of the thrust measurement is 2.556s. Therefore, there is a time delay represented by red box. Figure 6.19 (a), shows the distribution of the time differences, and periods of each cycle for one bench test, then all the time delays give a mean time delay with a standard deviation for one specific bench test. Then Figure 6.19 (b) summaries all the mean values and standard deviations of time delay for various bench tests. Sensitivity study shows that the time delay is within 0.01s, though it can reaches 0.25s as a maximum, which is rare to happen.

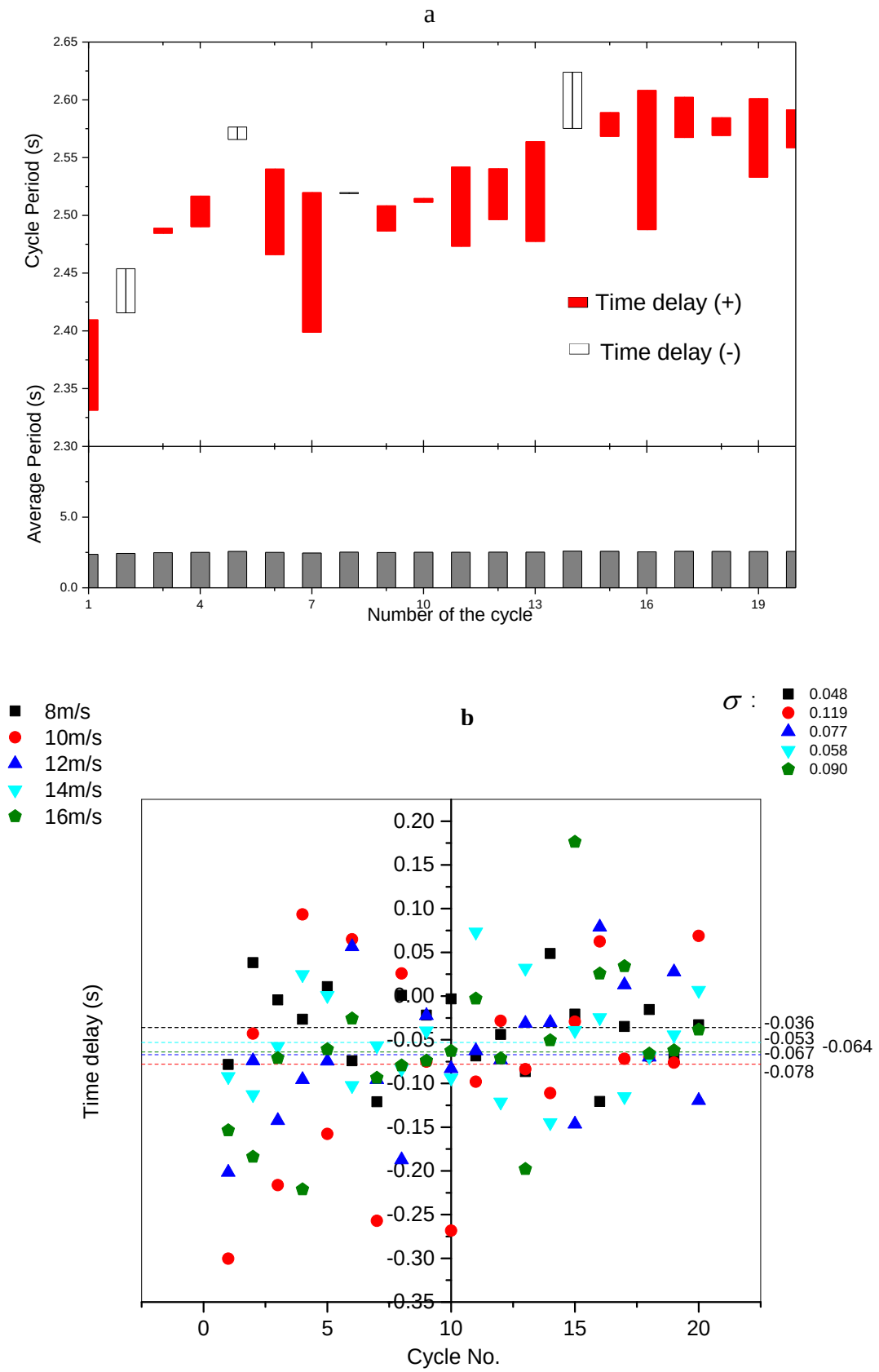

Figure 6.19 (a) distribution of the time difference of one typical test(wind speed =12m/s, surge at 0.557Hz); (b) statistical analysis of time delays of all the tests

As for the overall uncertainty, the rotor thrust is the parameter of interests. It is proven in section 6.1 and 6.2, that the mean values of thrust measurement agree well with its AI prediction under various wind speeds and numerous surge inputs. Therefore, the oscillating components of the thrust are mainly discussed concerning the overall uncertainty. However, it is not possible to use the time history of the residue directly as the uncertainty, due to the existence of the time delay. Thus, the statistical calculations of the time histories for both AI prediction and measurement are used to find the max, min, and mean amplitudes. Hence, the min and max values of per cycle for thrust prediction and measurement at the wind speed of 8m/s, 10m/s,12m/s,14m/s, 16m/s are given in Figure 6.20(a) correspondingly. Particularly, the results for wind speed 8m/s are enlarged as an example to be furtherly explained. What stands out from the enlarged plotting is that the thrust measurements all tend to be bigger than the AI prediction and less stable. This could be attributed by the uncertainties in the components we selected for building up the testing rig. Other experimental results for various wind speeds agree with that point, as observed from Figure 6.20(a).

Similarly, Figure 6.20(b) summarizes the mean score and standard deviation of the overall uncertainty in rotor thrust. It is revealed that AI prediction is quite steady and reasonable, but there is a varying uncertainty in the measurement of the rotor thrust, and it locates in between 5-15KN, which should be resulted from the systematic uncertainty in the testing rig. However, the rotor thrust is distributed from 508 to 795KN, which means the uncertainty is not big enough to affect the dominating results. Thus, this testing approach has been used on a Hywind spar-type FOWT model and a deepCwind type FOWT model in the Kelvingrove hydrodynamic laboratory of Strathclyde University.

a

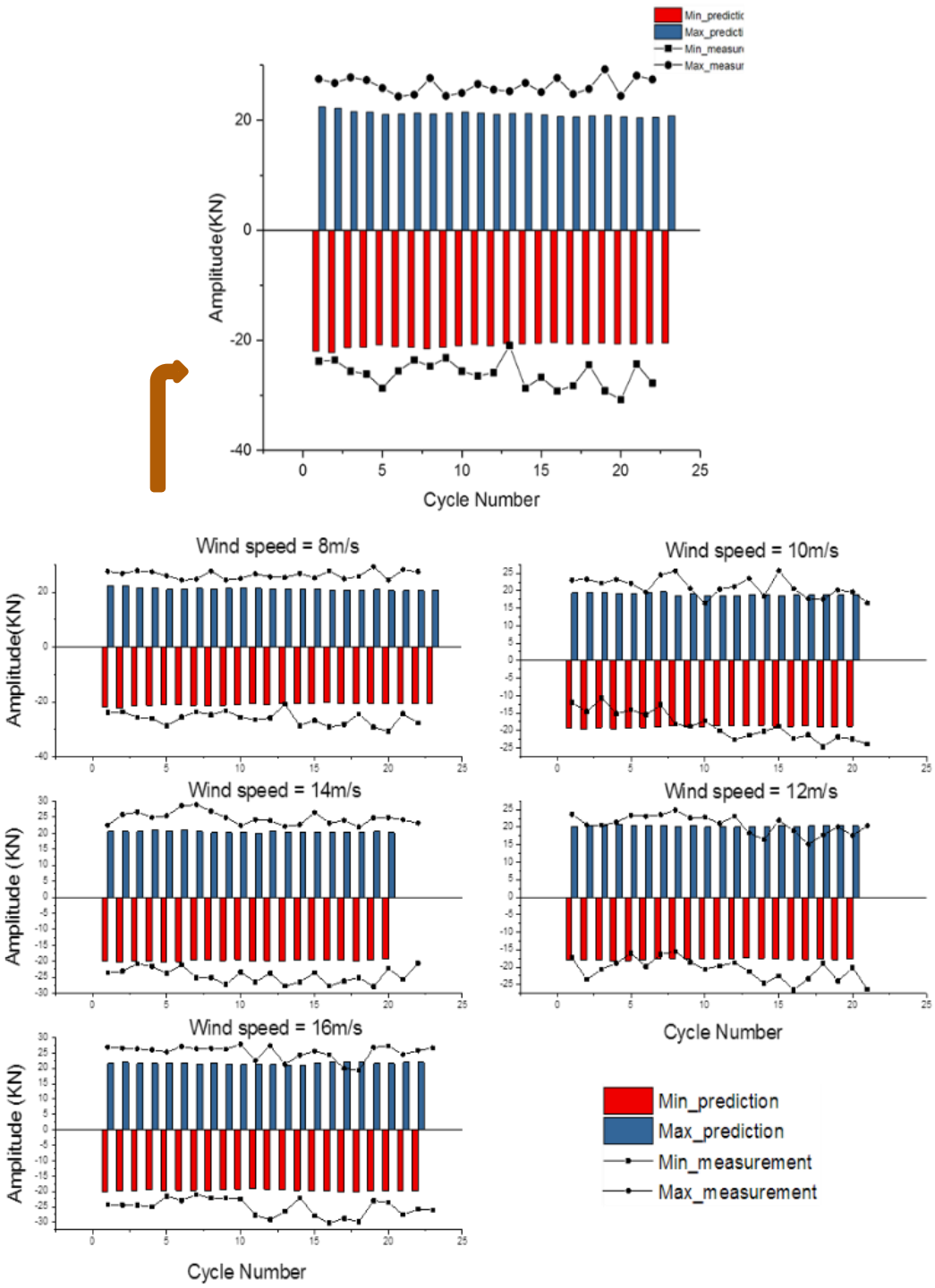
Min_predictic
Max_predicti
Min_measur
Max_measur
Amplitude(KN)
Cycle Number
Wind speed = 8m/s
Wind speed = 10m/s
Wind speed = 14m/s
Wind speed = 12m/s
Wind speed = 16m/s
Amplitude (KN)
Cycle Number
Min_prediction
Max_prediction
Min_measurement
Max_measurement

b

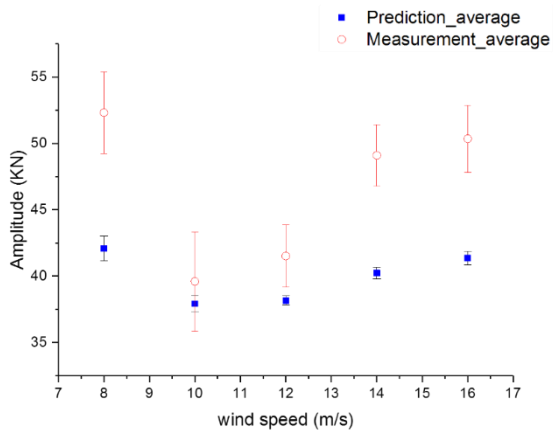

Figure 6.20 (2)Distribution of the overall uncertainty for different wind speeds;(b)statistical analysis of the overall uncertainty

6.5.2 THE UNCERTAINTY CAUSED BY THE OPTICAL MOTION CAPTURE SYSTEM

a

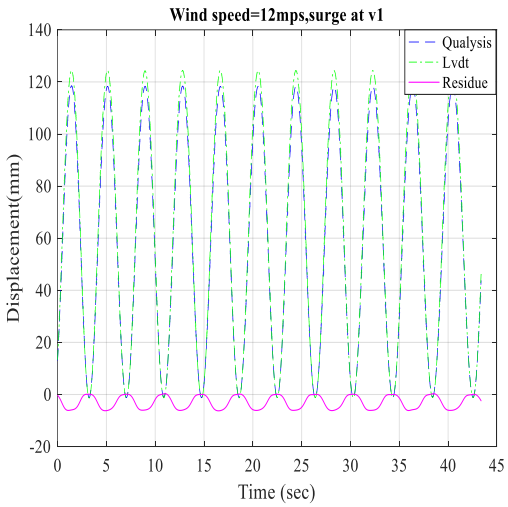

b

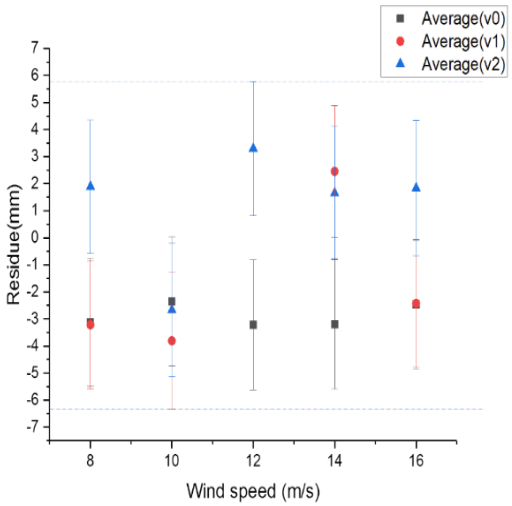

Figure 6.21 Uncertainty caused by Qualysis system.

The details of the uncertainty caused by the optical motion capture system are given in this section. As shown in Figure 6.21 (a), the LVDT measurement is used to be diminished from the Qualysis measurement, then the left residues are the pink line. The most interesting aspect of this graph is that the residue shows a sinusoid trajectory. Moreover, after gaining the mean scores and standard deviation of the resides, the

uncertainty of the Qualysis system is proven located in ± 6 mm. It is reasonable to claim uncertainty in motion capture it is the main uncertainty source, because the four-fifth inputs of the prediction module are based on the reading of the motion capture system.

6.6 Summary

This chapter sets out to develop and validate an AI-based real-time hybrid testing approach which enables the accurate experimental research of floating wind turbines. It has introduced the working principle regarding the software part and instrumental part. After calibration tests on the main components of the experimental platform, bench tests of the AIReaTHM testing method are carried out. The results discuss the presence of the initial force in the load cell at first. Afterwards, the measurements after removing the initial force are used to validate the testing approach, and the experimental measurements agree well with the AI prediction of the rotor thrust. The most significant output from this research are as follows:

- An AI-based hybrid testing rig is developed and validated. It is proven that the testing rig is able to provide a real-time rotor thrust with reasonable accuracy.
- The effect of the surge inputs of the testing rig on the targeted thrust is discussed
- The effect of different sea states, particularly different wave spectrum and wind models on the targeted thrust is analysed
- The time delay in the testing system is identified, it is within 0.1s, and the overall uncertainty from the testing rig is 5-15KN (the minimum rotor thrust is 508KN) when compared to the AI prediction
- The uncertainty in the optical motion capture system is ± 6 mm.

7 Model tests of a spar-type FOWT with the AIReaTHM testing rig

This chapter is organised as follows. At first, the 1/73 model of a spar-type FOWT is described, as well as the scaling laws used to obtain the parameters of interests at model scale. Secondly, the preparation for model tests in the tank, including experimental set-up and necessary calibrations are given, such as the tank details, facility installation, the location of the model, calibration tests and results of wave makers, wave probe, motion capture system and accelerometer. Thirdly, the free decay tests are carried out under two rotor thrust conditions, and in six degree-of-freedom motions. Besides, the natural frequencies for motions in six degree-of-freedom are obtained for the two testing modes, as well as compared to eigenanalysis results. In Section 7.4, the test arrangement, as well as the procedure of one typical experiment, are demonstrated. Section 7.5 discusses the testing results of regular wave tests in four ways:1) Performance of the rotor thrust under different wave frequencies, 2) Performance of the rotor thrust under different wind speeds, 3) Hydrodynamic response of the model under different wave frequencies and wind speeds, 4) Hydrodynamic response of the model in the cases used for comparison. Likewise, the discussion on testing results of irregular wave tests are given in two ways in Section 7.6: 1) Performance of the rotor thrust under various realistic environmental conditions, 2) Hydrodynamic response of the model under different experimental conditions. Finally, a summary is presented in Section 7.7.

7.1 Model description

Traditionally in a hydrodynamic tank, to assure the model tests be performed such that model and full-scale ships or structures exhibit similar behaviour, i.e. the results for the

model can be transferred to full scale by a proportionality factor. (We indicate in the following the model by the index m and the full-scale counterpart by the index s.). Geometrical similarity, kinematical similarity, and dynamical similarity are distinguished. For example, geometrical similarity means that the ratio of a full-scale 'length' (length, width, draft etc.) L_s to a model-scale 'length' L_m is constant, namely the model scale λ. Because the aerodynamic forces are obtained in a full-scale wind field in the AI machine (which is the SIL application for FOWTs), then other parts considered in the model tests of a spar-type FOWT are obtained by following the Froude scaling law, and the multipliers between full-scale and model-scale physical parameters are listed in Table 7.1.

Table 7.1 Model scaling laws

Quantity	Examples	Multiply full scale value by
Mass	Device mass	$\frac{\rho_m}{\rho_s \lambda^3}$
Length	Device length: all dimensions; surge, sway, heave, absolute and relative displacements; wave amplitudes and lengths; significant wave height	$\frac{1}{\lambda}$
Time	Wave and motion periods, run time, interval between events, modal wave period, mean zero crossing period etc.	$\frac{1}{\sqrt{\lambda}}$
Velocity	Device speed; surge, sway, heave, absolute and relative motion velocities; wave celerity and group velocity.	$\frac{1}{\sqrt{\lambda}}$
Acceleration	Surge, sway, heave, absolute and relative accelerations;	1
Angle	Roll, pitch and yaw angles; heading, stabiliser and rudder angles, phases	1
Angular velocity	Roll, pitch and yaw velocities; stabiliser and rudder rates	$\sqrt{\lambda}$
Angular acceleration	Roll, pitch and yaw accelerations;	λ
Pressure and stress	Hydrostatic pressure; dynamic pressure; stress	$\frac{\rho_m}{\rho_s \lambda}$
Frequency	Wave and encounter frequencies; turbine revs.	$\sqrt{\lambda}$
Force	Exciting force; shear force; tension; weight; thrust	$\frac{\rho_m}{\rho_s \lambda^3}$

Moment	Exciting moment; bending moment; torsional moment; torque	$\frac{\rho_m}{\rho_s \lambda^4}$
Inertia	Mass moment of inertia, roll inertia, pitch inertia, yaw inertia	$\frac{\rho_m}{\rho_s \lambda^5}$

We use a 1:73 model of a spar-type FOWT(see Figure 7.1), a physical model is constructed following Froude scaling laws. The measurement comes by measuring the physical model, before putting it into the towing tank, and they are listed in Table 7.1.Finally, the difference between the targeted and measured parameters of the model is given in term of a percentage of the targeted one.

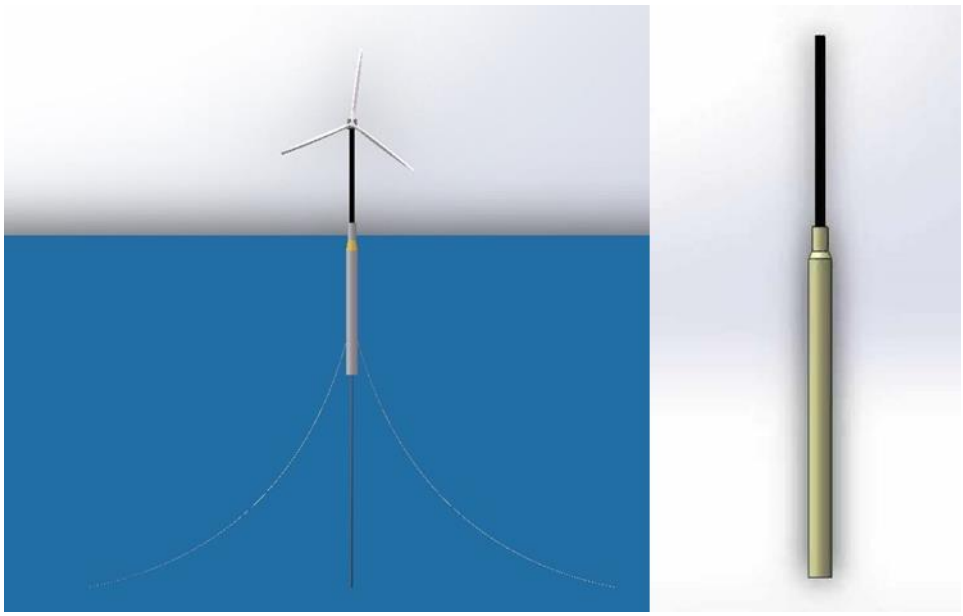

Figure 7.1 3-dimensional modelling of the full-scale spar-type FOWT and the spar

Table 7.2 Properties of the spar（λ =73)

Description	Measurement of model
Water depth	2.3m(maximum of the tank capability)
Rotor mass Hub mass Blade mass Nacelle mass	Replaced by a fan and the holder (1.124kg)
Tower height	1.08m

Tower top diameter	60mm
Platform length	1.8m
Platform top (Tower base) diameter	89mm
Platform base diameter	128mm
Draft with mooring lines (from bottom)	1.64m

As shown in Figure 7.2, the spar, which can be moored by catenary or taut lines, achieves stability by using ballast to lower the centre of mass (CM) below the centre of buoyancy (CoB). However, in current research, a soft mooring strategy is adopted in the tank for the spar-buoy. Traditionally, the centre of gravity (CG), as well as moment of inertia, should be determined by KG test prior to tank tests.

a b

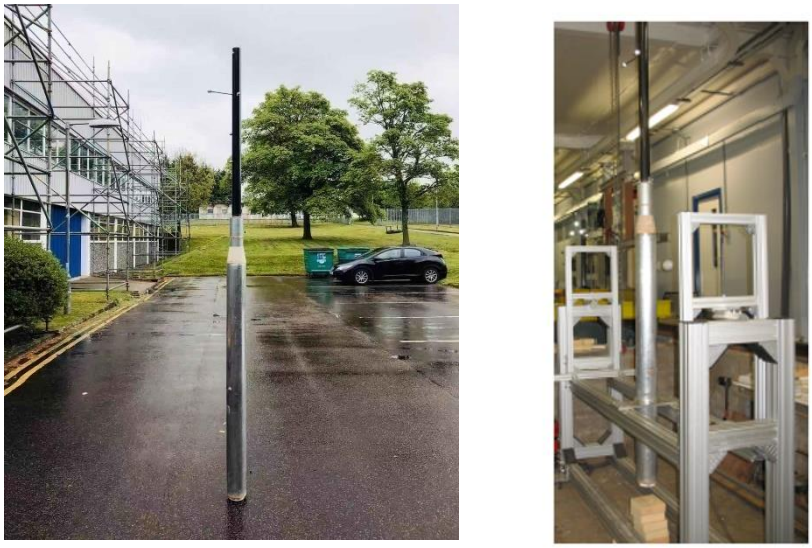

Figure 7.2 Model of the spar including the tower

Therefore, as shown in Figure 7.2(b), KG test of the model is carried out by a specialised swing system, which contains a frame and swing on which weights are placed. A probe sensor is used to detect the variation in inclination under a certain of weight, while the collar is securing the model into place on the swing. For example, if a weight of 0.5kg is placed on one side of the swing, the model will incline a certain degree to the side, then the inclination is detected by the probe sensor. The same test procedure is carried out for

both sides, and the average incline angle is used for calculation. In this way, the inertia is then obtained by giving the swing and collar an angular velocity and measuring the period, with the model in place. After removing the influence of the inertia of swing and collar, it is concluded that the inertia of the model itself is 11.28 kg*m^2. Furthermore, the COG of the model is 0.52m (it is assumed that the vertical centre of the gravity is the COG). The CG of the model, including the tower, is measured as 0.52m from the bottom.. The inertia of the total system including platform, ballast, tower, nacelle and rotor, is listed in the second column of Table 7.3.

Table 7.3 Results of the KG test

Description	Measured
Roll inertia	11.28 kg*m^2
Pitch inertia	11.28 kg*m^2
Yaw inertia	—
Overall centre of gravity (CG) from bottom	0.52m

7.2 Preparation for model testing

7.2.1 Experimental set-up

Model tests discussed in this thesis, are carried out in Kelvin Hydrodynamics Laboratory at the University of Strathclyde. The tank is 76m long, 4.6m wide, 2.5m deep, and it is equipped with four-paddle active-absorbing wavemakers, as shown in Figure 7.3. The wake makers can move vertically to adjust to water depths from 1.6m to 2.3m and generate either regular or irregular waves. Besides, an absorbing beach is constructed to reduce the influence of reflecting waves. The model is placed in the centre of the tank.

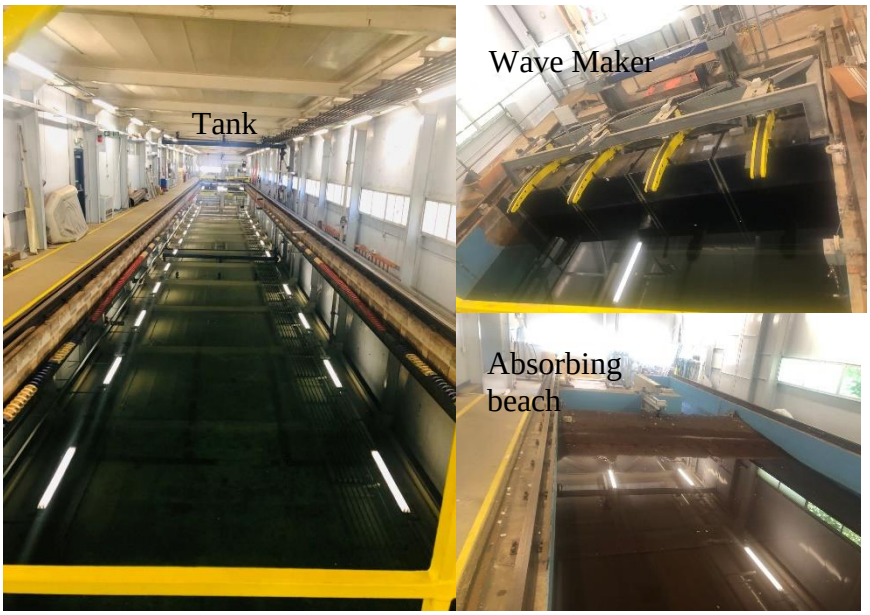

Figure 7.3 Facilities of the towing tank at the University of Strathclyde

As demonstrated in Chapter 5, the motions of the spar-buoy are captured by an optical motion capturing system Qualysis, and the install positions of the four cameras are given in Figure 7.4. Another wireless filming camera is used to record the performance of the model in the water for each test. The Qualisys markers are placed randomly along the spar-buoy. The wave probe is installed by hanging onto the yellow pedestrian bridge. Moreover, all the electrical parts are located on the monitoring deck. Afterwards, before formal tests, necessary calibrations, including calibration of accelerometer, wave probes, and waves, are carried out.

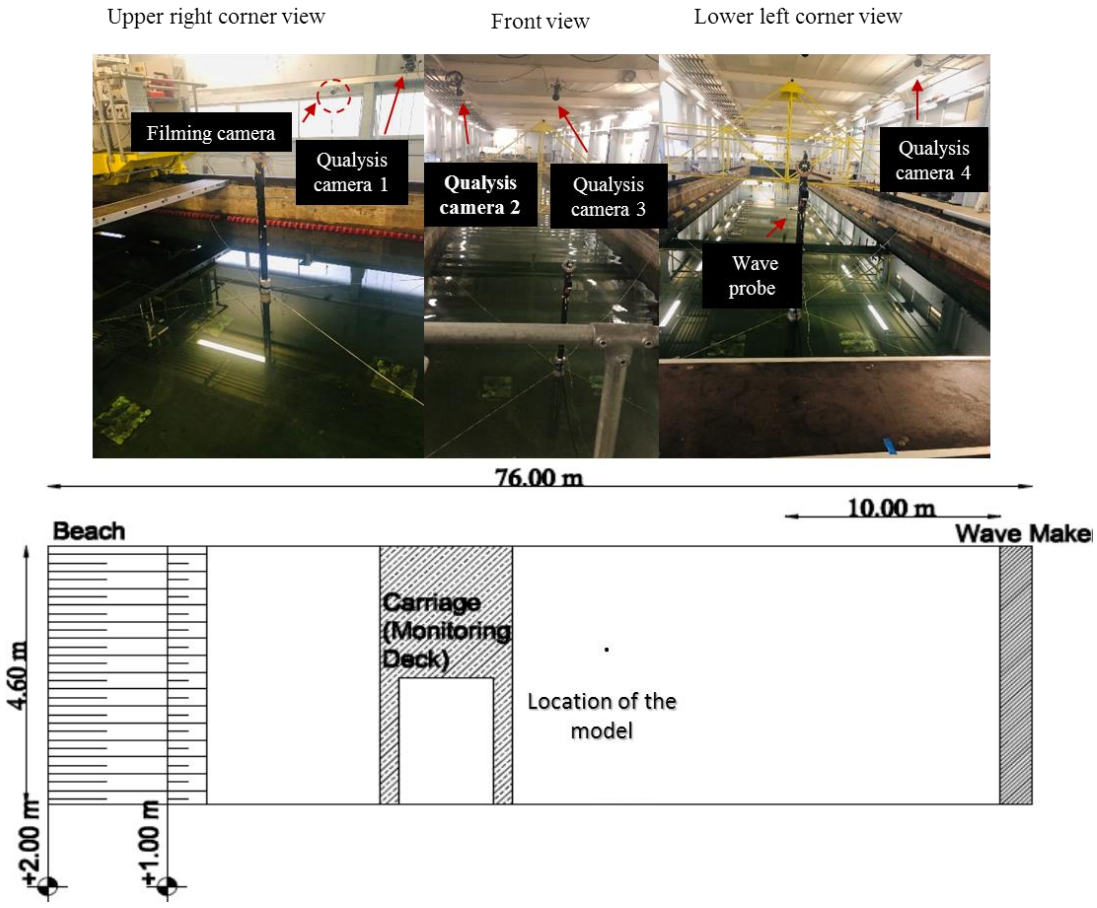

Figure 7.4 Experimental set-up of the model

7.2.2 CALIBRATIONS BEFORE MODEL TESTS

The Accelerometer is placed at the top of the spar-buoy, and it is calibrated by controlling the spar to tilt at known angles, and a linear relationship between the signal voltage and the physical acceleration is obtained, while the residues are within 0.06 m/s^2. Then the calibration of the wave probe is implemented, and details of the procedure have been given in Chapter 3. The calibration result of the wave probe before tank tests is shown in Figure 7.5.

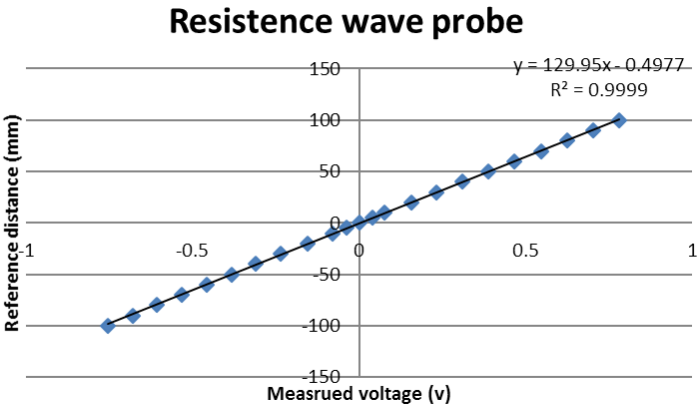

Figure 7.5 Calibration result of the wave probe

Prior to running the model tests, wave calibration is required to assure the effectiveness of the wave spectrum to be used. Therefore, a wave probe is sited at the centre of the model location in place of the model to record the wave data. As demonstrated in Chapter 5, five sea states are considered in this research, and the power spectral density (PSD) of the wave spectrum used in each sea state is obtained and compared with the theoretical one targeted at, as shown in Figure 7.6. It is seen that the energy spectrum agrees well with the target JONSWAP spectrum.

Table 7.4 Wave calibration results

	SeaState ID	SS1	SS2	SS3	SS4	SS5
Full scale	Tp (s)	6.36	6.61	6.86	7.8	9
	Hs (m)	1.25	1.5	1.75	2.75	4.55
	γ	1	1	1	1.41	2.45
Target model scale	Tp (s)	0.739335	0.768397	0.797459	0.906732	1.046229
	Hs (m)	0.016892	0.02027	0.023649	0.037162	0.061486
	γ	1	1	1	1.41	2.45
Synthetic	Tp (s)	0.705	0.7327	0.7604	0.8828	1.0341
	Hs (m)	0.0165	0.0198	0.0232	0.0367	0.0611
	γ	1	1	1	1.41	2.45
Measured	Tp (s)	0.6908	0.6911	0.7311	0.8501	1.0105
	Hs (m)	0.0161	0.0196	0.023	0.0354	0.0605
	γ	1	1	1	1.41	2.45
relative difference in Hs (compared with target)		-5%	-3%	-3%	-5%	-2%
relative difference in Hs (compared with synthetic)		-2%	-1%	-1%	-4%	-1%

The wave spectrum is generated by specifying Tp, Hs and γ in the JOHNSWAP spectrum formula. A time history of the generated spectrum can be described numerically, and the synthetic parameters are obtained by spectrum analysis of the numerical time history of the generated spectrum. All the parameters for each sea state in term of full-

scale, model-scale, numerical synthetic, and experimental measurement are listed in Table 7.4. All of the plots show similar trends which indicate that the waves have the correct statistical properties.

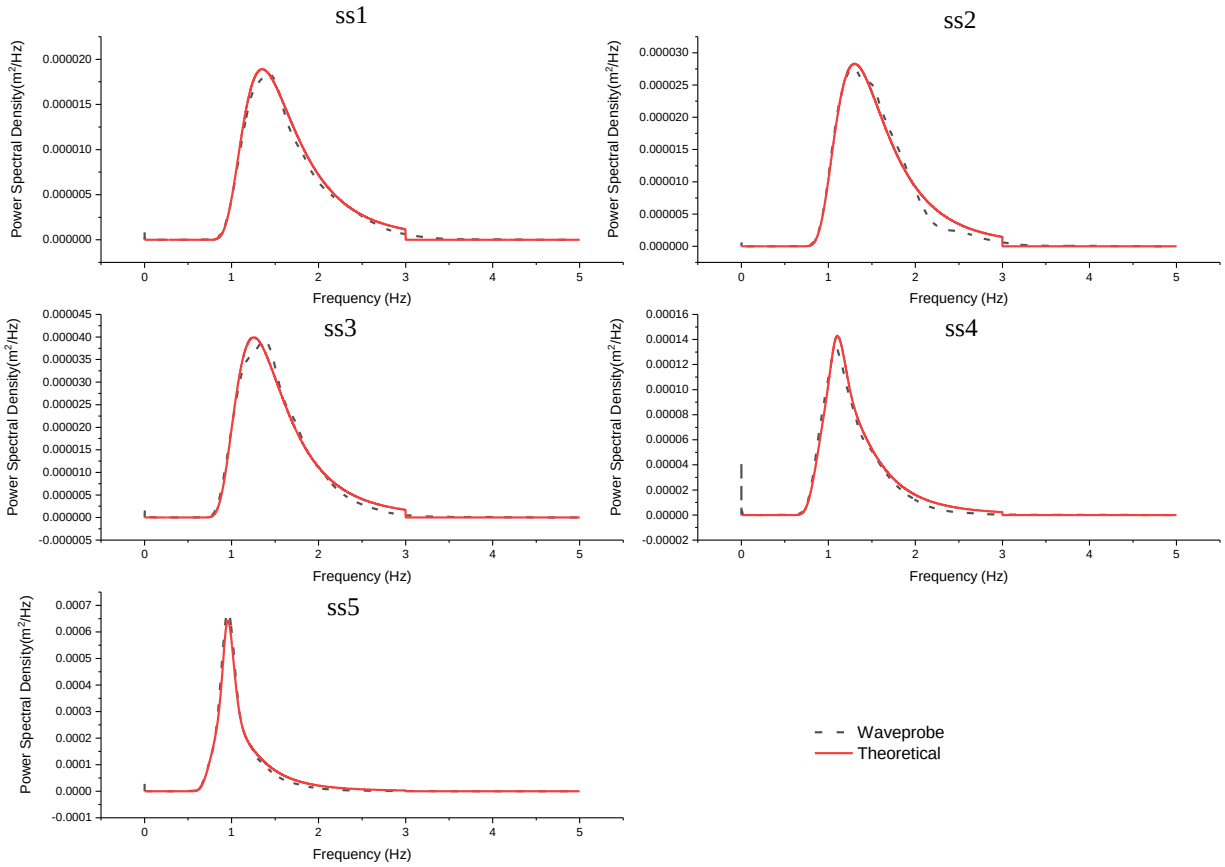

Figure 7.6 PSD analysis of the generated and targeted wave spectrums

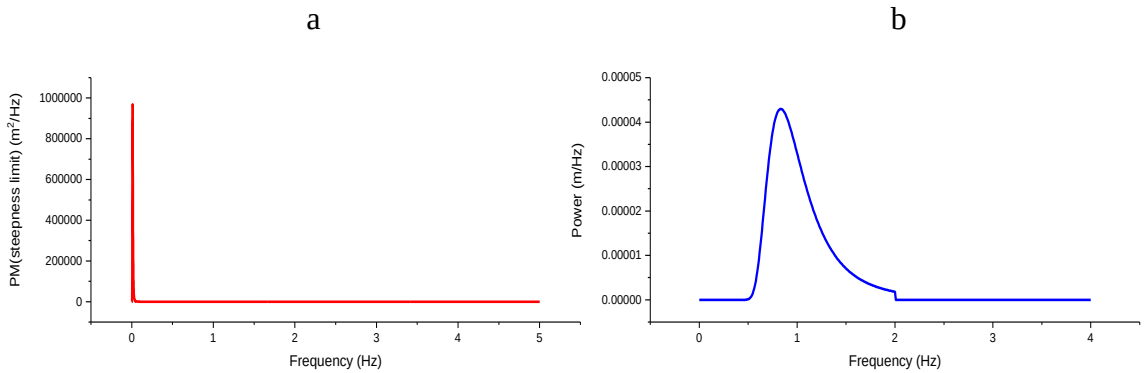

Figure 7.7 PM limit and wavefront

The Pierson-Moskowitz (PM) steepness limit (Figure 7.7 (a)) is used during the wave specification process as a reference, the resulting wave may break if the PSD exceed the PM steepness limit. However, none of the five sea states exceeded the PM steepness limit. Finally, the wavefront of one typical run is given in Figure 7.7(b), and it is noticed the power decrease to zero fast when the wave frequency is above 2 Hz, this is because the wave makers stop working when the targeted wave frequency is above 2Hz.

7.3 Free decay tests

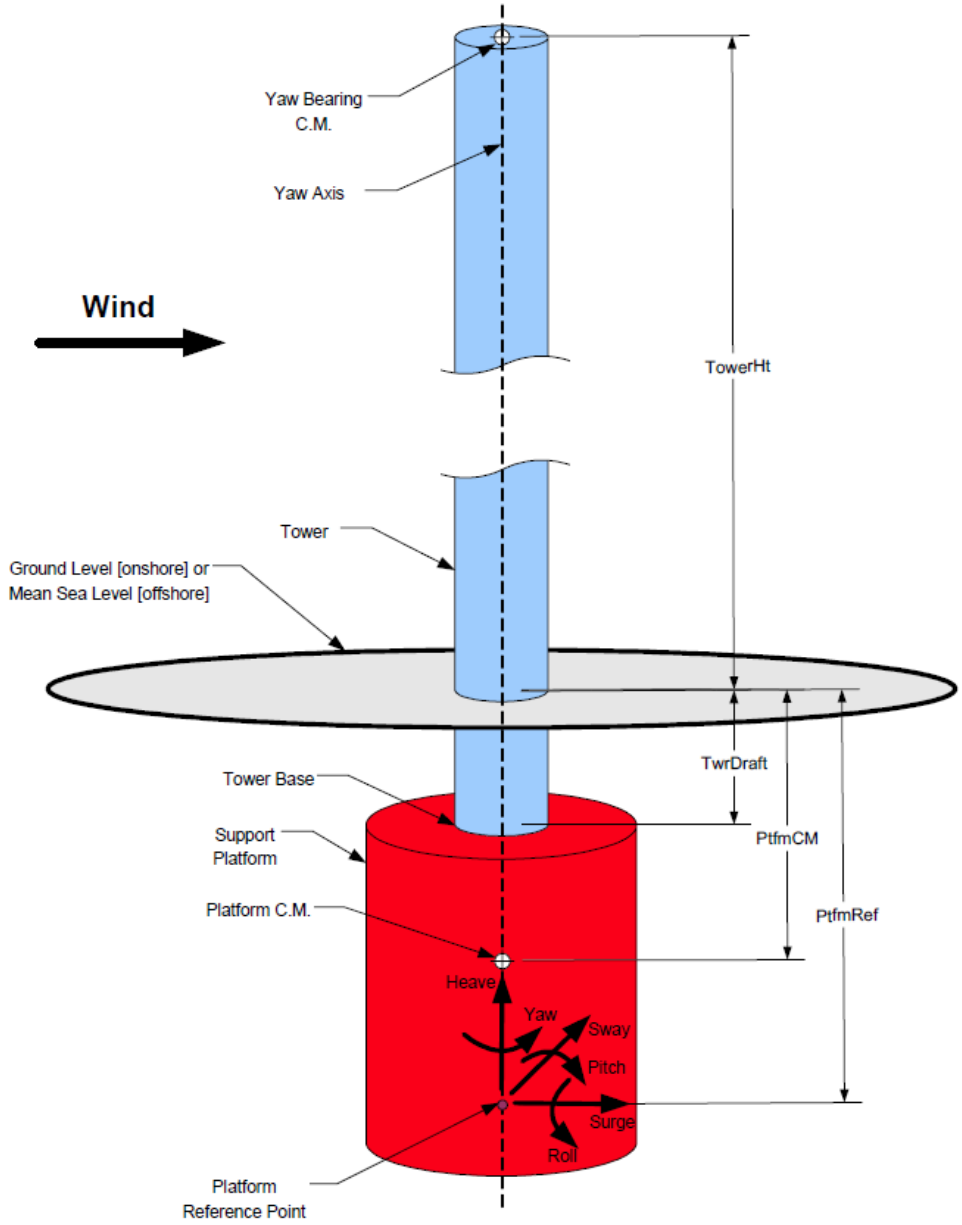

Figure 7.8 Motions in six-degrees of the spar-buoy[107]

The natural frequencies are essential parameters that affect the dynamic behaviour of FOWTs. Therefore, six sets of free oscillation tests in six degree-of-freedom are carried out to find the natural frequencies of the model under two wind conditions (zero rotor thrust, 800KN constant rotor thrust). 18 tests are carried out, and the qualified tests are selected as listed in Table 7.5. For each test, the spar-buoy is displaced and carefully released in the corresponding motion (Pitch, Surge, Sway, Heave, Yaw, Roll). Moreover, the six degree-of-freedom motions are defined as follow:

Table 7.5 Test matrix of free decay tests

	Motion	**Pitch**	**Surge**	**Sway**	**Heave**	**Yaw**	**Roll**
Zero	Test ID	FD001	FD006	FD008	FD010	FD012	FD014
Constant	Motion	Pitch	Surge	Sway	Heave	Yaw	Roll
800KN	Test ID	FD002	FD007	FD009	FD011	FD013	FD015

7.3.1 NATURAL FREQUENCY UNDER NO ROTOR THRUST (ZERO THRUST)

At first, the analysis results of other test IDs for free decay in other five degrees are given in Appendix 4. As one standard discussion, the testing result of contained in one free decay testing file FD001 is given in Figure 7.9. It is obvious tne typical free decay test is repeated three time by placing the platform with an initial pitch degree. three typical free decay tests are obtained during experiment FD001. The analysis results of other test IDs for free decay in other five degrees are given in Appendix 4 Hence, the motion response in six degree-of-freedom of one typical free decay test is zoomed in. Afterwards, Fast Fourier transform is used convert six signals of the motions in time domain to frequency domain to obtain spectral analysis. Though there are two peaks of the spectrum in surge and sway, the six motions all find a peak at around 0.3 Hz (which is the mean value of the x coordinate values of peak points). Therefore, it is concluded that the natural frequency of the model under free decay in platform pitch is 0.3Hz. Then, the same analysis procedure is used on the free decay in other five platform motions, in order to find the natural frequency of the model under free decay in different motions. Besides,

the two-peak phenomenon of surge and sway spectrum may be caused by the interaction with heave motion.

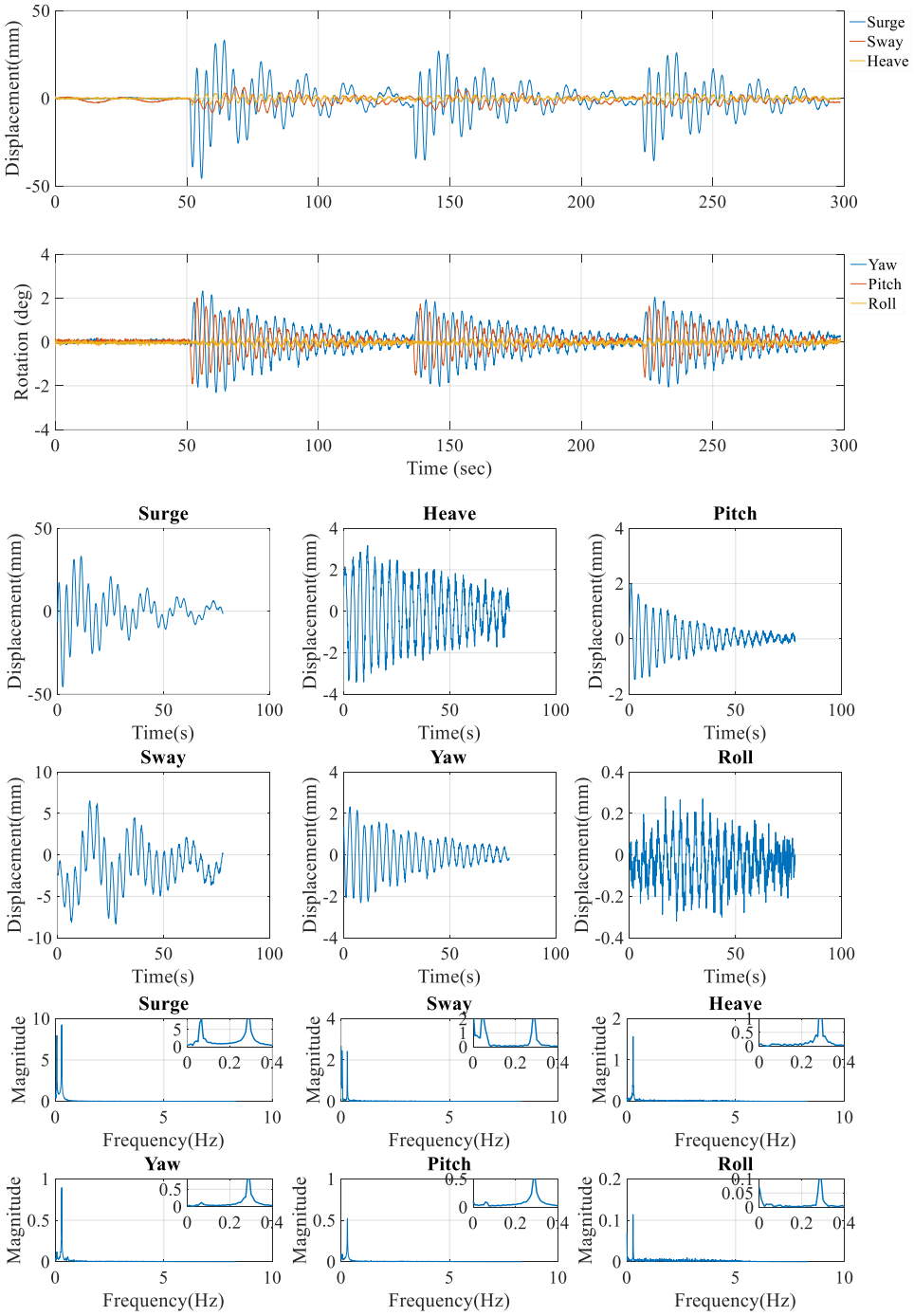

Figure 7.9 Free decay in platform pitch and the FFT of signals of the motions in six degree

For free decay in platform surge, it becomes difficult to impose a sufficient initial displacement without exciting motion in other degrees, and the oscillation decays very fast. Therefore, the FFT of one typical free decay test cannot show pronounced peaks, as

presented in Figure 7.9. However, it also can be concluded that the natural frequency of the model under free decay in surge is 0.08 Hz. Because the FFT of the other five motions tends to reach a peak at 0.08 Hz, except in heave (Figure 7.10).

For a spar-type FOWT, sway and surge should show a similar response theoretically. Furthermore, Figure 7.11 reveals that the FFT peaks of five motions are likely to fall at 0.08Hz. Hence, the natural frequency of the model under free decay in sway is also 0.08 Hz. Similar to free decay in the surge, it is also challenging to implement the free decay in platform sway without exciting other motions; therefore, the spectrum obtained by FFT is more extensive than in other cases. Free decay in platform heave is presented in the same manner. As shown in Figure 7.12, at first, time histories of the six motions of FD010 are given. Then the zoom-in of the six motions of one typical free decay is given. Then the FFT is used on the six time-domain signals, as the peaks of the FFT in six motions agrees, the natural frequency of the model under free decay in platform heave is 0.3 Hz, too. Likewise, the free decay test and analysis results for platform yaw, roll are given in Figure 7.13, Figure 7.14 respectively. Moreover, the natural frequency is obtained in the other two motions are both 0.3Hz. In summary, the natural frequency of the model under free decay in surge and sway is 0.08Hz, and for other motions are 0.3 Hz.

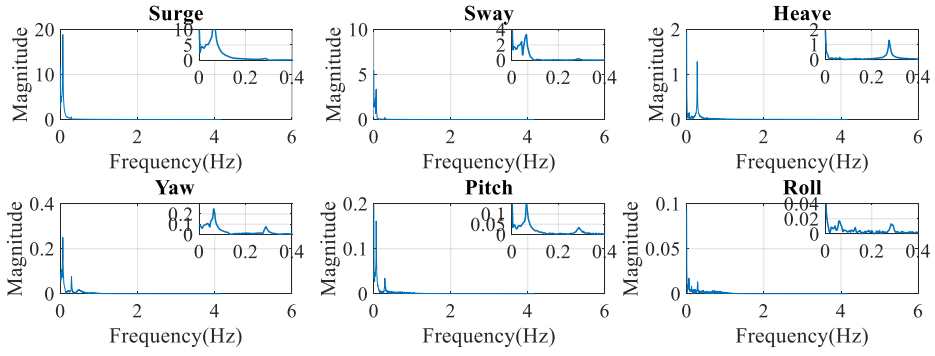

Figure 7.10 FFT of free decay in platform surge under zero thrust

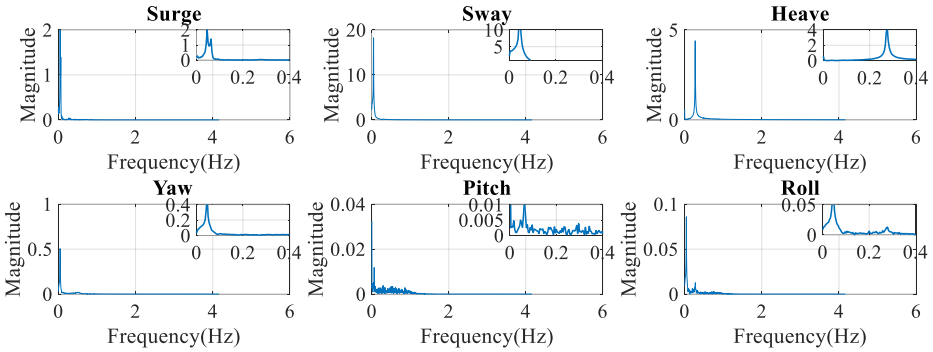

Figure 7.11 FFT of free decay in platform sway under zero rotor thrust

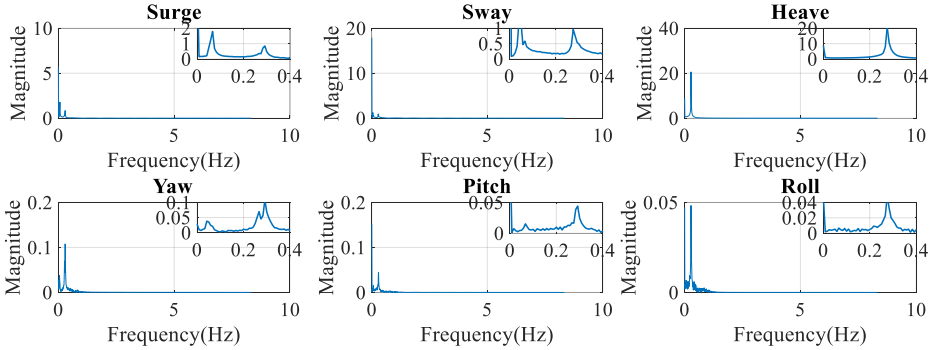

Figure 7.12 FFT of free decay in platform heave under zero rotor thrust

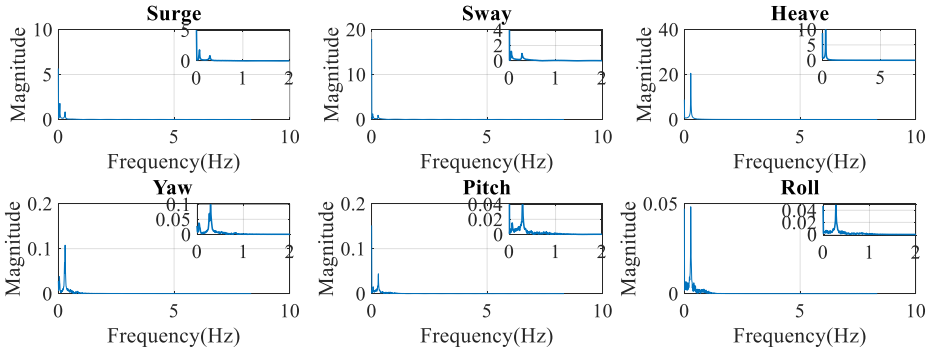

Figure 7.13 FFT of free decay in platform yaw under zero thrust

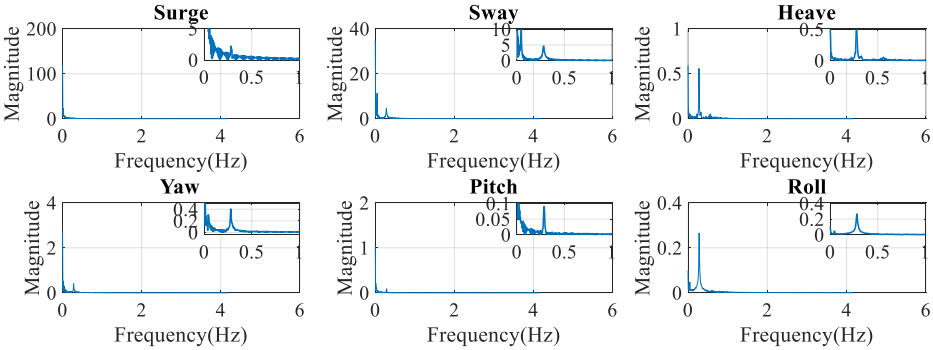

Figure 7.14 FFT of free decay in platform roll under zero thrust

7.3.2 NATURAL FREQUENCY UNDER A CONSTANT ROTOR THRUST

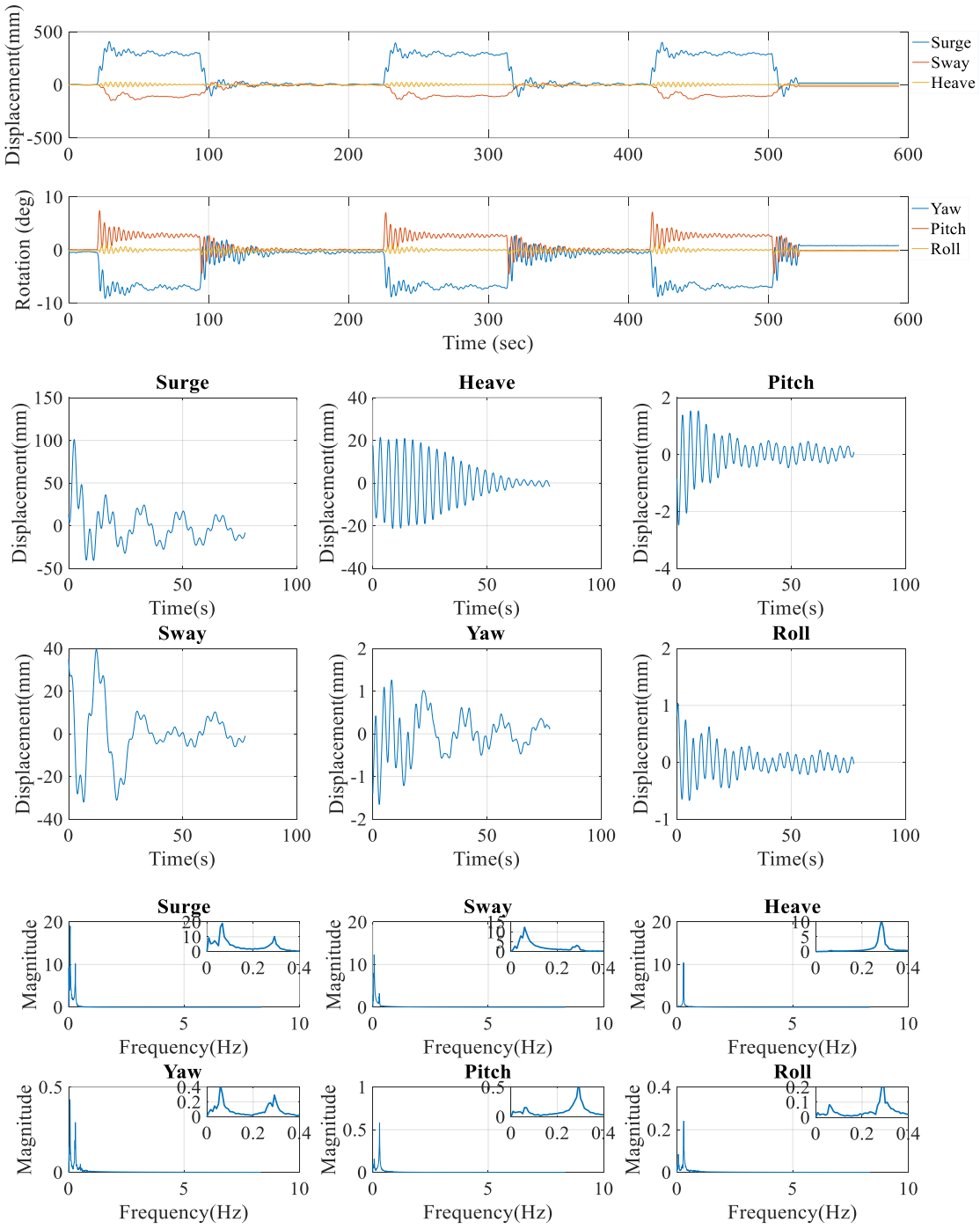

Figure 7.15 Free decay in platform pitch under a constant rotor thrust

In order to verify the natural frequencies obtained above, a series of free decay tests in six-degrees-of-freedom under a constant 800KN rotor thrust are carried out, and the complete analysis results including free decay in all six-degrees-of-freedom are given in

Appendix 4. Also, the free decay tests are exactly implemented in the same manners, except a constant rotor thrust is applied on the top of the spar-buoy by a rotating fan.

Likewise, taking the free decay in platform pitch under a constant rotor thrust (Figure 7.16) for an example(free decay details for other motion tests can be found in), the time histories of the motion in six-degrees-of-freedom for three free decay tests under a constant thrust are given at first. It is obvious that surge, heave, pitch and yaw reach a mean displacement or angle where starts the free decay, due to the existing of the constant rotor thrust. This differs from the free decay under no thrust in which mean values of the displacements or angles are zero. However, after removing the mean values from the oscillation, these free decays under the 800KN rotor thrust show similar behaviour as those under no thrust. Then the free decay of the six motions after removing the mean score is zoomed in for further observation. By comparing with the motion response under free decay shown in Figure 7.9, it is noticed that the motion free decay tends to become faster than in the cases without a rotor thrust. The FFT of surge, sway, yaw, pitch and roll all show dual-peak feature, but, in Figure 7.9, only surge and sway show dual-peaks. Thus, it might be difficult to conclude which is the natural frequency 0.08Hz or 0.3 Hz, if only looking at the dual-peaks of surge, sway, yaw, pitch and roll. However, the FFT of heave shows only one peak at 0.3 Hz. Hence, the natural frequency in pitch should be 0.3 Hz based on the principal of minority obeying majority under free decay in platform pitch with a constant rotor thrust.

Similarly, as shown in Figure 7.16, surge, heave, pitch and yaw reach a mean score displacement or angle, and they start the free decay there. However, the motion response zoom-in of one typical free decay after removing the mean score shows quite similar decay trends as those for the corresponding case without a rotor thrust. Though the FFT of heave, pitch and roll show dual-peak feature, it is still easy to conclude that the natural frequency is 0.08Hz under free decay in platform surge. As discussed above, for a spar-

type FOWT, sway and surge show the same response, with or without a constant rotor thrust. As given in Figure 7.17, it can be inferred that the natural frequency under free decay in platform sway is also 0.08 Hz. For free decay in platform heave, yaw and roll, the testing and analysis results of FD011, FD013, FD015, are given in Figure 7.18 to Figure 7.20 correspondingly. For those cases, it is easy to find out the natural frequency is 0.3 Hz.

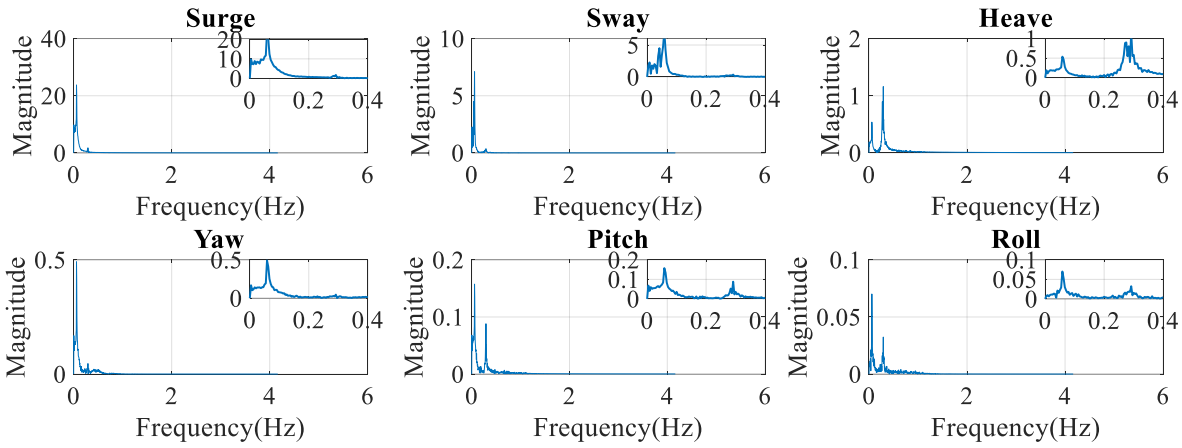

Figure 7.16 FFT of free decay in platform surge under a constant rotor thrust

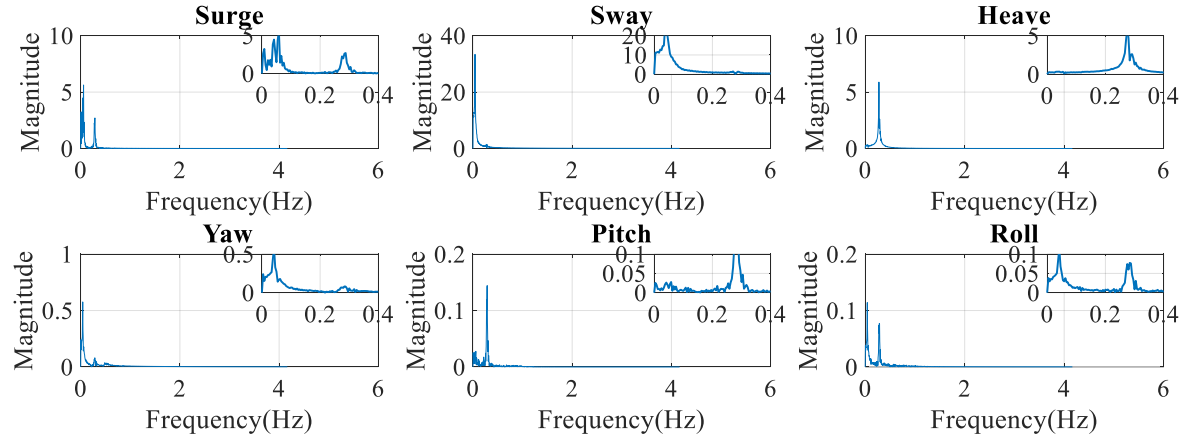

Figure 7.17 FFT of free decay in platform sway under a constant rotor thrust

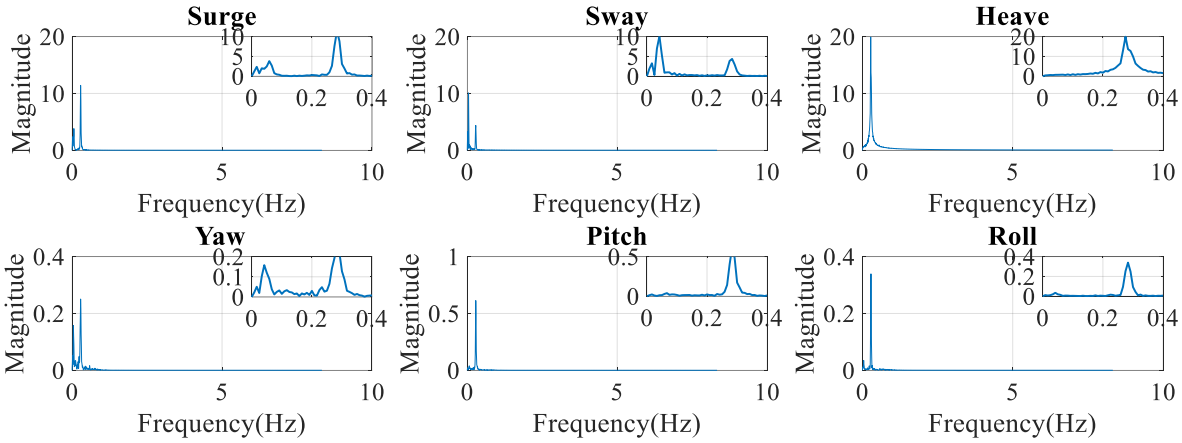

Figure 7.18 FFT of free decay in platform heave under a constant rotor thrust

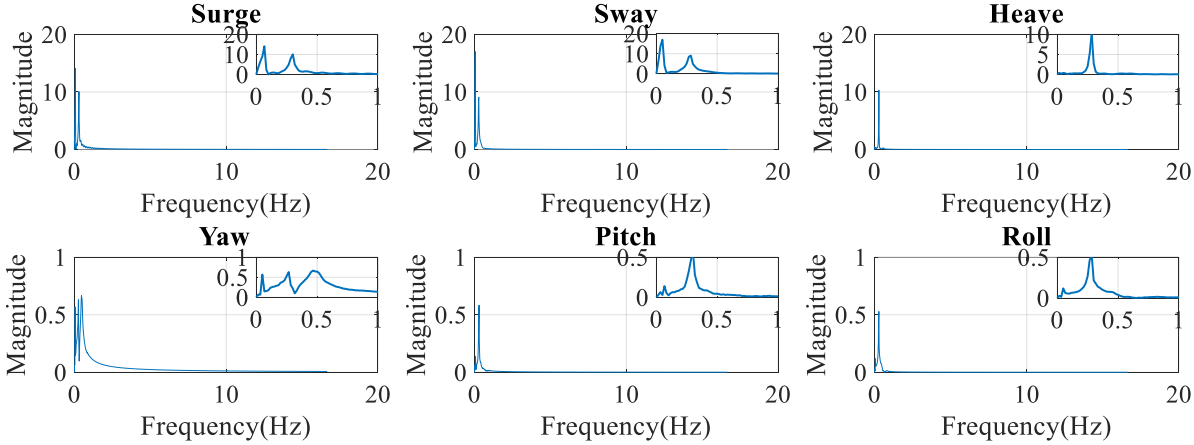

Figure 7.19 FFT of free decay in platform yaw under a constant wind speed

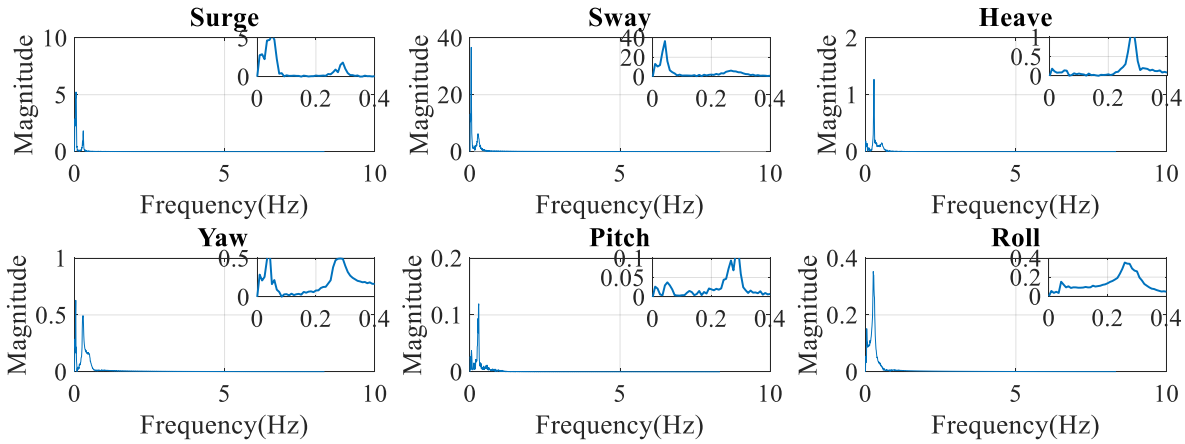

Figure 7.20 FFT of free decay in platform roll under a constant wind speed

7.3.3 COMPARING THE PLATFORM NATURAL FREQUENCIES UNDER TWO TESTING CONDITIONS

The natural frequencies obtained under two different testing conditions tend to agree with each other, as shown in Table 7.6.

Table 7.6 Natural frequencies of the six degree-of-free dom free decay under two testing conditions

Natural frequency(Hz)	Surge	Sway	Heave	Pitch	Yaw	Roll
Free decay under no rotor thrust	0.08	0.08	0.29	0.31	0.30	0.32
Free decay under constant rotor thrust	0.08	0.08	0.29	0.30	0.31	0.27

7.4 Test arrangement and experimental procedure

There are 303 tests carried out in total, and numerous qualified tests are selected and used for discussion, and they are listed in Table 7.8 to Table 7.11 respectively, depending on the testing purposes they are supporting. Besides standard AIreaTHM tests, three comparative testing patterns are used as references. The comparative testing patterns are:1) mode tests under constant rotor thrust, 2) model tests by AIReaTHM without in still water,34) model tests under corresponding wave conditions without applying any rotor thrust. Testing results of comparative tests are used to observe the effect of SIL application on the hydrodynamic response from different perspectives. The experiment is carried out in the same procedure as shown in the attached quick time movie file (see [108]), and the procedure can be described as a few steps on condition that all the electrical components are powered on.

Step 1: start the data monitoring of the DAQ system by the spike (which is the packaged software of the DAQ device we used), and it can be noticed that the time history is started.

Step 2: start the wave makers, but it takes a few seconds for the waves to pass to the wave probe, and another few seconds to pass to the spar-buoy.

Step 3: start the AI machine/ SIL application of FOWT, and the wind is in the meantime started working, because it is a file pre-stored in the AI machine. Then a rotor thrust under

the effect of wind is generated by the fan atop of the spar-buoy. Simultaneously, apparent changes in the motions of the buoy are observed, particularly in surge, pitch and yaw. Besides, a data recording in LabVIEW is also automatically switched on by starting the AI machine. Besides, the recording length is set to be 10995 steps, because those steps for a period long enough to fullfill one tests and also not too long to interrupt the test for too heavy data monitoring task..

Step 4: the data recording in the LabVIEW tends to reach the length threshold. Particularly, it is time to stop the AI machine when the thrust passes the transparent values and zoom in to the standard values.

Step 5: stop the data monitoring, and save all the files of data recorded by both spike and LabVIEW.

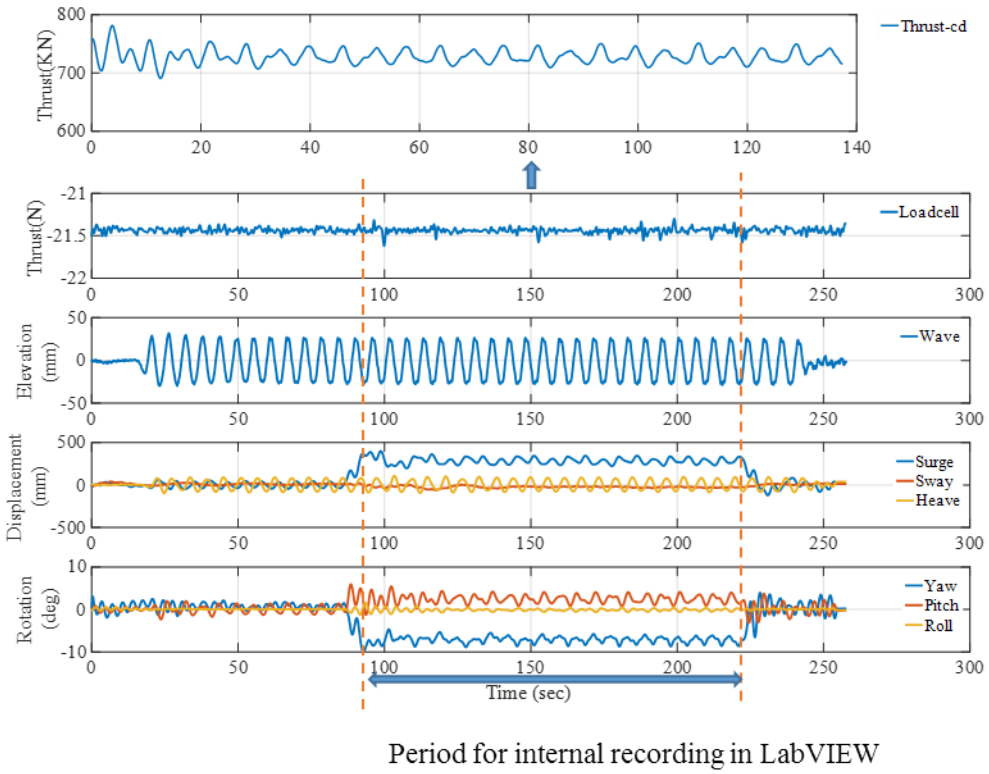

Figure 7.21 Experimental results of FD231

The raw data of FD 231 is shown in Figure 7.21, for DAQ spike from external measuring and the internal monitoring in LabVIEW(only stable data when switch on the AI machine is selected). As learned from Figure 7.21, the waves are observed at first, then when switch on th AI machine, the thrust increase significantly, and moves up and down around a mean value.

The load cell's reading is not used because it is not activated during the tank tests. Therefore, in this section, the observation for thrust performance is based on the internal monitoring, and the hydrodynamic performance observation relies on external measurements by sensors and the motion capture system. The reading of the load cell will not be mentioned in further plotting and discussions hereafter.

7.4.1 Data Processsing

The spike records the signals from Qualysis and other transmitter or sensors at a high frequency of raw 640Hz, and the spike file is converted to a txt file at 136Hz as the input file for analysis at MATLAB. Then the time histories are all the data recorded at 136Hz(which is the default monitoring frequency for Spike equipment used in the research). per channel in order to prevent potential aliasing due to the high frequency noise generated by the fan.

After being read into MATLAB, the offset in the data is firstly removed by removing the mean values of the data recorded in a still period during the test. The period is selected manually, because the till period is not at the same length for different tests.

Moreover, there are several distinct sources of noise on the data. The most troublesome is caused by fan rotating, which generated high-frequency mechanical vibrations and EM noise in the range of 100-200 Hz. Therefore, it is important to filter the data before analysis, and a fourth order low pass filter is applied. This filter removes noise at frequencies greater than the highest wave excitation frequency and highest natural

frequency of the system which is the heave natural frequency of 0.3Hz determined from the free decay tests.

7.5 Regular wave tests and results

The regular wave tests are carried out to put insight into the behaviour of the AI machine as well as the hydrodynamic response of the model by five sets of regular wave tests, with the wave frequency ranging from 0.17Hz to 0.88 Hz, a constant wave height of 2m. The five set regular wave tests are implemented under different steady wind, the wind speeds are 8m/s, 10m/s, 12m/s, 14m/s, 16m/s respectively. Only head seas are considered in tank tests, and the five sets regular wave tests in head seas are carried out in four different patterns: 1) AIReaTHM testing (with AI predicted rotor thrust under different wind conditions), 2) constant rotor thrust, 3) AIReaTHM no wave, 4) only wave no thrust. At first, the tests in first pattern listed in Table 7.7, are used to discuss the rotor-thrust performance under different wave frequencies or wind speeds. Moreover, the hydrodynamic response of the tests under different wave frequencies or wind speeds are demonstrated as well. Afterwards, the hydrodynamic response of the model in tests in other three testing patterns are observed and compared with the cases in AIReaTHM testing.

Table 7.7 Test matrix of regular wave tests for pattern 1

		Wind speed				
	Test ID	8m/s	10m/s	12m/s	14m/s	16m/s
Wave Frequency(Hz)	0.17	FD255	FD231	FD223	FD239	FD247
	0.27	FD079	FD080	FD279	FD082	FD083
	0.37	FD256	FD232	FD224	FD240	FD248
	0.47	FD257	FD233	FD225	FD241	FD249
	0.57	FD258	FD234	FD226	FD242	FD250
	0.688	FD045	FD025	FD278	FD031	FD033
	0.78	FD259	FD235	FD227	FD243	FD251
	0.88	FD260	FD236	FD228	FD244	FD252

7.5.1 PERFORMANCE OF THE ROTOR THRUST

As mentioned above, the internal recording in LabVIEW is used to observe the performance of the rotor thrust. Time histories of the rotor thrust for wind speed at 12m/s, under different wave frequencies are given in Figure 7.22. It is observed that as the wave frequency increases, the mean value of the rotor thrust varies slightly, stays around 800KN. However, the rotor thrust oscillates up and down at the mean level. Also, the oscillation frequency increases notably along with the wave frequency.

In order to observe the thrust performance under different wind speeds, the tests at wave frequency of 0.57 Hz are used for discussion, they are FD258, FD234, FD226, FD242, and FD250 respectively. The thrust for each test is given in Figure 7.23. it is observed that the mean value of the rotor thrust increases at first as the wind speed increases. It reaches at the maximum when the wind speed is 12m/s, and it starts decreasing.

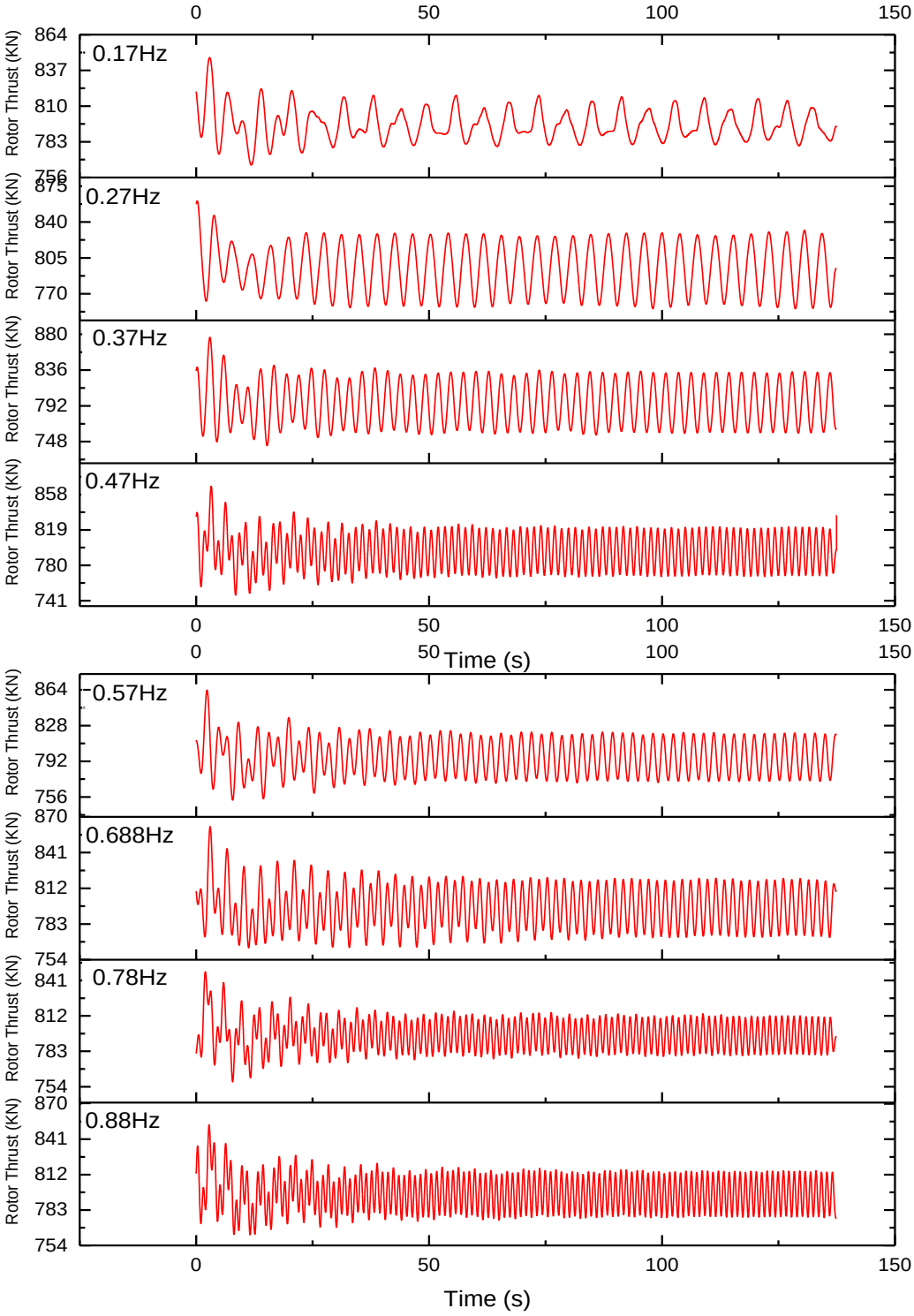

Figure 7.22 Thrust performance under different wave frequencies, wind speed=12m/s

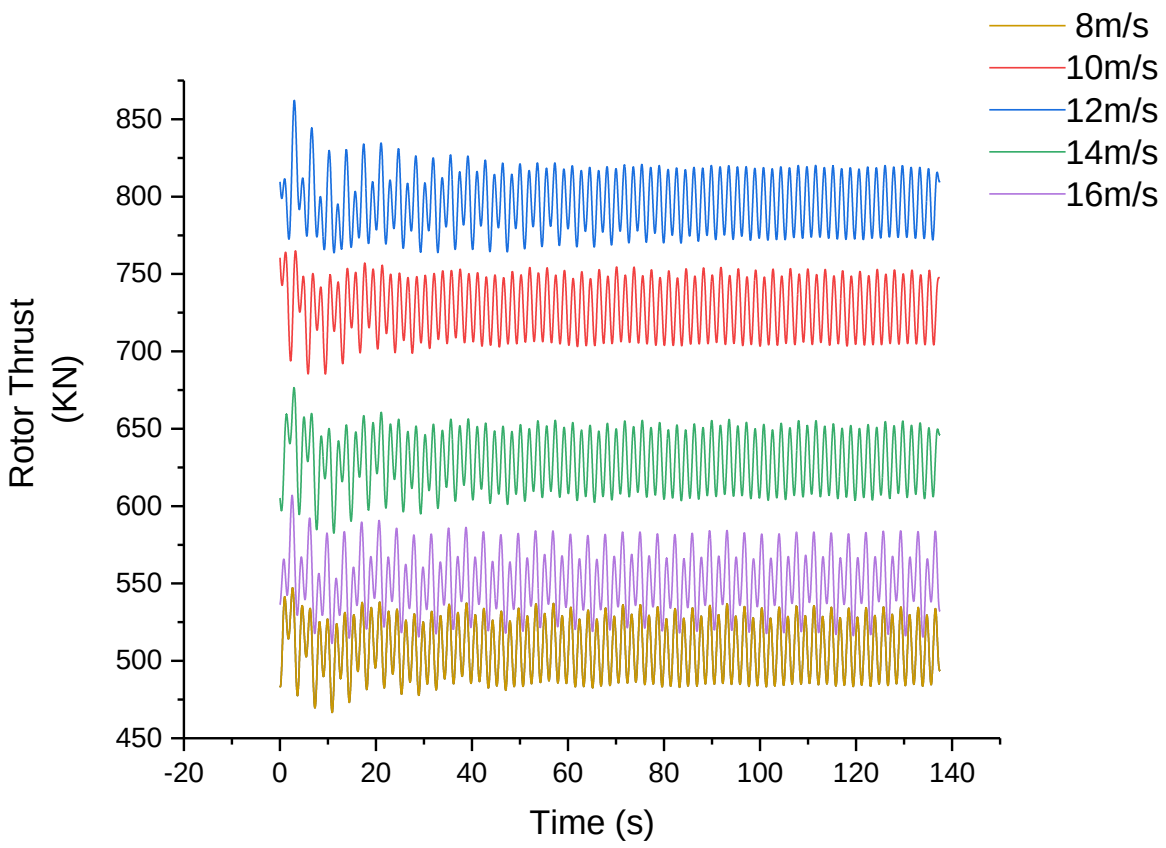

Figure 7.23 Thrust performance under different wind speeds, wave frequency=0.57Hz

7.5.2 HYDRODYNAMIC RESPONSE UNDER DIFFERENT WAVE FREQUENCIES OR WIND SPEEDS

Hydrodynamic performance analysis of the tests at a wind speed of 12m/s at wave frequency of 0.17Hz, 0.37Hz, 0.57Hz,0/78 Hz are given in Figure 7.24 to Figure 7.27. It is noticed that the change in wave frequency does impact the hydrodynamic response of the model. Taking surge for an example, as the wave frequency increases, the oscillating frequency increases, but the oscillation amplitude decreases, and it decreases to about zero in the end.

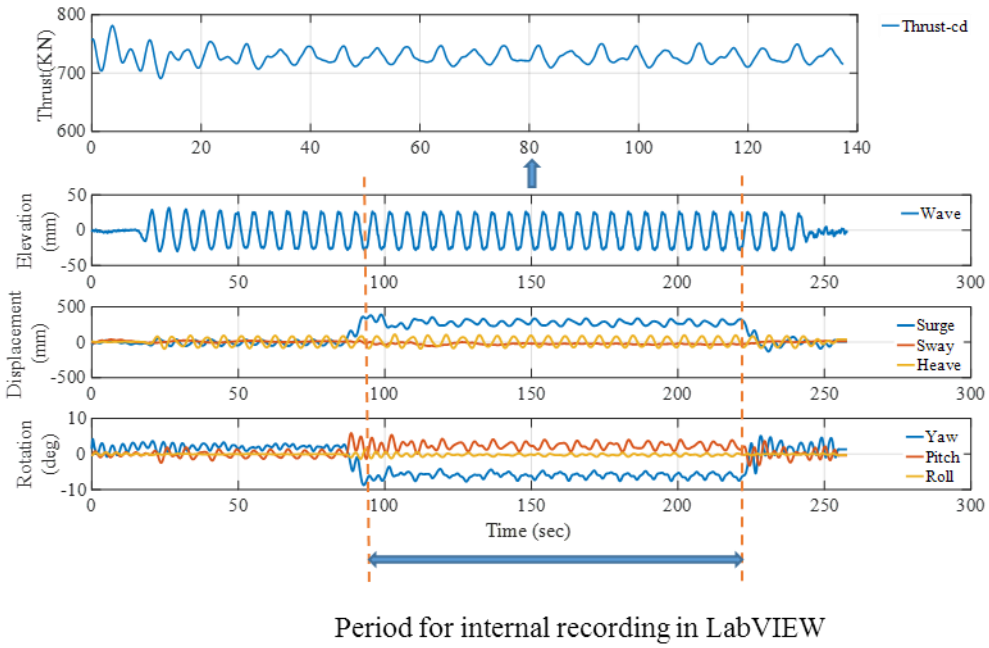

Figure 7.24 Hydrodynamic response of the model, FD231, 0.17Hz

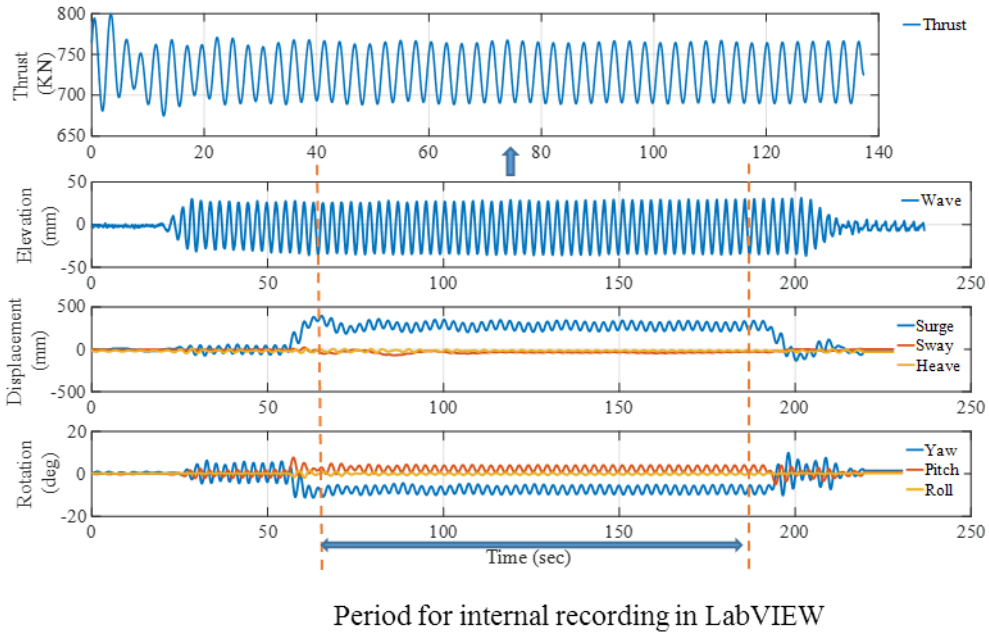

Figure 7.25 Hydrodynamic response of the model, FD232, 0.37Hz

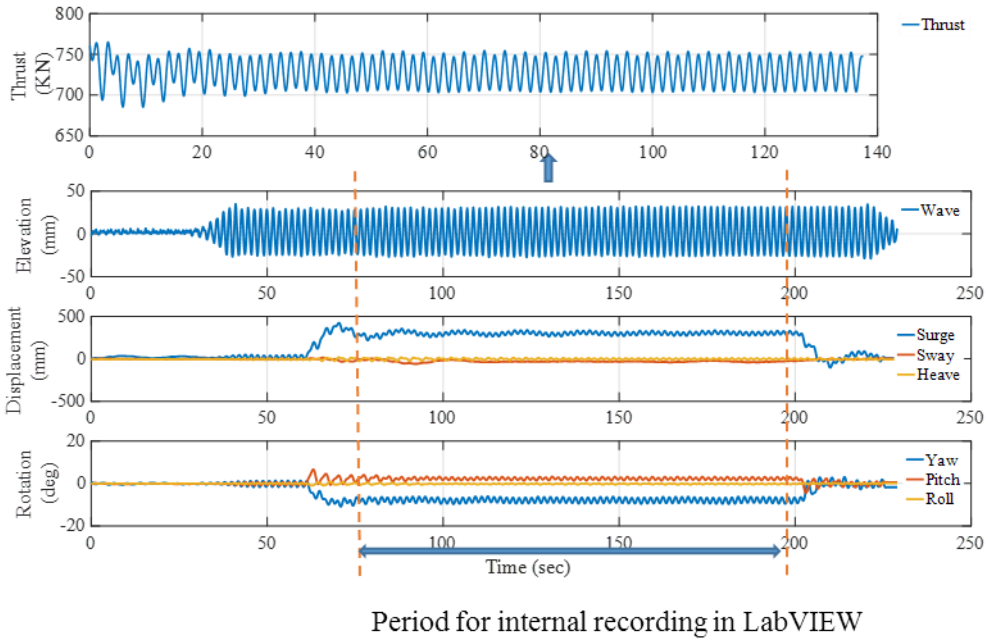

Figure 7.26 Hydrodynamic response of the model, FD234, 0.57Hz

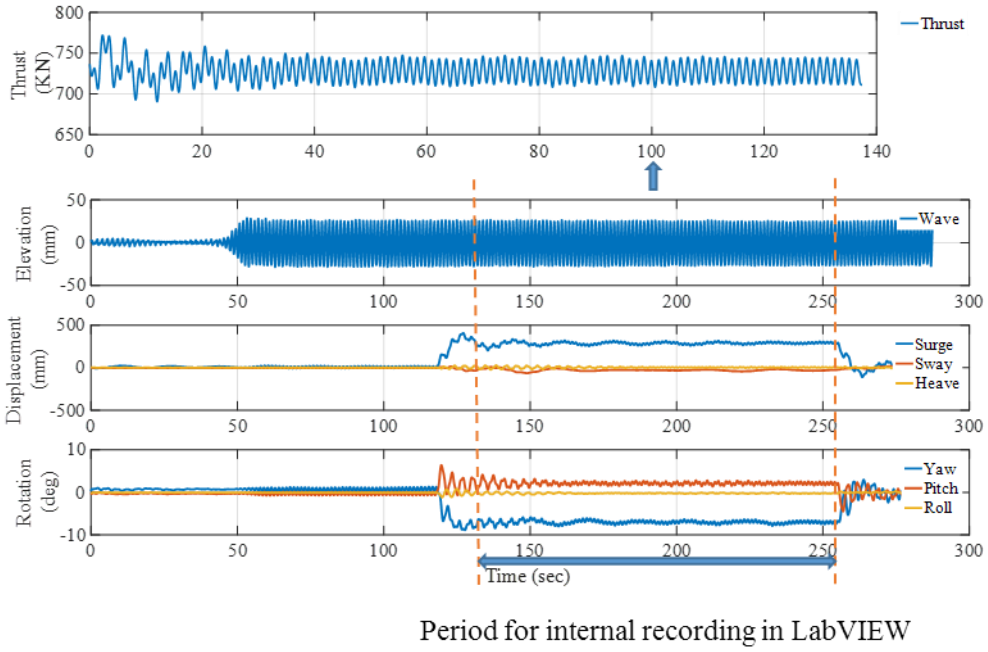

Figure 7.27 Hydrodynamic response of the model, FD235, 0.78Hz

Furthermore, to observe the effect of changing wind speed on the hydrodynamic response of the model. The tests under a wave frequency of 0.57 Hz are used for discussion, namely the FD258, FD234, FD226, FD242, Fd250, as listed in Table 7.7. It is noticed that the influence of the change in wind speed on the hydrodynamic response is not obvious, by

comparing Figure 7.28 with Figure 7.29. The displacements of surge, sway and heave increase slightly while the wind speed increases from 8m/s to 10m/s, and it starts to decrease from wind speed of 12m/s to 16m/s, and the oscillation becomes the most severe at the wind speed of 16m/s, as shown in Figure 7.30.

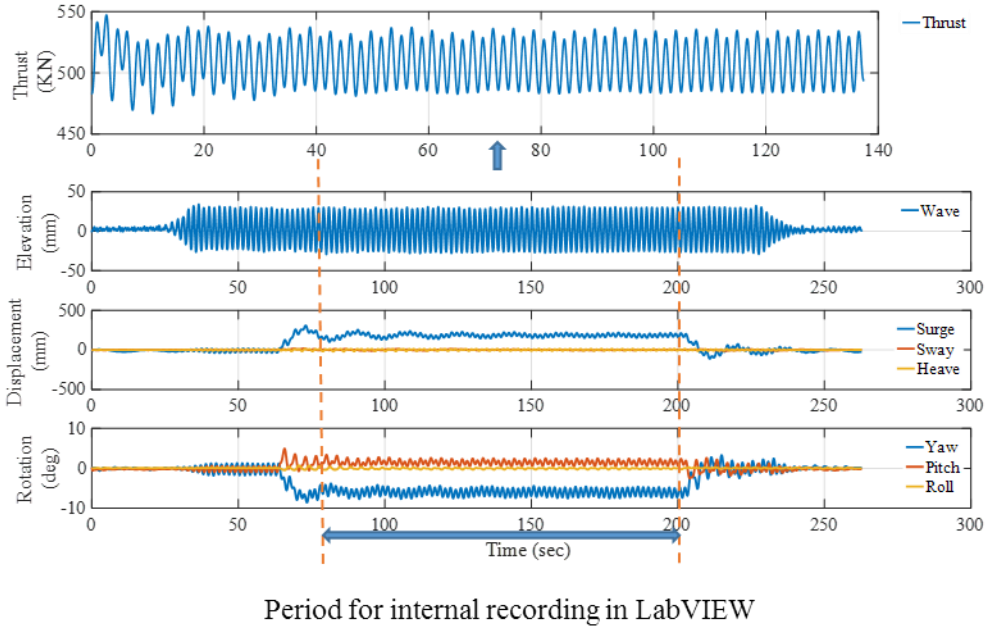

Figure 7.28 Hydrodynamic response of the model, FD258, 8m/s

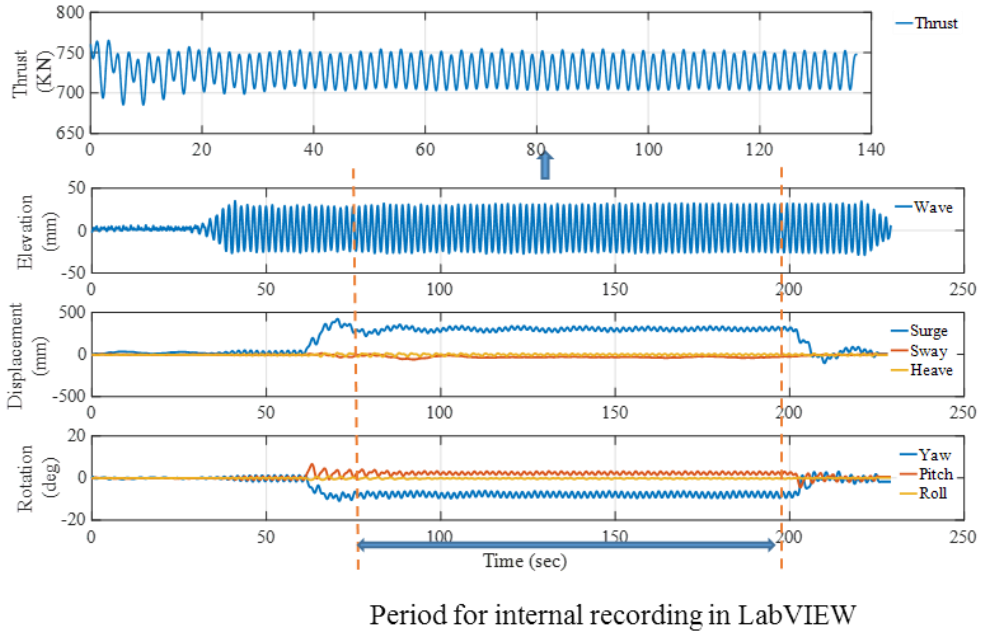

Figure 7.29 Hydrodynamic response of the model, Fd234, 10m/s

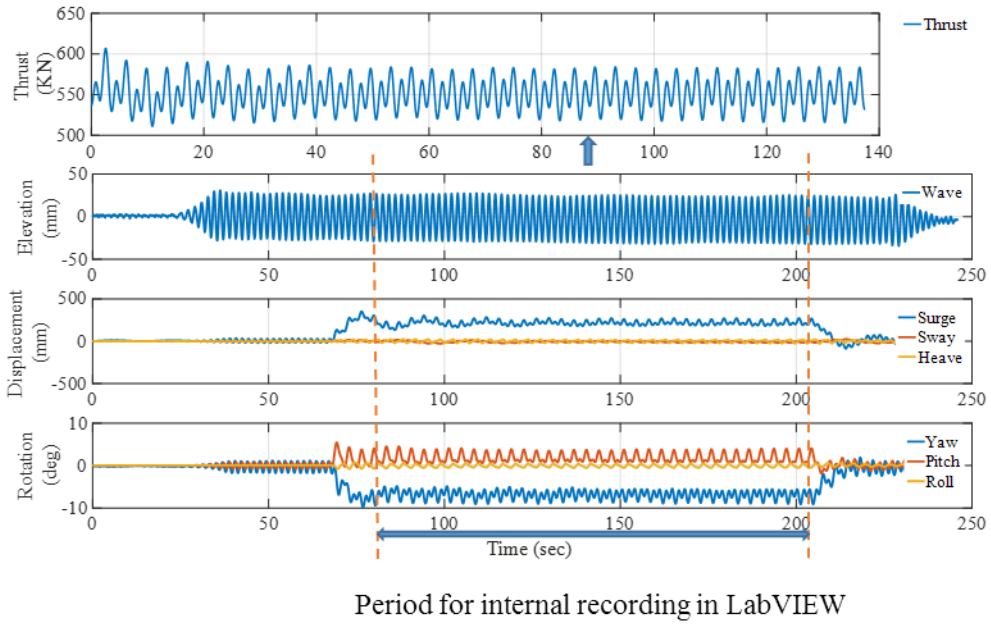

Figure 7.30 Hydrodynamic response of the model, FD250, 16m/s

7.5.3 HYDRODYNAMIC RESPONSE WHEN COMPARED WITH OTHER CASES

Table 7.8 Test matrix for wave frequency at 0.27Hz, including all cases

		Wind speed				
	Test ID	8mps	10mps	12mps	14mps	16mps
Cases for comparison	AIReaTHM	FD079	FD080	FD279	FD082	FD083
	constant rotor thrust	FD084	FD085	FD086	FD087	FD088
	AIReaTHM no wave	FD078	FD092	FD091	FD090	FD089
	only wave no thrust			FD093		

To examine the effect of the SIL application/AI machine for FOWT, it is necessary to compare the testing results under AI predicted rotor thrust, to designed comparative cases. As listed in Table 7.8, three cases are used for comparison, thus tests under a constant rotor thrust, tests under only AI predicted rotor thrust but in still water, tests under the corresponding regular waves but without any thrust, are carried out to compare with the AIReaTHM tests under different wind speeds. At first, the hydrodynamic response of the model in one AIReaTHM testing pattern is given in Figure 7.31. The hydrodynamic response of the model in other three comparison cases are given in Figure 7.32, Figure 7.33, and Figure 7.34.

By comparing Figure 7.32 with Figure 7.31, it is noticed that rather than a constant rotor thrust, the applying of AIReaTHM makes the hydrodynamic response of the model more related to wind conditions. However, in the case of constant rotor thrust, the motion oscillation is quite dominated by waves. Also, due to the existence of the rotor thrust, the Surge, sway, yaw and pitch notably increase dramatically at first and start the oscillation around a certain 800KN mean level. For the case under a constant rotor thrust, once the wave probe detected waves, the motions almost started the oscillation dominated by the waves immediately. Nevertheless, for the case of AIReaTHM testing, it takes a few more seconds before the motions show an observable difference.

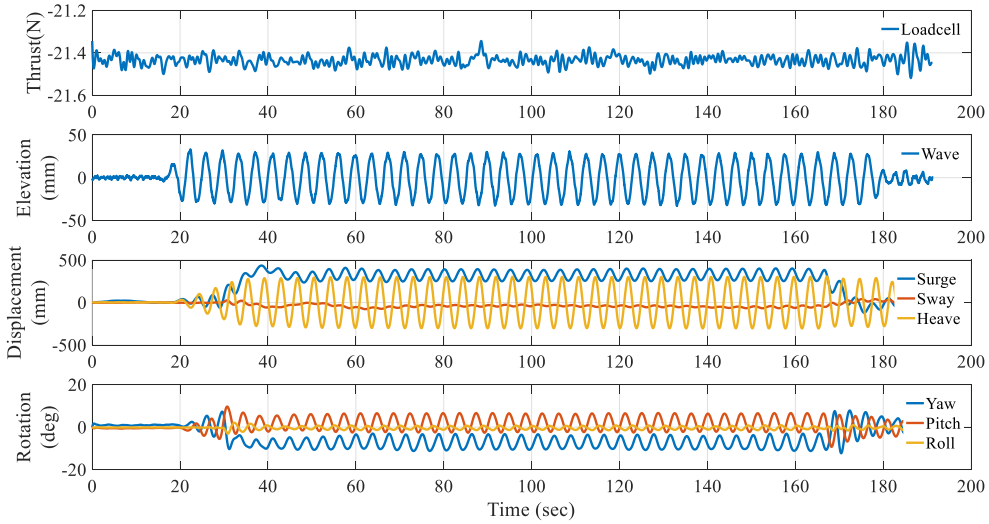

Figure 7.31 Hydrodynamic response of the model, FD279, AIReaTHM

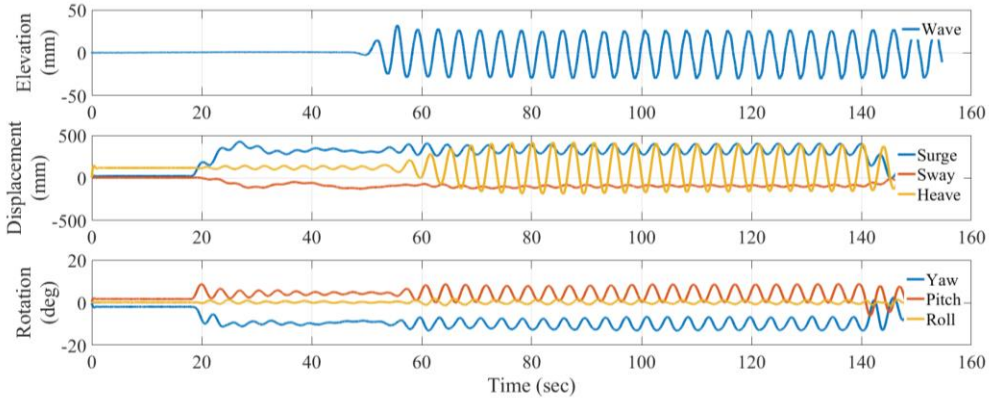

Figure 7.32 Hydrodynamic response of the model, FD086, Constant thrust

When contrasted with Figure 7.33, it is apparent that the hydrodynamic response in Figure 7.31 shows a distinct difference when the waves arrive at the spar-buoy. Interactively, the sea surface moves up and down due to the movement of the model in the water.

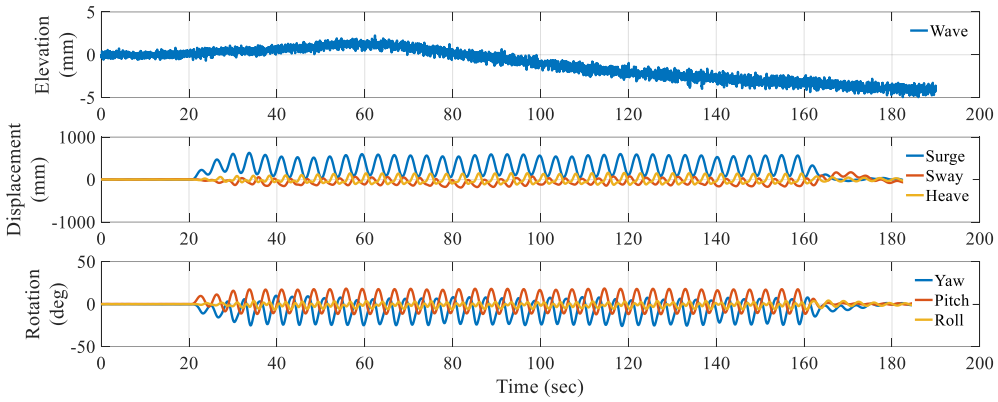

Figure 7.33 Hydrodynamic response of the model, FD093, AIReaTHM no wave

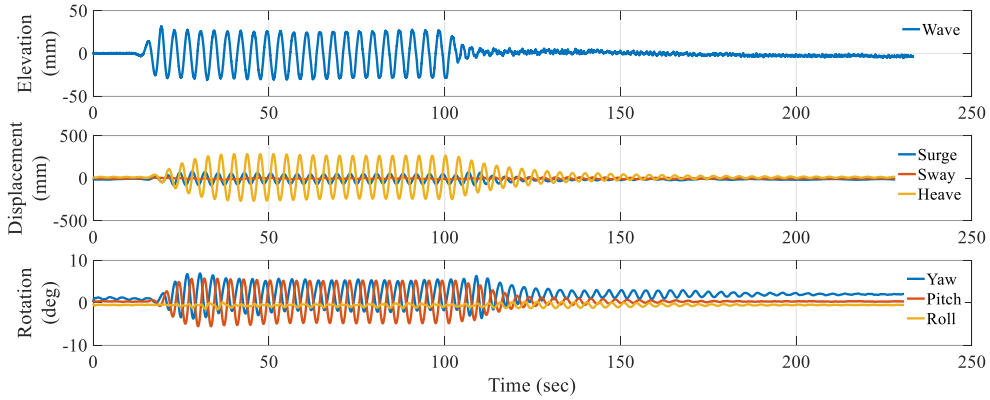

Figure 7.34 Hydrodynamic response of the model, FD093, only wave

However, recalling the most primitive experimental means, the model is settled in the water solemnly without applying any rotor thrust at the top. Moreover, the hydrodynamic responses are shown in Figure 7.34. There is no obvious increase of the six degree-of-freedom motions, except the movement along the wave elevation. The oscillations of the motions in all six-degrees-of-freedom is on the level of zero. Moreover, the same comparing tests are carried out for eight wave frequencies as listed in Table 7.9. In case the reader is interested in more testing results, the list contains all 303 tests are given in

appendix 4, including both regular wave tests and irregular wave tests. The original data recording files can be found in the online database [108].

7.5.4 RAOs ANALYSIS OF THE COMPARATIVE CASES

Definition of the Response Amplitude Operator (RAO):

$$RAO_x=(X_{max}-X_{min})/H \tag{7.1}$$

where H is the wave height, $(X_{max}-X_{min})$ is the amplitude of the response in six-degrees-of- freedom. For the regular wave tests in this thesis, constant wave heights are used, and the wave height is 2m in full-scale, and 27mm in model-scale. When post-processing the data of wave elevation produced by the wave probe by non-linear least-square fitting, it is found the amplitude of the wave elevation range from 26mm-28mm. Therefore, the Hs is selected to be 27mm in the analysis to be discussed in this section.

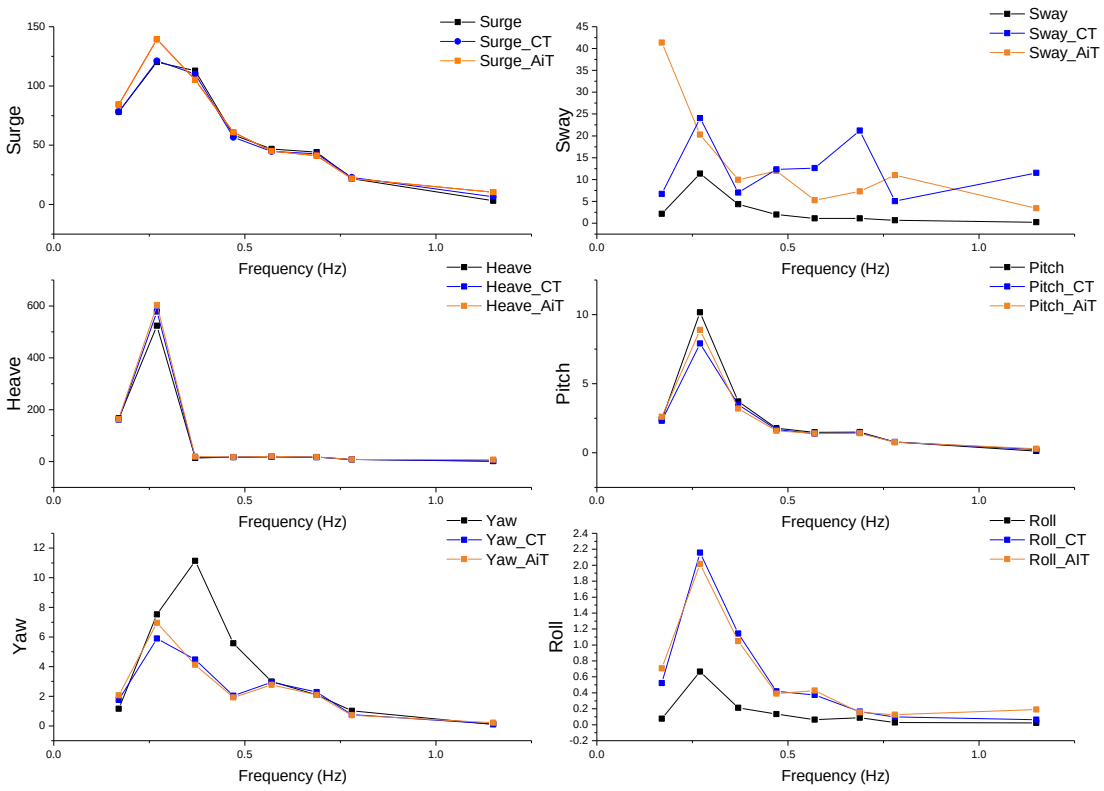

Figure 7.35 RAOs of motions in six degree-of-freedom for the three comparative cases

Table 7.9 Test matrix for wave frequency at 12m/s, including all cases

	Wind speed							
Test ID	0.17Hz	0.27Hz	0.37Hz	0.47Hz	0.57Hz	0.688Hz	0.78Hz	1.15Hz
AIReaTHM	FD223	FD279	FD224	FD225	FD226	FD278	FD227	FD230
constant rotor thrust	FD263	FD086	FD264	FD265	FD266	FD039	Fd267	FD270
only wave no thrust	FD285	FD093	FD286	FD287	FD288;	Fd040	Fd289	FD291

For one typical analysis, initially, a few (X_{max}-X_{min}) is obtained by selecting continuous cycles of the motions in six degree-of-freedom from the Testing file listed in, then a mean score of (X_{max}-X_{min}) is obtained and used to gain one RAO by dividing it by Hs. Then the RAOs of motion response of the platform under a range of frequencies can be obtained in the same manner. Those comparative cases are listed in the first column of Table 7.9. Meanwhile, the testing files used for analysis are listed in the other columns of Table 7.9 correspondingly. The RAOs for the three comparative cases are given in Figure 7.35.

7.6 Irregular wave tests and results

In order to observe the wave effect of the wave spectrum, the waves are designed to arrive later than switching on the SIL application. Because, if allowing the waves to reach the model before switching on the SIL application, the effect of waves is much less significant than the wind, as learned from regular wave tests. Consequently, it will be difficult to tell the effect of the waves on the performance of the SIL application, and the hydrodynamic response of the model. Hence, for irregular wave tests, in the procedure of the testing manner, step2 is swapped with step3. Similar to Section 7.4, the testing results of one typical irregular wave tests given in Figure 7.36. As listed in Table 7.11, five realistic sea states are considered in this section, SS1, SS2, SS3, SS4, SS5. Five comparative sea state SS1+, SS2, SS3+, SS4+, SS5+ are under the same wave conditions, and the corresponding steady wind, instead of turbulent wind in ‘SSi”. Besides, four testing patterns are used for the ten sea states, one is AIReaTHM testing pattern, and the other three patterns are designed to observe the effect of the SIL application from different perspectives. The testing results in Figure 7.36 is from test FD139, which is for SS1+,

AIReaTHM testing pattern. The details concerning the testing results are discussed below from three perspectives: 1) Performance of the rotor thrust under different realistic environmental conditions, 2) Hydrodynamic response of the model under different realistic environmental conditions, 3) Hydrodynamic response of the model when compared with designed comparative cases.

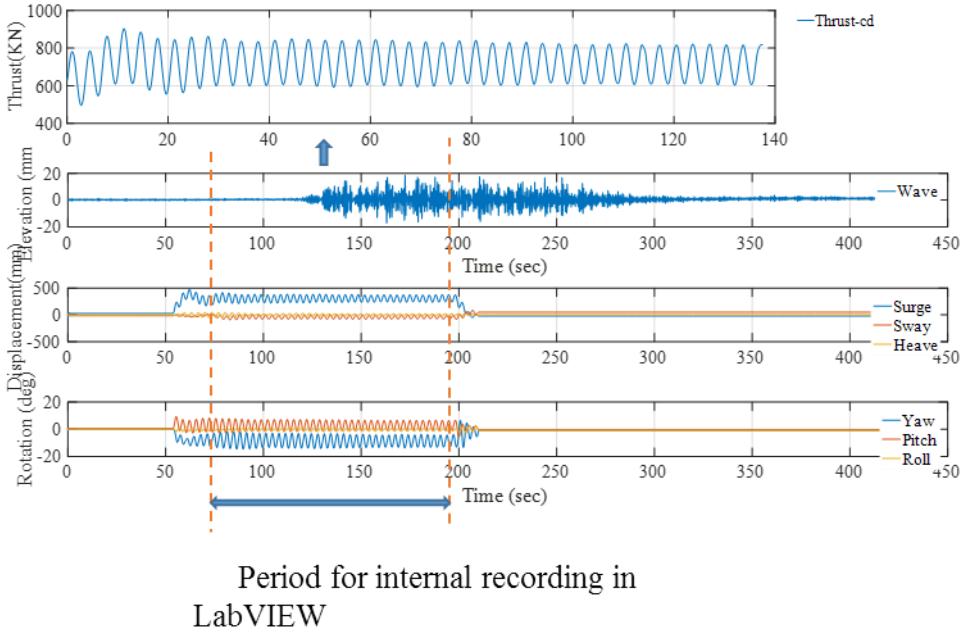

Figure 7.36 Testing result of one typical irregular wave test, FD139, SS1+

Table 7.10 Environmental conditions of sea states

Sea State	Wave Conditions(JONSWAP spectrum)	Wind Conditions(IECKAI model)
SS1	H_s =4.55 m, T_p =9.00s, γ =2.45	$\bar{u}$ =11.40 , TI=20.45
SS2	H_s =1.5 m, T_p =6.61s, γ =1	$\bar{u}$ =11.40 , TI=20.45
SS3	H_s =1.25 m, T_p =6.36s, γ =1	$\bar{u}$ =9.18 , TI=22.98
SS4	H_s =1.75 m, T_p =6.86s, γ =1	$\bar{u}$ =12.8 , TI=19.31
SS5	H_s =2.75 m, T_p =7.8s, γ =1.41	$\bar{u}$ =16.8 , TI=17.09
SS1+	H_s =4.55 m, T_p =9.00s, γ =2.45	$\bar{u}$ =11.40, TI=0
SS2+	H_s =1.5 m, T_p =6.61s, γ =1	$\bar{u}$ =11.40, TI=0
SS3+	H_s =1.25 m, T_p =6.36s, γ =1	$\bar{u}$ =9.18, TI=0
SS4+	H_s =1.75 m, T_p =6.86s, γ =1	$\bar{u}$ =12.8 , TI=0
SS5+	H_s =2.75 m, T_p =7.8s, γ =1.41	$\bar{u}$ =16.8 , TI=0

Table 7.11 Test matrix of irregular wave tests

	Sea-state									
Test ID (FD…)	SS1	SS1+	SS2	SS2+	SS3	SS3+	SS4	SS4+	SS5	SS5+
AIReaTHM	110	112	180	141	123	143	125	145	127	147
constant rotor thrust	129	130	131	132	133	134	135	136	137	138
AIReaTHM no wave	111	140	118	142	124	144	126	146	128	148
only wave no thrust	119		120		151		150		149	

7.6.1 PERFORMANCE OF THE ROTOR THRUST UNDER DIFFERENT REALISTIC ENVIRONMENTAL CONDITIONS

In the first place, the effect of the turbulent wind on the thrust performance is discussed by comparing the tests of 'SSi' with 'SSi+', likewise the effect of wave spectrum, wind speed are also demonstrated by comparing the testing results in term of the time histories of thrust of different tests listed in Table 7.11. As presented in Figure 7.37. it is apparent that the rotor thrust under 'SSi' contains a turbulent component apart from the vibration caused by the wave spectrum, by comparing with 'SSi+'. Besides, the mean values of the rotor thrust under 'SSi' do not distribute as scatterly as the cases of 'SSi+'.

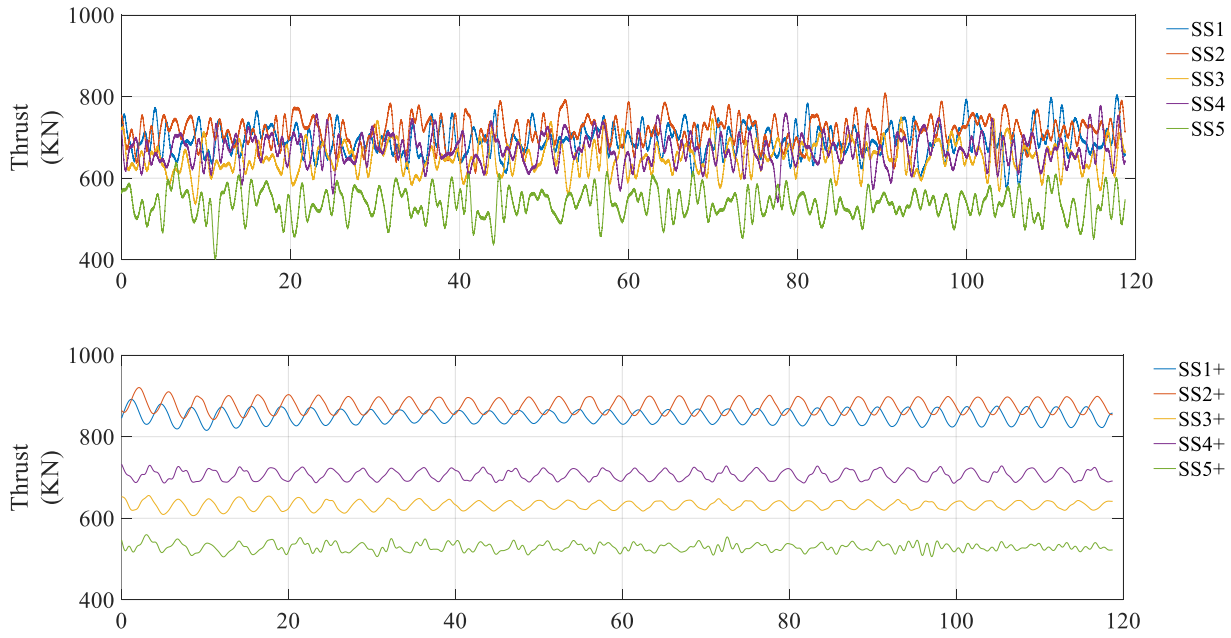

Figure 7.37 Thrust performance of all the sea states by AIReaTHM

Furthermore, it is observed that the change in wave spectrum under steady wind has a tiny influence on the mean value of the rotor thrust, by placing SS1+ by side of SS2+.

Because SS1+ and SS2+ represent the sea states under the same steady winds but different wave spectrums. However, when compare with SS1 and SS2, no obvious difference is observed which proves that the influence of the wave spectrum on the mean value of the rotor thrust is not notable when turbulent wind is applied. When putting insight into SS2+ to SS5+, it is noticed, that as the wind speed increases from 9.18m/s to 16.8m/s, the mean value of the rotor thrust increase initially, and reach the largest value at a wind speed of 11.4m/s, then starts reducing till 16.8 m/s. It is also noticed that, when the wind speed is lower than 9.8m/s or higher (and including) than 16.8m/s, the oscillating component of the rotor thrust becomes to be dominated by waves instead of wind.

The comparisons between 'SSi' with 'SSi+' are given separately in Figure 7.38. It is learned that the mean score of the rotor thrust deduces, due to the existing of the turbulent intensity of the wind. However, as the wind speed increases from 11.4m/s to 16.8m/s, the mean gap of the rotor thrust becomes less notable.

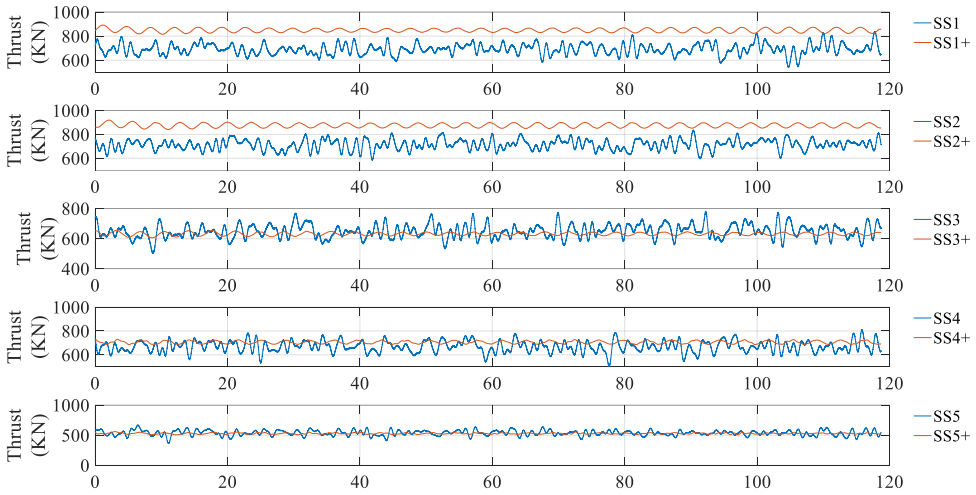

Figure 7.38 Thrust performance, Steady wind vs turbulent wind by AIReaTHM

7.6.2 HYDRODYNAMIC RESPONSES WHEN CHANGING WAVE SPECTRUM OR USING TURBULENT WIND FOR AIREATHM TESTS

As listed in Table 7.11, FD110 is a standard AIReaTHM test under sea-state SS1, and a turbulent wind field with the wind speed at 11.4m/s, FD 112 is also a standard AIReaTHM test, however under steady wind at the same wind speed of FD110. FD111 is carried out under the same wind conditions as for FD110, however in still water. FD140 is carried out under the same wind conditions as for FD112, in still water. Hence, the effects of wave spectrum on the hydrodynamic response of the model are discussed respectively in this section, by comparing the testing results of FD110 with FD111, and FD112 with FD 140, respectively. Likewise, by contrasting the results of test FD110 with FD112, it is intended to reveal the influence of turbulent wind on the hydrodynamic response of the model.

Table 7.12 Statistical analysis of FD110, 112, 111, 140

Test ID		Surge	Sway	Heave	Pitch	Yaw	Roll
FD110	Mean	201.89	64.338	2.201	-5.851	1.999	-0.117
	STD	54.272	34.202	13.174	5.256	2.975	1.261
FD112	Mean	333.41	145.39	2.587	-6.951	2.99	-0.182
	STD	38.864	19.502	30.552	2.453	2.212	0.725
FD111	Mean	208.43	69.866	4.546	-5.736	1.865	0.117
	STD	60.305	37.454	14.363	6.268	3.332	1.404
FD140	Mean	323.35	-57.28	-3.635	-8.896	3.017	-0.113
	STD	39.87	19.188	35.295	2	2.225	0.618

At first, the statistical analysis results of FD110,112, 111 and 140 are listed in Table 7.12. By comparing FD110 with FD112, it is observed that the motions in all six degree-of-freedom tend to decrease; however, the standard deviation increase, due to the existing of turbulent wind. Despite the fact that the surge and sway decrease significantly, the other motions decrease slightly. Moreover, the comparison of FD110 with FD111, FD112 with FD140 reveals that changing wave conditions does not have a significant influence on the six degree-of-freedom motions, for tests with a rotor thrust, which reflects the existence of wind influence. In other words, the influence of waves on the hydrodynamic response of the spar-buoy is much less than wind.

Afterwards, the testing results of FD111 is used to be compared with FD110. Hence, the testing results of FD 111 is shown in Figure 7.40. Similar to the behaviour of rotor thrust,

it is difficult to figure out the effect of the waves on the buoy under the turbulent wind. However, it is noticed that the oscillating frequency of the oscillating component in the motions increases slightly under the steady wind by comparing Figure 7.42 with Figure 7.41. It is also acquired that the oscillating amplitude of the oscillating component in six degree-of-freedom motions varies due to the existence of the turbulent intensity in the wind. This is also further validated by comparing Figure 7.39 with Figure 7.42, or Figure 7.40 with Figure 7.41.

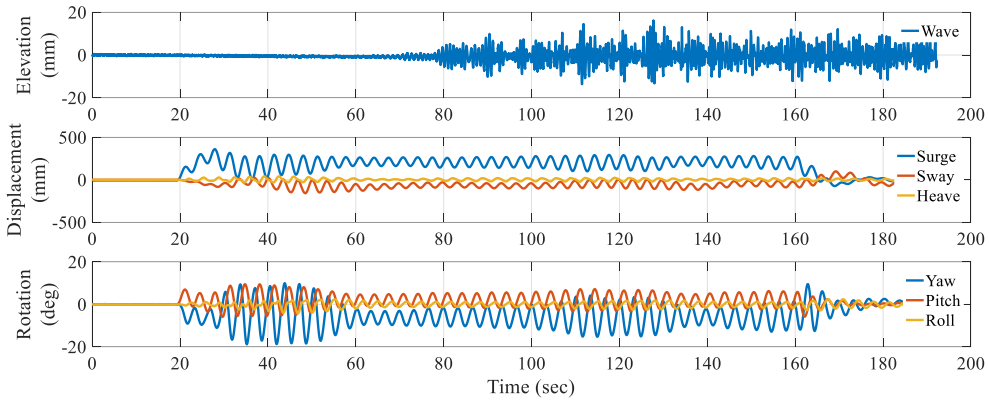

Figure 7.39 FD110, Turbulent wind, AIReaTHM testing, SS1

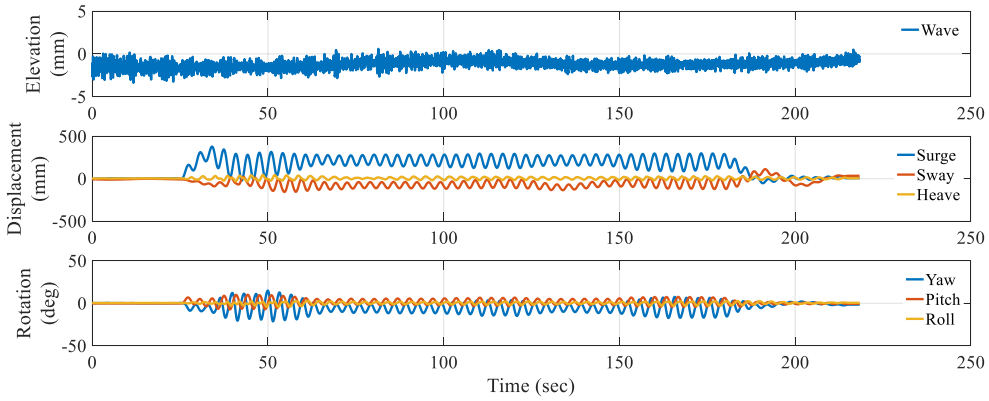

Figure 7.40 FD111, Turbulent wind, AIReaTHM, no wave

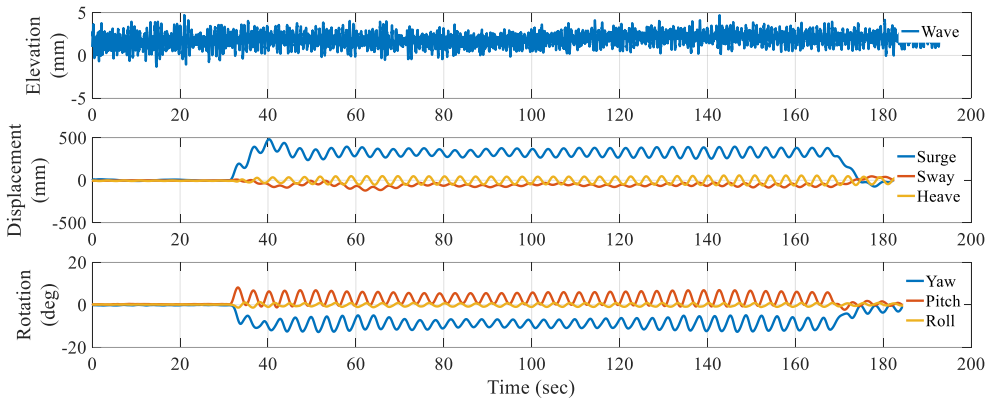

Figure 7.41 FD140, steady wind, AIReaTHM, no wave

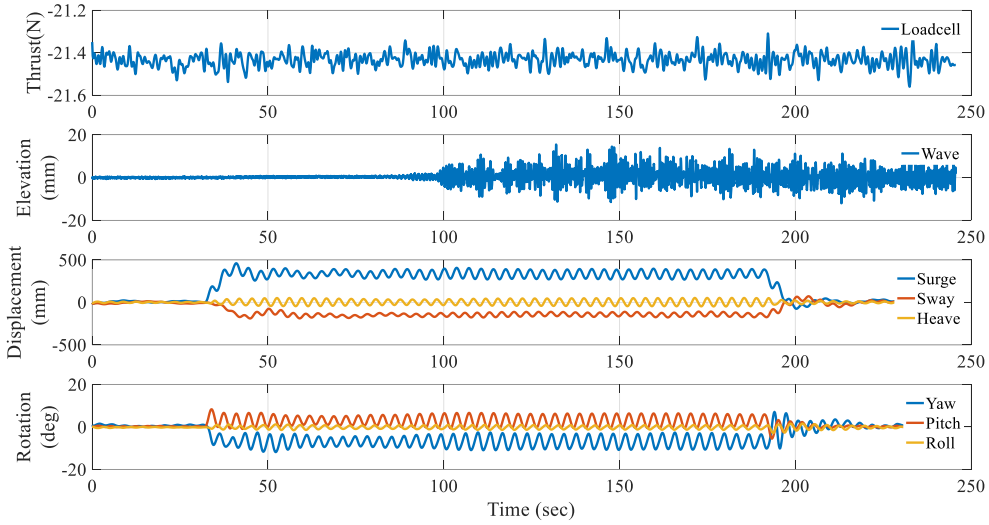

Figure 7.42 FD112, steady wind, AIReaTHM, SS1

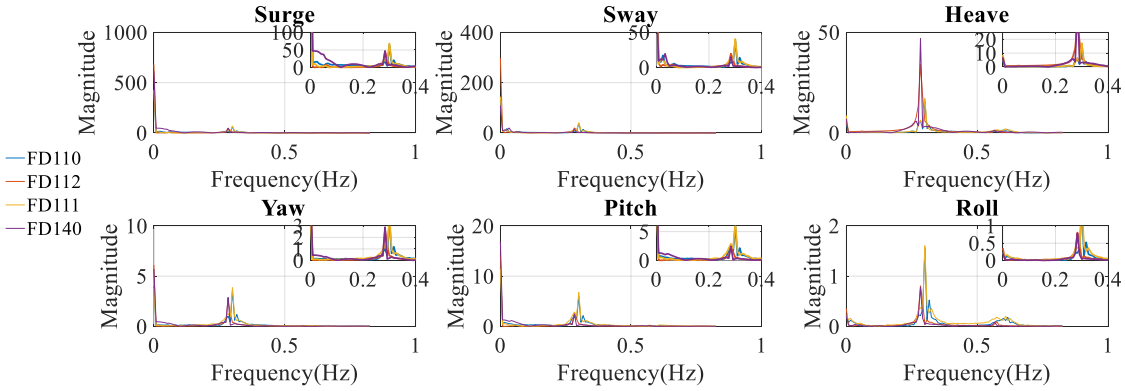

Figure 7.43 Spectral response of the six degree-of-freedom motions for test FD110, 112, 111,140

Finally, Figure 7.43 shows the spectral response of the motion in six degree-of-freedom, obtained by performing FFT analysis of the time histories of test FD 110, 112, 111, 140.

It can be referred from the figure that the peak frequencies of four tests are all around 0.3 Hz which is the natural frequency of heave, pitch, yaw and roll obtained by free decay tests in section 7.3. Furthermore, the peak frequency for the four tests are not precisely located at 0.3 Hz, the peak frequency of red line for FD112 and the purple line for FD140 are both 0.29Hz, the yellow line of FD111 peaks at 0.30Hz, blue line for FD110 peaks at 0.32Hz, except heave at 0.30 Hz.

7.6.3 HYDRODYNAMIC RESPONSE OF THE MODEL WHEN CHANGING TESTING PATTERNS

In addition to the standard AIReaTHM tests FD110, FD112, other two testing patterns (pattern1-under a predefined constant rotor thrust; pattern2- under no rotor thrust but only wave conditions) are used as comparisons. In the first place, FD130 is selected to compare with FD112, because they are under the same wave conditions. However, the difference is that FD 130 is carried out under a predefined constant rotor thrust, instead of the AI predicted rotor thrust. Likewise, the corresponding comparative case for FD110 is FD129. Then only one test FD119 is selected as the only-wave testing pattern for both because FD110 and FD112 are carried out under the same wave conditions. In the beginning, the summary of the mean values and standard deviations (STD) is presented in Table 7.13. It is evident that mean values and standard deviation of the six degree-of-freedom motions are significantly higher when compared with that of FD119, due to the existing of the rotor thrust at the top of the spar model.

Table 7.13 Statistical analysis of three comparative cases

Test ID		Surge	Sway	Heave	Pitch	Yaw	Roll
FD110	Mean	201.89	64.338	2.201	-5.851	1.999	-0.117
	STD	54.272	34.202	13.174	5.256	2.975	1.261
FD112	Mean	333.41	145.39	2.587	-6.951	2.99	-0.182
	STD	38.864	19.502	30.552	2.453	2.212	0.725
FD129	Mean	267.08	11.162	0.8	-7.56	2.23	-0.129
	STD	10.19	5.445	1.589	0.229	0.123	0.07
FD130	Mean	264.0	43.10	1.84	-6.467	2.307	-0.175
	STD	56.61	12.99	1.83	1.441	0.504	0.083
FD119	Mean	2.001	-1.973	0.428	0.17	0.026	0.024
	STD	0.82	0.381	0.632	0.055	0.027	0.014

The testing output of FD130 is provided in Figure 7.44, and it is obvious that the oscillating components in six motions decay to zero in time, instead, the oscillating components in six motions of FD 112 show constant amplitude. This proves the AIReaTHM application is better than applying a predefined constant rotor thrust. When the fan is switched off, the model is settled in the only-wave condition, and the hydrodynamic response is given in Figure 7.45, from 100s to 250s. No distinct discipline can be observed for the hydrodynamic response of the model in mere wave conditions.

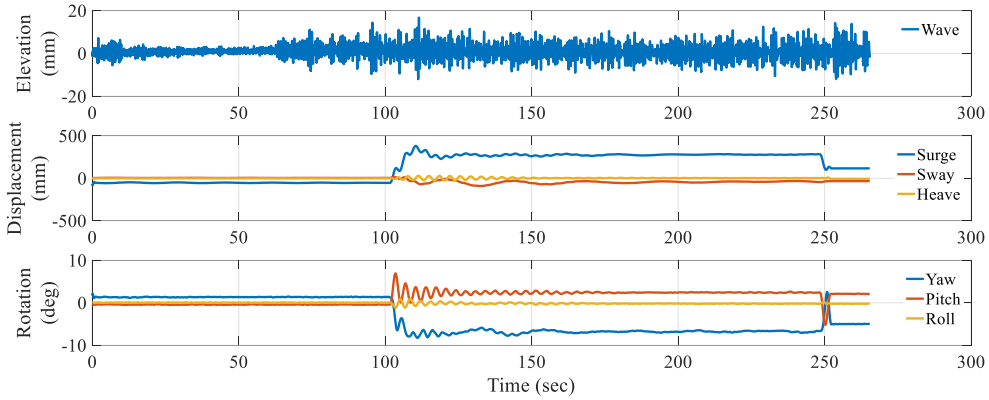

Figure 7.44 FD130, Constant Thrust, irregular wave

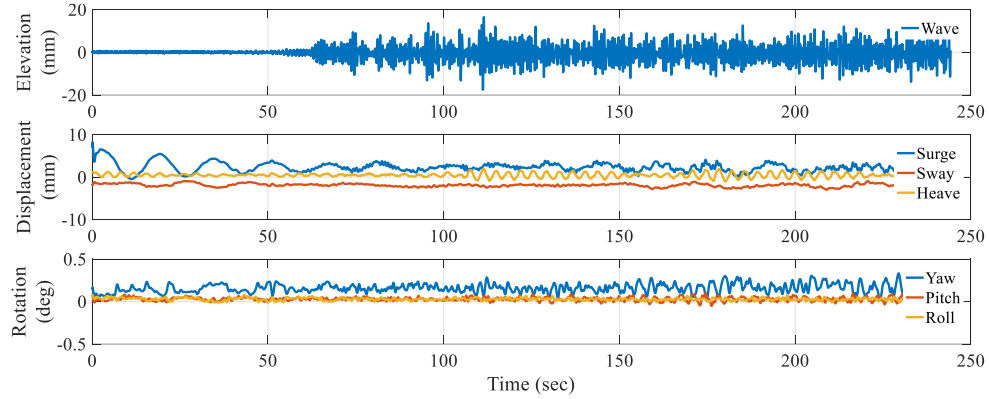

Figure 7.45 FD119, No constant thrust, No AIReaTHM, Irregular wave

The spectral response of the six degree-of-freedom motions for test FD110, 129, 119,112, 130 is given in Figure 7.46 and Figure 7.47 respectively for different comparisons. As seen for the red line and yellow line in Figure 7.46 and Figure 7.47, the FFT of the test under a predefined constant rotor thrust and the test under no rotor thrust shows the peak

at the frequency of 0.08Hz, coinciding with the natural frequency of surge and sway obtained from the free decay tests. However, the FFT of standard AIReaTHM tests of FD110 and FD112 show the peak frequency at 0.3Hz.

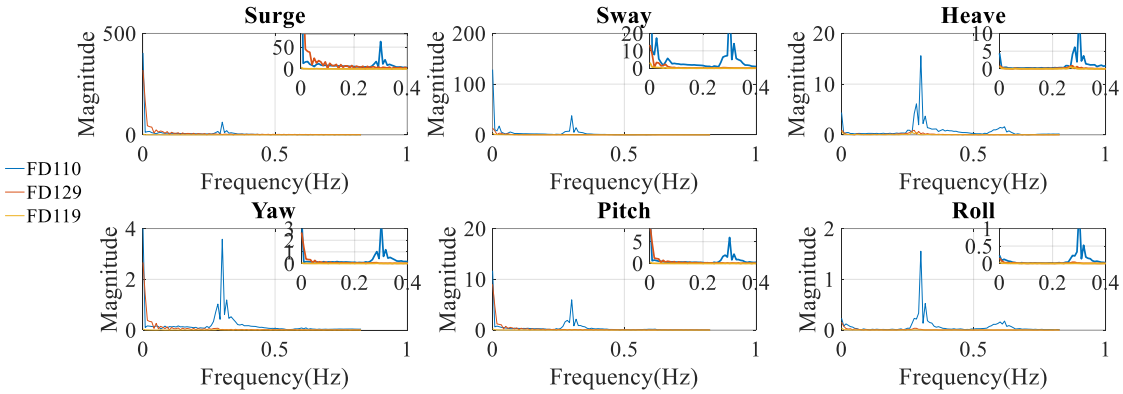

Figure 7.46 Spectral response of the six degree-of-freedom motions for test FD110, 129, 119

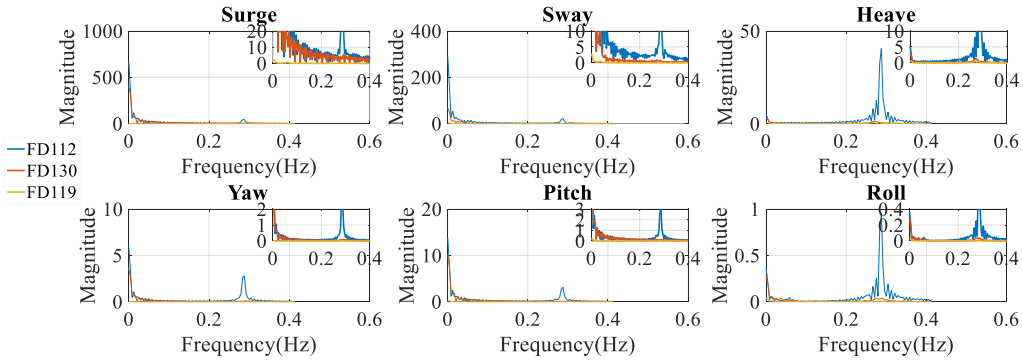

Figure 7.47 Spectral response of the six degree-of-freedom motions for test FD112, 130, 119

7.7 Summary

This chapter demonstrates the model tests of a spar-type FOWT, using the AIReaTHM testing rig developed and validated in chapter 5. Initially, the model description, as well as the necessary calibration and preparation at the Kelvingrove hydrodynamic laboratory, are given. Then the free decay tests of the model under two rotor thrust conditions are carried out. The natural frequencies of the model under free decay of platform pitch, surge, sway, heave, yaw and roll are obtained, and they are compared with that of cases under a constant 800KN rotor-thrust. Most importantly, the performance of the rotor thrust, as

well as the hydrodynamic response of the model under different environmental conditions are sensitively discussed with proper comparisons. Some significant output from this chapter can be concluded as follow:

- The natural frequencies of the model under six degree-of-freedom motions under different testing conditions are obtained, and they keep the same for cases with a 800KN constant rotor thrust or without.
- The performance of the rotor thrust by using the AIReaTHM testing rig under regular wave tests are given, which proves the AIReaTHM is better than applying a constant rotor thrust atop of the model.
- The effects of different wind speeds and wave frequencies on the SIL application of FOWT as well as the hydrodynamic response of the model are discussed, for regular wave tests.
- The effects of different wave conditions and wind models for ten sea-states on the targeted thrust, as well as the hydrodynamic response of the model, are discussed by analysing the testing results from irregular wave tests.
- The AIReaTHM testing method improves the model tests of FOWTs, and, it needs to be further improved to include other aerodynamic forces.

8 Original contribution and conclusions

This thesis addressed the SIL experimental methodology for accurate model tests of ORE devices. First, two conceptual design of two SIL applications for model tests of WECs, and FOWTs are proposed, respectively. Then a PTO simulating platform (providing real-time PTO forces) based on the SIL application for WECs is estimated in the wave tank and 1349 standard drop tests are carried out to characterise the PTO simulating platform. A 1:40 model-scaled OWSC WEC device is used in the tank tests under different PTO damping strategies simulated by the PTO simulating platform. an AI-based hybrid real-time hybrid model testing rig is developed based on the conceptual design of a SIL application for FOWTs. Furthermore, a core prediction module is established by AI training based on a signficant number of simulations using FAST computation. Then a real-time controller is used to execute the prediction module in the AIReaTHM testing rig. Bench tests using a manoeuvrable motion simulator are carried out to validate the AIReaTHM testing methodology, as well as to characterise the testing rig. A 1:73 model of a spar-type floating wind turbine is applied in the model test with the AIReaTHM testing rig conducted in the Kelvin Towing Tank at the Strathclyde University. The main

conclusions, original contributions, and the recommendations for future work are presented in this final chapter.

8.1 Original contributions

The main original scientific contribution of the thesis can be summarised as follows:

- *Establishing the innovative method of providing a real-time PTO damping force during model tests of WECs*

An innovative method is proposed to generate a real-time linear PTO damping force. By changing the exponent of the control function, it is also validated the capability of this method to generate a quadratic real-time damping force is also validated. Moreover, by changing the gain in the control function, real-time linear or quadratic damping forces at different sizes can be generated.

- *Constructing a generic PTO simulating platform based on the innovative method*

A low-cost innovative PTO simulation platform is developed, and itcan be used to simulate a real-time linear or quadratic PTO damping force. Thus making it possible to achieve an optimal design for different WEC/PTO combinations at the testing stage.

- *Carrying out model tests of a WEC device with different PTO strategies, under various linear and nonlinear damping*

This is the first time to enable both linear and nonlinear PTO damping forces at a large number of different sizes, to be simulated in the model tests of a WEC device. Additionally, the best PTO strategies for one specific model device in both regular wave conditions and irregular wave conditions have been recommended in terms of the best gains for linear control function and nonlinear control function.

- *Establishing the prediction module of the real-time rotor thrust for FOWTs*

The system identification techniques are adopted to derive the frame of the prediction module. The AI techniques are used to train the neural network structure within the frame of the prediction module, based on the data pool formed by the quantities of interests (such as rotor thrust, wind velocity, surge displacement, surge velocity, pitch displacement, pitch velocity and so on). With the establishment of the prediction module, a real-time controller is adopted in physical tests, and then an AI machine consists of the prediction module and the controller is used to indicate the SIL application for FOWTs.

- *Constructing the AIReaTHM testing rig with the AI machine/ SIL application*

An AIReaTHM testing rig is constructed, based on the AIReaTHM testing methodology, which enables the accurate model tests of FOWTs in the tank. This is the first time that artificial intelligence techniques have been applied in the hybrid testing method for FOWTs.

- *Carrying out model tests of a spar-type FOWT by using the AIReaTHM testing rig*

This is the first time to carry out model tests with the AIReaTHM testing rig, which is equipped with a real-time rotor thrust coupled with the motion input of the model in the water. This is also the first time with the comprehensive comparisons being carried out among four testing patterns available. It revealed the unique nature of the SIL application by comparing the testing results of AIReaTHM testing with other three comparative conditions.

8.2 Conclusions

The main conclusions based on the present study are drawn as follow:

- *The newly developed PTO simulation platform can produce linear PTO damping and nonlinear damping in a wide range (quadratic damping is taken as a simple*

nonlinear example). Reasonable correlation curves between the input gains of the PTO simulation platform and the coefficients of simulated PTO damping forces are achieved for both linear and nonlinear cases. The correlation indicates the PTO simulation platform's capacity of simulating linear PTO can reach 40-220 and 10-70 for nonlinear damping (the numbers are the damping coefficients drawn from fitted equations).

- *The study identified that the best PTO strategy is represented by gain of 80, and 160 for linear and nonlinear damping modes respectively in regular waves. The comparison of power efficiency under nonlinear PTO damping and linear damping shows that nonlinear PTOs have no distinct advantage in the amount of electricity output, but have better stability and broader damping range. Comparison of the output power in different wave spectrum indicates that the approach can be applied to represent a full range of ocean possibility. The electricity output power in the JONSWAP spectrum is found to be approximately 300% higher than in user-defined spectrum for the same wave parameters.*
- *Numerous simulations based on the classic model of 'OC3-Hywind' floating wind turbine have been carried out, and the data from simulations have been analysed in details, in order to obtain the structure of the thrust force prediction model. Moreover, artificial neural network techniques are used to train the primarily obtained structure to gain well estimated mathematical models which could be used as control functions in the experiments to provide real-time thrust varying with the input signals such as surge, surge velocity, pitch, pitch velocity, wind speed, and wave conditions.*
- *An AI-based hybrid testing rig is developed. The effect of the surge inputs of the testing rig on the targeted thrust is discussed. The effect of different sea states, particularly different wave spectrum and wind models on the targeted thrust is*

analysed. The time delay in the testing system is identified within 0.1s, and the overall uncertainty from the testing rig is 5-15KN compared to the AI prediction considering the uncertainty in the optical motion capture system is $\pm 6\,mm$.

- *By applying in the model tests of a spar-type FOWT in both regular waves and irregular waves, it is demonstrated that the AIReaTHM outperforms the traditional approach of applying a constant rotor thrust atop of the model. It is acknowledged that the AIReaTHM testing method indeed improves the model tests of FOWTs, certailyr, it requires further development to include aerodynamic couplings to reflect more realistic cases.*

8.3 Future work

- The control function of the SIL application for WECs testing used in this thesis is a direct expression of the aimed damping forces (linear or quadratic). Probably in the future, the author would like to improve the control function of the PTO simulating platform to include an AI-algorithm, which can be used to obtain the underline function of PTO force from the behaviour of a real PTO device.
- As for the uncertainty discussed in chapter 3, the iteration method probably could be used to adjusting damping spectrum to achieve a given value of correlation coefficient between the damping spectrum and the target one as the suthor described in the publication[3]. Moreover, varying damping in traditional vibration systems in and fractional vibrations reported may be useful for the future work to possibly explore the mechanism of varying damping in the ocean energy converters.
- Because more floating wind farms are under commercial design, in the soon future, if data-share becomes possible, cloud computing can be introduced to AIReaHMT testing process. Generally, a few basic features are revealed by the product- AIReaTHM testing approach: 1. The testing rig itself has a sensor system that can collect data in real-time. 2 The testing rig interacts with the physical model, so it can not only affect the experiments, but the data of experiments also needs to be included in the testing approach. The use of more and better data leads to product evolution, product evolution brings more accurate tests, and constitutes a closed loop.

9 Reference

[1] Xue Jiang, Longbin Tao, Xu Liang, "Development and validation of an AI-based hybrid testing approach for spar-type floating wind turbines ".

[2] X. Jiang, S. Day, D. Clelland, and X. Liang, "Analysis and real-time prediction of the full-scale thrust for floating wind turbine based on artificial intelligence," *Ocean Engineering,* vol. 175, pp. 207-216, 2019/03/01/ 2019, doi: .

[3] X. Jiang, S. Day, and D. Clelland, "An innovative generic platform to simulate real-time PTO damping forces for ocean energy converters based on SIL method," *Ocean Engineering,* vol. 170, pp. 209-221, 2018/12/15/ 2018, doi: .

[4] X. Jiang, S. Day, and D. Clelland, "Hydrodynamic responses and power efficiency analyses of an oscillating wave surge converter under different simulated PTO strategies," *Ocean Engineering,* vol. 170, pp. 286-297, 2018/12/15/ 2018, doi: .

[5] D. Magagna and A. Uihlein, "2014 JRC Ocean Energy Status Report," *European Commission Joint Research Centre,* 2015.

[6] F. d. O. Antonio, "Wave energy utilization: A review of the technologies," *Renewable and sustainable energy reviews,* vol. 14, no. 3, pp. 899-918, 2010.

[7] R. Alamian, R. Shafaghat, S. J. Miri, N. Yazdanshenas, and M. Shakeri, "Evaluation of technologies for harvesting wave energy in Caspian Sea," *Renewable and Sustainable Energy Reviews,* vol. 32, pp. 468-476, 2014.

[8] WindEurope, "Wind in power 2018_Annual combined onshore and offshore wind energy statistics," 2018.

[9] P. Breeze, *Power generation technologies*. Newnes, 2019.

[10] Wikipedia, "Hywind Scotland," in *Wikipedia*, ed , 2018.

[11] M. Folley and T. Whittaker, "Validating a spectral-domain model of an OWC using physical model data," *International Journal of Marine Energy,* vol. 2, pp. 1-11, 2013.

[12] S. Giorgi, J. Davidson, and J. V. Ringwood, "Identification of wave energy device models from numerical wave tank data—Part 2: Data-based model determination," *IEEE Transactions on Sustainable Energy,* vol. 7, no. 3, pp. 1020-1027, 2016.

[13] D. I. Forehand, A. E. Kiprakis, A. J. Nambiar, and A. R. Wallace, "A fully coupled wave-to-wire model of an array of wave energy converters," *IEEE Trans. Sustain. Energy,* vol. 7, no. 1, pp. 118-128, 2016.

[14] M. E. McCormick, *Ocean wave energy conversion*. Courier Corporation, 2013.

[15] J. Falnes, "A review of wave-energy extraction," *Marine Structures,* vol. 20, no. 4, pp. 185-201, 2007.

[16] S. Barstow, G. Mørk, D. Mollison, and J. Cruz, "The Wave Energy Resource," in *Ocean Wave Energy: Current Status and Future Prespectives*, J. Cruz Ed. Berlin, Heidelberg: Springer Berlin Heidelberg, 2008, pp. 93-132.

[17] M. Lehmann, F. Karimpour, C. A. Goudey, P. T. Jacobson, and M.-R. Alam, "Ocean wave energy in the United States: Current status and future perspectives," *Renewable and Sustainable Energy Reviews*, vol. 74, no. Supplement C, pp. 1300-1313, 2017/07/01/ 2017, doi: .

[18] J. Henriques, R. Gomes, L. Gato, A. Falcão, E. Robles, and S. Ceballos, "Testing and control of a power take-off system for an oscillating-water-column wave energy converter," *Renewable Energy*, vol. 85, pp. 714-724, 2016.

[19] J. Hals, J. Falnes, and T. Moan, "Constrained optimal control of a heaving buoy wave-energy converter," *Journal of Offshore Mechanics and Arctic Engineering*, vol. 133, no. 1, p. 011401, 2011.

[20] N. M. Tom, Y.-H. Yu, A. D. Wright, and M. J. Lawson, "Pseudo-spectral control of a novel oscillating surge wave energy converter in regular waves for power optimization including load reduction," *Ocean Engineering*, vol. 137, pp. 352-366, 2017.

[21] J. Hals, J. Falnes, and T. Moan, "A comparison of selected strategies for adaptive control of wave energy converters," *Journal of Offshore Mechanics and Arctic Engineering*, vol. 133, no. 3, p. 031101, 2011.

[22] F. d. O. António, "Phase control through load control of oscillating-body wave energy converters with hydraulic PTO system," *Ocean Engineering*, vol. 35, no. 3, pp. 358-366, 2008.

[23] L. Rusu and F. Onea, "The performance of some state-of-the-art wave energy converters in locations with the worldwide highest wave power," *Renewable and Sustainable Energy Reviews*, vol. 75, pp. 1348-1362, 2017.

[24] P. Maegaard, A. Krenz, and W. Palz, *Wind power for the world: the rise of modern wind energy*. Jenny Stanford, 2013.

[25] P. power. "World’s first floating wind farm has started production." (accessed.

[26] H. S. Hill, "Hywind Scotland, World's First Floating Wind Farm, Performing Better Than Expected," in *Clean Technica. Sustainable Enterproses Media, Inc*, ed, 2018.

[27] O. Tisheva, "Hywind Scotland trumpets 65% capacity factor," ed, 2018.

[28] R. K. Sykes, A. W. Lewis, and G. Thomas, "A numerical and physical comparison of a geometrically simple fixed and floating oscillating water column," in *ASME 2008 27th International Conference on Offshore Mechanics and Arctic Engineering*, 2008: American Society of Mechanical Engineers, pp. 659-668.

[29] R. Ekström, B. Ekergård, and M. Leijon, "Electrical damping of linear generators for wave energy converters—A review," *Renewable and Sustainable Energy Reviews*, vol. 42, pp. 116-128, 2015.

[30] Z. Zang, Q. Zhang, Y. Qi, and X. Fu, "Hydrodynamic responses and efficiency analyses of a heaving-buoy wave energy converter with PTO damping in regular and irregular waves," *Renewable Energy*, vol. 116, pp. 527-542, 2018.

[31] B. Drew, A. R. Plummer, and M. N. Sahinkaya, "A review of wave energy converter technology," ed: Sage Publications Sage UK: London, England, 2009.

[32] A. Henry, P. Schmitt, T. Whittaker, A. Rafiee, and F. Dias, "The characteristics of wave impacts on an oscillating wave surge converter," in *The Twenty-third International Offshore and Polar Engineering Conference*, 2013: International Society of Offshore and Polar Engineers.

[33] E. Renzi and F. Dias, "Hydrodynamics of the oscillating wave surge converter in the open ocean," *European Journal of Mechanics-B/Fluids*, vol. 41, pp. 1-10, 2013.

[34] T. Whittaker, D. Collier, M. Folley, M. Osterried, A. Henry, and M. Crowley, "The development of Oyster—a shallow water surging wave energy converter," in *Proceedings of the 7th European Wave and Tidal Energy Conference, Porto, Portugal*, 2007, pp. 11-14.

[35] F. G. Nielsen, T. D. Hanson, and B. r. Skaare, "Integrated dynamic analysis of floating offshore wind turbines," in *25th international conference on offshore mechanics and arctic engineering*, 2006: American Society of Mechanical Engineers Digital Collection, pp. 671-679.

[36] C. Cermelli, A. Aubault, D. Roddier, and T. McCoy, "Qualification of a semi-submersible floating foundation for multi-megawatt wind turbines," in *Offshore Technology Conference*, 2010: Offshore Technology Conference.

[37] T. Ishihara, M. B. Waris, and H. Sukegawa, "A study on influence of heave plate on dynamic response of floating offshore wind turbine system," in *Proc. of European Offshore Wind Conference & Exhibition*, 2009.

[38] L. Sethuraman and V. Venugopal, "Hydrodynamic response of a stepped-spar floating wind turbine: Numerical modelling and tank testing," *Renewable Energy*, vol. 52, pp. 160-174, 2013.

[39] D. Olinger, E. DeStefano, E. Murphy, K. Naqvi, and G. Tryggvason, "Scale-model experiments on floating wind turbine platforms," in *50th AIAA Aerospace Sciences Meeting including the New Horizons Forum and Aerospace Exposition*, 2012, p. 375.

[40] C. Wehmeyer, F. Ferri, P. B. Frigaard, and J. Skourup, "Experimental study of an offshore wind turbine TLP in ULS conditions," in *The Twenty-third International Offshore and Polar Engineering Conference*, 2013: International Society of Offshore and Polar Engineers.

[41] H. R. Martin, R. W. Kimball, A. M. Viselli, and A. J. Goupee, "Methodology for wind/wave basin testing of floating offshore wind turbines," *Journal of Offshore Mechanics and Arctic Engineering*, vol. 136, no. 2, p. 020905, 2014.

[42] A. J. Goupee, B. J. Koo, R. W. Kimball, K. F. Lambrakos, and H. J. Dagher, "Experimental comparison of three floating wind turbine concepts," *Journal of Offshore Mechanics and Arctic Engineering*, vol. 136, no. 2, p. 020906, 2014.

[43] M. Jeon, S. Lee, and S. Lee, "Unsteady aerodynamics of offshore floating wind turbines in platform pitching motion using vortex lattice method," *Renewable Energy*, vol. 65, pp. 207-212, 2014.

[44] S. Quallen, T. Xing, P. Carrica, Y. Li, and J. Xu, "CFD simulation of a floating offshore wind turbine system using a quasi-static crowfoot mooring-line model,"

in *The Twenty-third International Offshore and Polar Engineering Conference*, 2013: International Society of Offshore and Polar Engineers.

[45] A. J. Coulling, A. J. Goupee, A. N. Robertson, J. M. Jonkman, and H. J. Dagher, "Validation of a FAST semi-submersible floating wind turbine numerical model with DeepCwind test data," *Journal of Renewable and Sustainable Energy*, vol. 5, no. 2, p. 023116, 2013.

[46] T. Chujo, S. Ishida, Y. Minami, T. Nimura, and S. Inoue, "Model experiments on the motion of a spar type floating wind turbine in wind and waves," in *ASME 2011 30th International Conference on Ocean, Offshore and Arctic Engineering*, 2011: American Society of Mechanical Engineers, pp. 655-662.

[47] K. Müller, F. Sandner, H. Bredmose, J. Azcona, A. Manjock, and R. Pereira, "Improved tank test procedures for scaled floating offshore wind turbines," 2014.

[48] B. J. Koo, A. J. Goupee, R. W. Kimball, and K. F. Lambrakos, "Model tests for a floating wind turbine on three different floaters," *Journal of Offshore Mechanics and Arctic Engineering*, vol. 136, no. 2, p. 020907, 2014.

[49] H. Dagher, A. Viselli, A. Goupee, and C. Allen, "1: 50 Scale Testing of Three Floating Wind Turbines at MARIN and Numerical Model Validation Against Test Data," Univ. of Maine, Orno, ME (United States), 2017.

[50] H.-J. Ahn and H. Shin, "Model test & numerical simulation of OC3 spar type floating offshore wind turbine," *International Journal of Naval Architecture and Ocean Engineering*, 2017/11/11/ 2017, doi: .

[51] H. Shin, "Model Test of the OC3-Hywind Floating Offshore Wind Turbine," presented at the The Twenty-first International Offshore and Polar Engineering Conference, Maui, Hawaii, USA, 2011/1/1/, 2011.

[52] J. Azcona *et al.*, "Aerodynamic thrust modelling in wave tank tests of offshore floating wind turbines using a ducted fan," in *Journal of Physics: Conference Series*, 2014, vol. 524, no. 1: IOP Publishing, p. 012089.

[53] L. I. Lago, F. L. Ponta, and A. D. Otero, "Analysis of alternative adaptive geometrical configurations for the NREL-5 MW wind turbine blade," *Renewable Energy*, vol. 59, pp. 13-22, 2013/11/01/ 2013, doi: .

[54] C. Cermelli, D. Roddier, and A. Aubault, "WindFloat: a floating foundation for offshore wind turbines—part II: hydrodynamics analysis," in *ASME 2009 28th International Conference on Ocean, Offshore and Arctic Engineering*, 2009: American Society of Mechanical Engineers Digital Collection, pp. 135-143.

[55] E. E. Bachynski, M. Thys, T. Sauder, V. Chabaud, and L. O. Sæther, "Real-Time Hybrid Model Testing of a Braceless Semi-Submersible Wind Turbine: Part II—Experimental Results," in *ASME 2016 35th International Conference on Ocean, Offshore and Arctic Engineering*, 2016: American Society of Mechanical Engineers, pp. V006T09A040-V006T09A040.

[56] E. E. Bachynski, M. Thys, T. Sauder, V. Chabaud, and L. O. Sæther, "Real-time hybrid model testing of a braceless semi-submersible wind turbine: Part II—Experimental results," in *ASME 2016 35th International Conference on Ocean, Offshore and Arctic Engineering*, 2016: American Society of Mechanical Engineers Digital Collection.

[57] E. E. Bachynski, V. Chabaud, and T. Sauder, "Real-time Hybrid Model Testing of Floating Wind Turbines: Sensitivity to Limited Actuation," *Energy Procedia,* vol. 80, pp. 2-12, 2015, doi: 10.1016/j.egypro.2015.11.400.

[58] I. Bayati, M. Belloli, and A. Facchinetti, "Wind tunnel 2-DOF Hybrid/HIL tests on the OC5 floating offshore wind turbine," in *ASME 2017 36th International Conference on Ocean, Offshore and Arctic Engineering*, 2017: American Society of Mechanical Engineers Digital Collection.

[59] I. Bayati, A. Facchinetti, A. Fontanella, and M. Belloli, "6-DoF hydrodynamic modelling for wind tunnel hybrid/HIL tests of FOWT: the real-time challenge," in *ASME 2018 37th International Conference on Ocean, Offshore and Arctic Engineering*, 2018: American Society of Mechanical Engineers Digital Collection.

[60] T. Sauder, V. Chabaud, M. Thys, E. E. Bachynski, and L. O. Sæther, "Real-time hybrid model testing of a braceless semi-submersible wind turbine: Part I—The hybrid approach," in *ASME 2016 35th International Conference on Ocean, Offshore and Arctic Engineering*, 2016: American Society of Mechanical Engineers Digital Collection.

[61] B. J. Jonkman, "TurbSim user's guide: Version 1.50," National Renewable Energy Lab.(NREL), Golden, CO (United States), 2009.

[62] J. Jonkman, G. Hayman, B. Jonkman, R. Damiani, and R. Murray, "AeroDyn v15 User's Guide and Theory Manual," *NREL: Golden, CO, USA*, 2015.

[63] S. A. Vilsen, T. Sauder, A. J. Sørensen, and M. Føre, "Method for Real-Time Hybrid Model Testing of ocean structures: Case study on horizontal mooring systems," *Ocean Engineering,* vol. 172, pp. 46-58, 2019, doi: 10.1016/j.oceaneng.2018.10.042.

[64] V. Chabaud, "Real-time hybrid model testing of floating wind turbines," 2016.

[65] A. H. Day *et al.*, "Realistic simulation of aerodynamic loading for model testing of floating wind turbines," 2017.

[66] J. E. Carrion and B. F. Spencer Jr, "Model-based strategies for real-time hybrid testing," Newmark Structural Engineering Laboratory. University of Illinois at Urbana …, 1940-9826, 2007.

[67] D. De Klerk, "Dynamic response characterization of complex systems through operational identification and dynamic substructuring-An application to gear noise propagation in the automotive industry," 2009.

[68] D. d. Klerk, D. J. Rixen, and S. Voormeeren, "General framework for dynamic substructuring: history, review and classification of techniques," *AIAA journal,* vol. 46, no. 5, pp. 1169-1181, 2008.

[69] G. Li, "A generic dynamically substructured system framework and its dual counterparts," *IFAC Proceedings Volumes,* vol. 47, no. 3, pp. 10101-10106, 2014.

[70] X. Shao and C. Griffith, "An overview of hybrid simulation implementations in NEES projects," *Engineering Structures,* vol. 56, pp. 1439-1451, 2013.

[71] A. Pinto, P. Pegon, G. Magonette, and G. Tsionis, "Pseudo-dynamic testing of bridges using non-linear substructuring," *Earthquake Engineering & Structural Dynamics,* vol. 33, no. 11, pp. 1125-1146, 2004.

[72] O. S. Bursi, C. Jia, and Z. Wang, "Monolithic and partitioned L-Stable Rosenbrock methods for dynamic substructure tests," 2009.

[73] V. Johansen, "Modelling of flexible slender systems for real-time simulation and control applications," 2007.

[74] A. Maghareh, S. J. Dyke, A. Prakash, and G. B. Bunting, "Establishing a predictive performance indicator for real-time hybrid simulation," *Earthquake Engineering & Structural Dynamics,* vol. 43, no. 15, pp. 2299-2318, 2014.

[75] Y. Kyrychko, K. Blyuss, A. Gonzalez-Buelga, S. Hogan, and D. Wagg, "Real-time dynamic substructuring in a coupled oscillator–pendulum system," *Proceedings of the Royal Society A: Mathematical, Physical and Engineering Sciences,* vol. 462, no. 2068, pp. 1271-1294, 2006.

[76] V. Chabaud, S. Steen, and R. Skjetne, "Real-time hybrid testing for marine structures: challenges and strategies," in *ASME 2013 32nd International Conference on Ocean, Offshore and Arctic Engineering*, 2013: American Society of Mechanical Engineers Digital Collection.

[77] Y. Cao and G. Tahchiev, "A study on an active hybrid decomposed mooring system for model testing in ocean basin for offshore platforms," in *ASME 2013 32nd International Conference on Ocean, Offshore and Arctic Engineering*, 2013: American Society of Mechanical Engineers, pp. V001T01A080-V001T01A080.

[78] P. Lamont-Kane, M. Folley, and T. Whittaker, "Investigating uncertainties in physical testing of wave energy converter arrays," in *Proceedings, 10th European Wave and Tidal Energy Conference (EWTEC 2013), Aalborg, Denmark*, 2013.

[79] T. Whittaker and M. Folley, "Nearshore oscillating wave surge converters and," 2011.

[80] A. Henry, K. Doherty, L. Cameron, T. Whittaker, and R. Doherty, "Advances in the design of the Oyster wave energy converter," in *RINA Marine and Offshore Energy Conference*, 2010.

[81] T. Whittaker and M. Folley, "Nearshore oscillating wave surge converters and the development of Oyster," *Phil. Trans. R. Soc. A,* vol. 370, no. 1959, pp. 345-364, 2012. [Online]. Available: .

[82] A. G. Piersol and C. M. Harris, *Harri's Shock and Vibration Handbook Fifth Edition*. Mcgraw-hill, 2017.

[83] M. Li, "Three classes of fractional oscillators," *Symmetry*, vol. 10, no. 2, p. 40, 2018.

[84] M. Li, "Fractal time series—a tutorial review," *Mathematical Problems in Engineering*, vol. 2010, 2010.

[85] Y.-B. He, J.-X. Luo, X.-D. Li, Z.-Z. Gao, and Z. Wen, "Evidence of internal-wave and internal-tide deposits in the Middle Ordovician Xujiajuan Formation of the Xiangshan Group, Ningxia, China," *Geo-Marine Letters*, vol. 31, no. 5-6, pp. 509-523, 2011.

[86] I. ITTC, "Recommended Procedures and Guidelines," *Resistance Test,* 2011.

[87] S. J. Russell and P. Norvig, *Artificial intelligence: a modern approach*. Malaysia; Pearson Education Limited, 2016.

[88] C. Petzold, *The annotated Turing: a guided tour through Alan Turing's historic paper on computability and the Turing machine*. Wiley Publishing, 2008.

[89] N. J. Nilsson, *Principles of artificial intelligence*. Morgan Kaufmann, 2014.

[90] E. Guresen, G. Kayakutlu, and T. U. Daim, "Using artificial neural network models in stock market index prediction," *Expert Systems with Applications*, vol. 38, no. 8, pp. 10389-10397, 2011.

[91] M. H. Esfe, M. R. H. Ahangar, M. Rejvani, D. Toghraie, and M. H. Hajmohammad, "Designing an artificial neural network to predict dynamic viscosity of aqueous nanofluid of TiO2 using experimental data," *International Communications in Heat and Mass Transfer*, vol. 75, pp. 192-196, 2016.

[92] J. Jonkman, S. Butterfield, W. Musial, and G. Scott, "Definition of a 5-MW reference wind turbine for offshore system development," *National Renewable Energy Laboratory, Golden, CO, Technical Report No. NREL/TP-500-38060*, 2009.

[93] J. Jonkman, *Definition of the Floating System for Phase IV of OC3*. 2010.

[94] "2.019 Design of Ocean System_Lecture 9," in *Ocean Wave Environment*, ed, 2011.

[95] J. M. Jonkman, *Definition of the Floating System for Phase IV of OC3*. Citeseer, 2010.

[96] J. Jonkman, A. Robertson, and G. Hayman, "HydroDyn user's guide and theory manual," *National Renewable Energy Laboratory*, 2014.

[97] J. Jonkman and L. Kilcher, "TurbSim User's Guide: Version 1.06. 00, National Renewable Energy Laboratory," Technical Report. Draft available at: . nrel. gov/designcodes/preprocessors/turbsim/TurbSim. pdf, 2012.

[98] H. M. Irvine and H. M. Irvine, *Cable structures*. MIT press Cambridge, MA, 1981.

[99] M. Masciola, "Map++ Documentation Release 1.15," Technical report, National Renewable Energy Laboratory-NREL, 2016.

[100] S. Guntur *et al.*, "FAST v8 verification and validation for a MW-scale wind turbine with aeroelastically tailored blades," in *34th wind energy symposium*, 2016, p. 1008.

[101] A. J. Goupee, R. W. Kimball, and H. J. Dagher, "Experimental observations of active blade pitch and generator control influence on floating wind turbine response," *Renewable Energy*, vol. 104, pp. 9-19, 2017.

[102] M. Hall, A. Goupee, and J. Jonkman, "Development of performance specifications for hybrid modeling of floating wind turbines in wave basin tests," *Journal of Ocean Engineering and Marine Energy*, vol. 4, no. 1, pp. 1-23, 2018.

[103] A. Jain, " Butterworth Filter (), MATLAB Central File Exchange. Retrieved July 12, 2020.," ed, 2020.

[104] W. Oberkampf, J. Helton, and K. Sentz, "Mathematical representation of uncertainty," 2001, doi: 10.2514/6.2001-1645.

[105] R. D. Moser and T. A. Oliver, "Validation of Physical Models in the Presence of Uncertainty," pp. 129-156, 2017, doi: 10.1007/978-3-319-12385-1_2.

[106] "We help people measure and analyze motion." (accessed.

[107] J. M. Jonkman and M. L. Buhl Jr, "FAST user's guide," *National Renewable Energy Laboratory, Golden, CO, Technical Report No. NREL/EL-500-38230,* 2005.

[108] X. Jiang. Tank test database for FOWT

Appendix 1 List of drop tests for PTO simulator

For Linear PTO

mass(g)	v20a(rpm)	v20b(rpm	v20c(rpm)	mean	std	c20a(A)	c20b(A)	c20b(A)	std	v40a(rpm)	v40b(rpm)	v40c(rpm)	std	c40a(A)	c40b(A)	c40c(A)	std
400	14.71166	14.80501	14.79896	14.77188	0.0522	0.30793663	0.309463	0.308817	0.0008	7.6106293	7.861395	7.56764	0.1587	0.312681	0.294953	0.318654	0.0123
500	20.99338	20.95195	20.91949	20.95494	0.037	0.47652975	0.476822	0.473881	0.0016	10.526692	10.436822	10.32442	0.1013	0.458078	0.42367	0.460239	0.0205
600	27.6805	27.93069	27.59912	27.73677	0.1728	0.64183066	0.639051	0.639105	0.0016	14.801071	14.76541	14.65206	0.0778	0.652083	0.632015	0.665038	0.0166
700	30.41556	30.16191	30.14855	30.242	0.1505	0.80153977	0.802748	0.799636	0.0016	17.435654	17.50215	17.32107	0.0916	0.814306	0.809762	0.834077	0.0129
800	36.86287	36.91986	36.86253	36.88175	0.033	0.9777161	0.972634	0.974109	0.0026	21.482367	21.54329	21.39675	0.0736	0.976136	0.856098	1.023862	0.0864
900	42.18642	41.81263	41.70209	41.90038	0.2538	1.1436047	1.141071	1.135949	0.0039	23.967877	24.19183	24.09342	0.1122	1.150368	1.156439	1.149688	0.0037
1000	45.73228	45.75364	45.65007	45.712	0.0547	1.3161889	1.32192	1.31863	0.0029	26.277582	26.31308	26.36013	0.0414	1.311415	1.32585	1.320064	0.0073
1100	52.12095	52.56304	52.83712	52.50703	0.3614	1.4757655	1.471131	1.479389	0.0041	30.42267	30.44596	30.44321	0.0127	1.484749	1.491296	1.487769	0.0033
1200	54.90818	55.14335	54.66268	54.90474	0.2404	1.6318953	1.632424	1.633994	0.0011	32.502629	32.3412	32.67032	0.1646	1.639376	1.624599	1.663202	0.0195
1300	61.36008	61.32431	61.44163	61.37534	0.0601	1.7980383	1.792564	1.794474	0.0028	34.509109	34.49765	34.90234	0.2304	1.81291	1.81094	1.80996	0.0015
1400	65.07874	65.81409	66.64131	65.84471	0.7817	1.9695889	1.972532	1.971229	0.0015	38.606248	38.50643	38.56789	0.0504	1.991387	2.003401	2.998032	0.5777
1500	70.41527	69.92423	70.04576	70.12842	0.2557	2.1376963	2.141901	2.140863	0.0022	41.315802	41.09296	41.23095	0.1125	2.156945	2.150924	2.160122	0.0047
1600	76.44028	75.9773	75.96812	76.12857	0.27	2.2923323	2.300987	2.3096	0.0086	43.578462	42.85518	43.61153	0.4275	2.336742	2.326007	2.355629	0.015
-400	-15.4171	-15.3271	-14.9002	-15.2148	0.2762	-0.28079171	-0.28322	-0.28258	0.0013	-8.6932113	-8.87604	-9.07467	0.1908	-0.27387	-0.26837	-0.258463	0.0078
-500	-20.1133	-20.2503	-20.3169	-20.2268	0.1038	-0.44364796	-0.4395	-0.44481	0.0028	-13.620162	-13.70932	-13.6076	0.0554	-0.4453	-0.44509	-0.44397	0.0007
-600	-26.9408	-26.7761	-25.6798	-26.4656	0.6854	-0.6065989	-0.60505	-0.60783	0.0014	-15.782657	-15.69301	-15.9055	0.1067	-0.61609	-0.62091	-0.614033	0.0035
-700	-30.3142	-29.8945	-29.5565	-29.9217	0.3796	-0.77741171	-0.7774	-0.78564	0.0048	-18.168846	-18.59194	-18.4307	0.2135	-0.78274	-0.80769	-0.794021	0.0125
-800	-36.1107	-36.2962	-36.2393	-36.2154	0.095	-0.95262744	-0.95372	-0.957	0.0023	-22.944686	-22.87041	-22.908	0.0371	-0.95068	-0.95437	-0.96201	0.0058
-900	-38.7793	-39.2851	-40.2501	-39.4381	0.7472	-1.1195892	-1.12569	-1.12005	0.0034	-23.605796	-24.3155	-24.2056	0.382	-1.15063	-1.15732	-1.14872	0.0045
-1000	-44.5064	-44.2181	-44.3779	-44.3674	0.1444	-1.2828096	-1.29876	-1.282	0.0095	-27.001719	-27.07676	-26.8337	0.1245	-1.28616	-1.28505	-1.284322	0.0009
-1100	-51.5897	-51.6164	-51.3613	-51.5225	0.1402	-1.4572784	-1.45644	-1.45446	0.0014	-30.786724	-30.80603	-30.7962	0.0097	-1.47207	-1.4806	-1.47001	0.0056
-1200	-53.9394	-53.9308	-53.8444	-53.9049	0.0525	-1.6248143	-1.62678	-1.62587	0.001	-33.271834	-33.32016	-33.4011	0.0653	-1.62201	-1.6211	-1.619941	0.001
-1300	-60.5235	-60.1414	-60.181	-60.282	0.2101	-1.7855881	-1.80054	-1.79805	0.008	-35.01003	-35.0021	-35.23	0.1294	-1.77092	-1.77102	-1.77028	0.0004
-1400	-62.6704	-63.1523	-62.4747	-62.7658	0.3487	-1.9530048	-1.95289	-1.95618	0.0019	-38.802107	-38.79002	-38.9021	0.0615	-1.96061	-1.96023	-1.97001	0.0055
-1500	-68.6956	-68.8853	-69.0578	-68.8796	0.1812	-2.126425	-2.13153	-2.12122	0.0052	-40.84267	-40.86557	-40.2231	0.3645	-2.13011	-2.12937	-2.13203	0.0014
-1600	-72.9954	-72.2408	-71.3445	-72.1936	0.8265	-2.302942	-2.3005	-2.2939	0.0047	-43.117454	-43.71365	-43.6776	0.3343	-2.29511	-2.30262	-2.296059	0.0041

mass(g)	v60			std	c60			std	v80			std	c80			std
400	6.258989	6.202725	6.262789	0.0336	0.3185849	0.32084888	0.321178	0.0014	4.1737023	4.10307	4.068653	0.0536	0.311692	0.3302	0.31367	0.0102
500	9.007378	9.054481	9.037088	0.0238	0.4855885	0.48604349	0.486628	0.0005	5.9377369	6.00781	5.98823	0.0362	0.494832	0.50816	0.49223	0.0085
600	11.4895	11.74056	11.4987	0.1424	0.6468932	0.65196946	0.655714	0.0044	8.4548959	8.53207	8.46012	0.0431	0.667808	0.66242	0.65009	0.0091
700	13.13373	13.25794	13.34006	0.1039	0.8182837	0.81892951	0.822389	0.0022	10.509148	10.50202	10.59895	0.054	0.877009	0.88113	0.89203	0.0078
800	14.63401	14.57388	14.78756	0.1102	0.9843395	0.98526115	0.993223	0.0049	11.547648	11.48723	11.62091	0.0669	1.017664	1.02001	1.01802	0.0013
900	17.30781	17.32159	17.42548	0.0643	1.1532331	1.1535111	1.158872	0.0032	12.88133	12.8762	12.89083	0.0074	1.168662	1.16901	1.166309	0.0015
1000	19.53024	19.8064	19.95336	0.2148	1.320053	1.3220825	1.32169	0.0011	14.130939	14.1293	14.13129	0.0011	1.333121	1.3332	1.33204	0.0006
1100	21.32221	21.34069	21.35166	0.0149	1.4913677	1.4893542	1.49821	0.0046	16.98185	16.95401	16.91202	0.0352	1.506582	1.50023	1.500738	0.0035
1200	22.85935	22.78457	22.88613	0.0526	1.6704556	1.6703487	1.676586	0.0036	18.360383	18.51027	18.58216	0.1132	1.673076	1.68821	1.697977	0.0125
1300	25.50069	25.43546	25.42668	0.0404	1.8454669	1.8442682	1.847197	0.0015	19.637111	19.67801	19.69001	0.0277	1.84841	1.848209	1.846721	0.0009
1400	27.85168	27.98587	27.76387	0.1118	2.0089903	2.0154075	2.009382	0.0036	21.185615	21.1774	21.1869	0.0052	2.028032	2.02793	2.02901	0.0006
1500	29.44093	29.47518	29.47231	0.019	2.1836399	2.1860259	2.17688	0.0047	24.890812	24.9003	24.65006	0.1418	2.269234	2.26773	2.26529	0.002
1600	30.72975	30.82482	30.68106	0.0731	2.3421341	2.3468372	2.35708	0.0076	23.568977	23.78921	24.05631	0.244	2.329504	2.324	2.353142	0.0155
-400	-6.00217	-6.30674	-6.3966	0.2067	-0.279198	-0.28514327	-0.28805	0.0045	-4.4845536	-4.49224	-4.4788	0.0067	-0.27684	-0.27812	-0.27901	0.0011
-500	-9.83521	-9.92904	-9.98012	0.0735	-0.4747107	-0.47439636	-0.47527	0.0004	-6.768381	-6.81034	-6.66201	0.0765	-0.47655	-0.47599	-0.47703	0.0005
-600	-11.49	-11.6513	-11.6099	0.0838	-0.6467741	-0.64682114	-0.64708	0.0002	-9.8057036	-9.822	-9.849649	0.0222	-0.65465	-0.65392	-0.65425	0.0004
-700	-13.8096	-13.6422	-13.6046	0.1091	-0.8179099	-0.81683061	-0.82137	0.0024	-11.150278	-11.0992	-11.27033	0.0879	-0.81241	-0.82305	-0.81935	0.0054
-800	-16.0169	-16.0491	-15.7894	0.1416	-0.9948235	-0.99056125	-0.98652	0.0042	-12.443674	-12.4203	-12.40785	0.0182	-0.98286	-1.00327	-1.00137	0.0113
-900	-18.3583	-18.4074	-18.3961	0.0257	-1.1549708	-1.1677962	-1.16591	0.0069	-13.654543	-13.3211	-13.54444	0.1699	-1.16654	-1.1653	-1.16173	0.0025
-1000	-19.6698	-19.6358	-19.6148	0.0278	-1.3315653	-1.3270469	-1.32252	0.0045	-14.949174	-14.89226	-15.0321	0.0703	-1.32727	-1.32931	-1.32485	0.0022
-1100	-21.6289	-21.4903	-21.912	0.2149	-1.4981655	-1.5095211	-1.50204	0.0058	-17.604983	-17.6448	-17.61155	0.0213	-1.50698	-1.50932	-1.51308	0.0031
-1200	-24.2098	-23.919	-24.0642	0.1454	-1.6694899	-1.6683109	-1.66871	0.0006	-19.364581	-19.5609	-19.2903	0.1398	-1.68077	-1.68121	-1.68301	0.0012
-1300	-26.4903	-26.3244	-26.4324	0.0842	-1.8464628	-1.8406136	-1.84646	0.0034	-20.153884	-20.2088	-20.19884	0.0293	-1.81623	-1.81003	-1.81229	0.0031
-1400	-27.7081	-27.842	-27.946	0.1193	-2.0121083	-2.0190862	-2.02472	0.0063	-21.669715	-21.7032	-21.85453	0.0985	-2.03356	-2.02633	-2.01907	0.0072
-1500	-30.1484	-30.1757	-29.9538	0.121	-2.1932103	-2.1878345	-2.19454	0.0036	-23.356591	-23.412	-23.2977	0.0572	-2.19779	-2.19488	-2.20411	0.0047
-1600	-72.9954	-72.2408	-71.3445	-72.1936	0.8265	-2.302942	-2.3005	-2.2939	0.0047	-43.117454	-43.71365	-43.6776	0.3343	-2.29511	-2.30262	-2.296059	

v100			std	c100			std	v120		std	c120			std	mass(g)
4.039839	4.05572	4.04221	0.0086	0.309316	0.308914	0.309215	0.0002	3.871375	3.90732	0.0254	0.30838	0.321801	0.0095	0.003	400
5.445202	5.53291	5.4872	0.0439	0.477815	0.47842	0.475792	0.0014	4.946475	4.87321	0.0518	0.483886	0.482177	0.0012	0.0025	500
6.300973	6.640265	6.53981	0.1743	0.639664	0.666182	0.6528	0.0133	6.353891	6.340575	0.0094	0.669024	0.661219	0.0055	0.0042	600
8.03729	8.04281	8.14629	0.0614	0.817553	0.82053	0.818729	0.0015	7.426333	7.43162	0.0037	0.837636	0.840284	0.0019	0.004	700
9.566314	9.57812	9.6132	0.0244	1.016496	1.01284	1.01745	0.0024	8.265154	8.263349	0.0013	1.0118	1.010181	0.0011	0.001	800
11.08876	11.0375	11.04752	0.0272	1.170805	1.168484	1.16503	0.0029	9.280483	9.31316	0.0231	1.183958	1.184639	0.0005	0.0018	900
11.9979	12.07391	12.06315	0.0411	1.334937	1.345052	1.342323	0.0052	10.69855	10.66037	0.027	1.354754	1.358243	0.0025	0.0021	1000
13.81363	13.88137	13.85291	0.034	1.508536	1.508799	1.50793	0.0004	12.0723	12.13757	0.0462	1.5254	1.529086	0.0026	0.0025	1100
14.86987	14.6544	14.71933	0.1105	1.693389	1.691204	1.69335	0.0013	13.38712	13.3971	0.0071	1.699118	1.70075	0.0012	0.001	1200
15.98366	16.09632	16.0211	0.0574	1.850706	1.85384	1.85394	0.0018	14.57316	14.38749	0.1313	1.861065	1.83271	0.02	0.0018	1300
17.16025	17.20136	17.19283	0.0217	2.02743	2.02457	2.02804	0.0019	15.52774	15.31989	0.147	2.045151	2.024614	0.0145	0.0103	1400
18.37552	18.65886	18.45821	0.1457	2.193937	2.199845	2.19743	0.003	15.98394	15.89976	0.0595	2.209122	2.2124	0.0023	0.0019	1500
19.84781	19.8972	19.90425	0.0308	2.363783	2.36438	2.36095	0.0018	17.07327	17.02524	0.034	2.382148	2.389202	0.005	0.0037	1600
-3.75539	-4.22905	-4.03281	0.238	-0.29471	-0.32288	-0.30772	0.0141	-2.79937	-2.85088	0.0364	-0.29552	-0.30213	0.0047	0.0015	400
-5.36702	-5.83251	-5.83289	0.2689	-0.47653	-0.47829	-0.47225	0.0031	-4.41373	-4.45826	0.0315	-0.49932	-0.50101	0.0012	0.0008	500
-7.13918	-7.16283	-7.21003	0.0361	-0.6722	-0.67877	-0.67493	0.0033	-5.90865	-6.23879	0.2334	-0.66824	-0.6872	0.0134	0.0013	600
-8.27972	-8.27328	-8.27534	0.0033	-0.82814	-0.83824	-0.82439	0.0072	-7.33551	-7.26581	0.0493	-0.84633	-0.84982	0.0025	0.0016	700
-9.4657	-9.5519	-9.4528	0.0539	-0.99587	-1.00104	-1.00732	0.0057	-8.2665	-8.31394	0.0336	-1.01877	-1.0203	0.0011	0.0075	800
-11.0479	-11.0537	-11.0428	0.0054	-1.16537	-1.1679	-1.16538	0.0015	-8.94698	-9.07056	0.0874	-1.19119	-1.19094	0.0002	0.0598	900
-11.8328	-12.2578	-12.2159	0.2342	-1.33634	-1.33927	-1.33927	0.0017	-9.97708	-10.0097	0.0231	-1.36508	-1.36963	0.0032	0.0024	1000
-13.6937	-13.7762	-13.7732	0.0468	-1.50787	-1.50825	-1.50835	0.0003	-11.3533	-11.3048	0.0343	-1.53802	-1.53693	0.0008	0.0007	1100
-14.6373	-14.6524	-13.6432	0.5784	-1.67541	-1.67831	-1.67433	0.0021	-12.5531	-12.6821	0.0912	-1.70819	-1.71142	0.0023	0.0016	1200
-16.181	-16.092	-16.1232	0.0452	-1.86516	-1.85188	-1.86303	0.0071	-13.7372	-13.7525	0.0108	-1.8718	-1.87245	0.0005	0.0006	1300
-16.9932	-16.9928	-17.0023	0.0372	-2.0161	-2.01698	-2.0132	0.002	-15.0074	-15.0393	0.0226	-2.04004	-2.03704	0.0021	0.0049	1400
-18.3822	-18.2784	-18.3217	0.0521	-2.19994	-2.18603	-2.19324	0.007	-16.0517	-16.079	0.0193	-2.20839	-2.20624	0.0015	0.0011	1500

For Nonlinear PTO

mass	v40		std	meanv40	c40		meanc40	v80		std	meanv80	c80		meanc80	v120		std	meanv120
300	24.853865	24.69474	0.1125	24.7743	0.130897	0.123436	0.127166	24.85387	24.69474	0.1125	24.7743	0.14157	0.137025	0.139297	14.29987	15.29299	0.7022	14.79643
400	33.443864	34.17311	0.5157	33.80849	0.288438	0.293591	0.291014	33.44386	34.17311	0.5157	33.80849	0.296284	0.299873	0.298079	25.8481	25.97342	0.0886	25.91076
500	44.616777	44.52832	0.0625	44.57255	0.44914	0.440755	0.444947	44.61678	44.52832	0.0625	44.57255	0.469715	0.470802	0.470259	30.66867	30.59277	0.0537	30.63072
600	48.965871	48.45578	0.3607	48.71082	0.629799	0.628361	0.62908	48.96587	48.45578	0.3607	48.71082	0.63969	0.63688	0.638285	36.04565	36.37486	0.2328	36.21026
700	58.101687	58.17907	0.0547	58.14038	0.781189	0.790013	0.785601	58.10169	58.17907	0.0547	58.14038	0.808304	0.807192	0.807748	39.21684	39.31588	0.07	39.26636
800	63.668852	63.64	0.0204	63.65443	0.955961	0.957208	0.956584	63.66885	63.64	0.0204	63.65443	0.985065	0.980735	0.9829	44.81533	44.72951	0.0607	44.77242
900	68.761356	68.6194	0.1004	68.69038	1.122163	1.135959	1.129061	68.76136	68.6194	0.1004	68.69038	1.15565	1.150134	1.152892	48.1137	48.38339	0.1907	48.24854
1000	76.595022	75.97389	0.4392	76.28446	1.286864	1.297406	1.292135	76.59502	75.97389	0.4392	76.28446	1.322208	1.318848	1.320528	50.76911	50.73727	0.0225	50.75319
1100	78.716338	79.02727	0.2199	78.87181	1.457506	1.457472	1.457489	78.71634	79.02727	0.2199	78.87181	1.481501	1.491641	1.486571	53.40617	53.28664	0.0845	53.34641
1200	85.526342	85.68087	0.1093	85.6036	1.634383	1.628894	1.631638	85.52634	85.68087	0.1093	85.6036	1.657458	1.656227	1.656842	56.26025	57.06695	0.5704	56.6636
1300	88.010991	88.78267	0.5457	88.39683	1.79618	1.795207	1.795693	88.01099	88.78267	0.5457	88.39683	1.824434	1.825695	1.825064	59.01682	59.0166	0.0002	59.01671
1400	94.455659	94.22841	0.1607	94.34203	1.951303	1.960431	1.955867	94.45566	94.22841	0.1607	94.34203	2.010657	2.010657	2.010657	61.57966	61.68674	0.0757	61.6332
1500	99.754275	99.38391	0.2619	99.56909	2.127394	2.120684	2.124039	99.75428	99.38391	0.2619	99.56909	2.160765	2.160765	2.160765	64.07369	64.27147	0.1398	64.17258
1600	101.85921	101.7768	0.0583	101.818	2.28918	2.29571	2.292445	101.8592	101.7768	0.0583	101.818	2.339501	2.335847	2.337674	66.52949	66.53137	0.0013	66.53043
-300	-25.871052	-25.0183	0.603	-25.4447	-0.11811	-0.12043	-0.11927	-25.8711	-25.0183	0.603	-25.4447	-0.12544	-0.12737	-0.12641	-20.7658	-20.6639	0.0721	-20.7149
-400	-30.285891	-30.8866	0.4248	-30.5862	-0.2885	-0.28804	-0.28827	-30.2859	-30.8866	0.4248	-30.5862	-0.28639	-0.29503	-0.29071	-27.2739	-27.4975	0.1581	-27.3857
-500	-45.002375	-44.5916	0.2905	-44.797	-0.44541	-0.44243	-0.44392	-45.0024	-44.5916	0.2905	-44.797	-0.44596	-0.45326	-0.44961	-34.1703	-34.3693	0.1407	-34.2698
-600	-47.303968	-47.8593	0.3926	-47.5816	-0.5979	-0.60529	-0.6016	-47.304	-47.8593	0.3926	-47.5816	-0.61339	-0.61816	-0.61577	-35.1893	-35.4017	0.1501	-35.2955
-700	-58.00454	-58.4872	0.3413	-58.2459	-0.76468	-0.76942	-0.76705	-58.0045	-58.4872	0.3413	-58.2459	-0.78806	-0.79089	-0.78947	-39.7758	-39.7917	0.0112	-39.7838
-800	-61.310388	-61.5224	0.1499	-61.4164	-0.94225	-0.93941	-0.94083	-61.3104	-61.5224	0.1499	-61.4164	-0.96936	-0.96704	-0.9682	-45.1901	-44.2751	0.647	-44.7326
-900	-68.340287	-68.506	0.1172	-68.4231	-1.10164	-1.10535	-1.1035	-68.3403	-68.506	0.1172	-68.4231	-1.137	-1.14591	-1.14145	-47.2963	-47.6627	0.2591	-47.4795
-1000	-71.61863	-71.8674	0.1759	-71.743	-1.2717	-1.26716	-1.26943	-71.6186	-71.8674	0.1759	-71.743	-1.31165	-1.30954	-1.3106	-51.2912	-51.6602	0.2609	-51.4757
-1100	-78.929869	-78.8162	0.0804	-78.873	-1.42714	-1.43127	-1.4292	-78.9299	-78.8162	0.0804	-78.873	-1.48521	-1.48039	-1.4828	-54.0552	-53.7107	0.2436	-53.8829
-1200	-82.386595	-83.2816	0.6328	-82.8341	-1.59553	-1.59274	-1.59413	-82.3866	-83.2816	0.6328	-82.8341	-1.6479	-1.64895	-1.64843	-57.157	-57.8288	0.475	-57.4929
-1300	-88.066907	-88.0669	0	-88.0669	-1.75442	-1.75442	-1.75442	-88.0669	-88.0669	0	-88.0669	-1.81359	-1.98144	-1.89751	-60.0222	-59.9404	0.0578	-59.9813
-1400	-94.521189	-94.617	0.0677	-94.5691	-1.94713	-1.95441	-1.95077	-94.5212	-94.617	0.0677	-94.5691	-1.97998	-1.97618	-1.97808	-62.4475	-62.3483	0.0702	-62.3979
-1500	-96.535676	-96.7116	0.1244	-96.6236	-2.11247	-2.10595	-2.10921	-96.5357	-96.7116	0.1244	-96.6236	-2.15896	-2.15896	-2.15896	-64.3613	-64.0897	0.192	-64.2255
-1600	-102.7359	-102.736	0	-102.736	-2.29491	-2.29491	-2.29491	-102.736	-102.736	0	-102.736	-2.28525	-2.28525	-2.28525	-67.4157	-67.311	0.074	-67.3633

c120		meanc120	v160		std	meanv160	c160		meanc160	v200		std	meanv200	c200		meanc200	mass
0.142108	0.145011	0.14356	13.98816	15.02233	0.7313	14.50524	0.160768	0.156085	0.158426	17.37328	17.37328	0	17.37328	0.156832	0.156832	0.156832	300
0.313799	0.312585	0.313192	23.99988	23.62633	0.2641	23.8131	0.328882	0.325615	0.327248	21.61447	21.69874	0.0596	21.65661	0.32934	0.328164	0.328752	400
0.477294	0.47812	0.477707	28.86578	29.06473	0.1407	28.96525	0.495375	0.497245	0.49631	26.24359	26.29773	0.0383	26.27066	0.492998	0.497646	0.495322	500
0.650557	0.650322	0.65044	33.30619	33.28388	0.0158	33.29504	0.677642	0.660608	0.669125	30.33873	30.14355	0.138	30.24114	0.646863	0.656214	0.651538	600
0.821019	0.820296	0.820657	35.98087	36.15908	0.126	36.06998	0.832029	0.830312	0.831171	34.14897	33.89082	0.1825	34.0199	0.824712	0.827488	0.8261	700
0.988666	1.002746	0.995706	39.32595	39.25602	0.0494	39.29099	1.004022	0.999939	1.001981	36.38691	36.60279	0.1527	36.49485	0.993942	0.995375	0.994659	800
1.146194	1.155169	1.150681	43.46318	43.32477	0.0979	43.39397	1.173286	1.169281	1.171283	38.90898	38.97945	0.0498	38.94421	1.164221	1.163372	1.163797	900
1.321636	1.325068	1.323352	45.92719	46.14863	0.1566	46.03791	1.341267	1.338834	1.340051	41.31591	41.45931	0.1014	41.38761	1.323659	1.323694	1.323676	1000
1.496989	1.496976	1.496982	48.04306	48.14339	0.0709	48.09322	1.513675	1.508406	1.511041	43.54949	43.54949	0	43.54949	1.491719	1.491719	1.491719	1100
1.661796	1.664186	1.662991	50.55852	50.60211	0.0308	50.58032	1.688041	1.678143	1.683092	45.70814	45.78765	0.0562	45.7479	1.657313	1.660491	1.658902	1200
1.835415	1.833014	1.834215	53.24537	53.08216	0.1154	53.16376	1.848472	1.854132	1.851302	48.4028	48.33633	0.047	48.36956	1.827764	1.825226	1.826495	1300
1.995174	2.00257	1.998872	55.58954	55.75505	0.117	55.6723	2.016838	2.026333	2.021586	49.54871	49.78448	0.1667	49.6666	1.997927	1.993268	1.995598	1400
2.167512	2.174054	2.170783	57.77803	57.77803	0	57.77803	2.188595	2.188595	2.188595	51.51825	51.28179	0.1672	51.40002	2.168609	2.157119	2.162864	1500
2.33518	2.332128	2.333654	60.05749	60.17279	0.0815	60.11514	2.357685	2.359696	2.35869	53.63754	53.58775	0.0352	53.61264	2.355924	2.35989	2.357907	1600
-0.14574	-0.14843	-0.14708	-21.0132	-20.1347	0.6212	-20.574	-0.15254	-0.15099	-0.15177	-16.1151	-16.1151	0	-16.1151	-0.15043	-0.15043	-0.15043	300
-0.31287	-0.30986	-0.31136	-24.0774	-24.2793	0.1428	-24.1784	-0.31934	-0.31525	-0.31729	-21.3291	-21.4319	0.0727	-21.3805	-0.30251	-0.31164	-0.30708	400
-0.48186	-0.48527	-0.48356	-29.7454	-29.742	0.0025	-29.7437	-0.47938	-0.48195	-0.48067	-26.64	-26.5847	0.0391	-26.6124	-0.45911	-0.45238	-0.45575	500
-0.62879	-0.61733	-0.62306	-33.8112	-33.6905	0.0854	-33.7508	-0.64582	-0.64984	-0.64783	-30.9903	-30.7389	0.1778	-30.8646	-0.61999	-0.62625	-0.62312	600
-0.81816	-0.81493	-0.81654	-36.6243	-36.7788	0.1092	-36.7015	-0.81284	-0.81383	-0.81334	-33.2588	-33.218	0.0289	-33.2384	-0.79689	-0.80101	-0.79895	700
-0.96898	-0.98281	-0.97589	-40.051	-40.0867	0.0253	-40.0689	-0.98946	-0.98629	-0.98787	-35.6035	-35.6276	0.017	-35.6155	-0.9704	-0.97649	-0.97344	800
-1.15248	-1.15138	-1.15193	-42.713	-42.6327	0.0567	-42.6728	-1.15138	-1.15227	-1.15183	-39.7996	-39.7996	0	-39.7996	-1.14828	-1.14828	-1.14828	900
-1.31441	-1.30034	-1.30738	-46.0185	-46.0259	0.0052	-46.0222	-1.32174	-1.3118	-1.31677	-42.2664	-42.2776	0.008	-42.272	-1.32101	-1.31847	-1.31974	1000
-1.4885	-1.47952	-1.48401	-48.5817	-48.5231	0.0414	-48.5524	-1.49083	-1.49318	-1.49201	-43.5491	-43.7486	0.1411	-43.6489	-1.50751	-1.50022	-1.50386	1100
-1.664	-1.6667	-1.66535	-50.8585	-51.1026	0.1727	-50.9805	-1.66294	-1.664	-1.66347	-46.4257	-46.1454	0.1983	-46.2855	-1.65846	-1.65926	-1.65886	1200
-1.82447	-1.82459	-1.82453	-52.7313	-52.8876	0.1105	-52.8094	-1.81847	-1.82513	-1.8218	-47.8838	-47.7945	0.0631	-47.8392	-1.82964	-1.83002	-1.82983	1300
-1.99937	-1.99928	-1.99932	-55.9024	-55.3149	0.4154	-55.6086	-1.99911	-1.99979	-1.99945	-49.928	-49.9157	0.0087	-49.9219	-1.99352	-1.99901	-1.99626	1400
-2.16076	-2.16674	-2.16375	-57.8928	-58.2686	0.2657	-58.0807	-2.15887	-2.16186	-2.16036	-51.9777	-52.2483	0.1913	-52.113	-2.1601	-2.18122	-2.17066	1500
-2.35189	-2.34851	-2.3502	-60.6504	-60.5464	0.0736	-60.5984	-2.35038	-2.34204	-2.34621	-54.5157	-54.4865	0.0206	-54.5011	-2.35826	-2.32957	-2.34391	1600

Appendix 2 List of tank tests based on PTO simulator

linear PTO				nonlinear PTO				
gain2.083	file name		power	gain2.0833	file name			power
0.4	l2h4		2.126852	0.4	n2h4			1.575264
0.5	l2h5		3.899027	0.5	n2h5			12.42595
0.6	l2h6		16.96543	0.6	n2h6			16.88948
0.7	l2h7		23.14227	0.7	n2h7			20.54341
0.8	l2h8		25.53965	0.8	n2h8			22.49905
0.9	l2h9		27.55386	0.9	n2h9	n2h9+	18.80465	18.37111
1	l2h10		26.00793	1	n2h10			19.83586
1.1	l2h11		22.09705	1.1	n2h11			16.52282
1.2	l2h12		17.25731	1.2	n2h12			14.70764
1.3	l2h13	l2h13+	15.98685	1.3	n2h13			10.77679
1.4	l2h14		11.99179	1.4	n2h14			9.998146
1.5	l2h15		10.21426	1.5	n2h15			8.625464
gain4.166	file name		power	gain4.16667	file name			power
0.4	l4h4	l4h4+	2.499891	0.4	n4h4			1.532153
0.5	l4h5		3.356702	0.5	n4h5			14.26734
0.6	l4h6	l4h6+	5.798309	0.6	n4h6			17.86218
0.7	l4h7		16.54881	0.7	n4h7			22.16668
0.8	l4h8	l4h8+	22.37678	0.8	n4h8			23.9534
0.9	l4h9	l4h9+	28.9144	0.9	n4h9			24.38988
1	l4h10		25.42942	1	n4h10			22.15936
1.1	l4h11		21.02075	1.1	n4h11			16.47653
1.2	l4h12		21.07168	1.2	n4h12			14.48078
1.3	l4h13		16.48852	1.3	n4h13			11.89362
1.4	l4h14		13.76789	1.4	n4h14			9.589508
1.5	l4h15		10.10256	1.5	n4h15			8.115218
gain7.292	file name		power	gain8.3333	file name			
0.4	l7h4		0.22849	0.4	n8h4			0.16812
0.5	l7h5		1.418643	0.5	n8h5			1.255083
0.6	l7h6		5.396532	0.6	n8h6			5.666978
0.7	l7h7		12.05472	0.7	n8h7			10.55281
0.8	l7h8		19.63396	0.8	n8h8			15.92329
0.9	l7h9		25.65374	0.9	n8h9			19.07403
1	l7h10		28.45657	1	n8h10			20.66615
1.1	l7h11		24.38708	1.1	n8h11			17.57582
1.2	l7h12		23.58209	1.2	n8h12			15.74375
1.3	l7h13		20.28346	1.3	n8h13			14.27109
1.4	l7h14		17.00806	1.4	n8h14			10.34475
1.5	l7h15		13.94502	1.5	n8h15			9.127089
gain8.333	file name			gain12.5	file name			
0.4	l8h4		2.268433	0.4	n12h4			0.205497
0.5	l8h5		11.38862	0.5	n12h5	n12h5+	3.880446	1.382594
0.6	l8h6		15.91758	0.6	n12h6			6.57732
0.7	l8h7		21.26905	0.7	n12h7			10.703
0.8	l8h8		28.19487	0.8	n12h8			18.07901
0.9	l8h9	l8h9+	31.47562	0.9	n12h9			20.24966
1	l8h10		35.64547	1	n12h10			21.62742
1.1	l8h11		30.30645	1.1	n12h11			20.1306
1.2	l8h12		25.70568	1.2	n12h12			19.20518
1.3	l8h13		21.60613	1.3	n12h13			15.66934
1.4	l8h14		16.25685	1.4	n12h14			12.50026
1.5	l8h15		12.70901	1.5	n12h15			10.29631
gain9.375	file name		power	gain16.66667				
0.4	l9h4		0.226261	0.4	n16h4			1.691862
0.5	l9h5		1.337064	0.5	n16h5			14.95307
0.6	l9h6		4.898636	0.6	n16h6			18.74279
0.7	l9h7		15.17298	0.7	n16h7			23.8699
0.8	l9h8		23.08762	0.8	n16h8			27.13175
0.9	l9h9		34.27396	0.9	n16h9	n16h9+	22.8892	28.52431
1	l9h10		36.22836	1	n16h10	n16h10+	27.09211	28.34693
1.1	l9h11		31.66685	1.1	n16h11			21.90042
1.2	l9h12		25.47993	1.2	n16h12			18.45218
1.3	l9h13		21.84643	1.3	n16h13			16.11669
1.4	l9h14		16.19638	1.4	n16h14			13.4545
1.5	l9h15		12.32857	1.5	n16h15			10.27234

gain10.4166667			power	gain 18.75	file name			power
0.4	l10h4		0.094043	0.4	n18h4			0.003203
0.5	l10h5		1.326263	0.5	n18h5			3.647388
0.6	l10h6		5.65045	0.6	n18h6			5.940639
0.7	l10h7		12.25445	0.7	n18h7			12.0298
0.8	l10h8		19.81184	0.8	n18h8			17.76608
0.9	l10h9		26.77303	0.9	n18h9			21.43311
1	l10h10		31.97557	1	n18h10	n18h10+	23.08867	23.23385
1.1	l10h11		28.05292	1.1	n18h11			20.03657
1.2	l10h12		26.86885	1.2	n18h12	n18h12+	16.09628	16.92828
1.3	l10h13		22.82913	1.3	n18h13			17.60679
1.4	l10h14		19.45016	1.4	n18h14			12.05311
1.5	l10h15		14.3472	1.5	n18h15	n18h15+	48.28246	10.27548
gain12.5			power	gain20.833	file name			power
0.4	l12h4		-0.00931	0.4	n20h4			0.180002
0.5	l12h5		1.100286	0.5	n20h5			1.2739
0.6	l12h6		5.258874	0.6	n20h6			6.233396
0.7	l12h7		11.47932	0.7	n20h7			11.87353
0.8	l12h8		19.82483	0.8	n20h8			20.74849
0.9	l12h9		27.64789	0.9	n20h9	n20h9+	20.48626	24.23732
1	l12h10		32.41327	1	n20h10			22.91591
1.1	l12h11		31.48101	1.1	n20h11			21.7348
1.2	l12h12		25.17087	1.2	n20h12			19.92002
1.3	l12h13		24.03979	1.3	n20h13			15.57449
1.4	l12h14		19.15833	1.4	n20h14			14.75822
1.5	l12h15		14.41298	1.5	n20h15	n20h15+	41.66349	11.80592

Appendix 3 List of tank tests based on AIReaTHM

Regular wave tests

wave frequency	0.17				
wind	8mps	10mps	12mps	14mps	16mps
CaseID_ARX	fd255	fd231	fd222,fd223	fd239	fd247,
CaseID_constant thrust			fd263		
CaseID_only wave					
case_id only ARXnowave			fd285		
wave frequency	0.27				
wind	8mps	10mps	12mps	14mps	16mps
CaseID_ARX	FD079	FD080	FD081	FD082	FD083
CaseID_constant thrust	FD084	FD085	FD086	FD087	FD088
case_id only ARXnowave	fd078	FD092	FD091	FD090	FD089
case_id only ARXnowave	fd078	FD092	FD091	FD090	FD089
CaseID_only wave NO THRUST			FD093		
wave frequency	0.37				
wind	8mps	10mps	12mps	14mps	16mps
CaseID_ARX	fd256	fd232	fd224	fd240	f248
CaseID_constant thrust			fd264		
CaseID_only wave			fd286		
wave frequency	0.47				
wind	8mps	10mps	12mps	14mps	16mps
CaseID_ARX	fd257	fd233	fd225	fd241	fd249
CaseID_constant thrust			fd265		
CaseID_only wave			fd287		
wave frequency	0.57				
wind	8mps	10mps	12mps	14mps	16mps
CaseID_ARX	fd258	fd234	fd226	fd242	fd250
CaseID_constant thrust			fd266		
CaseID_only wave			fd288		
wave frequency	0.688				
wind	8mps	10mps	12mps	14mps	16mps
CaseID_ARX	FD016	FD019 FD022			
CaseID_constant thrust	FD017				
CaseID_no wind	FD018				
wave frequency	0.688				
wind	8mps	10mps	12mps	14mps	16mps
CaseID_ARX	FD045	FD024 FD025	Fd026 Fd027	FD030 Fd031	fd032 FD033
CaseID_constant thrust	FD43	fd41	FD039	FD037	FD035
case_id only ARXnowave	FD046	FD047	FD028	Fd029	FD034
CaseID_only wave	FD044	FD42	fd040	FD038	FD036
23/0					
wave frequency	0.78				
wind	8mps	10mps	12mps	14mps	16mps
CaseID_ARX	fd259	fd235	fd227	fd243	fd251
CaseID_constant thrust			fd267		
CaseID_only wave			fd289		
only ARX		fd281	fd280	fd283	fd284
wave frequency	0.88				
wind	8mps	10mps	12mps	14mps	16mps
CaseID_ARX	fd260	fd236	fd228	fd244	fd252
CaseID_constant thrust			fd268		
CaseID_only wave					
only ARX					
wave frequency	0.954				
wind	8mps	10mps	12mps 4/0	14mps	16mps
CaseID_ARX	FD066	FD068	FD069	FD070	FD071
CaseID_constant thrust	FD067	FD072	FD073	FD074	FD075 FD076 Fd077
case_id only ARXnowave		FD095			
CaseID_only wave NO THRUST			FD094		
23/0	fd276	fd293	fd271	fd294	fd295

wave frequency	1.05				
wind	8mps	10mps	12mps	14mps	16mps
CaseID_ARX	fd261	fd237	fd229	fd245	fd253
CaseID_constant thrust			fd269		
CaseID_only wave			fd290		
wave frequency	1.15				
wind	8mps	10mps	12mps	14mps	16mps
CaseID_ARX	fd262	fd238	fd230	fd246	fd254
CaseID_constant thrust			fd270		
CaseID_only wave			fd291		
wave frequency	1.23				
wind	8mps	10mps	12mps	14mps	16mps
CaseID_ARX	FD065	FD050	FD054	FD056	FD058
CaseID_constant thrust	FD064	FD52	FD061	FD062	FD063
case_id only ARXnowave		FD051	FD055	FD057	FD059
CaseID_only wave(temprarily ignored)			FD053		
Fixed(constant) thrust no wave		fd60			
wave frequency	1.4				
wind	8mps	10mps	12mps	14mps	16mps
CaseID_ARX	FD096	FD098	FD099	FD100	FD102
CaseID_constant thrust					
ONLY WAVE			fd292		
case_id only ARXnowave					FD101

Irregular wave tests

turbulent 1Case1	Seastate3	Seasate4	Seastate5							
CaseID_AI	FD170	FD171	FD172							
turbulent 3Case3	Seastate1	Seasate2	Seastate4	Seastate5						
	FD212	FD213,FD214	FD216	FD215						
turbulent 4Case4	Seastate1	Seasate2	Seastate4	Seastate5						
SEASATE3Case3	Turbulent 1	turbukent2	turbulent4	turbulent5						
	fd300	fd301	fd302	fd303						
HALF PERIOD SEASTATE										
CASE description	CASE1	CASE1+	CASE2	CASE2+	CASE3	CASE3+	CASE4	CASE4+	CASE5	CASE5+
CaseID_ARX	FD110 FD114	FD112	FD115	FD156	FD153	FD162	FD154	FD163,FD164	FD155	FD165
CaseID_constant thrust										
case_id only ARXnowave	FD111,FD161	FD113,	FD160	FD169	FD159	FD168	FD158	FD167	FD157	FD166
CaseID_only wave NO THRUST										
WHOLE PERIIOD SEASTATE										
CASE1	CASE1	CASE1+	CASE2	CASE2+	CASE3	CASE3+	CASE4	CASE4+	CASE5	CASE5+
CaseID_ARX	FD116,FD122,fd181	FD139	FD117.fd179	FD141	FD123	FD143	FD125	FD145	FD127	FD147
CaseID_constant thrust	FD129	FD130	FD131	FD132	FD133	FD134	FD135	FD136	FD137	FD138
case_id only ARXnowave	FD121	FD140	FD118	FD142(INVALID)	FD124	FD144	FD126	FD146	FD128	FD148
CaseID_only wave NO THRU	FD119		FD120		FD151		FD150		FD149	

Appendix 4 Figures for free decay tests in Section 7.3

A4. 1 Free decay in platform surge under zero thrust

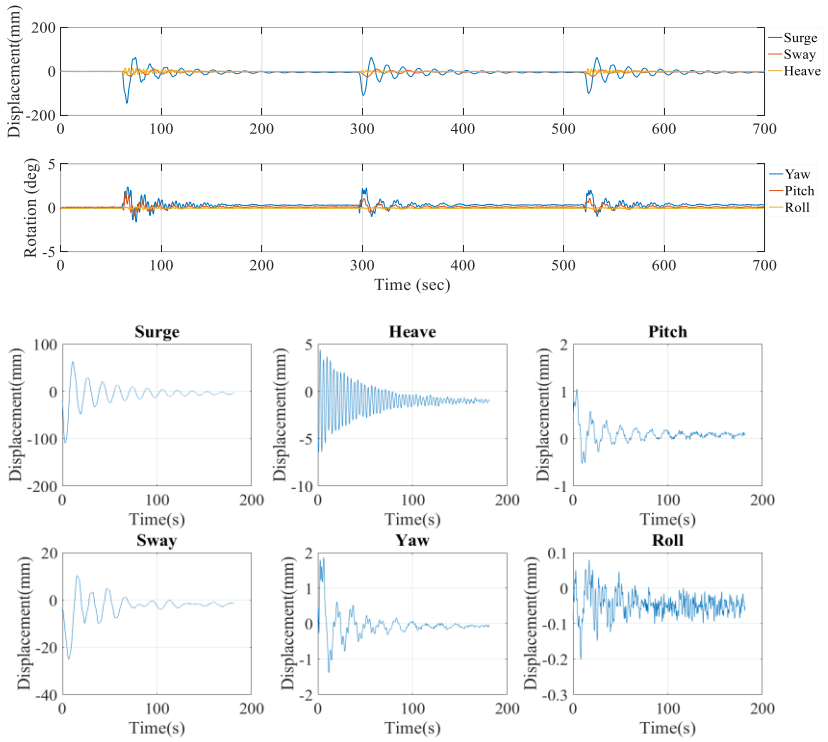

A4. 2 Free decay in platform sway under zero thrust

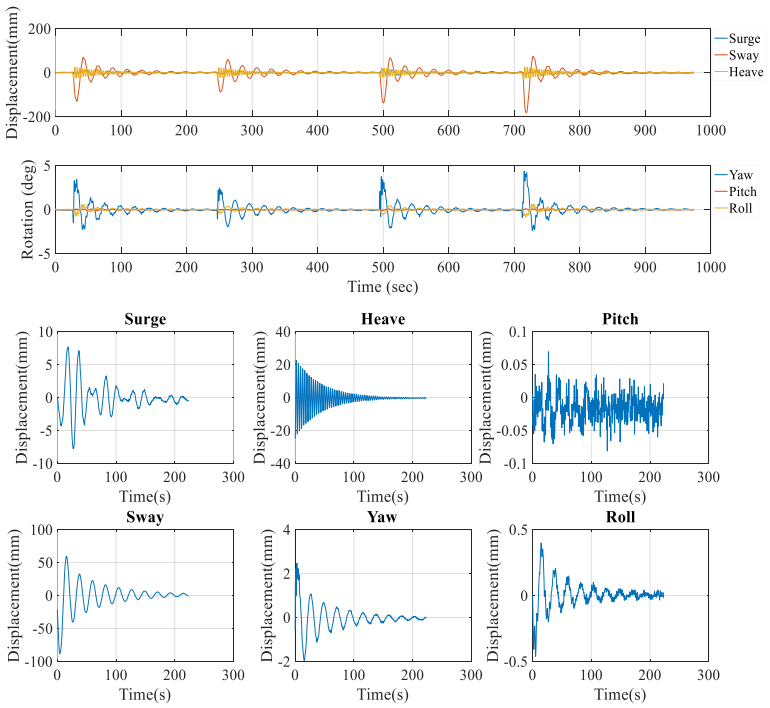

A4. 3 Free decay in platform heave under zero thrust

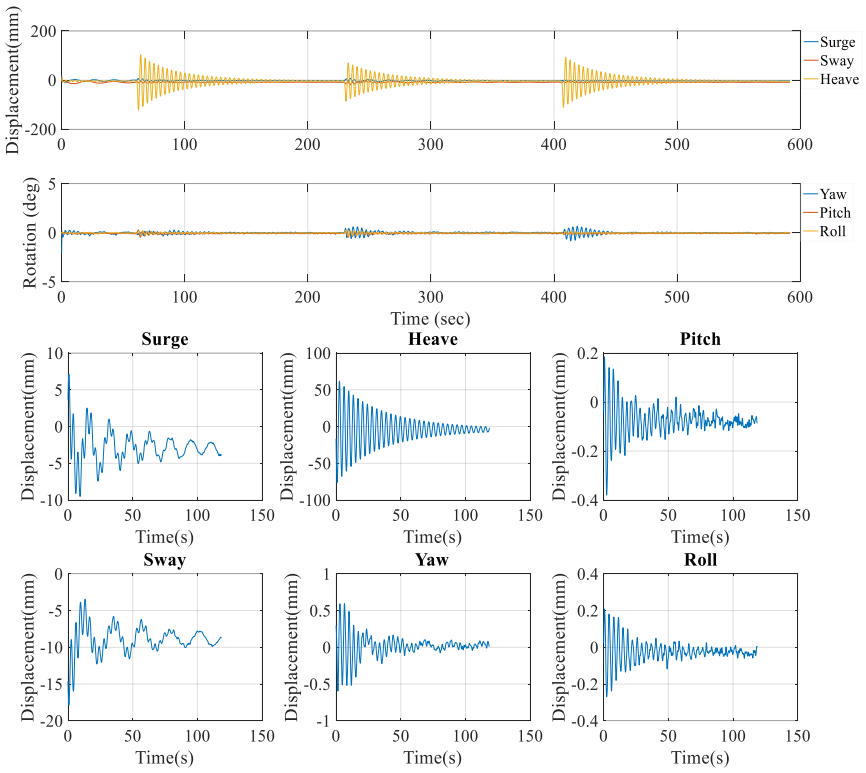

A4. 4 Free decay in platform yaw under zero thrust

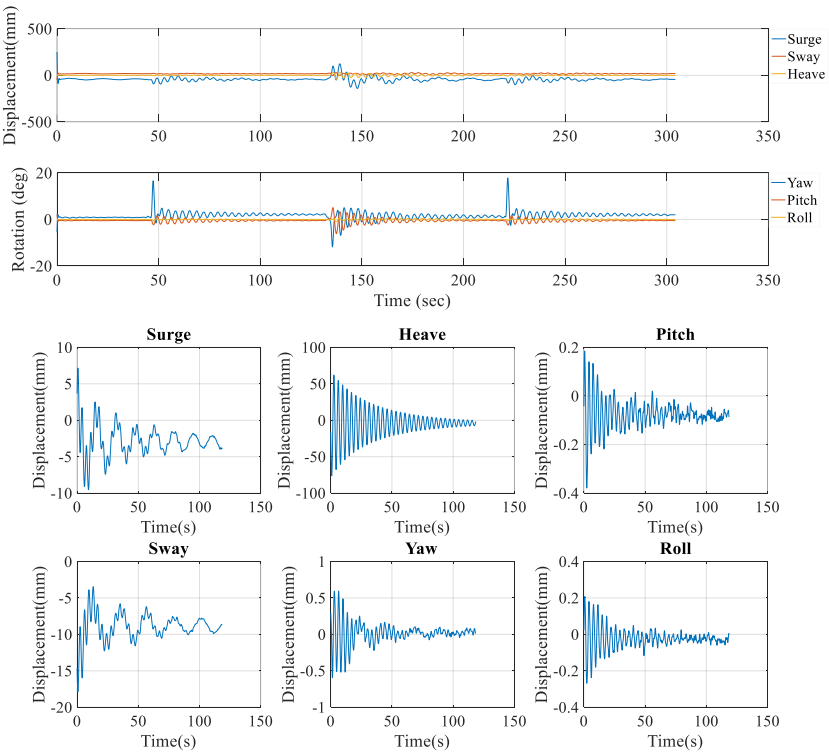

A4. 5 Free decay in platform roll under zero thrust

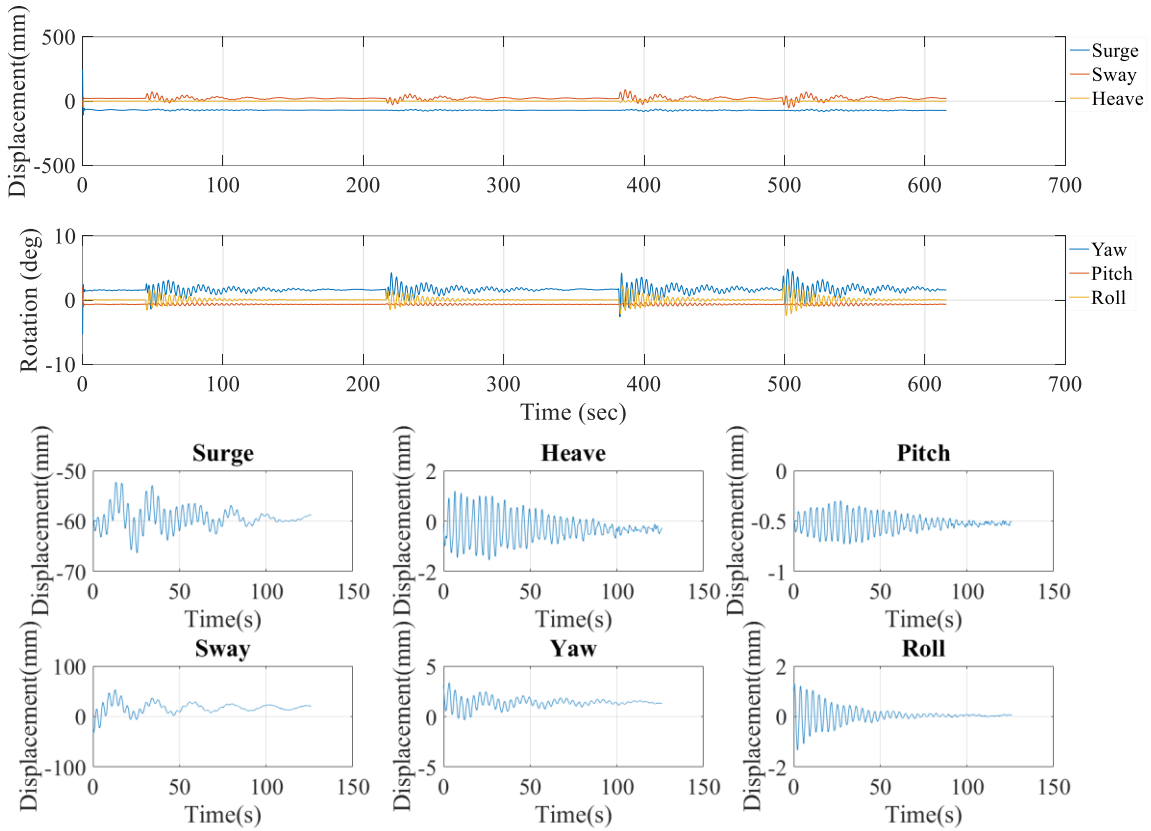

A4. 6 Free decay in platform surge under a constant rotor thrust

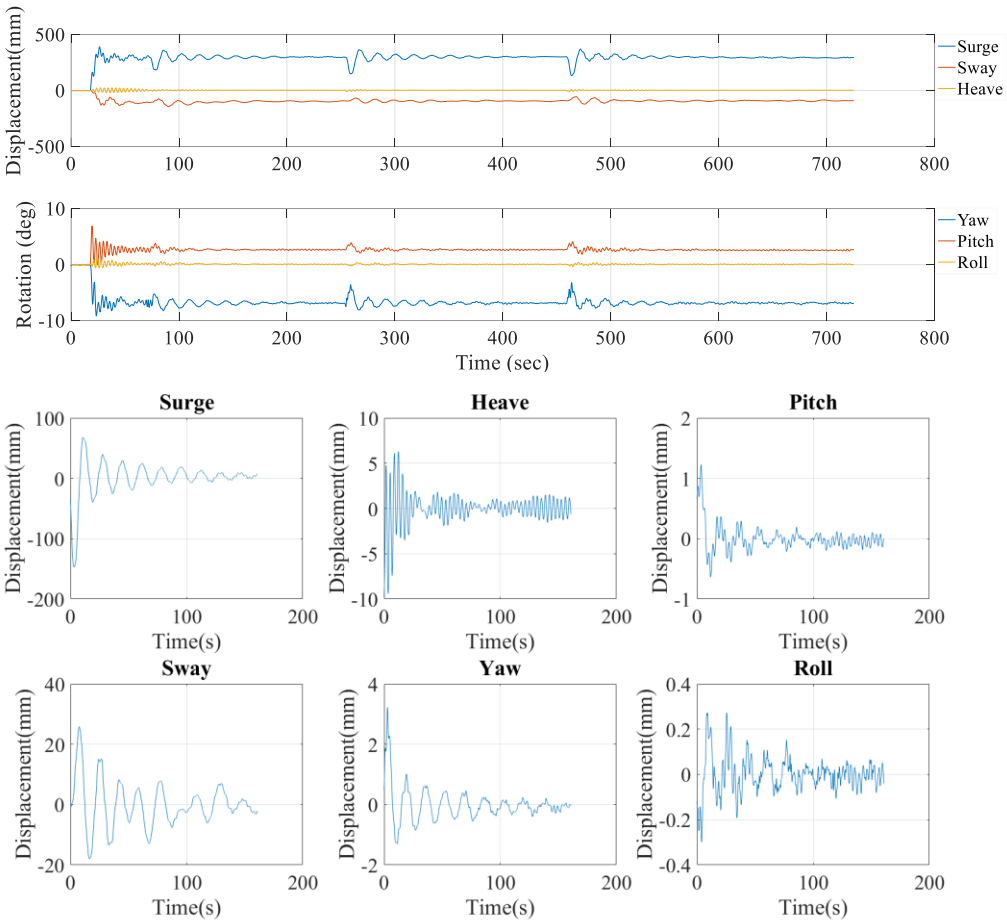

A4. 7 Free decay in platform sway under a constant rotor thrust

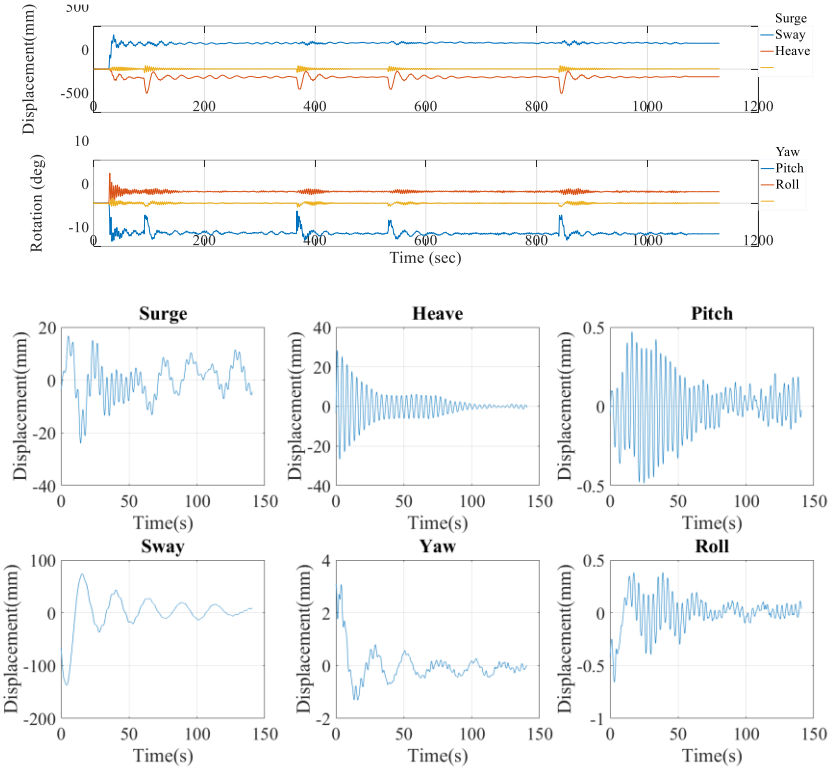

A4. 8 Free decay in platform heave under a constant rotor thrust

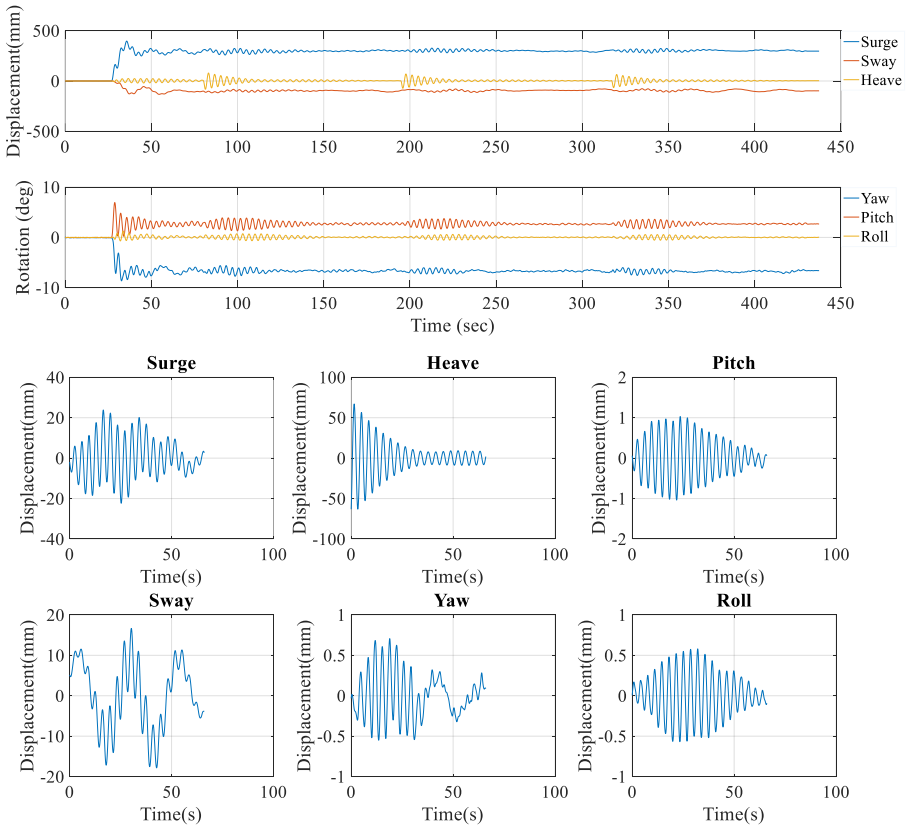

A4. 9 Free decay in platform yaw under a constant wind speed

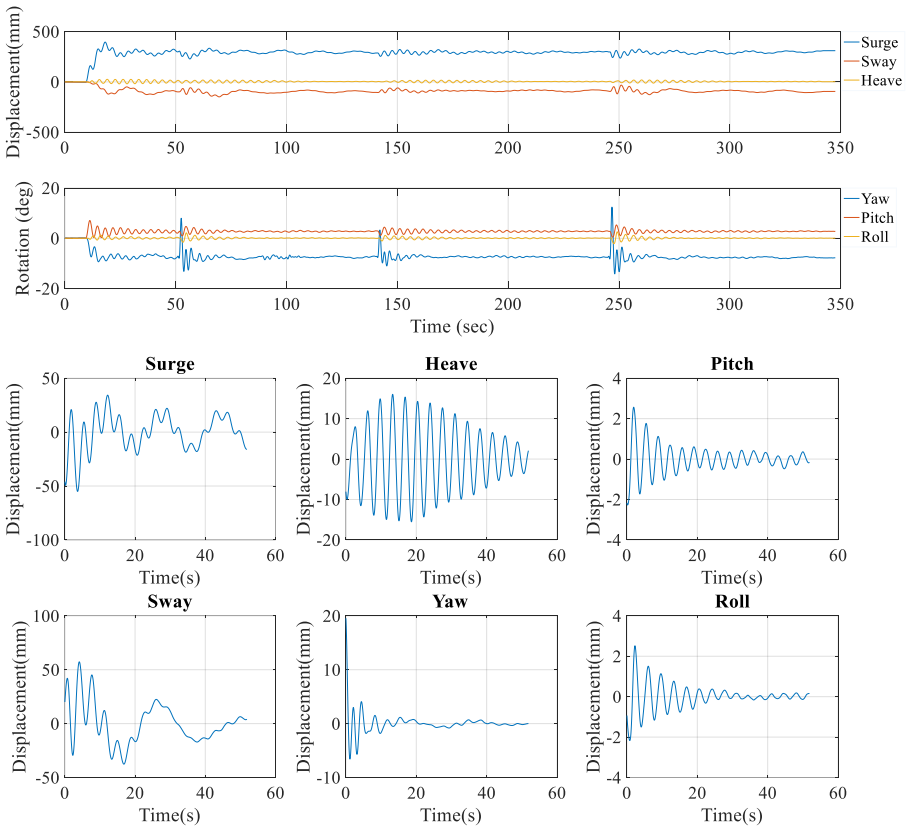

A4. 10 Free decay in platform roll under a constant wind speed

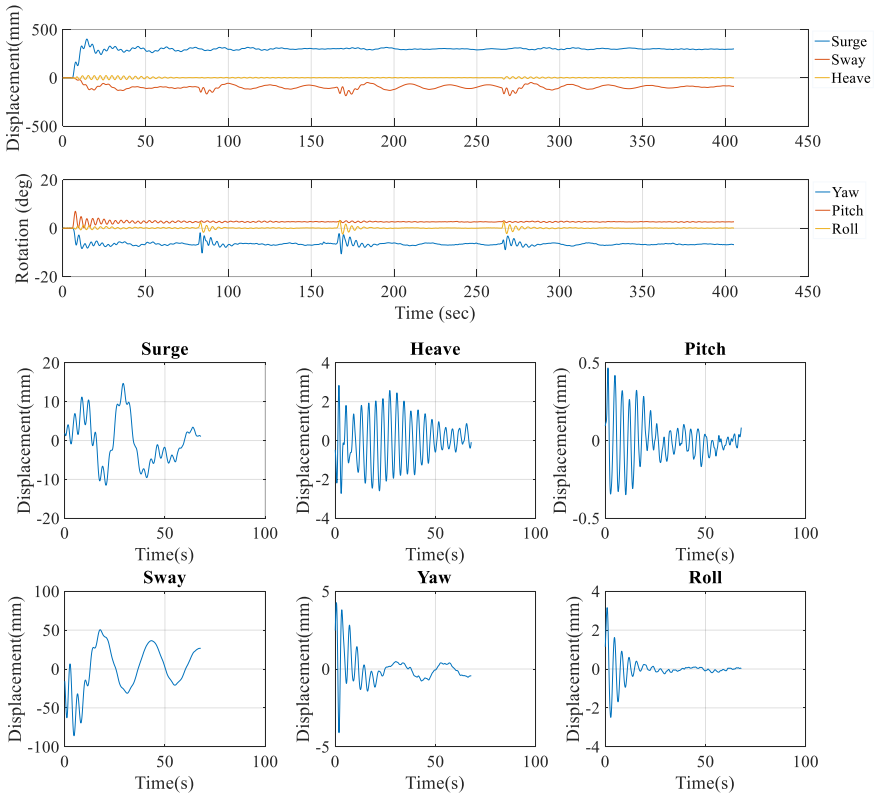

Appendix 5 Video files for experiment procedure

Find the files by the link below, because of the file size is too big to share directly here

https://strathcloud.sharefile.eu/d-sbde0469dfe14422a

Appendix 6 Supplementary data for Chapter 6

You can download the supplementary data for chapter 6 by the link below

https://www.sciencedirect.com/science/article/pii/S0029801818319103#appsec1